Functional magnetic resonance imaging of the mouse brain

Arun Niranjan

Submitted in fulfilment of the requirements for the degree of

Doctor of Philosophy of University College London

March 2017

Supervisors

Prof. Mark Lythgoe

Dr. Jack Wells

Centre for Advanced Biomedical Imaging

University College London

UK

Declaration

I, Arun Niranjan, confirm that the work presented in this thesis is my own. Where information has been derived from other sources, I confirm that this has been indicated in the thesis. This thesis describes independent research undertaken by myself, from September 2013-16.

Arun Niranjan

12th October 2016

Abstract

Functional magnetic resonance imaging (fMRI) measuring a blood-oxygen-level dependent (BOLD) signal is the most commonly used neuroimaging tool to understand brain function in humans. As mouse models are one of the most commonly used neuroscience experimental models, and with the advent of transgenic mouse models of neurodegenerative pathologies, there has been an increasing push in recent years to apply fMRI techniques to the mouse brain. This thesis focuses on the development and implementation of mouse brain fMRI techniques, in particular to describe the mouse visual system.

Multiple studies in the literature have noted several technical challenges in mouse fMRI. In this work I have developed methods which go some way to reducing the impact of these issues, and I record robust and reliable haemodynamic-driven signal responses to visual stimuli in mouse brain regions specific to visual processing. I then developed increasingly complex visual stimuli, approaching the level of complexity used in electrophysiology studies of the mouse visual system, despite the geometric and magnetic field constraints of using a 9.4T pre-clinical MRI scanner. I have also applied a novel technique for measuring high-temporal resolution BOLD responses in the mouse superior colliculus, and I used this data to improve statistical parametric mapping of mouse brain BOLD responses. I also describe the first application of dynamic causal modelling to mouse fMRI data, characterising effective connectivity in the mouse brain visual system.

This thesis makes significant contributions to the reverse translation of fMRI to the mouse brain, closing the gap between invasive electrophysiological measurements in the mouse brain and non-invasive fMRI measurements in the human brain.

Acknowledgements

I would like to thank both my supervisors, Jack Wells and Mark Lythgoe, for the opportunity to conduct the research described in this thesis. They have both been incredibly patient with me, and given me space, time, and most importantly trust, to develop into an independent scientist. I additionally thank my collaborators Sam Solomon and Peter Zeidman for their advice on biological theory and fMRI analysis.

I am incredibly grateful to have worked at the Centre for Advanced Biomedical Imaging (CABI), where I have made great friends and generally had a very positive experience. Thanks go to all past and present CABI members, and in particular to Isabel Christie, Ben Duffy, Raj Ramasawmy, Tom Roberts, Holly Holmes, James O'Callaghan, Nick Powell, Ma Da, Bernard Siow, Tammy Kalber, John Connell, Ian Harrison, Morium Ali, Oz Ismail, Laurence Jackson, Yanan Zhu, Angela d'Esposito, Eoin O'Finnerty and Ben Jordan, amongst others. Best of luck to Payam Nahavandi who will be building on much of the work presented in this thesis.

I also wish to thank my family; my parents, my two younger brothers and my grandmother, for all their love and support. Finally the strongest thanks go to my partner Emma, without whom I wouldn't have made it at all.

Publications arising from this research

Papers in peer-reviewed journals

1. **Niranjan A**, Christie IN, Solomon SG, Wells JA, Lythgoe MF.

   fMRI mapping of the visual system in the mouse brain with interleaved snapshot GE-EPI (*NeuroImage (2016), Vol 139, pg. 337-345*).

2. **Niranjan A**, Siow BM, Lythgoe MF, Wells JA.

   High temporal resolution BOLD responses to visual stimuli in the mouse superior colliculus (*Science Matters, 2017*).

3. **Niranjan A**, Zeidman P, Wells JA, Lythgoe MF.

   Effective connectivity of the mouse visual pathway characterised using dynamic causal modelling for fMRI (*in preparation*).

4. Hosford PS, Christie IN, **Niranjan A**, Wells JA, Lythgoe MF, Tinker A, Gourine AV.

   Mice lacking the Kir6.1 subunit exhibit mild brain hypoxia but no differences in sensory evoked fMRI BOLD responses (*in preparation*).

Selected conference abstracts

2016

Niranjan A, Zeidman P, Wells JA, Lythgoe MF. Exploring visual network connectivity in the mouse brain using DCM fMRI; *International Society for Magnetic Resonance in Medicine Annual Meeting (abstract no. 1675)*

2015

Niranjan A, Wells JA, Lythgoe MF. Mapping the Visual Pathway in the Mouse Brain using Snapshot fMRI; *The Physiological Society Annual Meeting (abstract no. C69)*

Niranjan A, Wells JA, Lythgoe MF. Mapping the Visual Pathway in the Mouse Brain using Snapshot fMRI; *International Society for Magnetic Resonance in Medicine Annual Meeting (abstract no. 2036)*

2014

Niranjan A, Wells JA, Lythgoe MF. Mapping the Visual Pathway in the Mouse Brain using Snapshot fMRI; *British Chapter of the International Society for Magnetic Resonance in Medicine Annual Meeting*

Niranjan A, Wells JA, Lythgoe MF. Development and Optimisation of Resting State fcMRI in the Mouse Brain at 9.4T; *International Society for Magnetic Resonance in Medicine Annual Meeting (abstract no. 3054)*

Niranjan A, Wells JA, Lythgoe MF. Development and Optimisation of Resting State fcMRI in the Mouse Brain at 9.4T; *Postgraduate Symposium of the British Chapter of the International Society for Magnetic Resonance in Medicine*

Awards and achievements

Niranjan A, Wells JA, Lythgoe MF. Mapping the Visual Pathway in the Mouse Brain using Snapshot fMRI; *The Physiological Society Annual Meeting (abstract no. C69) – Oral Communication Prize*

Contents

List of figures

List of tables

1 Introduction

This chapter introduces the thesis, and gives context and motivation for the research described. Section 1.1 gives the motivation for using fMRI to understand brain function. Then in section 1.2, the use of animal models for neuroscience research is described, with the importance of translation and reverse translation covered. Section 1.3 briefly covers alternative techniques for measuring mouse brain function, and in section 1.4, a review of task-based BOLD fMRI studies of the mouse brain is provided. Sections 1.5 and 1.6 introduce the mouse brain and key visual areas, and in section 1.7 the concept of neurovascular coupling in the context of BOLD fMRI is described. Finally in section 1.8, an outline of the thesis is given.

1.1 Motivation for using fMRI

The human brain is one of the most difficult organs to study [1]. There are numerous techniques which attempt to generate knowledge about brain structure and function. Unlike other organs such as the heart or lungs, it is often unclear how brain function derives from structure, and so surrogate markers for brain function are often used instead. More interestingly, it also not obvious how brain function generates such complex behaviours in humans, and one task of neuroscience is to hypothesise, test and model such mechanisms.

Consequently, diseases which affect the brain can be extremely difficult to understand. Such diseases include Alzheimer’s disease, Parkinson’s disease, epilepsy and others. An understanding of healthy brain function allows diseased brains to be better defined, and lead to new treatments for these diseases.

The human brain can be examined in multiple ways, depending on the scope of the research question [2]. It is common to study the brain at one of four levels of scale, which in increasing scale are: the molecular level, the cellular level, the cell population level and the network level. Additionally, neuroscience methods can study the brain before death (*in vivo*) or after (*ex vivo*), or in terms of brain tissue artificially kept alive (*in vitro*). Many gains in understanding brain structure have been achieved using *ex vivo* human brains. However studying brain function *ex vivo* is somewhat limited, and whilst *in vitro* studies are useful for answering questions on the molecular and cellular level, they can struggle to generalise to the cell population or network level. Therefore *in vivo* studies are critical for understanding brain function.

However, studying the human brain *in vivo* is challenging. Historically, case studies of individuals surviving accidental brain injuries, such as Phineas Gage suffering from a personality disorder [3] after an iron bar was driven through the front of his brain, have been used to make direct causal inferences on brain function. More recently, minimally invasive methods of studying the human brain have been developed and are widely used, such as functional magnetic resonance imaging (fMRI) [4, 5], electroencephalography (EEG) [6, 7], or positron emission tomography (PET) [8, 9]. The use of non-invasive imaging techniques reduces the ethical burden of performing scientific experimentation on humans, and makes it more straight-forward for studying patient populations.

This thesis focuses on the use of fMRI, which typically uses regional changes in blood oxygenation (the BOLD signal, using image contrast endogenous to the brain) to make inferences on brain function. The discovery of BOLD contrast is credited to Seiji Ogawa, who demonstrated BOLD weighted images with highlighted vasculature in the rat brain in 1990 [5], and suggested that temporal changes in BOLD contrast might reflect neuronal activity. The first description of BOLD fMRI in the human brain was given by Brady in 1991 [10], however the first published work was completed by Bandettini et al. in 1992 [11] using a motor paradigm. Brady’s work was published soon after (Kwong et al. 1992) [12], and was the first work to describe BOLD responses in the human brain to blocks of visual stimuli. This was followed by work by Blamire et al. [13], which for the first time implemented an event-related fMRI paradigm. Since these studies, there has been a continued discussion on how to interpret the BOLD signal and make inferences on neuronal activity based on neurovascular coupling (see section 1.7) [14-19]. However, it is generally accepted that changes in the BOLD signal can be used as a proxy variable to represent changes in neuronal activity [20], although the idea of neuronal activity is itself difficult to define [21].

Inevitably, each technique used to study brain function has certain advantages and limitations. It is therefore important for the scientific community to use multiple complementary methods. Furthermore, it is important that these techniques can be applied across species for two reasons. One, that more invasive techniques can be used for validating conclusions made with non-invasive techniques, overall strengthening the body of scientific evidence. Two, animal models of disease can be investigated with both invasive and non-invasive techniques, where it would be unethical to use human patients, in order to better understand disease progression and treatment.

1.2 The use of mouse models

Where invasive measurements in humans cannot be performed, animal models are often used as a substitute. Animal models used in neuroscience have ranged from insects through to monkeys, with varying degrees of complexity and ethical considerations. For examining brain function with fMRI, monkey models have been the focus of much previous research [22], although cats [23], dogs [24] and rats [25] have also been used. Indeed, rodent fMRI is increasingly on the rise, as rodents are cheaper, safer and easier to use relative to larger mammals [26].

Increasingly, the mouse is becoming an attractive neuroscience model. This is because of the possibility of using transgenic mouse models [27] as a way of using genetic manipulation to test scientific hypotheses on brain function [28, 29]. This makes the reverse translation of current human imaging techniques extremely important – transgenic mouse models of disease can be used to make inferences on pathology and treatment, with biomarker readouts matching those used in human patients.

The work in this thesis uses the most commonly used mouse strain for animal research, the C57BL/6 mouse[1], which was the first mouse strain to have its entire genome sequenced [30]. The use of this model is advantageous for two reasons. First, it is the genetic background for many transgenic mouse models, and therefore protocols should be generalisable in studying these models. Second, the widespread use of the C57BL/6 mouse means that it is increasingly seen as a standard subject for functional neuroscience experiments, allowing better comparison in the literature between the work in this thesis and other studies using alternative techniques.

1.3 Alternative techniques for studying mouse brain function

One of the reasons fMRI is commonly used in humans for investigating brain function is the non-invasiveness of the technique. However for asking questions about mouse brain biology, fMRI has not been used historically used due to its many technical challenges, and more invasive techniques have been used to

---

[1] see http://www.criver.com/files/pdfs/rms/c57bl6/rm_rm_d_c57bl6n_mouse.aspx

investigate mouse brain function. A summary of the advantages and disadvantages of a range of experimental techniques used in mouse functional neuroimaging is given in Table 1.1. To the best of my knowledge, functional PET and SPECT imaging has never been applied in the mouse brain, and these techniques are therefore not considered here.

Table 1.1 Overview of functional neuroimaging methods used in the mouse brain (partially adapted from Martin et al. 2014 [1])

Technique	Data acquired	Advantages	Disadvantages
fMRI - BOLD [31-40]	BOLD signal, weighted by ratio of oxy-deoxy-haemoglobin.	Cross-species, whole brain acquisition. Generally non-invasive. Can be easily combined with 3D structural MRI data.	Expensive, requires strong magnetic field, mediocre spatial and temporal resolution (~500 microns in-plane, 2 seconds)
Optical imaging spectroscopy [41-43]	Oxy-, deoxy-, total haemoglobin concentration	Good spatial and temporal resolution (~150 ms)	Limited depth penetration (cortical surface only)
multi-photon microscopy [44, 45]	Blood flow, tissue oxygen, microcirculation, cellular activity	Excellent spatial and temporal resolution, can measure both neuronal and vascular variables	Expensive, limited depth penetration
Invasive electrophysiology [46-51]	Single or multi-unit activity, local field potentials	Highly localised recording, optimal temporal resolution	Risk of tissue damage from electrodes, limited compatibility with other techniques, limited spatial coverage
Electroencephalography (EEG) [52]	Event-related potentials, current sources/sinks	High temporal resolution, low cost in humans, non-invasive	Limited spatial resolution, poor spatial localisation of signal

As can be seen in Table 1.1, fMRI is limited in terms of spatial and temporal resolution relative to all other techniques, and requires a strong magnetic field. Additionally, this is balanced against the type of data that is acquired, (in this thesis only BOLD fMRI is considered), which is at best a proxy variable for neuronal activity.

Although this thesis specifically considers the implementation of BOLD fMRI in the mouse brain using visual stimuli, it is worth briefly considering how the alternative techniques operate and the data they generate.

Invasive electrophysiology and electroencephalography

The history of electrophysiology is long and varied, and a detailed account is given by Verkhratsky and Parpura [53]. A brief summary of the technique is given here. In the case of neuroscience, electrophysiology refers to the measurement of electrical activity in neurons, in particular signals derived from action potentials. The measurement of these signals in electrophysiology is characterised by the use of electrodes, either solid conductors or hollow glass pipettes filled with an electrolyte solution. The interpretation of the electrical signals (voltage and current) measured depends on the size and positioning of the electrode. Electrodes with the finest tips (scale on the order of microns) can be used to perforate or adhere to cells to make intra-cellular recordings in single neurons. Larger electrodes may be placed in the space next to multiple cells to make extra-cellular recordings. As electrodes increase in size their coverage increases, but the specificity of the signal they report is reduced. The net activity of many cells is termed a local field potential (LFP). Electroencephalography (EEG) builds on invasive electrophysiology by placing electrodes on the scalp, and whilst being non-invasive in humans, is limited by poor spatial localisation of signal. As shown in Table 1.1, for investigating mouse brain function, invasive measures are far more common than the use of EEG.

Electrophysiology with invasive electrodes directly measures neuronal activity, with temporal resolution of the order of milliseconds. However, there is a strict compromise between coverage of the brain and spatial localisation of the signal acquired.

Optical imaging spectroscopy

Optical imaging spectroscopy was first described by Grinvald et al. [54], implemented in both rat and cat cortex. As with microscopy techniques, a cranial window or thinning of the skull is required for light to reach the surface of the brain. Incident light (of wavelength ~590 nm) on the surface is then reflected into a photo-detector, and changes in reflectance used to infer changes in haemoglobin content, specifically relative changes in oxy – and de-oxy haemoglobin. Under certain assumptions this can be used to calculate direct concentrations of these haemodynamic variables, and then used to also infer changes in blood flow (CBF), blood volume (CBV) and oxygen consumption ($CMRO_2$) [55].

Multi-photon microscopy

A detailed review of two-photon microscopy is given by Svoboda and Yasuda [56], from which Figure 1.1 is reproduced below.

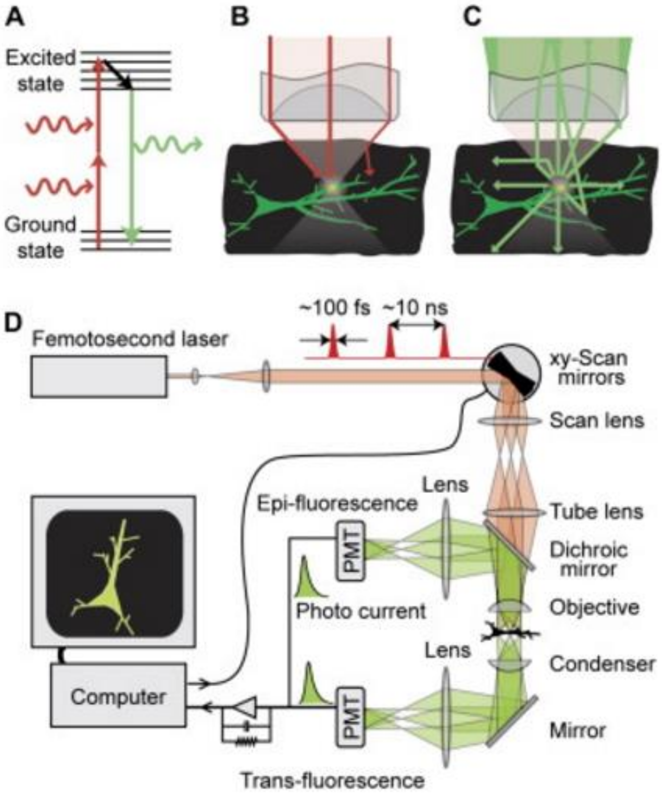

Figure 1.1. Two-photon excitation microscopy (adapted from Svoboda and Yasuda 2006, Figure 1 [56]). The original caption reads as follows, “
Two-Photon Excitation [*2PE*] Microscopy
(A) Simplified Jablonski diagram of the 2PE process.
(B) Localization of excitation in a scattering medium (black). The excitation beam (red) is focused to a diffraction-limited spot by an objective where it excites green fluorescence in a dendritic branch, but not in a nearby branch. The paths of two ballistic photons and one scattered photon are shown (red lines). Scattered photons are too dilute to cause off-focus excitation. The intensity of the beam decreases with depth as an increasing number of excitation photons are scattered.
(C) Fluorescence collection in a scattering medium. Fluorescence photons are emitted isotropically from the excitation volume (red lines). Even scattered fluorescence photons contribute to the signal if they are collected by the objective. Since the field of view for detection is larger than for excitation, the fluorescence light exiting the objective back-aperture will diverge substantially (green).
(D) Schematic of a 2PE microscope with epifluorescence and transfluorescence detection.”

More traditional microscopy techniques (either fluorescence or reflectance based) are limited in depth penetration due to light scattering from tissue above and below the focal plane of the image. In two-photon microscopy, a fluorescent dye molecule is used which must absorb two photons (in infrared region, 700 – 1000nm) before emitting a photon at a shorter wavelength than the excitation wavelength [57]. This means that the excitation photons can travel further into the tissue without being scattered, and with a line scanning mechanism, only excitation in a focal volume can occur. Due to nonlinear excitation, excitation photons which are scattered by tissue are too dilute to induce fluorescence.

It is the use of calcium ion specific fluorescent dyes such as Oregon Green BAPTA [58] which allow two-photon microscopy to image brain function. This allows the calcium ion concentration within cells to be imaged, an important mediator of the electrical activation of a neuron.

Summary

Of the listed techniques, it is only fMRI that offers concurrent signal measures with whole brain coverage and good spatial localisation of signal. Under the assumption that the BOLD signal is an accurate reflection of neuronal activity, responses to stimuli at multiple locations can be measured near simultaneously in the same experiment. In addition to the importance of reverse translation of a commonly used neuroimaging technique from human to mouse, it is also reasonable to suggest that fMRI is a sensible choice for investigating networks in the mouse brain, and how deeper brain structures might communicate and function with respect to the cortex.

1.4 A review of mouse brain fMRI

There is an increasingly growing body of literature describing task-based BOLD fMRI (i.e. fMRI conducted with the use of external stimuli, with measurement of the BOLD signal) applied to the mouse brain [31-40]. However, these studies all note that generating robust and reliable data is difficult in the mouse brain. The small size of the mouse brain necessitates the use of MRI scanners with strong magnetic field (ranging from 7-11.7 Tesla, approximately 200,000 times stronger than the Earth's magnetic field) to ensure adequate signal-to-noise. The difficulties of maintaining suitable physiological conditions for mouse fMRI have also been described, with a number of different protocols and strategies advocated.

The first study implementing mouse brain fMRI was conducted by Huang et al. 1996 [31]. This study used a visual stimulus, and reported extremely atypical data relative to current knowledge of mouse brain function [26] and data since acquired in the rat brain using similar paradigms [59, 60]. The next description of a task-based fMRI study in the mouse was given by Ahrens and Dubowitz in 2001 [34], using somatosensory stimuli (electric shocks to the mouse hindpaw), and this is the first study to report BOLD responses that correlate with the stimulus paradigm and were somewhat specific to somatosensory regions of the mouse brain. The use of paw stimulation in mouse fMRI, with BOLD responses in the somatosensory cortex as a functional read-out, has since been extensively used by Nair and Duong [32], Adamczak et al. [33], the Rudin group in Zurich [35, 36, 38, 40, 61], and Nasrallah et al. [37]. The aims of these papers have ranged from trying to better understand neurovascular coupling in the mouse brain to investigations of pain. However as Schroeter et al. [38] demonstrated in 2014, the use of paw stimulation as a stimulus paradigm for mouse fMRI is problematic due to non-specific BOLD responses and global changes in physiology directly induced by the stimulus. This means that commonly used analysis techniques such as statistical parametric mapping could over-report BOLD responses that are not directly due to neuronal activity.

All of these studies used anaesthetised mice, with isoflurane, medetomidine and alpha-chloralose the most commonly used, and based on these studies medetomidine was chosen as a suitable anaesthetic agent for the work in this thesis. It should be noted that there is a single task-based fMRI study in the awake mouse by Harris et al. [39], which uses a visual cue to mediate a fear task. This study is discussed with the study conducted by Huang et al. [31] in some detail in section 3.3.

At the beginning of this project, only the study by Huang et al. had described an attempt at mouse brain fMRI with visual stimuli, whereas increasingly rich fMRI data for visual stimuli in the rat was available [59, 60, 62-64]. Hence the first aim of this thesis was to develop a robust protocol for mouse fMRI with visual stimuli, using up-to-date data processing and analysis commonly used in human fMRI studies. The next aim was to better understand the differences between mouse and human fMRI signals, and understand connectivity in the mouse brain visual system. In working towards these aims, this thesis significantly contributes to knowledge in terms of acquiring robust mouse brain fMRI data. The work described in this thesis provides a platform for future studies to further understand visual processing in the healthy mouse brain and to investigate transgenic mouse models of both disease and of impaired brain function.

1.5 The mouse brain

The mouse brain has a mass of 0.42 g on average and consists of approximately 71 million neurons, occupying a volume of approximately 0.4 cm^3 [65]. For context, the rat, marmoset and human brain has an average mass of 1.80 g, 7.78 g and 1400 g respectively [66]. Using typical BOLD fMRI acquisition parameters used in human studies, the mouse brain would be covered by approximately 6 'volume pixels' or voxels [4]. This is one of the main reasons why fMRI in the mouse brain can be extremely challenging, as magnetic field strengths of > 7 T must be used to achieve reasonable spatial resolution and signal (for further details on how the fMRI signal is acquired, see section 2.1).

One common tool used by neuroscientists to visualise how the brain is sub-divided into either structural or functional units is the brain 'atlas'. Atlases provide a common reference space for describing a particular system. Brain atlases have been developed for multiple species using a variety of methods. For this work, mouse brain atlases generated using MRI [67, 68] and histological sections [69] are considered and evaluated for mouse fMRI applications in section 3.2.2. Visualising brain structure can be difficult, and in the bulk of this thesis cross-sectional views of mouse brain structural images will be used to provide spatial context to functional data, as shown in Figure 1.2.

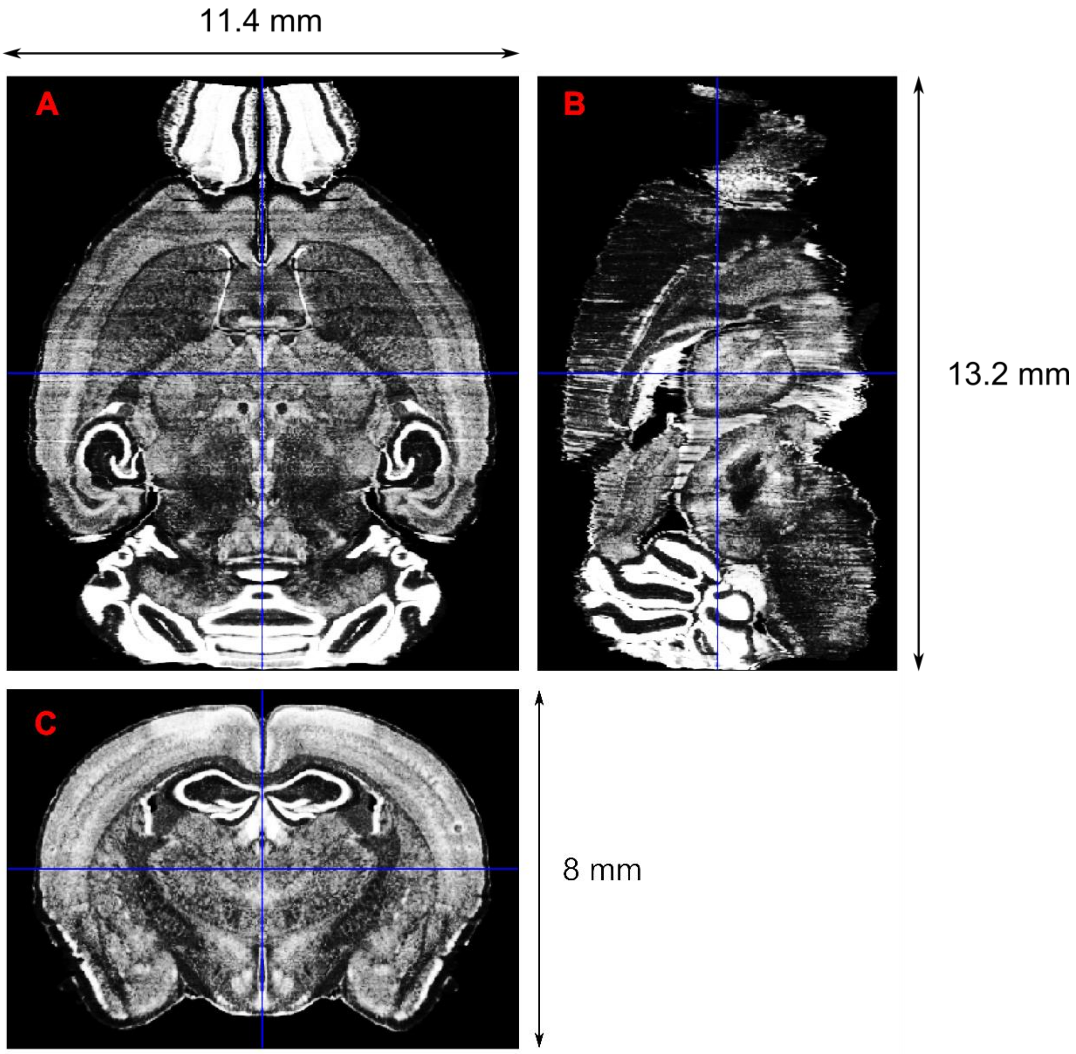

Figure 1.2. Cross section views of the Allen Mouse Brain Atlas [69], viewed using the SPM12 toolbox (25 micron resolution). Each panel shows the mouse brain from a different viewpoint: A) Transverse view B) Sagittal view C) Coronal view. Crosshairs in each panel correspond to the same spatial location.

Figure 1.2 corresponds to a volume (11.4 x 8 x 13.2 mm^3) incorporating an entire mouse brain. It is necessary to define some terminology with respect to these dimensions. In panels A) and B), moving from the bottom of the panel to the top corresponds to moving from the cerebellum at the back of the mouse brain to the olfactory bulbs at the front (posterior-to-anterior). In panels A) and C), moving from left-to-right corresponds to the left-right axis from the point of view of the mouse. In panel B), moving from left-to-right corresponds to moving from top-to-bottom in panel C) (superior-to-inferior).

1.6 The mouse visual system

The human visual system arguably plays one of the largest roles in how we interact with our environment [70]. A historical way of interpreting how important sensory systems are relative to each other is through the schematic of the ‘homunculus’, first suggested by William Penfield and Edwin Boldrey in 1937 [71].

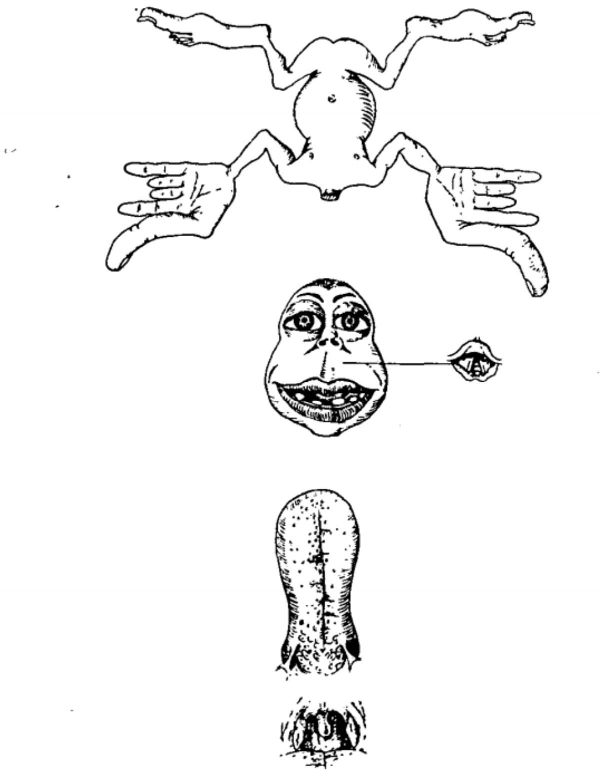

FIG. 28.—Sensory and motor homunculus. This was prepared as a visualization of the order and comparative size of the parts of the body as they appear from above down upon the Rolandic cortex. The larynx represents vocalisation, the pharynx swallowing. The comparatively large size of thumb, lips and tongue indicate that these members occupy comparatively long vertical segments of the Rolandic cortex as shown by measurements in individual cases. Sensation in genitalia and rectum lie above and posterior to the lower extremity but are not figured.

Figure 1.3. Schematic of the human homunculus, adapted with permission from Penfield et al. [71].

Whilst the size of the eyes in the homunculus appear relatively small with respect to somatosensory areas, our understanding of the world immediately out of physical reach is almost entirely dominated through passive sensing of light and sound, and a much weaker sense of smell. A full review of the human visual system is beyond the scope of this thesis.

In the mouse, vision is generally ranked as less important than somatosensory or olfactory inputs. This is illustrated by a mouse homunculus, shown in Figure 1.4.

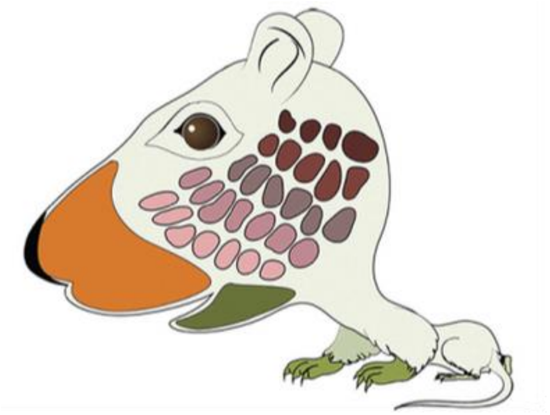

Figure 1.4. Schematic of the mouse homunculus, adapted with permission from Zembrzycki et al. (Figure 3g) [72]. The brown and pink blobs correspond to the mouse whiskers.

Historically, cats and non-human primates have been the primary models for animal studies of the visual system, as they have large eyes and high visual acuity. Mice have relatively poor spatial resolution [73] and as prey animals, also have low binocular overlap [46].

Despite this, mice have increasingly been used to understand visual processing in general [26], due to their flexibility as a neuroscience model – the ability to label and manipulate specific types of cell or circuit in the mouse potentially allow stronger inferences to be made on questions of visual processing than might be made with other animal models. In particular, the availability of transgenic mouse models [27] make mice an attractive target of visual neuroscience research. This has further applications to studying diseases which affect the visual system, e.g. Alzheimer’s disease [74], which have a genetic component [75].

It is necessary to describe the basic visual system anatomy of the mouse, and note important differences with other mammalian visual systems that may limit the scientific questions that they could be used to answer. The retina is the first visual organ that differs sharply from that of the human. The retina is composed of ‘rod’ and ‘cone’ photoreceptor cells, which convert optical input into electrical signals. Rod cells are specialised for monochrome, low light intensity inputs, whereas cone cells detect different colours and are suited for higher light intensities. The human and primate retina has the bulk of cone cells concentrated in the fovea, which is used for high-contrast tasks. The human retina has approximately 4.6 million cone cells and 90 million rod cells [76]. The mouse retina in contrast has approximately 180,000 cone cells and 6.4 million rod cells [77]. Whilst the relative proportions of cone-rod cells may appear similar between humans and mice (5.1% against 2.8%), the mouse retina does not have a fovea where cone cells are concentrated, massively reducing their visual acuity. However, this means mice rely almost entirely on peripheral vision, and the mouse eye is efficient at detecting large objects at a distance, or small objects at close range, or moving objects. This is to be expected from a nocturnal prey animal [78]. Another large difference between mouse and human vision at the retina level is that mice (like cats) are dichromatic, whereas humans and primates are trichromatic. However, a transgenic mouse model with trichromatic retinas does exist [79], which means that studies of colour interpretation could be conducted on mouse models.

Photoreceptor cells then propagate (via interneurons) to retinal ganglion cells (RGCs). All visual information entering the brain is encoded in neuronal activity of RGCs [26], and together with glial cells comprise the optic nerve [80]. There are nominally 22 sub-types of RGC noted in the mouse brain, against 20 in the primate retina. How they map between each other in terms of function is unclear [26, 81].

From the optic nerve, approximately 70% of RGCs project to the superior colliculus, with the remainder projecting to the lateral geniculate nuclei (dorsal and ventral) [82], part of the thalamus, which then projects onto the primary visual cortex [83] (see Figure 1.6 and Figure 1.7 for their locations within the mouse brain). This is different to primates and humans, where only a minority of RGCs project to the superior colliculus [81].

However, before these projections occur, it is necessary to consider the cross-over of different visual field inputs at the chiasma. Figure 1.5 shows how inputs from both monocular and binocular fields project to the lateral geniculate nuclei and from there to the visual cortex. The proportion of the visual field which is binocular is dependent on the balance of RGCs that project contralaterally (i.e. to the opposite hemisphere) rather than ipsilaterally (i.e. to the same hemisphere). Across mammalian species, this balance appears to correspond with the position of the eyes on the head: in the mouse, 2-3% of RGCs project ipsilaterally [46], in the rabbit this value is approximately 0.6%, whereas in cats the value is in the range of 25-30% [81].

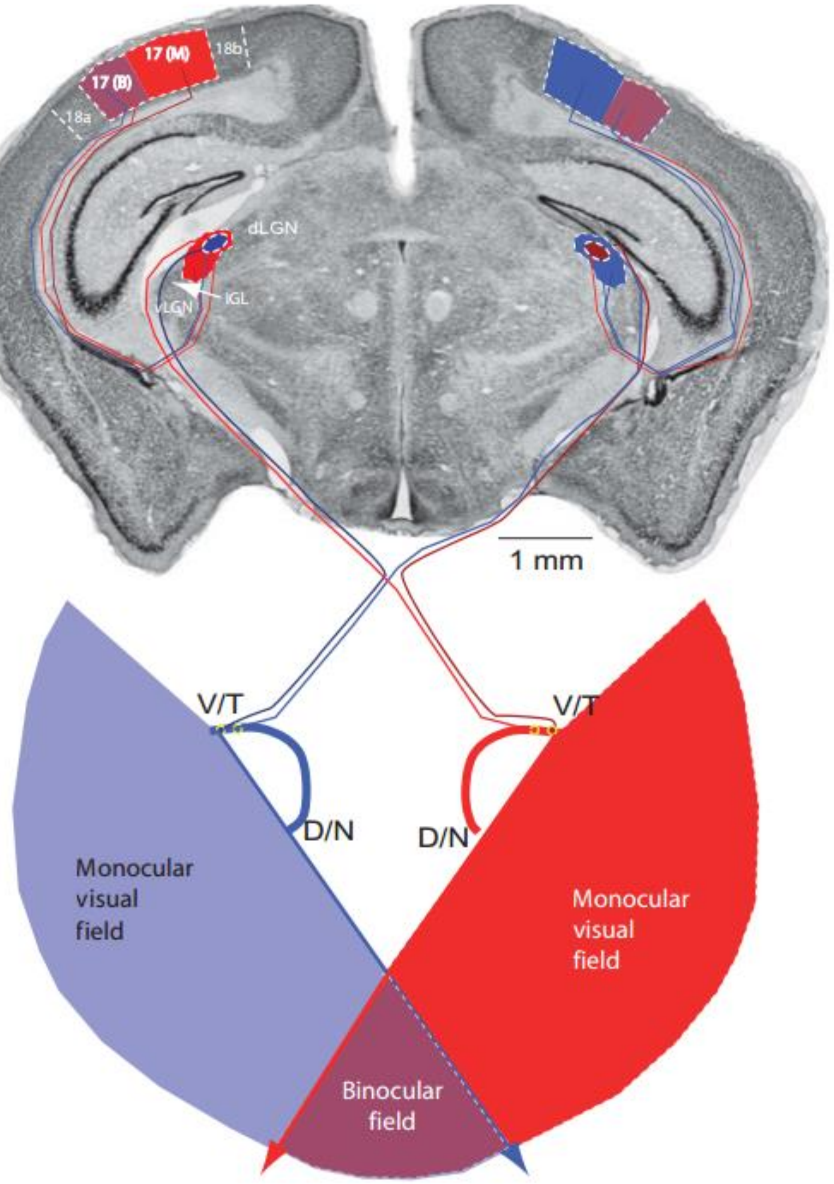

Figure 1.5. Plate 1 reproduced from Chalupa et al. 2008 [81]. Original caption is as follows, "Schematic diagram showing the organization of the ipsilateral and contralateral visual pathways in mice. Blue and red indicate fibers and regions representing the left and right eyes, respectively. Purple indicates binocular regions. Ipsilateral projections arising from the ventrotemporal retina terminate in dorsomedial dLGN. Contralateral retinal projections fill the rest of the dLGN. The locations of other retinorecipient nuclei in the dorsal thalamus, the intergeniculate leaflet (IGL), and ventral LGN (vLGN) are also shown. The dLGN projects topographically to primary visual cortex (area 17). The medial two-thirds of area 17 receives monocular input from the contralateral eye (17M). The lateral one-third receives binocular inputs (17B). Adjacent to area 17 laterally is area 18a; area 18b is medial…"

A similar schematic also showing projections to the superior colliculus from the retinas is shown in section 3.3.1 [26].

Historically, the function of mouse brain visual areas has largely been studied with invasive electrophysiological techniques [26, 47, 49, 84], requiring craniotomies and injection of micro-electrodes into the brain region of interest. These studies measure electrical signals (spikes and local field potentials) from individual regions of the brain, covering a range of approximately 350 microns from the electrodes of interest [85]. Whilst these techniques can directly measure neuronal activity, they are limited in terms of their field of view and effective spatial resolution. Two-photon imaging of calcium ions in neurons in the primary visual cortex has recently been conducted [86], but this technique also has a similarly limited field of view (and is surface limited). Optical spectroscopic imaging of haemodynamic responses (a proxy for neuronal activity, see section 1.7) in the mouse cortex with a larger field of view is possible [43, 87], however these methods still have limited depth penetration. None of these techniques can be used to image brain function across the mouse brain visual system simultaneously, as was done using BOLD fMRI as described in this thesis.

To that end, it is necessary to consider the three key grey matter regions of the visual system in the mouse brain described in this section: the dorsal lateral geniculate nucleus (LGd), the sensory layers of the superior colliculus (SCs) and the primary visual area (VISp), often referred to in the literature as V1. The LGd, SCs and VISp as defined by the Allen mouse brain atlas [69] are shown in Figure 1.6 and Figure 1.7.

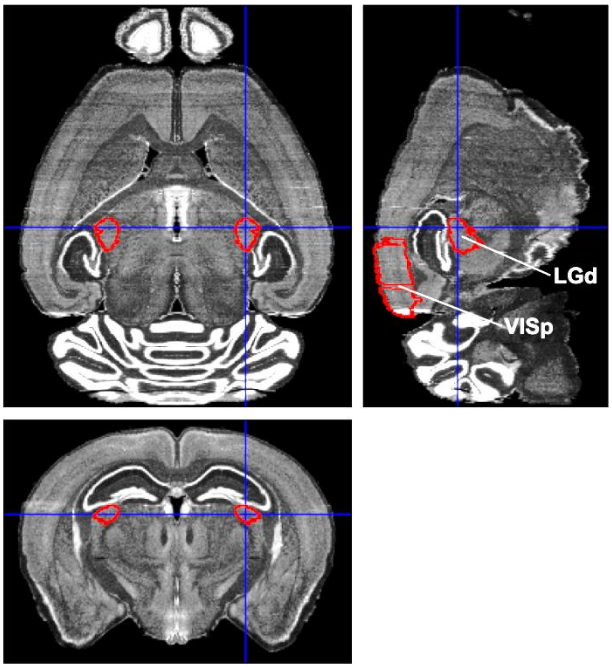

Figure 1.6. Cross sectional views of the Allen MBA structural image, with the visual system overlaid as contours. The crosshairs are centred on the right LGd, and in the sagittal view the LGd and the VISp are labelled.

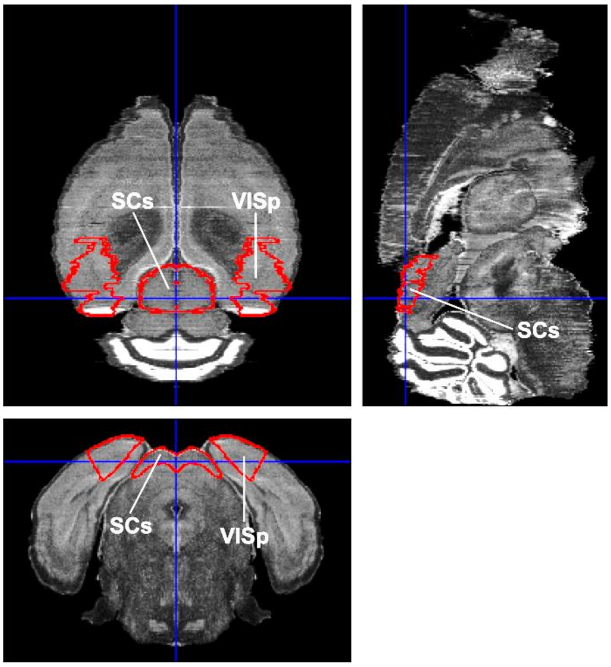

Figure 1.7. Cross sectional views of the Allen MBA structural image, with the visual system overlaid as contours. The crosshairs are centred on the SCs.

Measuring how these regions respond to visual stimuli using MRI is the subject of section 3.3, and chapters 4 and 5. Understanding the connections between them using fMRI is described in chapter 6.

1.7 Neurovascular coupling

Information processing in the brain is conducted by the behaviour of neuronal cells (although there is some debate as to whether another cell type called astrocytes also play a role in information processing [88]). Neurons combine input signals from other neurons, and send output signals to more neurons. Broadly, each neuron is made up of a cell body, dendrites and an axon. Dendrites take inputs from other neurons, and axons feed outputs to the dendrites of other neurons. Information combination and transmission by neurons is performed by the movement of ions across cell membranes. This movement of charged particles across voltage-gated ion channels create fluctuations in electric and magnetic fields, which travel as action potentials along axons. Action potentials are commonly referred to as ‘spikes’ by the electrophysiological community. Changes in electric and magnetic fields due to neuronal action potentials can be invasively measured using electrodes, or non-invasively using magnetoencephalography (MEG) and electroencephalography (EEG). Electrode measurements are the most direct measure available for measuring neuronal electrical behaviour, however they are limited due to their invasive nature (which may affect the neuronal behaviour they try to measure), difficulty of placement, and limited spatial coverage. EEG and MEG are non-invasive, and so can be readily implemented in human studies, but suffer from limited spatial resolution and challenging signal localisation.

MRI cannot currently measure neuronal activity directly. However, it is possible to use MRI to measure regional changes in blood oxygenation, a physiological proxy variable for neuronal activity. The link between neuronal activity and the downstream vascular responses is called neurovascular coupling.

Neurovascular coupling is believed to involve a series of events which begin with the release of glutamate (an amino acid that is also a neurotransmitter) at synapses [89]. The brain has extremely large energy demands relative to the rest of the body, mostly due to action potentials (generation and recovery from) and postsynaptic effects of glutamate [90]. The brain is also inefficient at storing energy (in the form of glycogen), and neurons themselves store no glycogen at all [91]. Therefore the brain requires high levels of blood perfusion, in order that oxygen and glucose is supplied to neurons as necessary. Neurovascular coupling is the mechanism by which brain regions in which neurons are active receive a local increase in blood flow. This is also known as functional hyperaemia, which results in increased local oxygen delivery by the vascular network. This is distinct from central autoregulation, which maintains a roughly constant perfusion of the brain despite variations in systemic blood pressure [4].

In order for the vascular network to generate local increases in blood flow, it is necessary for vasodilation (the dilation of blood vessels) to occur. The precise mechanisms underlying neurovascular coupling are not fully understood, but it is currently believed to be mediated by astrocytes [89, 92], which respond to increases in K^+ ions and glutamate in the extracellular space (released by active neurons). These in turn induce calcium waves throughout the astrocyte, which terminate at the astrocytic end-feet located on arterioles. The end-feet release vasoactive substances, which induce vasodilation [4]. As the fractional increase in blood flow is approximately twice as large as the increase in the metabolic rate of oxygen [93], this results in a net decrease in the oxygen extraction fraction. This in turn causes an increase in oxygenated blood relative to deoxygenated blood within a given voxel, which then induces an increase in the MRI signal relaxation constant T_2^*, which in turn drives BOLD contrast for fMRI as described in section 2.1.5. This chain of events is summarised by Martin [1] in Figure 1.8.

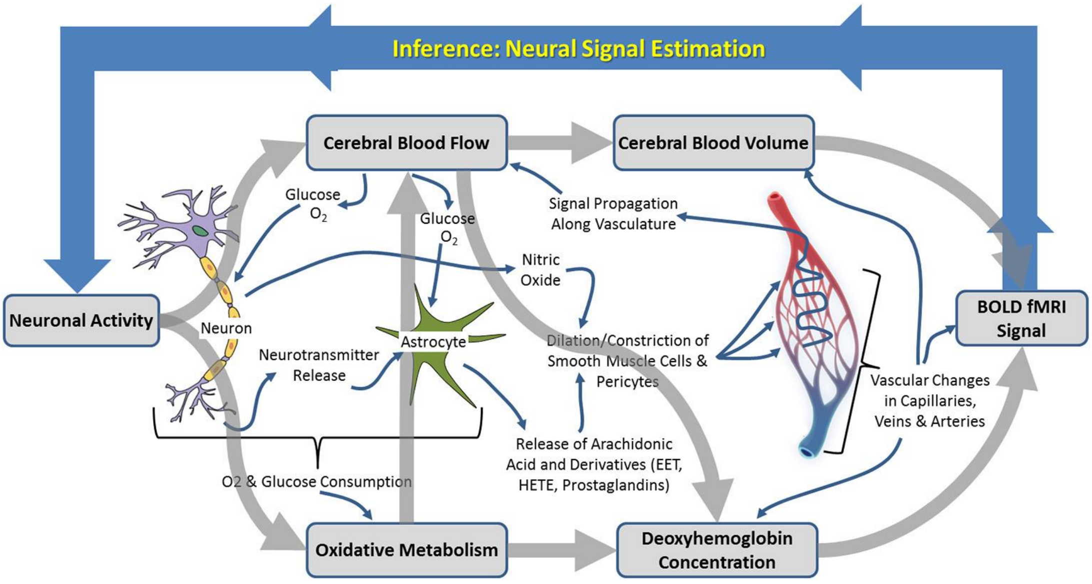

Figure 1.8. Figure 1 adapted from Martin 2014 [1] (Creative Common Attribution ("CC BY") licence). The original caption reads as follows, "Schematic illustration of the neurophysiological processes underpinning hemodynamic neuroimaging signals. The boxed processes linked by thick gray arrows around the outside represent components of interest to those focussing on "parametric neurovascular coupling," whereas the more detailed processes illustrated in the center [sic] represent important concepts in for [sic] investigation of "physiological neurovascular coupling."

This section has provided a brief overview of neurovascular coupling and for the purposes of this thesis neurovascular coupling is assumed to be robust in the anaesthetised mouse brain under medetomidine (see also section 3.1.1). For a more detailed explanation of neurovascular coupling, see Logothetis et al. [15, 16], and Buxton [93].

1.8 Thesis outline

Chapter 2 provides the necessary background theory to understand the experiments and results described in this thesis. This includes a detailed explanation of the physics behind fMRI, and the theory behind standard fMRI analysis. Chapter 3 describes a series of experiments conducted to develop and optimise a protocol for mouse fMRI. Chapter 4 describes work developing increasingly complex visual stimuli, with select results from both chapters 3 and 4 published in J. NeuroImage [94]. Chapter 5 then describes efforts to better characterise fMRI data, using a technique called line-scanning fMRI to measure the BOLD signal at high temporal resolution. Then in chapter 6, the application of dynamic causal modelling to mouse brain fMRI data is described, in order to characterise mouse brain effective connectivity. Finally, chapter 7 discusses the main findings of the thesis.

2 Background theory

In this chapter, the necessary background theory required for the thesis is presented. Section 2.1 covers the theory behind magnetic resonance imaging. Then in section 2.2, theoretical background for standard fMRI analysis is given. More advanced fMRI data analysis is considered separately in chapter 6. Finally, the chapter is summarised in section 2.3.

2.1 Magnetic resonance imaging

Nuclear Magnetic Resonance (NMR) was first described independently by Bloch and Purcell [95, 96] in 1946, and is now an extremely common spectroscopic tool for inferring chemical structure and composition. It was in 1973 that Mansfield and Lauterbur [97, 98] described methods for inferring physical structure from NMR signals. Then in 1983 the idea of acquiring information in ‘k-space’ was described by Brown [99]. Since these key developments, MRI has become a key tool for progress in fundamental biological science and for diagnostics in clinical settings. This section covers the basic theory behind magnetic resonance imaging.

2.1.1 Magnetic resonance theory

All sub-atomic particles (protons, neutrons and electrons) have an intrinsic quantum mechanical (QM) property known as ‘spin’ angular momentum, and can be considered as analogous to classical angular momentum. However, the following caveats apply: the particle does not literally spin on its axis, QM spin is a fundamental property of the particle, QM spin interacts with electromagnetic fields (rather than gravitational fields), and QM spin magnitude can only have discrete values.

The bulk of MRI experimentation is concerned with ^{1}H nuclei, commonly referred to as protons, and only ^{1}H MRI is considered in this thesis. The words spin and proton are often used interchangeably when discussing magnetic resonance.

Atomic nuclei act as a single body with a collective nuclear spin $\boldsymbol{I}$. A single particle can be said to have a magnetic moment $\boldsymbol{\mu}$ linked to $\boldsymbol{I}$ by the gyromagnetic ratio γ, as shown by equation (2-1).

$$\boldsymbol{\mu} = \gamma \boldsymbol{I} \tag{2-1}$$

The value of γ is a property of the atomic species in question. For ^{1}H, γ takes the value of 42.58 MHz/T.

It is manipulation of magnetic moment/spin which ultimately gives rise to MRI signals. Quantum theory says that for an atomic nucleus with quantum spin I, there are a total of ($2I$ + 1) spin eigenstates that can be occupied by the nucleus. For ^{1}H, I = ½, giving rise to a total of two possible spin states that could be occupied by a single proton. These states are often described as ‘spin-up’ and ‘spin-down’, although this is should not be taken literally. This quantised effect was first demonstrated in 1922 by Stern and Gerlach [100] with silver atoms (which also have I = ½).

On the spatial scales of interest (micron and above) it makes more sense to describe spin ensembles, rather than individual spins. This is advantageous for the following reason. With a sufficiently large population of spins, the precise quantum description of each spin’s behaviour can be disregarded, and the expected behaviour of the population can be used instead. This is analogous to using temperature as a macroscopic average quantity to summarize the kinetics of large numbers of particles in a gas. A population of spins behaving in the same way is called a ‘spin isochromat’, and the expected value of the magnetic moment of the isochromat can be treated in a classical manner. However, the discrete nature of the spin states remains.

The application of an external magnetic field to a spin isochromat with a non-zero magnetic moment (given by equation (2-1)) will induce a torque τ given by equation (2-2).

$$\tau = \frac{d\boldsymbol{I}}{dt} = \boldsymbol{\mu} \times \boldsymbol{B} \qquad \textbf{(2-2)}$$

The application of a torque to the magnetic moment causes the moment to precess i.e. rotate around the axis defined by $\boldsymbol{B}$. The angular frequency ω at which the magnetic moment precesses is given by the Larmor equation (2-3), and is independent of the polar angle and the direction of the magnetic moment. The direction of movement of the magnetic moment vector is always perpendicular to the direction of the magnetic moment vector itself and the applied $\boldsymbol{B}$ field due to the nature of the cross product in equation (2-2).

$$\omega = \gamma B \qquad \textbf{(2-3)}$$

In the absence of external fields, the different quantum spin states are degenerate i.e. they have the same energy. By applying external, static magnetic fields to spins, the energy levels of spin states can be made to differ. This is the phenomenon known as Zeeman splitting. The size of the energy difference ΔE as a function of the applied static magnetic field $\boldsymbol{B_0}$, for the two level energy system of ^{1}H is given by equation (2-4). For clarity later on in the section, we will assume that $\boldsymbol{B_0}$ points in the positive z-direction, and has no transverse component.

$$\Delta E = \boldsymbol{\mu_1}.\boldsymbol{B_0} - \boldsymbol{\mu_2}.\boldsymbol{B_0} = \gamma\hbar B_0 \tag{2-4}$$

Planck's constant $\hbar$ is a constant of proportionality linking the energy of a photon and its angular frequency ω, as shown in equation (2-5).

$$E = \hbar\omega \tag{2-5}$$

A particle moving between energy states will emit or absorb a photon that corresponds to the energy gap between the states, which also corresponds to the precession frequency. For ^{1}H nuclei, at an applied magnetic field of 9.4T, ω corresponds to approximately 400 MHz, in the radiofrequency range of the electromagnetic spectrum.

When a population of particles can occupy a two-level energy system, their occupancy numbers at equilibrium obeys a Boltzmann distribution, given by equation (2-6).

$$\frac{N_{high}}{N_{low}} = e^{\frac{\Delta E}{k_B T}} \tag{2-6}$$

In equation (2-6), N_{high} and N_{low} are the occupancies of the higher energy and lower energy states respectively, k_B is the Boltzmann constant and T is the temperature of the system. At normal temperature ranges (for example 300K), and at applied magnetic field strengths of 1.5T, this ratio is approximately one part in one million. However, this imbalance in population states is enough to create a net magnetisation vector $\boldsymbol{M}$ (magnitude of µT) in the direction of the applied field $\boldsymbol{B_0}$ which can be manipulated and detected. However detecting such a small difference against the background of $\boldsymbol{B_0}$ is inefficient, and it is possible to 'tip' $\boldsymbol{M}$ into the transverse plane, and detect it there with a minimal magnetic background.

At equilibrium, the spins all precess incoherently (with a random phase distribution), and so the net component of $\boldsymbol{M}$ in the transverse plane is zero. For clarity, we can transform from the laboratory frame $\boldsymbol{S}$ (with coordinates (x, y, z)) into a frame $\boldsymbol{S'}$ (with coordinates (x', y', z)) which rotates around the z-axis at the Larmor frequency ω. In this rotating frame, a fictitious (analogous to the centrifugal force described in rotational mechanics) magnetic field given by $\frac{\boldsymbol{\omega_0}}{\gamma}$ is experienced by the spin isochromat, and $\boldsymbol{M}$ is now static rather than precessing.

In the frame $\boldsymbol{S'}$, what we call a ‘90° radiofrequency (RF) pulse’ rotates $\boldsymbol{M}$ by 90° into the transverse plane. The frequency of the pulse must be the same as the Larmor frequency (condition for resonance, i.e. photon absorption). In $\boldsymbol{S'}$, this appears as a static B_1 field, oriented along x' in the (x', y') plane. For as long as the pulse is applied (t_{pulse}), $\boldsymbol{M}$ will precess about the x' axis at an angular speed of $\omega_1 = \gamma B_1$. The resultant flip angle α is given in equation (2-7).

$$\alpha = \gamma B_1 t_{pulse} \tag{2-7}$$

Because $B_1$is much smaller than B_0, the precession around the x' axis is much slower (of magnitude 100 Hz, rather than 100 MHz for B_0).

2.1.2 Magnetisation relaxation

After the application of an RF pulse to manipulate $\boldsymbol{M}$, the system is perturbed into a higher energy state which drives a return to equilibrium. This relaxation to equilibrium occurs by energy exchange within the system and between the system and the surrounding environment. The full behaviour of $\boldsymbol{M}$ in the presence of a constant external B_0 field and an RF pulse characterised by B_1 can be described by a set of equations known as the Bloch equations (equation set (2-8)).

$$\begin{aligned}
\frac{dM_{x\prime}}{dt} &= \gamma M_{y'}\left(B_0 - \frac{\omega_0}{\gamma}\right) - \frac{M_{x\prime}}{T_2} \\
\frac{dM_{y\prime}}{dt} &= \gamma M_{z'}B_1 + \gamma M_{x'}\left(B_0 - \frac{\omega_0}{\gamma}\right) - \frac{M_{y\prime}}{T_2} \\
\frac{dM_{z\prime}}{dt} &= \gamma M_{y'}B_1 - \frac{(M_{z'} - M_0)}{T_1}
\end{aligned} \tag{2-8}$$

This formulation of the Bloch equations is set in the rotating frame of reference $\boldsymbol{S'}$. T_1 is the ‘spin-lattice’ relaxation constant, and scales the process through which the system exchanges energy with the surrounding environment. T_2 is the ‘spin-spin’ relaxation constant, scaling the process of spins exchanging energy with each other. These relaxation constants are the most common ways of generating image contrast in MRI. For water in tissue, T_1 is typically on the order of seconds, whereas T_2 is on the order of tens of ms. If the $\boldsymbol{B_0}$ field is not homogenous, the decay due to spin-spin exchange will be faster, and characterised by an effective T_2 relaxation constant called T_2^*. It is T_2^* contrast that is of particular value to BOLD fMRI and the work conducted in this thesis.

By using an RF pulse with flip angle α, we can obtain solutions in time to equation set (2-8), immediately after the application of the RF pulse as shown in equation set (2-9).

$$M_{x'}(t) = M_0 \sin(\alpha) \sin(\omega_0 t) \exp(-\frac{t}{T_2})$$
$$M_{y'}(t) = M_0 \sin(\alpha) \cos(\omega_0 t) \exp(-\frac{t}{T_2})$$
$$M_{z'}(t) = M_0 \left(1 - (1 - \cos(\alpha)) \exp\left(-\frac{t}{T_1}\right)\right) \tag{2-9}$$

Once a 90° RF pulse has increased the transverse magnetisation, an electrical signal is induced in the RF receiver coil (transverse to the direction of the B_0 field). By using phase sensitive detection a complex signal is generated, given by equation (2-10).

$$S = S_0 \exp(-\frac{t}{T_2})[\exp(i(\omega - \omega_0)t)] \tag{2-10}$$

The shape of S is an exponential decay governed by T_2 (or T_2^*), and modulated by an oscillation at frequency $(\omega - \omega_0)$. This signal is called the Free Induction Decay (FID). The Fourier transform of S has the shape of a Lorentzian curve centred on $(\omega - \omega_0)$, with width inversely related to T_2. It should be noted that the proportionality constant S_0 is dependent on many hardware factors, in addition to proton density ρ (a property of the tissue), which will be described in more detail in section 2.1.3.

In summary, the application of external magnetic fields and RF pulses can be used to manipulate particle spins into excited energy states, and when they relax back to lower energy states they emit photons with predictable frequency and phase. These photons can be detected with a RF receiver and coded as an electrical signal. The precise application of magnetic fields, their gradients and RF pulse sequences can generate a huge number of contrasts and types of image, suitable to very different biological and chemical applications.

2.1.3 Image formation in MRI

The act of elevating spins to higher energy levels and recording their relaxation to equilibrium with a single $\boldsymbol{B_0}$ field and single RF pulse is not enough to generate an image. It is the application of magnetic field gradients or multiple RF pulses that allow spatial position to be encoded into the received signal. These will be discussed further in this section.

From equation (2-3), it is shown that the resonance frequency of a spin isochromat is linearly dependent on the magnetic field it experiences. By spatially varying the magnetic field, the resonant frequency of the received signal can encode position $\boldsymbol{r}$ – this is known as frequency encoding. Consider the application of a linear magnetic field gradient $\boldsymbol{G}$ on top of the applied $\boldsymbol{B_0}$ field, yielding equation (2-11).

$$\omega(\boldsymbol{r}) = \gamma(\boldsymbol{B_0} + \boldsymbol{G}(\boldsymbol{r}).\boldsymbol{r}) \tag{2-11}$$

The maximum size of $\boldsymbol{G}$ used for most of the work in this thesis is 600 mT/m. At 9.4 T, and for a field of view of 3 cm, the frequency range of ω is approximately [399.681 400.447] MHz, centred on 400.064 MHz where $\boldsymbol{G}$ is zero.

Given the spatial information included in equation (2-11), it is now convenient to recast the FID equation (2-10) in the following way.

$$S(t) = \iiint \rho(\boldsymbol{r})\exp(\boldsymbol{i\gamma}(\boldsymbol{G}.\boldsymbol{r})\boldsymbol{t})\, d\boldsymbol{r} \tag{2-12}$$

In equation (2-12), the non-spatial component from the $\boldsymbol{B_0}$ field has been omitted for clarity. By defining a reciprocal space vector $\boldsymbol{k} = \boldsymbol{\gamma G t}$, and substituting into equation (2-12) yields equation (2-13).

$$S(\boldsymbol{k}) = \iiint \rho(\boldsymbol{r})\exp(\boldsymbol{i k}.\boldsymbol{r})\, d\boldsymbol{r} \tag{2-13}$$

From equation (2-13) and the definition of $\boldsymbol{k}$, we can see that $\boldsymbol{k}$ and $\boldsymbol{r}$ are inverse variables related by Fourier transformation. MRI images are almost always reconstructed by acquiring ‘k-space’ information and applying a Fourier transform to generate an image in ‘real-space’. By mapping k-space using gradient pulses with variable amplitude (and fixed durations), the ‘spin-warp’ method [101] is now the most common way of acquiring MRI data.

2.1.3.1 Slice-selection

Whilst acquiring k-space data in three dimensions is possible, commonly slices of k-space are acquired sequentially, particularly for fMRI, and so the idea of slice-selection will be briefly covered here. Applying an RF pulse at the Larmor frequency would in theory excite all spin isochromats that experience the same B_0 field (by convention pointing in the positive z-direction). By applying a linear gradient G_{ss} in the same direction as B_0, but which has a value of 0 at the location of the slice of interest, spins experience an effective $\boldsymbol{B}$ field based on z-value. As the spin distance increases, $\Delta\boldsymbol{B}$ increases and the spin becomes increasingly off-resonance. This ensures that only spins within the slice are excited. The slice profile is a

Fourier transform of the RF pulse profile, and therefore a sinc function RF pulse excites a ‘slab’ of spins in the sample. For a perfect slab, an infinitely long sinc pulse would be required, which is impractical. A truncated sinc function is used in practise.

One issue of using a finite RF pulse is that during the application of G_{ss} for time t, a phase shift of $\gamma G_{ss} z t/2$ is accumulated by spins in the slice. This shift can be reversed by applying $-G_{ss}$ for duration $t/2$ seconds, and is called ‘slice-refocusing’.

2.1.3.2 Phase encoding

However, for a slice z, if we consider applying frequency encoding in the x and y directions, an ambiguity arises – the received signal no longer has a unique position in space, as it could either be coming from one position or its reflection across the xy-axis. It is for this reason that phase encoding is used as well. Briefly, a phase-encoding gradient G_{PE} is applied in e.g. the y-direction for a finite time. The larger the size of G_{PE} at position y, the greater the phase shift. When G_{PE} is removed, the phase shift remains (until either the application of another gradient or the signal undergoes complete relaxation), and therefore can be used to determine position.

2.1.4 Sampling k-space

At this point, it is often clearer to use a pulse sequence diagram to demonstrate the various gradients and RF pulses used in an MRI sequence to generate an image. The central aim of the pulse sequence is to sample k-space as efficiently as possible, in order to apply the Fourier transform and generate an image. This section will show pulse sequence diagrams for two basic pulse sequences which feature in this work with some modifications: the gradient echo (GE) and the gradient echo – echo planar imaging (GE-EPI) sequences. Both sequences use the idea of sampling the ‘echo’ of the signal, rather than the FID itself – as the duration of the echo is longer than that of the FID, it is easier to sample.

2.1.4.1 Gradient Echo

A schematic of the gradient echo pulse sequence is shown in Figure 2.1.

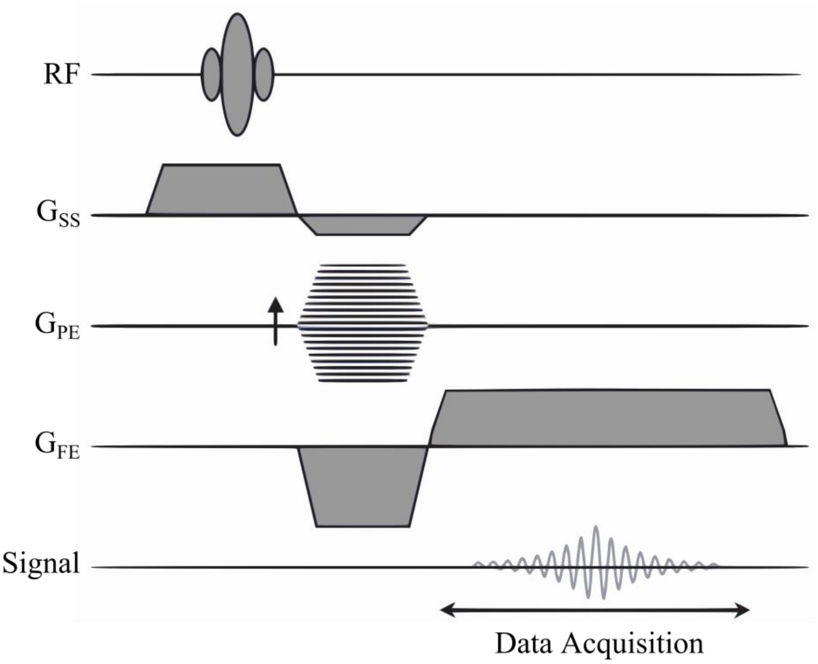

Figure 2.1. Diagram for gradient echo pulse sequence (adapted from [102]).

Here we make the simplification that $\boldsymbol{G}$ for frequency encoding is only applied in a single direction, and can be represented by G_{FE}. In turn from the top line going down:

1. The RF pulse rotates the net magnetisation into the transverse plane.

2. The initial positive lobe of G_{SS} ensures only the slice of interest is excited by the RF pulse, whilst the second, negative lobe refocuses the slice by negating the accumulated phase shift.

3. G_{PE} is applied to encode position with phase, with the peak value of the gradient looping over values (each value corresponds to a different k_{PE} line).

4. G_{FE} is first applied with an initial negative dephasing gradient, for which the effect is to de-phase spins contributing to the FID. Once all other gradients have been applied, the positive lobe of G_{FE} refocuses the spins, creating a gradient echo signal. The positive lobe is left on for a time duration that is twice as long as for the negative lobe. This ensures that the peak of the echo corresponds to the centre of k-space, and that both the rising and trailing parts of the echo are equally sampled, improving signal-to-noise. This echo contains information to fill an entire line of k-space in the frequency-encoding direction.

The time between successive RF pulses in this schematic is the TR or repetition time. The time between the initial RF pulse and the echo peak is the TE or echo time. The acquisition in k-space for each excitation is represented in Figure 2.2.

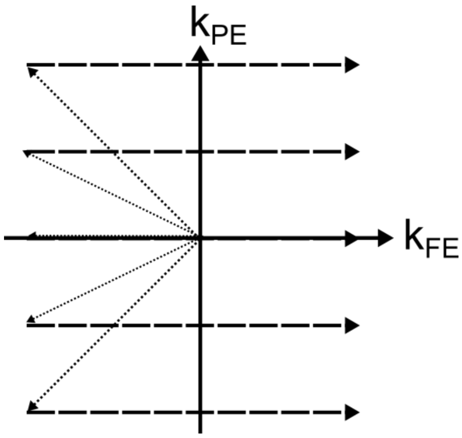

Figure 2.2. Acquisition of k-space using a GE sequence. The finely dotted arrows correspond to the G_{PE}lobe (which changes magnitude on each TR) and the negative G_{FE}lobe. The coarsely dotted arrows correspond to the positive G_{FE}lobe, acquiring the gradient echo signal. The sequence is stepped through as many lines of k_{PE} are required.

Nominally, with a 90° flip angle, it would be necessary to wait for full T_1relaxation before starting the next acquisition. However, with T_1 having values on the order of seconds, this would make scan times extremely long. A more efficient way of proceeding is to use a small flip angle in conjunction with TR < T_1. The flip angle that maximises signal for a particular TR in tissue with a given T_1 is known as the Ernst angle [103], and meets the condition shown in equation (2-14).

$$\cos(\alpha) = \exp(-\frac{TR}{T_1}) \tag{2-14}$$

The behaviour of the Ernst angle as a function of TR for a range of T_1 values is shown in Figure 2.3.

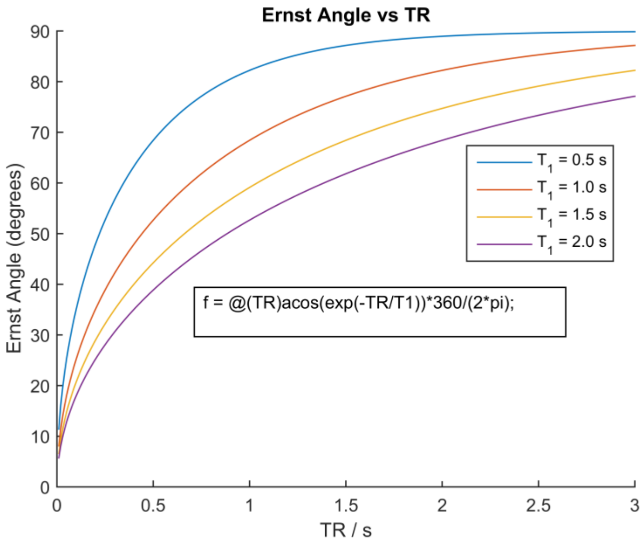

Figure 2.3. Plot showing Ernst angle as a function of TR. Shorter TRs require smaller flip angles

It can be shown that the amount of magnetisation available to sample in the transverse plane follows a similar pattern, as in Figure 2.4.

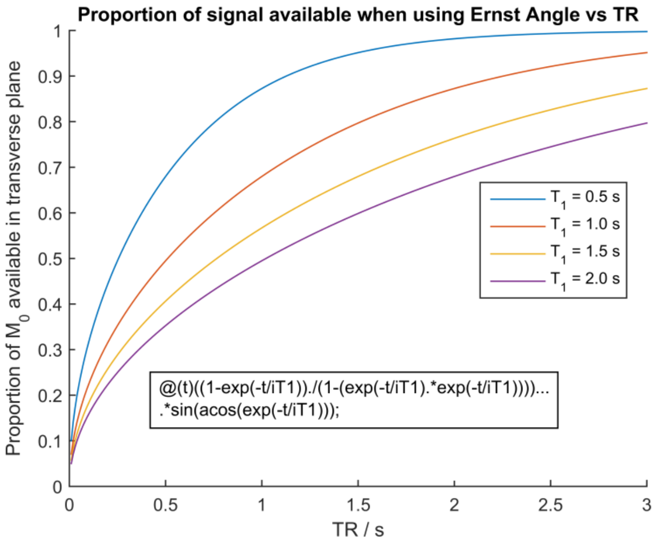

Figure 2.4. Plot of the maximum signal available to sample in the transverse plane following the Ernst angle RF pulse as a function of TR.

As can be seen from Figure 2.4, choice of TR and flip angle can have a large effect on recovered signal.

2.1.4.2 Gradient Echo – Echo Planar Imaging (GE-EPI)

For fMRI purposes, it is desirable to acquire multiple slices in a short time period (<5 seconds) repeatedly, in order to sample the signal magnitude rapidly through time. With the gradient echo sequence described earlier, using one RF pulse/FID per line of k-space limits how rapidly successive GE images can be acquired. With GE-EPI, the entirety of k-space can be acquired from a single FID. A schematic pulse sequence representing ‘single shot’ GE-EPI, the most common sequence used for fMRI, is shown below in Figure 2.5.

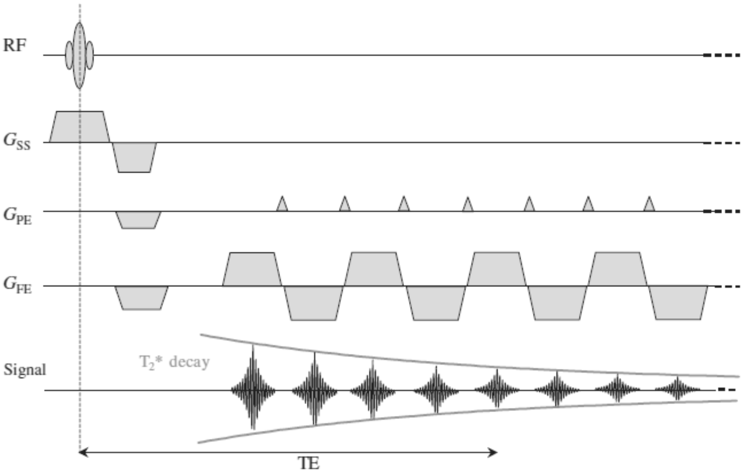

Figure 2.5. Diagram for GE-EPI pulse sequence (reproduced from [102]).

Much of the mechanics remains the same, with the exception of the G_{PE} ‘blips’ and the additional large, fast-switching G_{FE} lobes. Their significance is explained by considering k-space sampling, as shown in Figure 2.6.

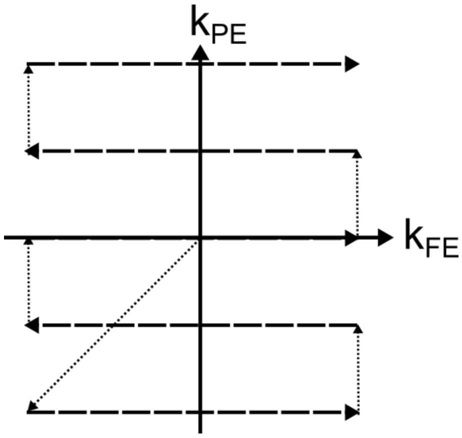

Figure 2.6. Acquisition of k-space using a GE-EPI sequence. The diagonal dotted arrow corresponds to the initial G_{PE} lobe and initial negative G_{FE} lobe. The short, vertical dotted arrows correspond to the G_{PE} ‘blips’. The coarsely dotted arrows correspond to the switched G_{FE}lobes, acquiring each gradient echo corresponding to a line of k-space.

As evident in Figure 2.5, the readout gradient must be switched fast enough in order to sample the entirety of k-space before signal decay by T_2^* mechanisms is too great. The basic theory of GE-EPI has been covered here, and details of GE-EPI artefacts and strategies for overcoming these are described in later chapters.

2.1.5 Defining the BOLD signal for fMRI

Using blood behaviour as a proxy for neuronal activity has been of interest since the late 1800s, and the history of this approach is summarised well by Raichle [104]. In classical fMRI, the standard approach is to use the GE-EPI sequence with T_2^* contrast to measure what is known as the BOLD (Blood Oxygenation Level Dependent) signal, first described by Ogawa et al. [5, 105]. Spin echo EPI (SE-EPI) has been applied to the mouse brain for fMRI [32, 39], however this comes at a price of reduced sensitivity and BOLD contrast [106], (due to T_2 weighting instead of T_2^*) and is not commonly used in human fMRI studies. Rather, SE-EPI is more commonly used in conjunction with contrast agents (such as super paramagnetic iron oxide particles) for measuring changes in cerebral blood volume [107].

Blood contains haemoglobin, a protein containing iron which acts as an O_2 carrier. The presence of oxygen within the haemoglobin compound (oxyhaemoglobin, which has no unpaired electrons) renders it weakly diamagnetic, whereas in oxygen deficient haemoglobin (deoxyhaemoglobin, which has four unpaired electrons) the compound is highly paramagnetic [108]. The effect of paramagnetic substances on surrounding protons is to reduce T_2^*, and in turn reduce the signal intensity for a given TE. Deoxyhaemoglobin is naturally present in large enough concentrations for its effect on protons to be detected by MRI, and so an externally administered contrast agent is unnecessary, making such measurements completely non-invasive.

It would be reasonable to expect that as neurons in a brain region fire at a higher rate, they would consume more oxygen, deoxyhaemoglobin concentration would increase, and therefore signal intensity should be lower in a more ‘active’ brain region. However, it was shown by Fox and Raichle, using ^{15}O PET imaging that regional cerebral blood flow (CBF) strongly increases upon regional activation (defined as local increases in neuronal firing), but the increase in cerebral metabolic rate of oxygen consumption ($CMRO_2$) is relatively modest [109]. The consequence of this is that upon an increase in brain activity, the BOLD signal increases with the increase in oxyhaemoglobin relative to deoxyhaemoglobin, and correspondingly increases T_2^*. A greater value of T_2^* corresponds to less decay of the acquired signal, and therefore the signal is increased relative to the signal before activation.

2.2 fMRI data – preprocessing and analysis

In this section, sources of unwanted variance and the practicalities of processing fMRI data to improve the quality of the measured BOLD signal are covered, and two standard techniques for interpreting the BOLD signal across the brain – statistical parametric mapping and region-of-interest analysis – are introduced.

2.2.1 The nature of fMRI data

fMRI conducted with BOLD imaging generates data which is multi-level and multidimensional. First, the hierarchical levels of data that might be used in an fMRI experiment are given, depending on the experimental design.

Individual *subjects* are scanned in *sessions* (defined as a continuous single time period when the subject is imaged without leaving the scanner). Each subject may undergo multiple sessions, in the case of a longitudinal study. Each session is composed of a number of *runs*, where each run is a series of functional images acquired continuously. Breaking a session into runs is more common for human fMRI studies to allow subjects to take short breaks within a session, in order to increase task compliance and avoid fatigue, but this is less important for anaesthetised rodent imaging. However, runs are a useful functional unit to consider, and in between runs the physiological status of the subject and the performance of the scanner can also be checked.

Within each run, a *volume* image is acquired during each TR period, and concatenated to make up a time series of volumes. For a 2 s TR and a total imaging time of 5 minutes, a total of 150 volumes (also referred to as timepoints in this thesis) would be acquired. However each point in the volume image is not acquired simultaneously, instead each volume is acquired as a series of 2D slices equally within the TR period. Therefore for sequential slice imaging, the BOLD signal from a point in the first slice can appear to be phase-shifted by almost one TR relative to the same point in the last slice. Within each slice, rows of k-space are acquired on the order of milliseconds, and later Fourier transformed to reconstruct a slice consisting of *voxels* (volume pixels). The number of voxels in a slice is dependent on the matrix size used for acquisition (commonly square, and a power of 2 to enable a more efficient discrete Fourier transform in the reconstruction, e.g. 64x64), and therefore the brain is covered by thousands of voxels. Therefore for each run, an fMRI dataset has three spatial dimensions (2 in-plane, slice), and time, making a 4D dataset.

Within each run, and depending on the experimental design, multiple *blocks* of stimuli or stimulus *events* may be presented to the subject. This thesis only uses block-related design as blocked effects are easier to detect, and in this case each block is referred to as a ‘trial’. A stimulus block may be of the order of 10-30 seconds, relative to a baseline block of the same order of magnitude. This allows the assumption to be made of linear behaviour of the BOLD signal with respect to neuronal activity, and the use of a canonical haemodynamic response function convolved with a boxcar function representing stimulus presentation for BOLD signal modelling with a general linear model.

2.2.2 fMRI data preprocessing

2.2.2.1 Defining preprocessing

There are different ways of preprocessing fMRI data, but it is generally accepted to account for both spatial and temporal sources of non-neuronally driven variance in the BOLD signal before attempting to make statistical descriptions of or inferences from the data. This is because the measured BOLD signal change in response to a stimulus is often a small proportion of the total signal (approximately 1 part in one hundred for most of the results in this thesis). In addition, BOLD signal changes of interest are often smaller than those due to unwanted sources of variance in both the spatial and temporal domain. Preprocessing in fMRI is defined as a series of actions to be performed on data that reduce unwanted sources of BOLD signal variance, and is generally applied to fMRI experiments independently of the experimental manipulation.

2.2.2.2 Evaluating the quality of fMRI data

Typically in MRI, image signal-to-noise ratio (SNR) is often used as a measure of the quality of data. The average signal intensity within a sample is divided by the standard deviation of the signal outside the sample. Another common metric is the image contrast-to-noise ratio (CNR), where the difference in intensities between two tissue types is divided by an estimate of the noise.

However, these image quality metrics are not entirely useful in fMRI, as they make no account for the temporal domain. More useful for the purposes of detecting BOLD signal changes is the temporal contrast-to-noise ratio (tCNR). This is calculated by the contrast of the BOLD signal in the temporal domain (the BOLD signal during activation minus the BOLD signal at rest) divided by the standard deviation of the BOLD signal at baseline or rest. A greater tCNR means that detection of BOLD responses to a given experimental manipulation is more likely.

2.2.2.3 Sources of noise in fMRI data

Noise in fMRI data can be broadly split into two categories – system noise and physiological noise. System noise includes intrinsic thermal noise within the sample and the electronics used to acquire the signal, and imperfections in the MRI hardware. Physiological noise includes BOLD signal artefacts resulting from sources determined by the biological sample e.g. head motion, respiration, cardiac rate, anaesthesia, or variability in the neuronal response to the external stimulus. A physiological noise source for higher order mammals, but unlikely to be an issue in anaesthetised rodents, is differing behavioural strategies/cognitive processes for the same stimulus.

Both system noise and physiological noise are commented on extensively in this thesis. Correcting for system noise is generally easier, as phantom experiments using tubes of agarose allow scanner parameters to be optimised in order to minimise the effects of system noise. However preprocessing is also important for reducing system noise. One of the largest contributions to variation in the measured BOLD signal is scanner drift [110]. This is the term given to drifts in the BOLD signal, caused by gradual shifts in the main resonant frequency of the superconducting magnet, and potentially temperature variations in the gradient systems used in the MRI scanner [111]. These are of low frequency relative to BOLD signal fluctuations driven by neuronal activity, and can be corrected for in preprocessing using high-pass temporal filters.

Another source of noise is thermal noise, which for mouse fMRI has been suggested as an important source [36]. Currently, the only way of minimising this at acquisition is through the use of cryogenically used surface coils; however these are significantly more expensive than standard coils, were not available for the MRI scanner used in CABI, and therefore were not considered for this thesis.

Regarding physiological noise; motion artefacts; cardiac and respiration rates can often have a marked detrimental effect on BOLD signal measures. In particular for mouse brain fMRI with the use of electric shock stimuli, physiological noise can easily correlate with stimuli, reducing the specificity BOLD signal responses and spatial inferences that can be made from statistical parametric maps [38]. The use of anaesthesia can reduce motion artefacts, but can itself interfere with neurovascular coupling [112, 113]. One mouse fMRI study has attempted awake mouse fMRI to investigate learned responses to fear, avoiding this potential confound [39], and used training regimes to minimise motion artefacts. However, this strategy removes the potential confounder of anaesthesia and replaces it with the confounder of animal stress, which is arguably more difficult to reproduce across subjects.

There are currently two schools of thought for maintaining the physiology of the anaesthetised mouse for fMRI. One uses invasive mechanical ventilation to maintain the mouse respiration rate at a constant level (Bosshard et al. and others [35, 36, 38]). This method as suggested requires endotracheal intubation, and use of a neuromuscular blocking agent (pancuronium bromide in this case). Whilst neuromuscular blockers additionally remove the effects of head motion, the use of these agents makes each experiment non-recoverable, removing one of the main potential benefits of fMRI. The second school of thought allows the subject to maintain its own physiology, aided by oxygen-enriched air [33, 34, 37]. It is likely that the first option, whilst significantly technically challenging, does reduce physiological noise more than the second.

2.2.2.4 Image Preprocessing

The fMRI data set for a given run is 4-dimensional, covering space and time. In this thesis, this data was stored using the NifTi file format [114], as a series of 3D image volumes. Most data-analysis assumes that each voxel in a dataset corresponds to the same spatial location in the brain for all subjects, and that temporal sampling of the BOLD signal is at a constant, known rate. Preprocessing generally tries to remove sources of noise that violate these assumptions, and the implementation of these techniques is covered in section 3.2.

Spatial normalisation

Spatial normalisation accounts for the fact that subject brains can vary in size and shape. Techniques like voxel-based morphometry [115] are based on using image registration to map subtle changes in brains across subjects. However for the purposes of fMRI, it is desirable that subject data are spatially normalised to a template image, in order that the same voxel corresponds to the same functional region. Implementation of this using image registration for mouse fMRI is covered extensively in section 3.2.2.

Motion correction

Image registration is also used for motion correction of fMRI data. It is generally better to minimise head motion at the point of acquisition, using anaesthesia and head restraints (which for mice often consist of ear bars and a bite bar, see Figure 3.32), but preprocessing fMRI data sets by registering functional runs to an initial image or mean image reduces the effect of the BOLD signal ‘leaking’ across voxels [4]. Estimates of motion from this registration procedure can also be propagated through to the statistical analysis as nuisance regressors.

Slice-timing correction

In the temporal domain, slice-timing correction [116] can be applied to account for the differences in temporal sampling used by 2D slice based MRI pulse sequences. In this thesis, this is done by temporal sinc-interpolation, using information from neighbouring timepoints to phase-shift the BOLD signal to a reference time common to all slices. There is some criticism of this technique when used for analyses requiring accurate temporal information in the BOLD signal [117], however this is more pertinent to event-related fMRI designs, which are not considered in this thesis.

Spatial smoothing

The application of a spatial low-pass filter data is common in fMRI, although somewhat controversially [118]. This is often implemented using a Gaussian kernel, and effectively averages the BOLD signal across several neighbouring voxels, depending on the shape of the kernel used. One line of reasoning suggests that by using a spatial filter on the order of magnitude of the spatial functional response expected to be measured, tCNR is optimised. This is not the equivalent of simply increasing voxel dimensions at the point of acquisition to the equivalent size of the smoothing kernel, because each voxel will experience noise differently (although this is unlikely to be completely independent), and so collecting multiple voxels in the same functional region and then smoothing over all voxels is preferable to using larger voxels [4]. Furthermore, a larger voxel will experience greater signal dephasing due to magnetic field inhomogeneities (see section 2.1), and therefore may actually have lower tCNR than smaller voxels covering the same space.

As well as increasing tCNR, the spatial smoothing is also used to make assumptions used by common statistical analyses (covered in the following section) more valid [119]. In particular, the use of statistical parametric mapping conducts a statistical test at every voxel and either accepts or rejects the null hypothesis that the BOLD signal is explained by a model signal based on timings of the experimental stimuli. If each test is treated as independent, then the Bonferroni correction for multiple comparisons should be used, and the significance threshold divided by the number of statistical tests conducted. However, voxel timecourses are not independent (multiple voxels sample the same functional region), as they are spatially correlated, and this allows the use of random field theory to determine how many effective independent tests are actually applied. In general, the smoother the data, the fewer independent tests, and lower the significance threshold used to constrain the false positive rate.

2.2.3 Standard fMRI analysis

Given that the changes in the BOLD signal relative to stimuli can be easily masked by unwanted sources of variance, statistical analysis is often used to describe fMRI data and make inferences. This thesis uses two common approaches for analysis, statistical parametric mapping and region-of-interest analysis, which are briefly summarised here.

2.2.3.1 Statistical parametric mapping

Null hypothesis testing

This thesis commonly uses statistical parametric mapping (using the SPM toolbox [120]) for indicating the specificity and effect size of the BOLD response to stimuli. The entire theoretical underpinnings of this toolbox are beyond the scope of this thesis, however the salient points of its operation are provided.

Although logically problematic, null hypothesis testing is used extensively in science to decide if effects are real, or unlikely to occur by chance [121]. The formal statement of the logic is as follows:

- H_0: condition 1 = condition 2 (null hypothesis)
- H_0: condition 1 ≠ condition 2 (model tested by the experimenter)

Then data, which is assumed to independent and unbiased, is used to calculate a test-statistic. The test-statistic is compared to a known theoretical probability distribution that it should obey under H_0. By integrating this distribution a p-value can be calculated, which has the formal definition: the probability of observing data as (or more) extreme than that actually observed *assuming the null hypothesis is true*. A common approach that is used is to state a significance threshold α below which the null hypothesis is rejected. Commonly $\alpha = 0.05$ is used for such decision making.

The simplest application of hypothesis testing to fMRI images in a blocked design as used in this thesis would be (for each voxel) to perform a Student's t-test under the null hypothesis that the mean BOLD signal during a stimulus block is different than during a baseline block (assuming that the neuronal activity in a responsive voxel is perfectly correlated with the stimulus pattern). The t-statistic would be calculated by dividing the difference in the means by the shared standard error.

However, this does not account for the shape of the haemodynamic response function that links neuronal activity to the measured BOLD signal (as covered in chapter 5). One way of accounting for this, under the assumption of linearity of the BOLD response, is to use the general linear model (GLM) approach, of which the above simple method is an instance of the GLM.

The general linear model

The GLM is a generalised example of linear regression, represented by the matrix equation (2-15).

$$y = X\beta + \varepsilon \tag{2-15}$$

In equation (2-15), the measured BOLD data for a given voxel is represented by vector y, regressor variables (either of interest or nuisance regressors) by the design matrix X, weighting parameters for each regressor by the column vector β, and a residual error term by the column vector ε. Each column of the design matrix corresponds to a specific regressor, and the linear combination of the regressors (weighted by β) represents the modelled signal variance. Any variance which is unexplained by the regressors chosen then determines ε. Linear regression optimises the parameter values in order to minimise the sum of square errors, which is reasonable under Gaussian assumptions on the error term. Using this cost-function allows the optimal parameter values to be estimated through matrix operations, by the normal equation shown in (2-16).

$$\hat{\beta} = (X^T X)^{-1} X^T y \tag{2-16}$$

The variance of the error is necessary for the calculation of the test statistic. The residual of the model (i.e. the error term) is given by rearranging equation (2-15). Then the variance of the error term is given in equation (2-17).

$$\hat{\sigma}^2 = \frac{\varepsilon^T \varepsilon}{T - (p + 1)} \qquad \textbf{(2-17)}$$

In equation (2-17), T is the number of timepoints and p the number of parameters in the model (i.e. columns in the design matrix).

More complicated and computationally intensive cost-functions may necessitate using gradient descent. Given the case of typical fMRI experiments where thousands of voxels are covering the brain, and a GLM must be estimated for each one, it is prudent to use the least-squares error cost-function.

An example design matrix for a fixed effects (FFX) analysis is given in Figure 2.7.

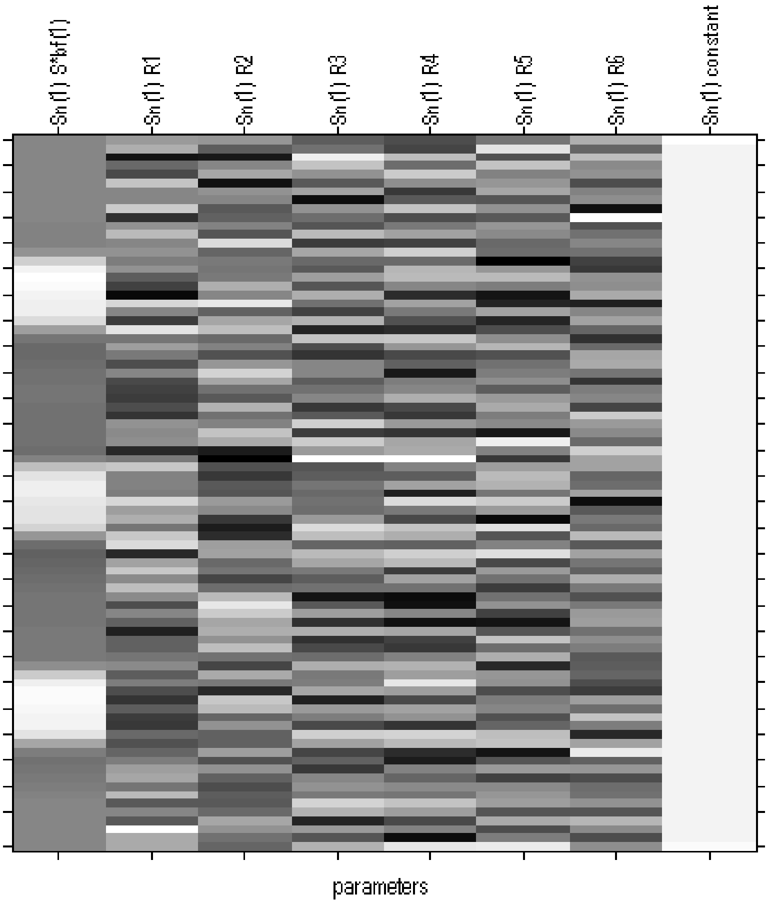

Figure 2.7. Example design matrix for a GLM for a single functional run. Dark values are low and bright values are high (arbitrary units). Time runs down the columns, and each column is a separate regressor (see main text for details).

This design matrix has three blocks of stimulus relative to 4 blocks of baseline, and this convolved with the SPM canonical haemodynamic response function [122] is the stimulus regressor, visualised in column 1. This is done under the assumption that neuronal activity in a voxel covering a brain region associated with the stimulus is perfectly correlated with the stimulus block. Columns 2-7 correspond to nuisance regressors – in this case estimates of motion from image registration. Column 8 is a constant session regressor which accounts for linear trends.

In order to decide whether to reject the null hypothesis that the BOLD signal in this voxel is not explained by stimulus regressor, a contrast row vector c must be used when constructing the t-statistic, which is derived from a linear combination of regression coefficients using $c\beta$. Contrast in this case means 'experimental contrast', rather than image contrast as commonly referred to in MRI. For the design matrix used in Figure 2.7, the contrast vector required is [1 0 0 0 0 0 0 0], and this will create a test statistic given by equation (2-18).

$$t = \frac{c\beta}{\sqrt{c(X^TX)^{-1}c^T\hat{\sigma}^2}} \tag{2-18}$$

The theoretical derivation of equation (2-18) is beyond the scope of this thesis. It is however important to note, that by including nuisance regressors in the design matrix, the size of the residuals is decreased, and this increases the detection power for the contrast of interest i.e. the stimulus regressor. However, if regressors are correlated, then the matrix inversion in (2-16) can fail, and parameters may not be uniquely determined. This is where the issue of physiological confounding variables can reduce the interpretability of results described by Schroeter et al [38] for mouse fMRI using electrical shocks.

For a random effects (RFX) analysis in SPM, FFX statistics at the 1st-level (single-subject) are treated as independent samples from a population, and the RFX statistic at a given voxel is calculated from the population mean μ (calculated as the average of the sample t-statistics) and the standard error of the mean (Equation (2-19)).

$$t = \frac{\mu}{S.E.M} \tag{2-19}$$

Whether a FFX or RFX analysis is used, by constructing a suitable design matrix, nuisance regressors and contrast vector, a t-statistic can be generated at each voxel. Under parametric assumptions and the null hypothesis, the probability of acquiring an extreme t-statistic or greater is given by the area of the tail of the Student's T-distribution defined by the statistic. Based on random field theory, a critical value of the t-statistic corresponding to a p < α threshold can be derived, and used as a bar below which the null hypothesis is accepted i.e. the BOLD signal at this voxel could reasonably be generated under the null hypothesis. One limitation of this approach is that the haemodynamic response function is assumed to be identical across brain regions. For block designs however, the convolution with the boxcar neuronal stimulus model reduces the effect of variability in the haemodynamic response. The compromise here is that it is more difficult to estimate parameters defining the haemodynamic response from block-design experiments – event-related fMRI is more suitable for this task [4].

Because the GLM is used to apply a statistical test at every voxel, some correction for the multiple comparisons problem must be made. The Bonferroni correction simply divides the p-value threshold by the number of voxels, although this assumes independent voxels (which they are not, as mentioned in section 2.2.2.4). The SPM toolbox approach uses Gaussian random field theory to estimate how many equivalent independent tests accounting for smoothness of the data, and thus determines a suitable threshold for null hypothesis rejection.

Descriptive vs Inferential GLM approaches

This thesis uses both descriptive and inferential GLM approaches for group analysis statistical parametric maps. The difference between the two can be simplified to different definitions and assumptions made on the data. A descriptive GLM (often referred to as a fixed effects (FFX) analysis) assumes that the sample provided is the entire population, and an inferential GLM (referred to as a random effects (RFX) analysis) assumes that the data is a random sample from a population. For group analyses either is valid [120, 123, 124], however care must be taken at the inferences that can be made from each. Group RFX analyses can suffer from low power, as the number of degrees of freedom (defining the Students' T-distribution for the null hypothesis against which the statistic is compared) are typically lower than for FFX analyses. Combined with the correction for multiple comparisons problem, the statistical thresholds required to reject the null hypothesis can be unreasonably high, risking Type II errors. Generally in this thesis, FFX analysis is used for mapping unless otherwise stated; accurately describing the data acquired in each study, but cannot strictly be used for formal inference for future studies.

2.2.3.2 Region-of-interest analysis

Current voxel-wise approaches are suitable for broad hypotheses about where BOLD responses will occur to a given stimulus, and indicate the specificity of the BOLD response relative to an uninformative spatial prior. However, they do not account for *a priori* knowledge of which regions are expected to show BOLD responses to a particular stimulus. Region-of-interest (ROI) analysis is used to ask questions of how the BOLD signal responds in a particular region, ignoring other parts of the brain.

It is extremely important to not follow up statistical parametric mapping with ROI analysis *using ROIs chosen using maps of the same data*, as this is circular logic [125]. Instead, anatomical ROIs or functional localisers should be used. For example, in this thesis three structural ROIs are commonly used, the LGd, the SCs and VISp in relation to visual stimuli, given that they are key regions of the mouse visual system. A benefit of ROI analysis is that the signal over multiple voxels is averaged, and as long as all voxels within a defined ROI are functionally responsive, tCNR is increased. However, if too coarse a ROI is chosen, then non-functional voxels will be included in the average, reducing tCNR.

Care must be taken in the definition of structural ROIs, whether by registration or manual segmentation. It is sensible to define ROIs on structural images with high image contrast (e.g. T_2 weighted) rather than BOLD weighted functional images. Even with anatomical images, image contrast between different functional regions (e.g. visual cortex as opposed to somatosensory cortex) may be poor. For this reason, image registration using a previously labelled structural image or atlas can reduce bias and provide useful anatomical ROIs that can be compared across subjects and studies.

2.3 Chapter summary

In this chapter, the theoretical background to the thesis was provided. Section 2.1 covered the theory behind magnetic resonance imaging, including measurement of the T_2^* weighted BOLD signal. Then in section 2.2, basic theory behind the fMRI data processing and statistical analyses used in this thesis to map BOLD responses was provided. In the next chapter, development of a mouse fMRI protocol using visual stimulation is described.

3 Establishing a mouse fMRI protocol

Before starting this project, mouse brain fMRI had not been performed at CABI, and to my knowledge there were no prior publications from any UK universities. The aim of this chapter was therefore to develop a protocol for robust mouse brain fMRI at CABI.

Mouse brain fMRI is known to be challenging for several reasons:

1. The small size of the mouse brain relative to other mammals requires the use of high-field (> 7T) MRI to acquire sufficient signal, as well as large magnetic field gradients to achieve sufficient spatial resolution.
2. When operating at high field strengths with a small, anatomically heterogeneous sample (such as the mouse brain), field inhomogeneities caused by bulk magnetic susceptibility discontinuities at tissue boundaries can cause severe image distortion and signal loss. These effects become more severe as the sample reduces in size, as the volume/surface area ratio decreases.
3. fMRI requires the preservation of neurovascular coupling in order to make inferences about neuronal population activity from the BOLD signal. Neurovascular coupling can be disrupted by anaesthesia, blood gas levels, and abnormal respiration and temperature values. Furthermore, correlation of these confounds with a stimulus used for task-based fMRI (e.g. electric shocks to the paw inducing an increase in respiration) can induce non-specific BOLD signal changes, masking BOLD responses functionally specific to the stimulus [38].

Section 3.1 covers experimental protocol development work (section 3.1.1 describes a bench experiment using a medetomidine anaesthetic protocol, whilst section 3.1.2, 3.1.3 and section 3.1.4 use agarose phantoms to examine GE-EPI temporal stability and evaluate the use of an interleaved snapshot GE-EPI pulse sequence). In section 3.2, work on mouse fMRI data processing is covered, with a particular focus on spatial normalisation and image registration. Then in section 3.3, the first mouse brain task-based fMRI study conducted at CABI is described, showing consistent BOLD responses and also demonstrating the benefits of using interleaved snapshot GE-EPI in vivo. The chapter is then summarised in section 3.4.

3.1 Protocol development for mouse fMRI

In this section, I aimed to develop a protocol for mouse fMRI at CABI, investigating mouse physiology and MRI pulse sequence parameters. The following subsections consist of separate minor experiments conducted to better inform an *in vivo* mouse fMRI protocol.

3.1.1 Mouse pulse oximetry

A previous study [33] had shown that medetomidine anaesthesia can yield robust BOLD responses to paw stimulation in the mouse brain. Given medetomidine had not previously been used at CABI, I aimed in this pilot study to implement a medetomidine anaesthesia protocol in the C57BL/6 mouse. Specifically, to test whether a previously described dosing strategy can provide stable anaesthesia (evaluated with hindpaw reflex testing) and yield stable physiology (assessed using arterial oxygen saturation).

3.1.1.1 Introduction

The bulk of the mouse brain fMRI (both resting state and task-based BOLD imaging) literature [31-38, 126-128], with a few exceptions [39, 129], use some sort of anaesthetic agent during the course of a mouse fMRI experiment. The main advantages of using anaesthesia are; the ease with which a mouse can be handled without time-consuming training, reduction of stress suffered by the animal, and the reduction in head motion which can introduce severe artefacts in the acquired fMRI data. The main disadvantage is that the anaesthetic agent is a potential confounding factor in the interpretation of all experimental results. Furthermore, some anaesthesia regimes such as α-chloralose have considerable side-effects [130], meaning experiments are often non-recoverable.

The most common anaesthetic agent used in mouse brain MRI is isoflurane, as it is recoverable, fast acting, and can be administered in gaseous form. However, the vasodilatory effect of isoflurane has been documented multiple times [112, 113, 131], and so presents as a confounder for the neurovascular coupling between neuronal activity and measured BOLD signal responses [112, 113].

Previous studies in the literature show that robust BOLD responses can be elicited in response to sensory stimulation in the mouse brain using the α_2-adrenergic agonist medetomidine, [33, 37]. However, it must be delivered in liquid form as an injectable, and before the work described in this thesis, had never been used in CABI.

Previous studies of neurovascular coupling in the rat have demonstrated the importance of maintaining blood gases (partial pressure of oxygen and carbon dioxide, arterial oxygen saturation) within a physiologically relevant range [132]. These parameters are most accurately measured from extracted blood samples. Repeated blood sampling in the mouse is invasive and extremely difficult, as the mouse has such a small volume of blood (~1.5 ml), and so instead I used a pulse oximeter to measure arterial oxygen saturation continuously and non-invasively.

In order to assess the suitability of a medetomidine anaesthetic protocol, it was deemed necessary to carry out physiological monitoring in a ‘bench’ experiment, ensure arterial oxygen saturation did not leave standard ranges, and assess depth of anaesthesia through examination of the hindpaw reflex, in order to fulfil the criteria of the relevant UK Home Office project licence.

3.1.1.2 Methods

All experiments were performed in accordance with the European Commission Directive 86/609/EEC (European Convention for the Protection of Vertebrate Animals used for Experimental and Other Scientific Purposes) and the United Kingdom Home Office (Scientific Procedures) Act (1986) with project approval from the Institutional Animal Care and Use Committee.

A single female C57BL6/J mouse weighing 20.2 g was used. Anaesthesia was induced with isoflurane (2%) and reduced to 1.5% for preparation. At anaesthesia induction, the subject was supplied with a mix of 0.1 L/min O_2 and 0.4 L/min medical air. This mix of oxygen-enriched air was chosen based on a previous rat fMRI protocol used at CABI [133, 134], and a mouse fMRI study [37] which reports cortical BOLD responses to paw stimulation on the order of 2% relative to baseline signals.

Animal preparation included shaving a square patch of fur across the stomach for the injection of the subcutaneous infusion line, and shaving the hind leg for the placement of the oximeter. Removing non-white fur was required for maximising optical transmission and thereby increasing SNR. The mouse was then transferred to the mouse imaging cradle (Agilent), but kept on the bench. Physiological monitoring was conducted using a MouseOx pulse oximeter (Starr Life Sciences). A mouse thigh clip to hold the transmitter/receiver cables in place was applied to the shaved mouse thigh.

The subcutaneous bolus of medetomidine was delivered via a programmable infusion pump (Harvard Instruments). Isoflurane was slowly discontinued over the course of the next 10 minutes, by approximately 0.2% every 1 minute starting 3 minutes after bolus administration, as following a previously developed protocol [33]. The medetomidine dosage was dependent on the mass of the mouse, set at 0.4 mg/kg for the initial bolus, and 0.8 mg/kg/hr for the constant infusion. The animal was free breathing throughout, and did not respond to hind-paw reflex test multiple times during the experiment.

Once the animal was stable at 1.5% isoflurane (ISO) and ready for the initial bolus of medetomidine, SaO_2 was measured using the pulse oximeter at a sampling frequency of 15 Hz. One initial 10 minute run was conducted on 1.5% isoflurane alone. Then the subject was switched to medetomidine, and three 10 minute runs were conducted in succession, the approximate expected imaging time window for future fMRI studies.

Then, as a positive control to demonstrate the dynamic range of the pulse oximetry measurements, two 5 minute runs were conducted with gas challenges: first with the 0.1 L/min O_2 removed, and the second with a mix of 0.1 L/min O_2 and 0.2 L/min medical air. Prior to the challenges, the mixture was 0.1 L/min O_2 and 0.4 L/min medical air. This was done to examine the sensitivity of the measurements of SaO_2 on the inhaled gas mixture.

3.1.1.3 Results

SaO_2 results for the four anaesthesia runs are shown in Figure 3.1.

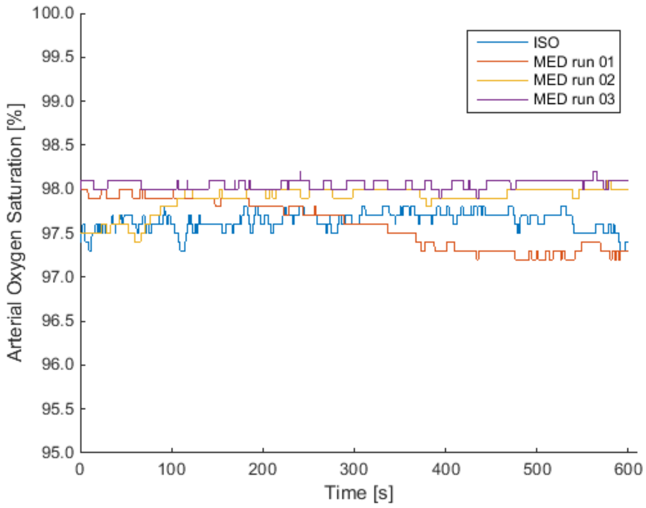

Figure 3.1. Arterial oxygen saturation under isoflurane and medetomidine anaesthesia.

Switching from 1.5% isoflurane to injectable medetomidine did not appear to have an effect on SaO_2. The mean SaO_2 values over each 10 minute period are provided in Table 3.1.

Table 3.1 Mean values of arterial oxygen saturation SaO_2 under anaesthesia

Anaesthesia/run	Mean Arterial Oxygen Saturation ± standard deviation [%]
1.5% Isoflurane / 01	97.6 ± 0.1
Medetomidine / 01	97.6 ± 0.3
Medetomidine / 02	97.9 ± 0.2
Medetomidine / 03	98.05 ± 0.05

These results show that using medetomidine anaesthesia does not have an appreciative effect on SaO_2 relative to 1.5% isoflurane. The mean value of all measurements under medetomidine is (97.8 ± 0.3) %, which appears to be physiologically stable and close to values measured in the awake mouse [135].

The results from the two gas challenge runs are shown in Figure 3.2.

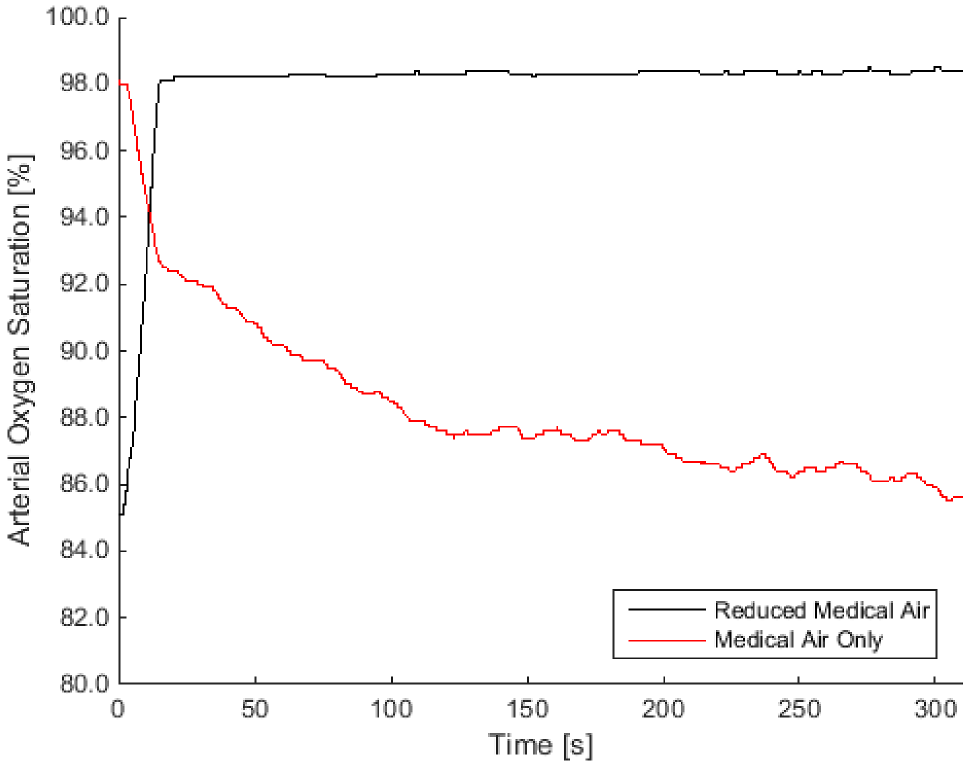

Figure 3.2. Arterial oxygen saturation under medetomidine anaesthesia with gas challenges. Removing pure O_2 from the gas mixture has a marked effect on SaO_2.

Figure 3.2 clearly shows the decay in SaO_2 to the removal of 0.1 L/min O_2 (red line, 0.4 L/min medical air). This decay is not suitably represented by a mean value. For the 0.2 L/min medical air + 0.1 L/min O_2 run, the mean SaO_2 in the period of stabilisation (50-300 seconds) is (98.3 ± 0.07) %. This run was conducted immediately after the 0.4 L/min medical air run, which is why the initial SaO_2 value is approximately 85%. This also shows how that arterial oxygen saturation can recover to a hypoxic gas challenge in less than a minute, but that additional oxygen is required to be added to medical air for physiologically normal arterial oxygen saturation.

3.1.1.4 Discussion

Despite SaO_2 remaining close to constant throughout separate runs under both isoflurane and medetomidine anaesthetic, there was still some variation present. The mean values of SaO_2 without gas challenges agree with results in the literature [37, 135, 136]. It was noticed during the experiment that the ‘type’ of breathing changed on switching from 1.5% isoflurane to medetomidine. Under high levels of isoflurane (> 1.5%), breathing was gasping, erratic and less frequent. Under medetomidine, the style of breath was similar to normal physiological conditions (smoother, shallower and faster). Measuring the respiration rate using the oximeter proved difficult, and for significant periods the respiration rate was severely under-reported. When the oximeter produced low breathing rate values, the animal was watched in detail and could clearly be seen to be breathing at a rate greater than the calculated rate (data not shown).

A limitation of this experiment is that only SaO_2 was measured as a physiological variable of interest. Other parameters of interest that could affect BOLD responses include acidity (pH), and the partial pressure of oxygen and carbon dioxide. These are all contributing factors to neurovascular coupling (for a thorough review, see Buxton 2013 [93]). However, directly measuring these in the mouse is extremely challenging. This is primarily due to their small blood volume (~1.5 ml) and the blood volume requirement of many blood-gas analyser systems could directly affect the physiology [135]. Only one animal was used, and therefore no information on animal variability under this protocol can be gained from this experiment. However, published work conducted by Schroeter et al. [38] and Nasrallah et al. [37] show similar results.

3.1.1.5 Conclusion

This experiment was conducted to investigate the stability of mouse physiology under medetomidine anaesthesia. Measurements of arterial oxygen saturation levels were taken in one wild-type mouse using a MouseOx pulse oximeter (Starr Life Sciences), under isoflurane and then a medetomidine anaesthesia protocol. Using medetomidine did not alter arterial oxygen saturation levels relative to using isoflurane ((97.8 ± 0.3) % against (97.6 ± 0.1) %). All baseline values remained stable throughout within physiologically relevant boundaries [37, 38] whilst using oxygen-enriched air in a ratio of 4:1 (medical air : oxygen). Following this result, this medetomidine dosing strategy and inhaled gas mixture was carried forward for subsequent fMRI experiments. Robust BOLD responses in the mouse brain under this protocol are described in section 3.3.

3.1.2 GE-EPI temporal instability: phantom study

In this early study, I aimed to evaluate the GE-EPI pulse sequence available at CABI on the Agilent 9.4T pre-clinical MRI scanner in terms of temporal stability, using an agarose phantom.

3.1.2.1 Introduction

Good temporal signal stability is required for fMRI, in order to reduce the risk of false negatives. Temporal instability was found in previous *in vivo* mouse resting state fMRI pilot studies that I conducted (data not shown). In order to optimise the *in vivo* fMRI protocol, experiments were first conducted on an agarose phantom in order to reach a compromise between spatial resolution, temporal resolution and temporal stability. This experiment aimed to test the dependence of temporal stability on the fMRI imaging field of view (FOV) in an agar phantom. This hypothesis is based on the reduced gradient amplitude (and hence reduced ‘strain’ on the hardware) required for a larger FOV at a given matrix size.

3.1.2.2 Methods

A cylindrical tube of agar (approx. 3 cm tall, radius approx. 0.5 cm) was imaged on an Agilent 9.4T MRI scanner, with a shielded gradient (SGRAD 205/120/HD) set with a maximum strength of 400 mT m^{-1}. A 4-channel surface coil (Rapid) was used in conjunction with a 72 mm diameter birdcage volume coil (Rapid). Conventional single shot GE-EPI was used with a repetition time (TR) of 2000 ms and an echo time (TE) of 18.5 ms. 12 axial slices of thickness 0.5 mm with a slice gap of 0.1 mm were acquired at every time point. 300 volume images were taken for a given scan (total running time of 10 minutes). Two square FOVs were investigated - 30 mm and 25 mm, at a matrix size of 96 x 96. ROIs were drawn and signals extracted using a custom graphical user interface (GUI) written in MATLAB (see section 3.2.2.1).

3.1.2.3 Results

At a FOV of 30 mm, the mean signal across the region of interest (ROI) was stable, with a temporal SNR (tSNR) of 192. For a FOV of 25 mm, the mean signal suffered severe intensity drop out across the ROI, and the tSNR dropped to 2.4. Mean timecourses for a single slice are shown in Figure 3.3.

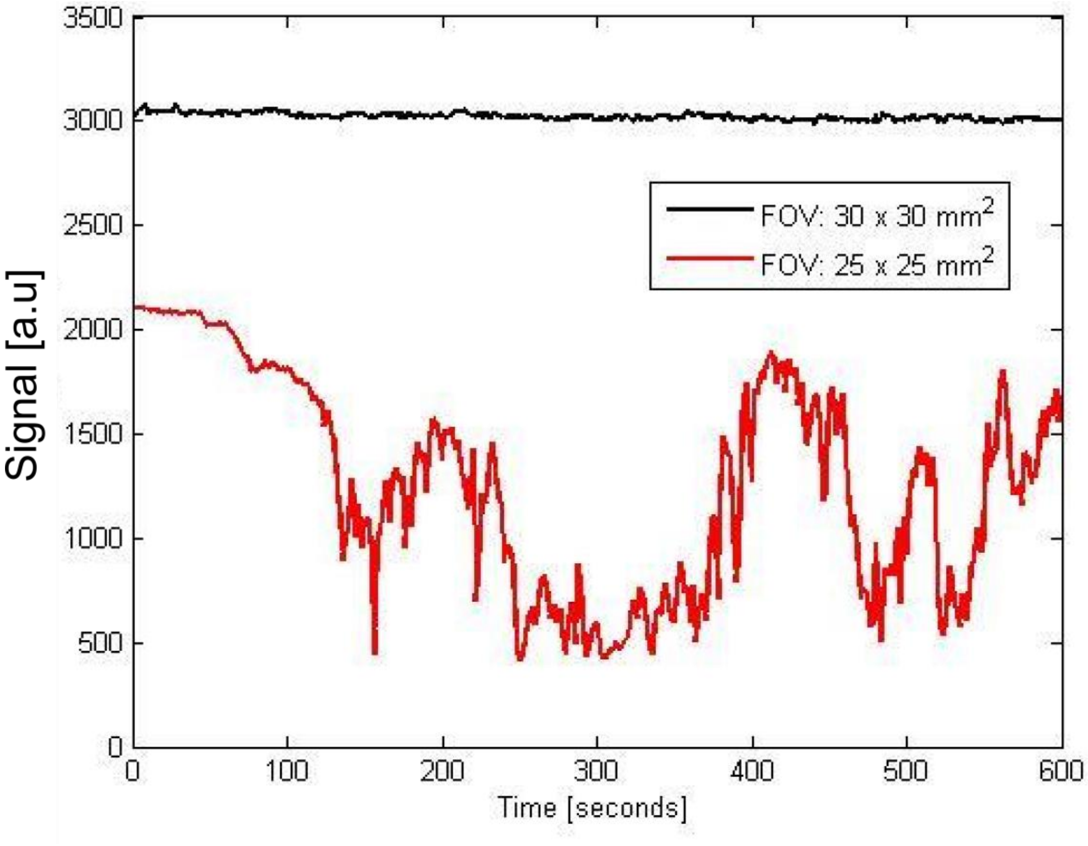

Figure 3.3. Plot of mean GE-EPI intensity from an ROI in the phantom against time for two different FOVs.

Representative images from stable and unstable sections of the timecourses in Figure 3.3 are shown in Figure 3.4.

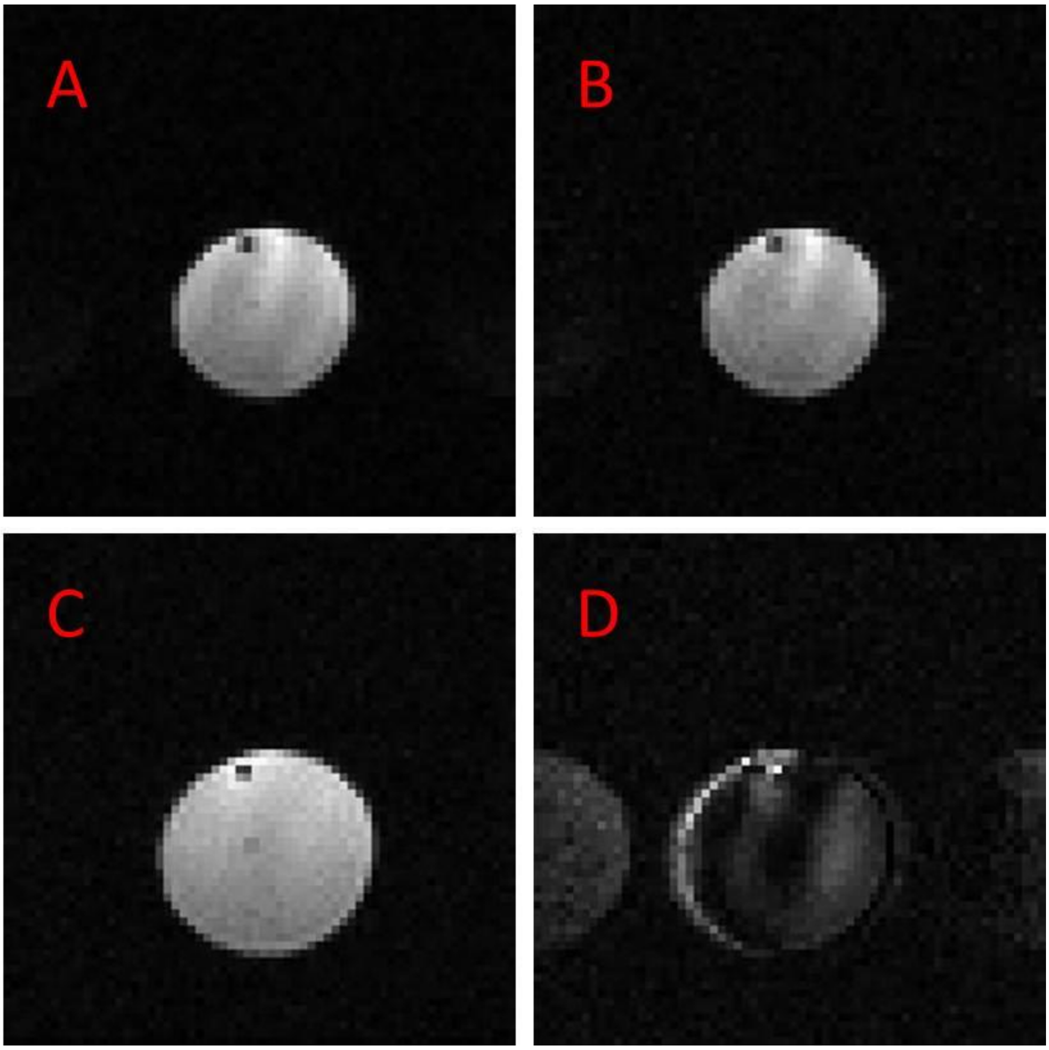

Figure 3.4. GE-EPI images of an agar phantom. Images A) and B) were taken from t = 0 and 300 s respectively, at a FOV of 30 mm. Images C) and D) were taken at the same timepoints but at a FOV of 25 mm. The loss of signal quality is clear in D).

3.1.2.4 Discussion

The fact that image artefacts are apparent at smaller FOVs suggests that the source of signal instability is the magnetic field gradient set. By reducing the gradient duty cycle, the artefacts are suppressed.

3.1.2.5 Conclusion

With a FOV of 25 x 25 mm^2 (taken from a previous mouse brain resting state fMRI study [126]), GE-EPI signal stability was poor. Physiological noise and motion artefacts were eliminated as causes by using an agar phantom. At a smaller FOV, image degradation beyond typical Nyquist ghosting was seen. The cause was believed to be the failure of the magnetic gradient hardware to cope with a heavy duty cycle. Future experiments should use GE-EPI with sequence parameters that require a lower duty cycle e.g. longer TR, larger FOV, smaller matrix size, etc.

Exhaustively exploring the GE-EPI parameter space in a phantom may not prove particularly relevant for future *in vivo* experiments, instead parameters should be chosen that provide adequate temporal stability, suitable spatial and temporal resolution, slice coverage and sensitivity to BOLD signal changes. For more details on GE-EPI parameters used *in vivo*, see section 3.3.2.

3.1.3 GE-EPI parameter optimisation: phantom study

In this experiment, I aimed to optimise the single-shot GE-EPI pulse sequence with respect to tSNR in an agarose phantom.

3.1.3.1 Introduction

An attempt to implement similar GE-EPI parameters used in a mouse brain resting state study [126], resulted in intolerable temporal signal instability. It was suggested that one potential cause was a failure of the magnetic gradient hardware to cope with heavier duty cycles. To that end, an experiment was conducted in an agar phantom to attempt to partially optimise GE-EPI parameter space for future *in vivo* experiments.

3.1.3.2 Methods

A cylindrical 15 ml Falcon tube of agarose was imaged on an Agilent 9.4T MRI scanner, with a shielded gradient (SGRAD 205/120/HD) set with a maximum strength of 400 mT m^{-1}. A 2-channel surface coil (Rapid) was used in conjunction with a 72 mm diameter birdcage volume coil (Rapid). Conventional single shot GE-EPI was used with a square FOV of width 35 mm and an echo time (TE) of 19 ms. Slices of thickness 0.5 mm with a slice gap of 0.1 mm were acquired at every time point. The parameters varied were TR, matrix size and number of slices. TR was set to 1.5, 2.0 or 2.5 seconds, matrix size either 64 x 64 or 96 x 96, and number of slices to either 12 or 24. Each scan was set to a total imaging time of approximately 10 minutes. Shimming was done manually, and a linewidth of 13 Hz (FWHM) was achieved.

Signals were extracted using a 0.5 mm diameter spherical ROI (approximately the same volume of the mouse LGd) placed at the centre of the phantom, and signals were extracted using the MarsBaR toolbox [137], and a 128 s high-pass temporal filter applied to each voxel timecourse before averaging. Temporal signal-to-noise ratio (tSNR) was calculated by dividing the mean signal value by the standard deviation.

3.1.3.3 Results

For each timecourse, extracted, no signal instabilities or Nyquist ghosting was seen in any GE-EPI images. Temporal SNR measurements are shown in Table 3.2.

Table 3.2. Temporal SNR measurements for a varied GE-EPI parameter space.

TR [s]	Matrix size	Number of slices	Temporal SNR
1.5	64x64	12	290
2.0	64x64	12	293
2.5	64x64	12	289
1.5	96x96	12	420
2.0	96x96	12	416
2.5	96x96	12	**432**
1.5	64x64	24	279
2.0	64x64	24	289
2.5	64x64	24	270
1.5	96x96	24	390
2.0	96x96	24	403
2.5	96x96	24	371

From Table 3.2, the combination with the greatest temporal SNR is the use of a TR = 2.5 seconds, matrix size 96 x 96 and acquisition of 12 slices.

3.1.3.4 Discussion

As no parameter combination elicited the large signal instabilities seen in section 3.1.2, little information can be offered by this data set on the causes of those previously observed instabilities. However, temporal SNR did vary depending on the parameter choice. Matrix size affected temporal SNR most strongly (as would be expected), as the 0.5 mm diameter sphere was sampled by more voxels for a greater matrix size at a fixed FOV, and therefore signal averaging has a greater effect on increasing tSNR. Acquiring more slices within a given TR period also reduced tSNR as expected, although this effect was small. For a given matrix size and number of slices, changing TR did not appear to make any systematic changes to tSNR. For experiments using single-shot GE-EPI, it would be reasonable to use up to 24 slices. However, when considering that the all of the mouse visual grey matter regions in the mouse brain can be successfully covered with 12 slices, this could be considered unnecessary, and would require a larger volume to be shimmed, potentially reducing signal quality in the regions of interest.

Echo time was not varied in this study, despite it being an important parameter for fMRI sensitivity [138]. It is expected that choosing an echo time of approximately the same value as the baseline T_2^* should maximise sensitivity to changes in T_2^* and therefore the BOLD signal. Based on a summary of the literature of mouse [35-38] and rat [59, 63, 133] studies using GE-EPI at 9.4T, an echo time of 19 ms was chosen, as a compromise between signal decay at longer TEs, and reduced BOLD sensitivity at shorter TEs.

3.1.3.5 Conclusion

In this phantom study, the dependence of temporal signal-to-noise ratio and stability on the TR, spatial resolution and number of slices used in the GE-EPI sequence, for scan duration of 10 minutes. Based on these phantom results, it would be reasonable to use a TR of 2.5 seconds, and matrix size of 96x96 with a FOV of 35 mm^2 for future GE-EPI applications. The long TR also has the benefit of reducing the gradient duty cycle relative to shorter TR, which may be beneficial given the signal instability observed in section 3.1.2 that appeared to be associated with high gradient duty cycle.

3.1.4 Interleaved snapshot GE-EPI: phantom study

Following sequence parameter optimisation on an agarose phantom, I proceeded to apply the single shot sequence in vivo. Figure 3.5 shows a representative EPI image where marked spatial distortions can be observed. In this study, I aimed to investigate the effect of using interleaved snapshot GE-EPI [139, 140] to reduce image artefacts in a phantom. The effect on temporal SNR was also considered.

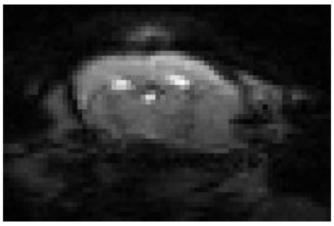

Figure 3.5. Image distortion in the mouse brain. Coronal slice demonstrating a ‘smearing’ of signal across the field of view.

3.1.4.1 Introduction

A single-shot GE-EPI pulse sequence is the standard method of acquiring fMRI data. However single-shot GE-EPI is vulnerable to local magnetic field gradients caused by bulk magnetic susceptibility discontinuities, resulting in signal loss and image distortion. This is particularly apparent in the mouse brain, due to the low volume/surface area ratio [33]. Interleaved snapshot GE-EPI has been suggested by Guilfoyle and Hrabe [140] as an alternative acquisition protocol for mouse fMRI that can reduce susceptibility induced artefacts without compromising temporal resolution. Briefly, the conventional EPI sequence is separated into a series of excitation/acquisition snapshots conducted in succession at varied flip angles within one TR period. Each snapshot partially fills k-space and the entirety of k-space is composed of the interleaved snapshots. Each slice is acquired in turn with n snapshots, reducing vulnerability to respiration artefacts faced by conventional segmented EPI sequences. To further explain this, figures 1 and 2 from Guilfoyle and Hrabe's paper are reproduced in Figure 3.6 and Figure 3.7 respectively, for the case where $n = 3$ interleaved snapshots.

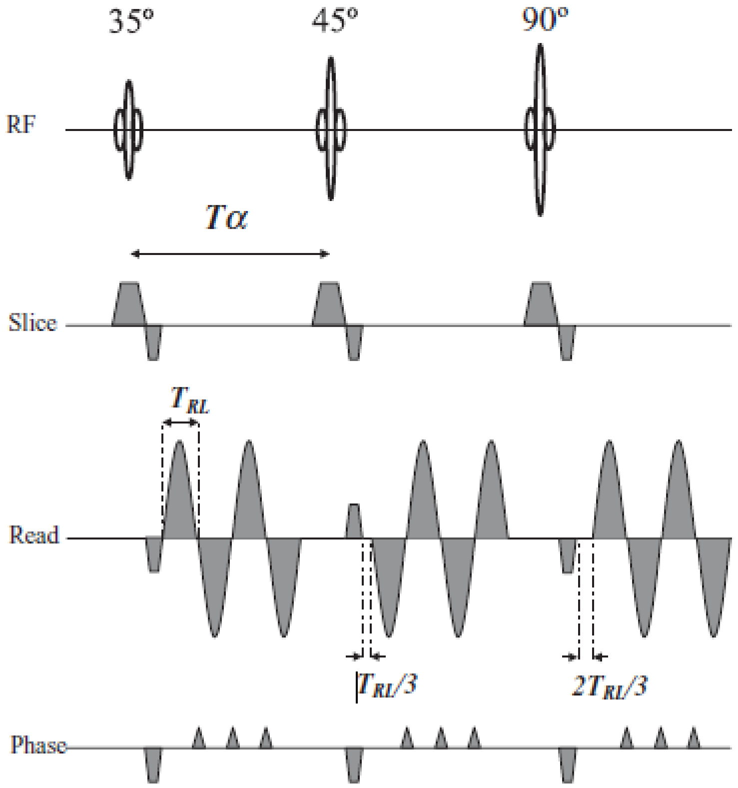

Figure 3.6. Schematic of interleaved snapshot GE-EPI pulse sequence reproduced from Guilfoyle and Hrabe [140], illustrating the pulse sequence required for interleaved snapshot GE-EPI, $n = 3$. The original caption reads as follows, "Diagram of an interleaved snapshot EPI sequence consisting of three excitation-acquisition blocks, each lasting T_{α}. The segments follow in immediate succession with increasing flip angles, thus preserving the snapshot nature of conventional EPI. The second acquisition is delayed by $T_{RL}/3$ and the third by $2T_{RL}/3$, where T_{RL} is the duration of a single gradient lobe. This ensures a smooth T_2^* decay in the combined data set…"

The pulse sequence shown in Figure 3.6 is similar to that shown in Figure 2.5 for the single-shot GE-EPI, except that in this case, one excitation does not cover the entirety of k-space. This coverage is described in Figure 3.7.

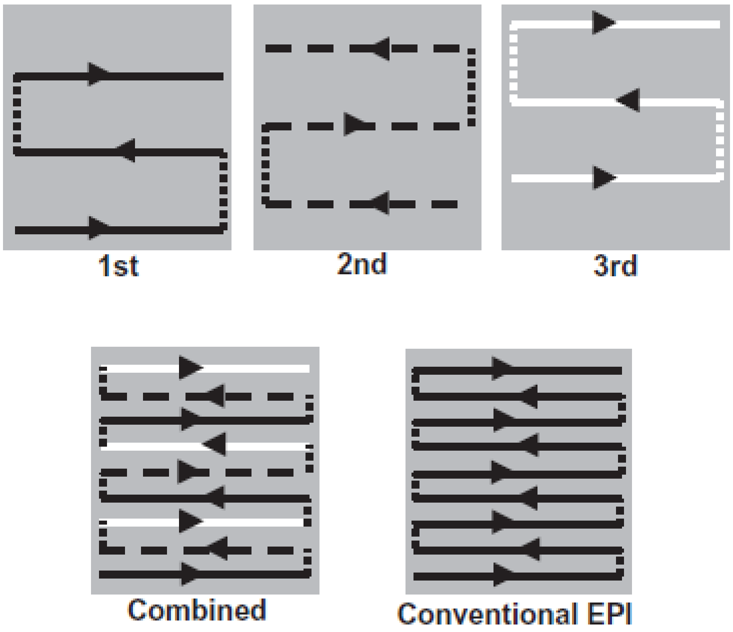
1st 2nd 3rd

Combined Conventional EPI

Figure 3.7. Schematic of k-space acquisition for interleaved snapshot GE-EPI, reproduced from Guilfoyle and Hrabe [140], illustrating the coverage of k-space with each snapshot, and how the data is interleaved to resemble conventional single-shot GE-EPI. The original caption reads as follows, "The k-space coverage of an interleaved snapshot EPI compared with a conventional EPI. The three segments in the top row are combined into a complete interleaved kspace data set (bottom left), providing coverage identical with that of a conventional EPI data set (bottom right)".

Each snapshot of k-space for the slice in question is acquired using a different flip angle, specified in equation (3-1) (for a full derivation and proof by induction, see the methods section of Guilfoyle and Hrabe [140]).

$$\sin(\alpha_i) = \frac{1}{\sqrt{n-i}} \tag{3-1}$$

In equation (3-1), α_i is the flip angle for the i^{th} interleaved snapshot. This definition of α_i ensures each snapshot samples the same transverse magnetisation. With multiple snapshots acquired at the same flip angle and then interleaved, adjacent lines in k-space would be modulated by step increases – leading to artefacts in the Fourier transformed reconstruction.

Spatial distortion is reduced by this method because the average sampling interval between excitation and acquisition is reduced for each line of k-space. The longer sampling interval used in conventional EPI gives off-resonance (B_0 inhomogeneities) effects longer to corrupt an image during acquisition [139]. The equivalent way of reducing distortion with conventional EPI would be to increase the spectral bandwidth, however this in turn increases the duty cycle placed on the magnetic gradient hardware, and consequently may require further compromises in either temporal or spatial resolution. Conventional multi-slice segmented EPI sequences are more susceptible to motion artefacts than interleaved snapshot EPI, as there is a longer time between segment acquisitions [140].

However, there is a decrease in imaging efficiency (SNR per square root of imaging time [141]) when using interleaved snapshot EPI, which in turn theoretically predicts a reduction in image signal-to-noise ratio (SNR) by a factor of $\sqrt{n}$ (for a full derivation, see Guilfoyle and Hrabe [140]). For mouse fMRI, this reduction is only problematic if it in turn reduces the temporal quality of the BOLD signal. In a simple phantom with no way of modulating T_2^*, the most appropriate measure of temporal signal quality is the temporal signal-to-noise ratio (tSNR), whereas for in vivo task-based fMRI the temporal contrast-to-noise (tCNR) is more appropriate.

The relation between image SNR and tSNR is not trivial, and dependent on many external factors [142]. The broad expectation before conducting this experiment was that with increasing n, image SNR would decrease by $\sqrt{n}$, and tSNR would also decrease.

3.1.4.2 Methods

A cylindrical 15 ml Falcon tube of agarose was imaged on an Agilent 9.4T MRI scanner, with a shielded gradient (SGRAD 205/120/HD) set with a maximum strength of 400 mT m^{-1}. A 72 mm inner diameter volume coil for RF transmission (Rapid Biomedical), and a room-temperature 2 channel array surface coil (Rapid Biomedical) for signal reception. VNMRJ 3.1 software was used for image acquisition and reconstruction.

GE-EPI was used with a repetition time (TR) of 2500 ms and an echo time (TE) of 19 ms, and a FOV of 35 mm^2. 12 axial slices of thickness 0.5 mm with a slice gap of 0.1 mm were acquired at every time point and 100 volume images were acquired for a given run. Interleaved snapshots were used in the range $n = 1:4$. After manual shimming, a linewidth of 18.33 Hz was achieved.

Signals were extracted using a 2.5 mm diameter spherical ROI placed at the centre of the phantom, and signals were extracted using the MarsBaR toolbox [137], and a 128 s high-pass temporal filter applied to each voxel timecourse before averaging. Temporal signal-to-noise ratio (tSNR) was calculated by dividing the mean signal value by the standard deviation. Image SNR was calculated by the mean signal in the same ROI of the first image divided by the standard deviation of the signal in an equivalent size ROI placed outside the phantom.

3.1.4.3 Results

The effects of using multiple snapshots on GE-EPI image quality of a cylindrical phantom are shown in Figure 3.8. On visual inspection, increasing the number of snapshots reduces the distortion in the acquired images.

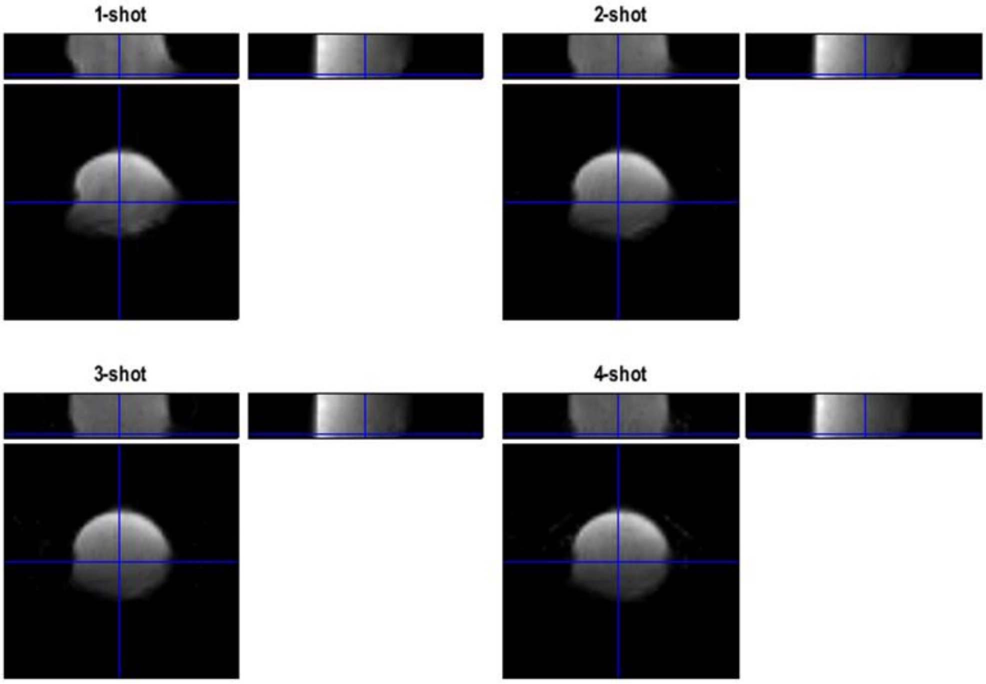

Figure 3.8. Distortion reduction using multiple interleaved snapshots with FOV = 35 x 35 mm^2.

SNR results were calculated using a 2.5 mm diameter spherical voxel ROI and are included in Table 3.3.

Table 3.3. Dependence of temporal SNR on number of interleaved snapshots.

n interleaved snapshots	Image SNR	Temporal SNR
1	189	1369
2	173	1330
3	182	1200
4	162	873

These results indicate that indeed, image and temporal SNR generally fall with the use of interleaved snapshots.

3.1.4.4 Discussion

Increasing the number of interleaved snapshots used during acquisition reduced the amount of spatial distortion, assessed using visual inspection. Both image and temporal SNR reduced with increasing snapshot number.

Up to this point, physiological noise has not been considered, and this is likely to strongly affect tSNR, in addition to hardware effects.

The current shimming strategy is to use a GE 3D shim protocol [143, 144]; with both 1st and 2nd order shims optimised in a user defined cubic shim voxel (approximately 5 x 8 x 9 mm^3) with voxel corners set at the sample edges. As mentioned in section 3.3, typical line-width (FWHM) within this shim voxel for *in vivo* data is approximately 60 Hz, which is reasonable when compared with other values in the literature [37].

There are alternative methods that could be tried to better improve spatial localisation of the BOLD signal in single-shot GE-EPI. For example, the method of acquiring a magnetic field map and using it to unwarp the GE-EPI images is well documented for human fMRI [145, 146]. I had previously tried this method at CABI for mouse GE-EPI images, however problems with phase-wrapping and low signal-to-noise were not overcome (data not shown).

3.1.4.5 Conclusion

For a range of GE-EPI sequence parameters, image quality was assessed using visual inspection, and tSNR calculated with an ROI analysis. The use of interleaved snapshot EPI improved spatial localisation of T_2^* weighted images, with an overall reduction in tSNR with increasing n. However, it should be noted that phantom tSNR only gives information on baseline stability. Therefore it was decided that interleaved snapshot GE-EPI should be tried *in vivo* and the tCNR of the BOLD signal investigated as well (see section 3.3).

3.1.5 Protocol development – conclusion

In this section, a series of experiments were conducted to better inform a mouse fMRI experimental protocol. Four experiments were conducted, which addressed the following issues: anaesthesia strategy, GE-EPI temporal stability and image distortion in GE-EPI data. The next section covers methods development of fMRI data processing.

3.2 fMRI data processing

In this section, I describe computational work I completed to prepare mouse brain task-based fMRI data for further analysis, and the automatic data processing pipeline I constructed utilising routines from the SPM12 toolbox [120] and others.

3.2.1 Introduction

The size of the signal of interest in BOLD fMRI data relative to the numerous noise sources is extremely low relative to many other scientific disciplines [147], and therefore data processing/pre-processing is often required to reduce bias and non-interesting variance from measured BOLD data, in both the spatial and temporal domains. There is an enormous body of literature on best practises for fMRI processing, and also a number of free, open source toolboxes for researchers to use, such as the SPM [120], the FSL [148] and AFNI [149] toolboxes.

This work predominantly uses code and routines from the SPM toolbox, predominantly SPM12, version spm_r6767, although SPM8 was used initially for some of the development. MATLAB 2013a was used throughout this thesis unless otherwise stated.

A general approach to fMRI data processing and analysis in humans is summarised in Figure 3.9.

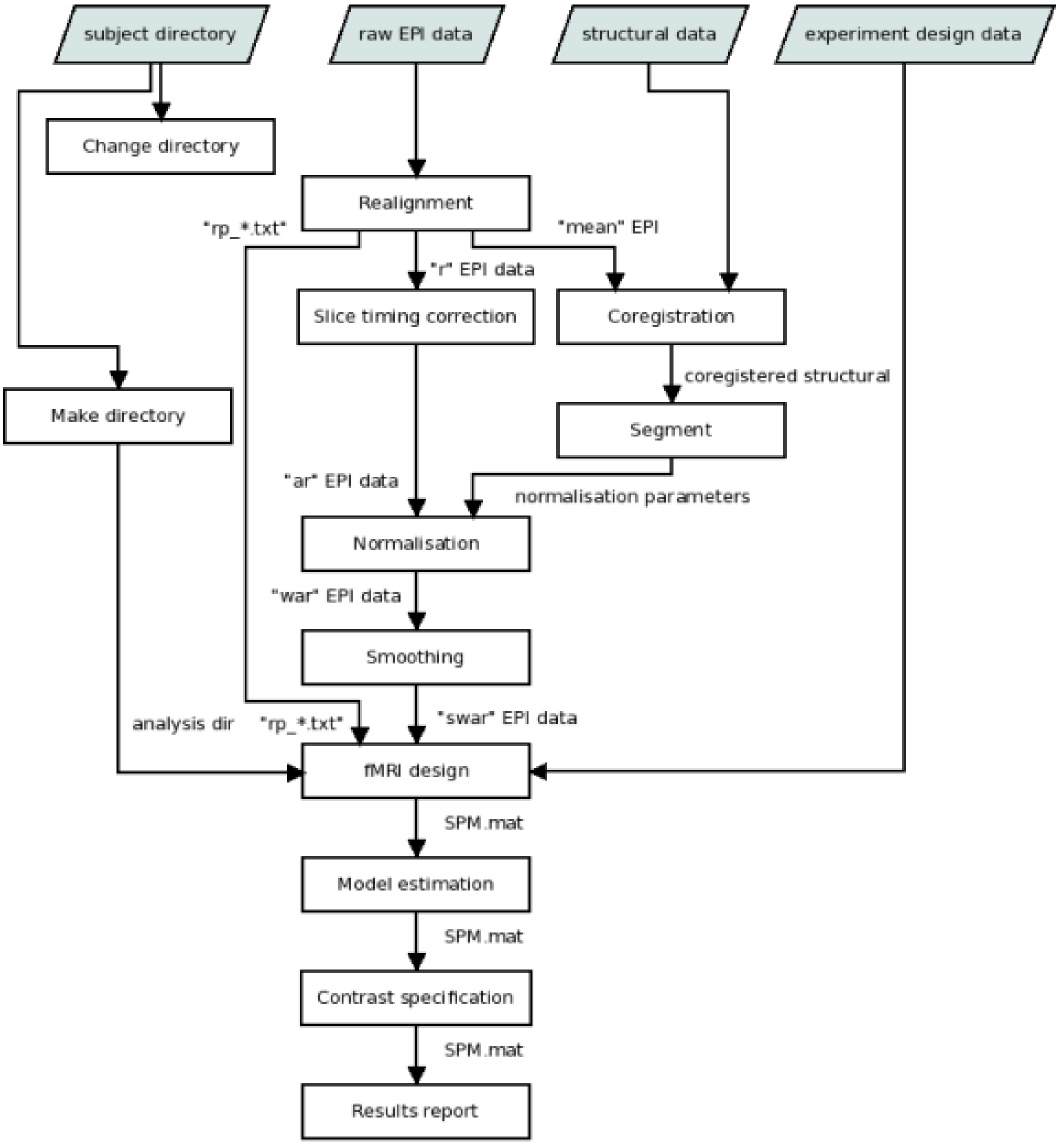

Figure 3.9. Schematic for human fMRI data processing, reproduced from the SPM8 manual (http://www.fil.ion.ucl.ac.uk/spm/)

The four steps of fMRI data processing mentioned in Figure 3.9 that are considered in this section are: Spatial normalisation (coregistration), realignment (motion correction, slice timing correction, and smoothing.

As the SPM toolbox was designed for human data, some of these steps were not possible without some modification or adaptation of this pipeline. In particular, the spatial normalisation step for mouse fMRI data required significant work, as the default human priors in SPM were simply not suitable. The other three steps are considered, but only briefly as they worked consistently with mouse brain fMRI data without significant intervention.

3.2.2 Spatial normalisation

This part of the pipeline underwent the largest improvements throughout the course of the project. Spatial normalisation in some form is required for comparing data across multiple subjects; however the complexity of the normalisation process can vary widely depending on the approach taken.

3.2.2.1 MATLAB GUI for data extraction

The initial attempt to compare BOLD timecourses from the same region across multiple subjects required manual definition of an ROI directly from the GE-EPI images. In order to do this, a graphical user interface (GUI) was developed in MATLAB, and took as an input the 4D image matrix of intensity values. An example GE-EPI dataset viewed in the GUI is shown in Figure 3.10. The GUI allowed multiple slices to be viewed, the timepoints to be scrolled through, and a timecourse of the raw intensity values corresponding to the mouse location to be displayed. The GUI also enabled visual inspection of all the acquired GE-EPI images for visual assessment of temporal stability and image distortion. Clicking the ‘Select ROI’ button would allow a polygon to be drawn in a single slice and the mean signal extracted.

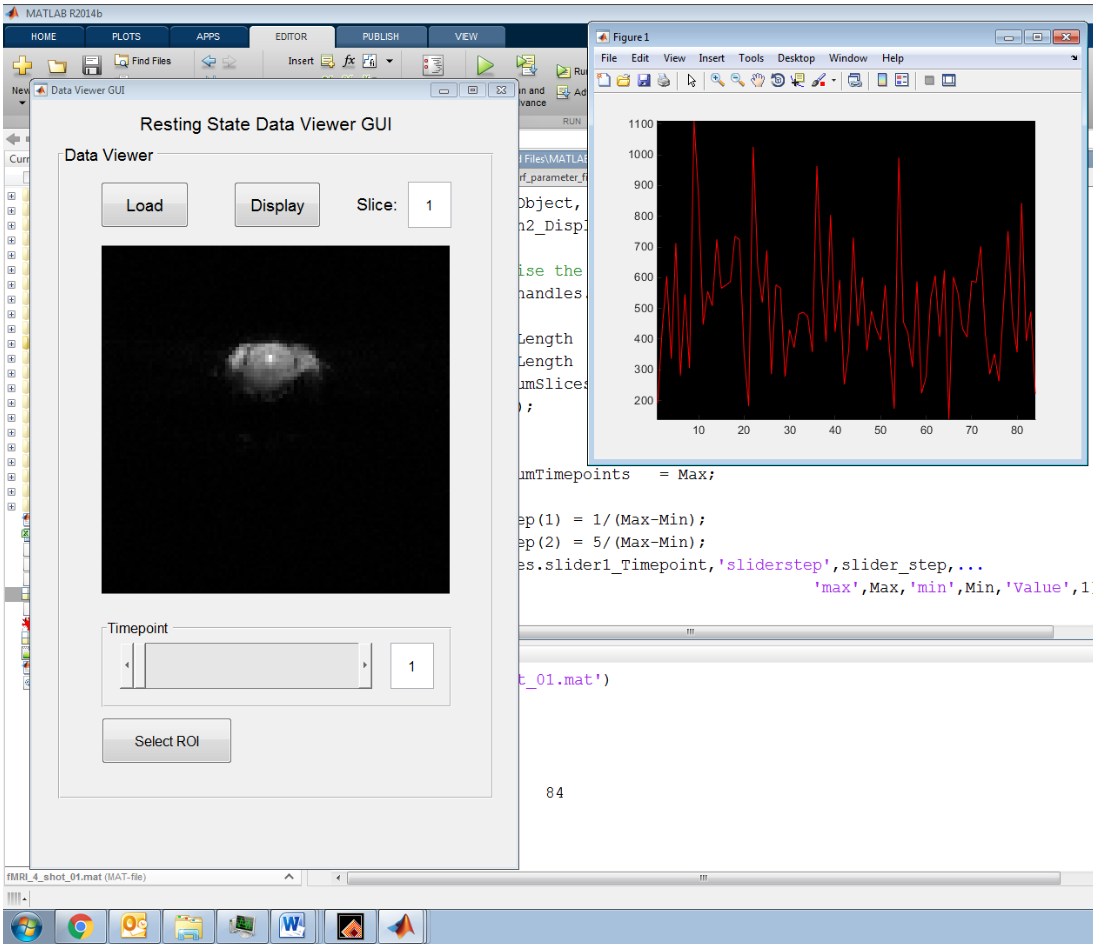

```
bject,
2_Disp
ise the
andles.
ength
ength
mSlice
);

mTimepoints    = Max;

p(1) = 1/(Max-Min);
p(2) = 5/(Max-Min);
s.slider1_Timepoint,'sliderstep',slider_step,...
                                  'max',Max,'min',Min,'Value',1

_01.mat')

84
```

Figure 3.10. Custom GUI for viewing GE-EPI data. The timecourse on the right corresponds to the bright region (ventricle) in the GE-EPI image on the left.

Using this GUI was time-consuming for a human operator, and difficult due to low spatial contrast in the GE-EPI images. In addition, later versions of the SPM toolbox included similar/enhanced functionality whilst incorporating header information from The Neuroimaging Informatics Technology Initiative (NifTi) file format [114], rather than just the image matrix. For these reasons, after this update to the SPM toolbox in late 2014, the in-house developed GUI was no longer used.

3.2.2.2 Initial image registration

An improved method for spatial normalisation that was investigated was to use image registration. Briefly, image registration works by deforming an image in some way with respect to another. This can be seen as a machine learning problem where an algorithm ‘learns’ the optimal deformation to be applied by the minimisation of a cost-function. Image registration is an extremely large field of research, and for brevity only a few methods will be described here.

Directly registering GE-EPI data (which has inherently low spatial contrast and only partial brain coverage) across subjects was expected to be extremely difficult. In addition, the presence of structural data already assumed to be in the same space as the GE-EPI was already being acquired in order that functional results could be overlaid (for single subject analysis). The structural scan used was a T_2 - weighted Fast Spin Echo Multi Slice (FSEMS) sequence, with the same slice thickness as the functional data, same field of view, but higher resolution and full head coverage.

By making the assumption of zero head motion in between the acquisition of a structural (also referred to as an anatomical reference) scan and the acquisition of functional data, it was possible to perform affine registration of the structural data and propagate the affine transformation through to the functional data.

The simplest way of deforming a 3D image (called the ‘floating’ image) to match another (called the ‘target’ image) is a 3x1 vector representing a translation in 3D space. A logical extension to this is to include rotations about three different axes, which could be represented with a 3x3 matrix (although the rotation matrix is symmetric, so in total there are only three rotational degrees of freedom). The use of only translations and rotations for registration is called a ‘rigid registration’. Rigid registration is useful in the case where the floating and target images can be assumed to be the same size and shape – and is therefore often used for motion correction (see section 3.2.3).

However, if the floating and target images are of different shapes (say for example, different subject brains) then rigid registration is insufficient for accounting for these differences. By including shears and scaling, an affine transformation is the most complicated transformation that can be applied to map one space to another whilst preserving points, planes, straight lines and sets of parallel lines. The advantage of using affine registration over more complicated (often non-linear registration) is that the affine transformation matrix generated by the registration process is general to the image space. This means that the affine transformation generated from registering structural data can be applied to lower resolution, partial coverage functional data – under the assumption that the functional and structural data are in the same space.

A second advantage of using affine registration is that all affine transformations can be represented by an ‘augmented’ matrix $\boldsymbol{T}$ – a 4x4 matrix shown below in equation (3-2), with the $\boldsymbol{A}$ matrix representing all affine transformations except for translations, and the t vector representing translations. In total an affine transformation has 12 degrees of freedom.

$$\boldsymbol{T}\begin{bmatrix} x \\ y \\ z \\ 1 \end{bmatrix} = \begin{bmatrix} A_{11} & A_{12} & A_{13} & t_x \\ A_{21} & A_{22} & A_{23} & t_y \\ A_{31} & A_{32} & A_{33} & t_z \\ 0 & 0 & 0 & 1 \end{bmatrix}\begin{bmatrix} x \\ y \\ z \\ 1 \end{bmatrix} \tag{3-2}$$

Once generated, the transformation matrix $\boldsymbol{T}$ can be applied to other images of different resolution, field of view, contrast etc. In the initial application of this registration technique, the target image was the structural image of a subject from the experiment described in section 3.3. This subject was chosen because it was judged by visual inspection to be the most level (minimal rotations around the scanner bore z-axis. The original images are shown in cross-sectional views in Figure 3.11.

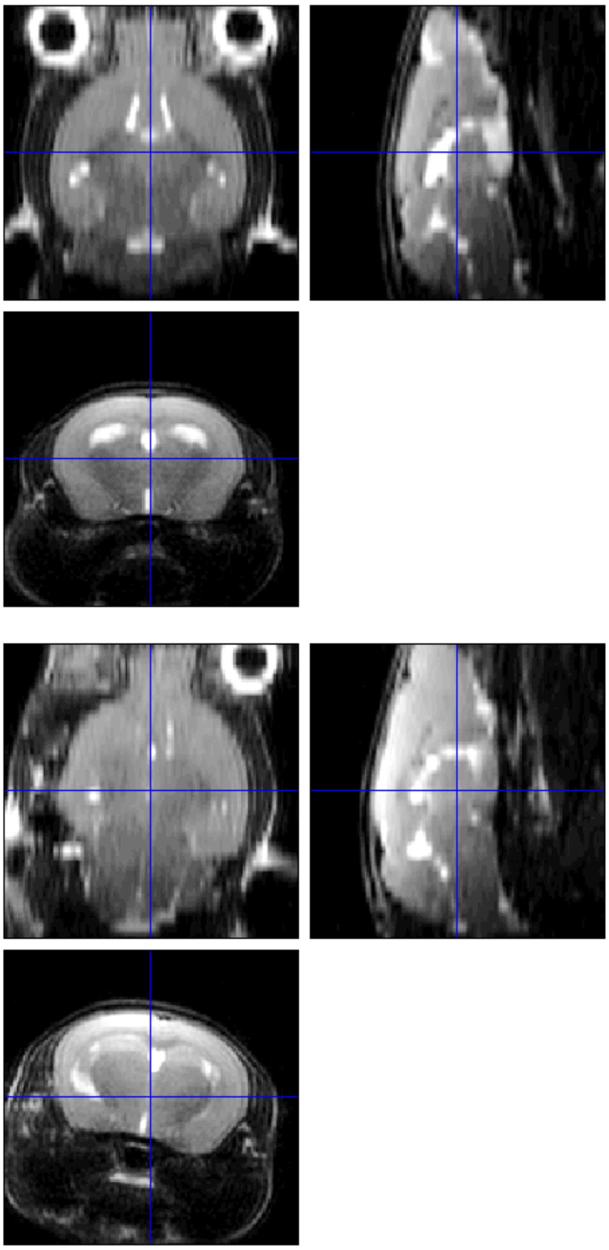

Figure 3.11. Cross section views of two different subjects anatomical reference scans. The mouse at the top is more level and was chosen to be the target image for registration, whereas the mouse at the bottom was chosen to be the floating image. Each image was acquired with the same sequence parameters, but because the mice were positioned differently, their brains are in different spaces, as evidenced by the crosshair positions. The width of the bottom most coronal view corresponds to 16 mm in real space (zoomed from 35 mm).

To perform affine registration of this combination of floating and target image, the NiftyReg Toolbox [150, 151] was used with a MATLAB wrapper function shown in Appendix A.

The results of this registration are shown in Figure 3.12.

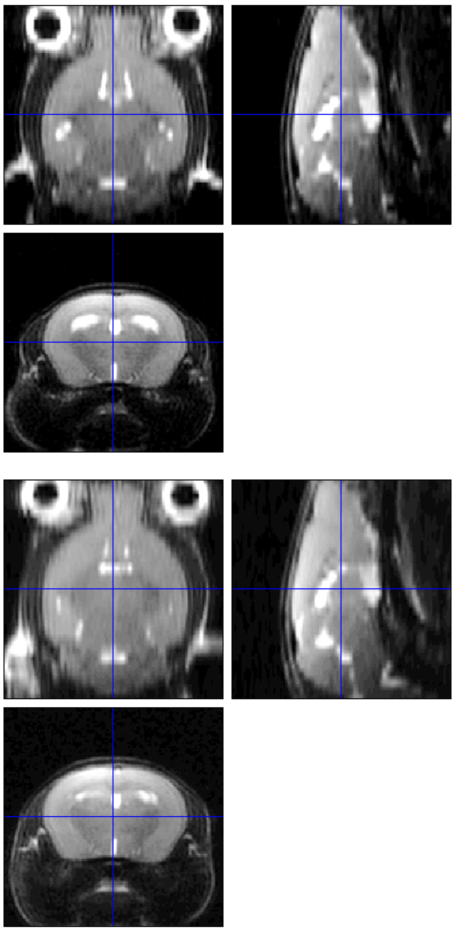

Figure 3.12. Cross section views (after affine registration) of two different subjects anatomical reference scans. The mouse at the top is the target image and remains unchanged. The mouse at the bottom is the floating image transformed into the space of the target image. The width of the bottom most coronal view corresponds to 16 mm in real space (zoomed from 35 mm).

The affine transformation matrix for this registration is given in equation (3-3).

$$\boldsymbol{T} = \begin{bmatrix} 0.997 & 0.159 & 0.052 & -5.300 \\ -0.177 & 0.981 & -0.034 & 9.360 \\ -0.055 & 0.036 & 0.997 & 4.845 \\ 0 & 0 & 0 & 1 \end{bmatrix} \qquad (3\text{-}3)$$

It should be noted that when reconstructing image data into the nifti file format, all voxel size information in the image header were increased by a scale factor of 10, in order that they could be read by the SPM12 toolbox. Therefore a translation in the x-direction of -5.3 corresponds to a translation of -0.53 mm, which in this example is approximately 3 voxels. Further improvements to the spatial normalisation will be discussed, but first the motivations for this will be covered.

3.2.2.3 Defining regions of interest

With the ability to register multiple subjects into the same space, more advanced group analysis became possible, as described later in this chapter and later ones. Drawing an ROI on the target image should correspond to the same region in all other subjects, reducing the burden on a manual operator. However, the existence of brain atlases where brain regions have already been drawn gave rise to the following option: register a mouse brain atlas into the space of the already registered group data, and use the atlas labels as ROIs. Two mouse brain MRI atlases were initially available during the course of this work, the Toronto mouse brain atlas (TMBA) [67] and the National University of Singapore mouse brain Atlas (SMBA) [152]. Cross sectional views are shown in Figure 3.13.

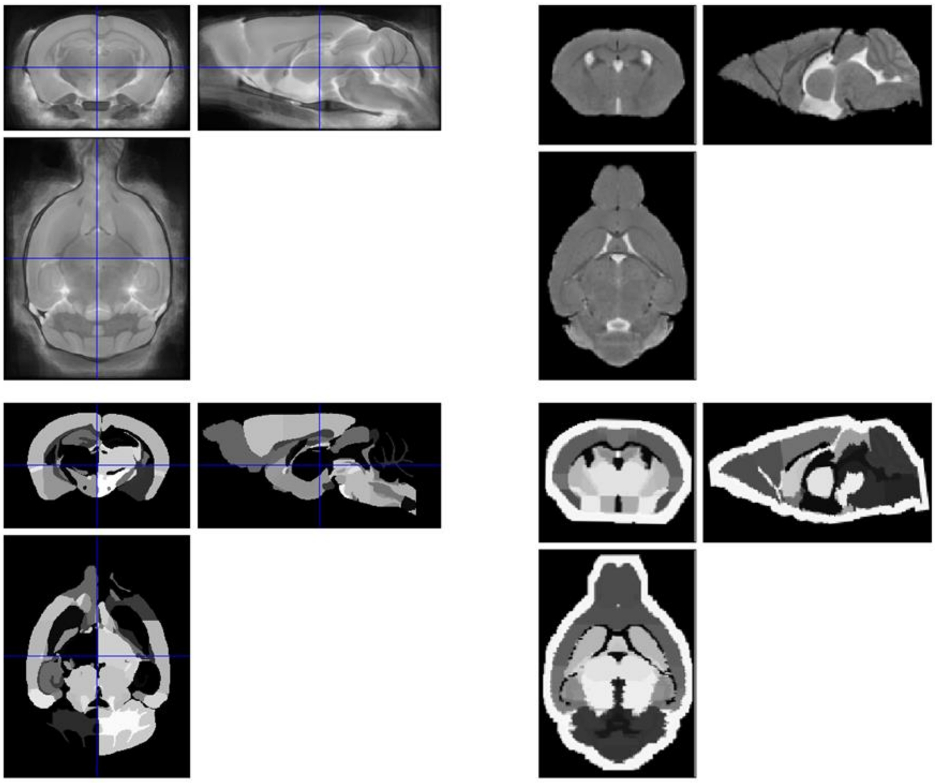

Figure 3.13. Cross sectional views of two atlases, the Toronto mouse brain atlas (TMBA) (left) and the National University of Singapore mouse brain atlas (SMBA) (right). The images at the top are of the MRI template images, and images on the bottom are of the brain region labels.

The TMBA is the average of a set of nine registered age and sex matched 129SV/S1 mouse brains, scanned ex-vivo. The SMBA used here is the first subject of a multi-subject atlas, with five C576BL/6 mice scanned in vivo. Both atlas template images are T_2 weighted, and so similar tissues have similar contrasts (e.g. cerebral spinal fluid has higher intensity values than grey matter, making the ventricles easily distinguished).

In general, the more different the target and floating images are, the more difficult the registration process. This line of reasoning suggested that these atlases might prove straight-forward to register. In a similar way to registering subjects' structural data and propagating the affine transform to the functional data, the atlas template images could be registered to the target subject structural data, and the affine transform propagated to the atlas labels. Then each ROI could be created by looking up the corresponding atlas label value. The results from registering the atlases to a target subject structural scan are shown in Figure 3.14.

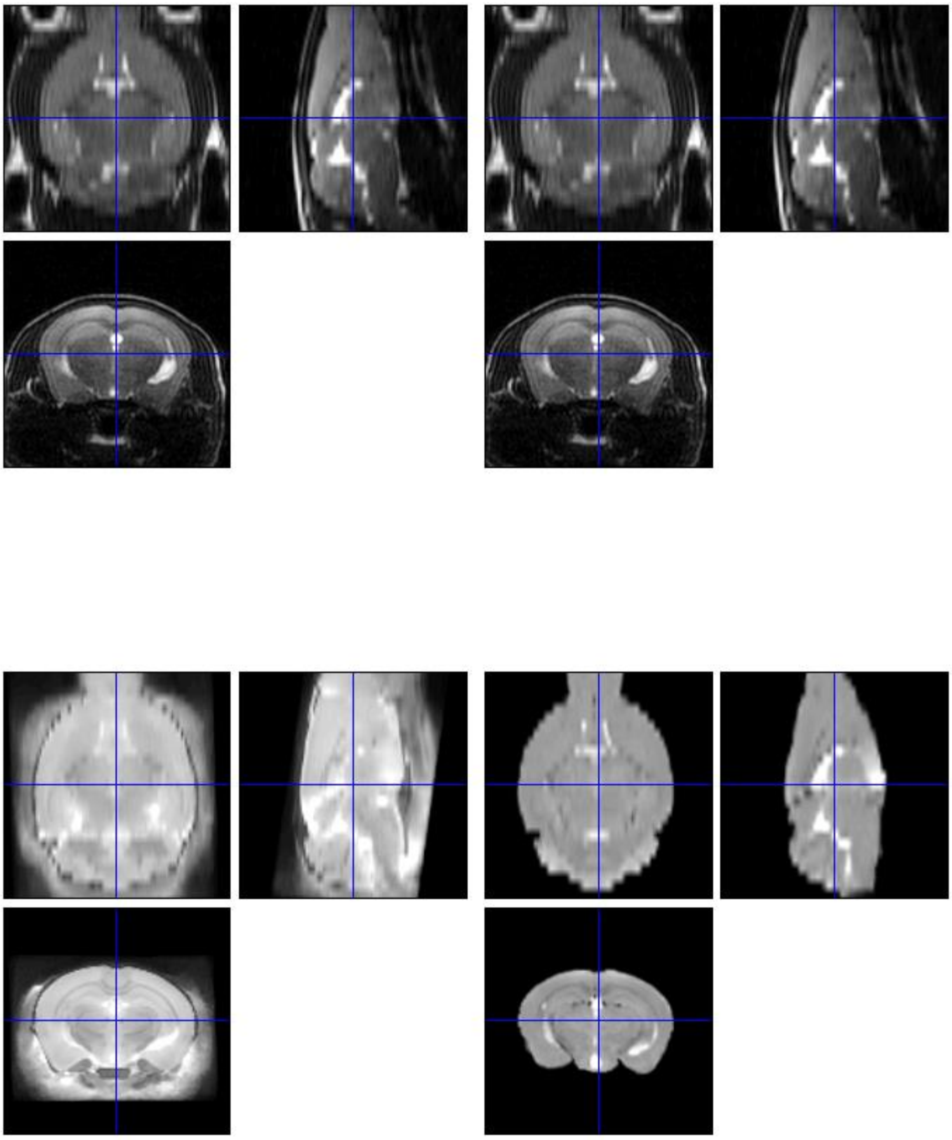

Figure 3.14. Cross sectional views (after registration) of the target subject structural scan (top row, repeated), Toronto mouse brain atlas (TMBA) (lower left) and the National University of Singapore mouse brain atlas (SMBA) (lower right).Both atlas templates were registered into the subject space with an affine transformation. The width of the coronal view corresponds to 16 mm in real space (zoomed from 35 mm).

One limitation of these MRI atlases is the labelling resolution. Although the spatial resolution of the atlas templates is much greater than target images, the labels of both atlases were coarse relative to the needs of mouse brain functional imaging with visual stimuli. For example, neither atlas subdivide the thalamus, only the

TMBA had a specific label for the superior colliculus, and the only the SMBA had a visual cortex label. For signal extraction, this would mean that signals from functionally delineated regions which respond to a stimulus, e.g. the lateral geniculate nuclei, would be averaged with surrounding structures unrelated to the stimulus, with the likely consequence of reduced temporal contrast-to-noise ratio.

3.2.2.4 The Allen Mouse Brain Atlas

The next approach considered the use of a histology atlas, the Allen mouse brain atlas (AMBA) [69]. This atlas was created to provide genome-wide image data for approximately 20,000 genes in the adult mouse brain. The template image for this atlas was created by reconstructing 2D histology sections, using high frequency section-to-section registration combined with low frequency histology-to-MRI registration.

The main advantage of using this atlas is that the labelling resolution is much richer than the MRI atlases mentioned previously – for example, the lateral geniculate nuclei is delineated, the superior colliculus is sub-divided and the cortex is divided into multiple visual regions and also layers. Furthermore, the labels have hierarchical parent-child metadata, allowing the labels to be viewed at different functional ‘depths’. Concretely, this means that upon development of functional imaging approaches with different spatial resolutions and levels of coverage, more appropriate labels can be chosen for timecourse extraction.

There were significant challenges to using this atlas, mostly concerned with visualisation and registration. These are discussed in the following subsections. To my knowledge, this was the first time that MRI data from the mouse brain had been successfully registered to the Allen Brain atlas.

Visualisation

The first issue arose with visualisation of the AMBA labels. Although not essential for signal extraction or registration, visual inspection of the labels was desired for comparing with other atlases. After an initial reconstruction, the following images were obtained, shown in Figure 3.15.

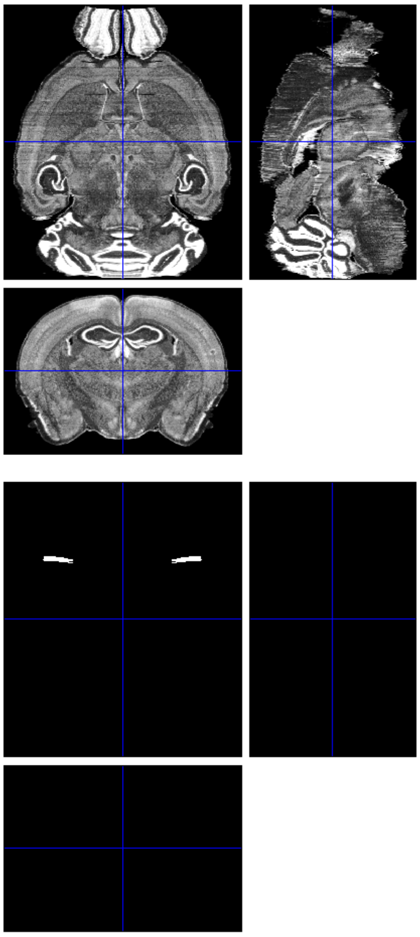

Figure 3.15. Cross sectional view of the AMBA template and the label image. Only two of the atlas labels appear to exist when viewing the intensity images.

The reason for this is that the label numbers (IDs) are counter-intuitively distributed, with the bright regions in the label image having intensity values of approximately 300,000,000, when a maximum of 1235 structures have identification numbers. Figure 3.15 shows a display of the atlas labels with these extremely large label values, which then precludes viewing of contrast orders of magnitude lower (which can be understood as a ‘windowing’ effect). A plot of label IDs against labels after sorting into ascending ID order is shown in Figure 3.16.

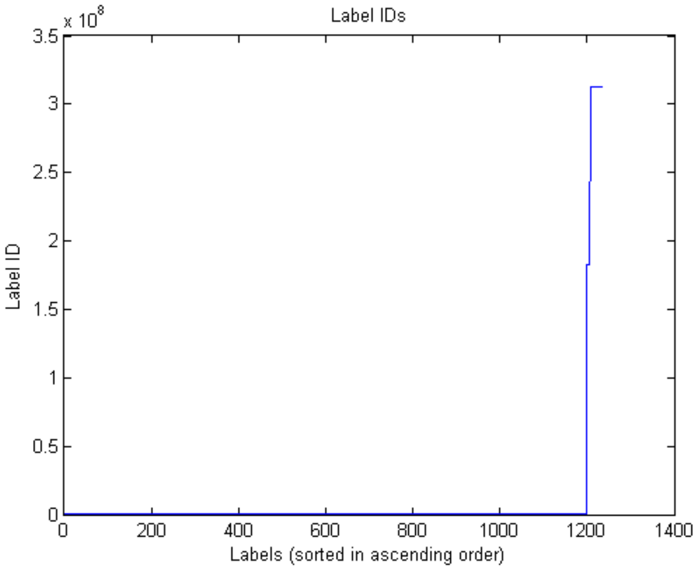

Figure 3.16. Raw Allen mouse brain atlas label IDs. The presence of label IDs at extremely large values (~3x10^{8}) makes viewing the label image difficult due to poor windowing.

To allow better visualisation of the atlas labels, they were recalibrated to approximately linearly increase, as shown in Figure 3.17.

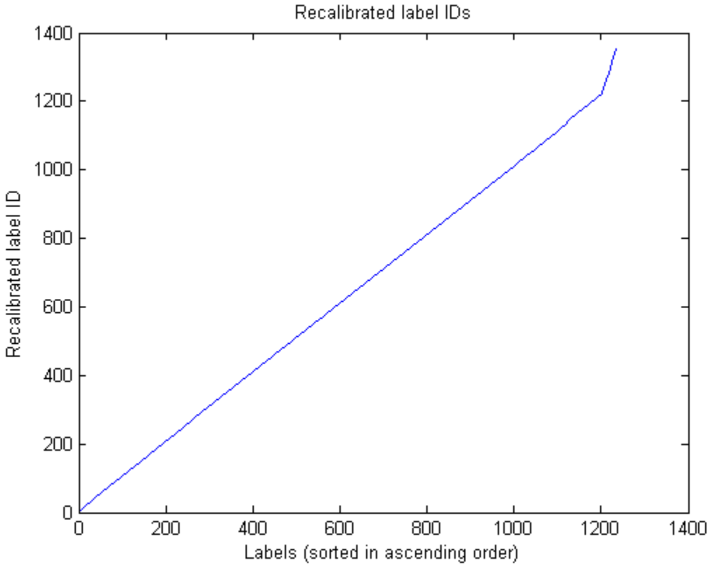

Figure 3.17. Recalibrated Allen Mouse Brain Atlas label IDs. The range of IDs is approximately the same as the number of regions included in the atlas.

Visualisation of the recalibrated label IDs is shown in Figure 3.18.

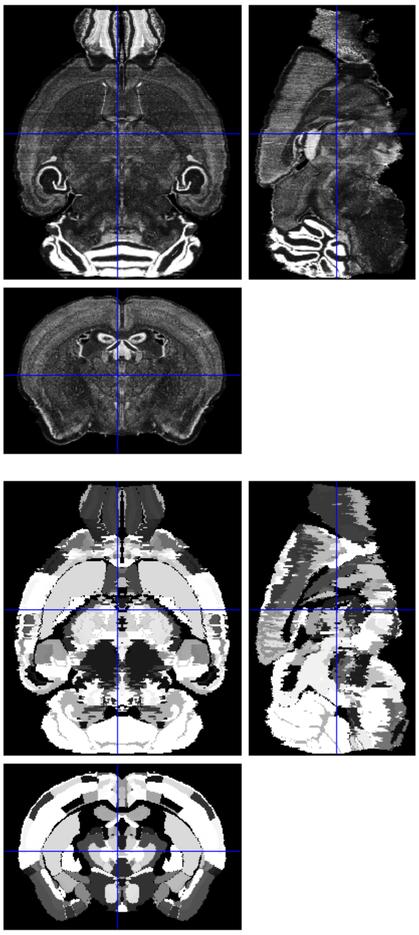

Figure 3.18. Cross sectional view of the AMBA template and the recalibrated label. With recalibrated label IDs, the windowing problem is solved and the labelling resolution can be visualised much more clearly.

3.2.2.5 Refined image registration

As can be seen from Figure 3.18, the natural contrast of the AMBA template image is very different from the T_2 weighted structural images acquired previously. It should be remembered that both the TMBA and SMBA atlases both had accompanying T_2 weighted structural images. One possible option was for subsequent experiments, to acquire T_1 weighted structural images which would have more similar image contrast (e.g. CSF having darker signal than grey matter). However, at the time the AMBA was being considered, multiple experiments had been conducted with only T_2 weighted structural images. For ease of comparing past data with future work, it was decided to attempt to register the AMBA to the T_2 weighted structural images.

The initial attempt at affine registration using NiftyReg with the default parameters previously used failed in this case. An example of the failed registration is shown in Figure 3.19.

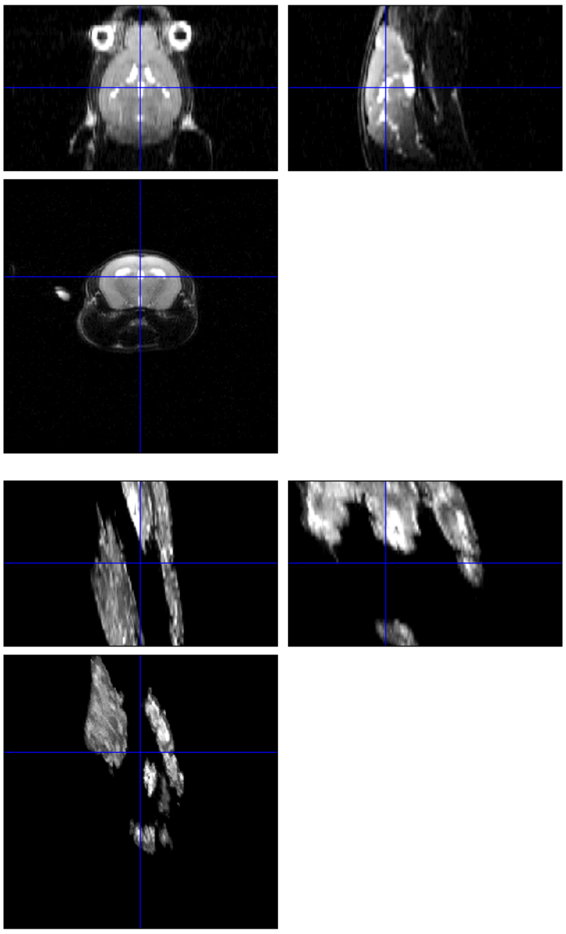

Figure 3.19. Example of failed affine registration of the AMBA to a T2 weighted structural scan. The width of the bottom most coronal view corresponds to 35 mm).

In order to improve the registration, it is necessary to consider in more detail the algorithm used by NiftyReg and the hyper-parameter space of the algorithm.

In order to generate the affine transformation matrix $\boldsymbol{T}$, the NiftyReg routine ‘reg_aladin’ was used, which uses the Aladin block-matching algorithm with a least-trimmed squares cost minimisation approach. Briefly, the block-matching algorithm works by establishing dividing the floating and target images into blocks of uniform size. Each block in the target is compared with blocks in corresponding neighbourhood of the floating image. The matching floating image block is chosen as the one with the highest maximum normalised cross correlation [151]. The affine transformation which maps the block in the floating to the block in the target is computed using linear regression, but with a least-trimmed squares cost function for more robust outlier rejection. The two steps of block matching and transformation optimisation are computed over many iterations, where the blocks begin at a coarse level and become progressively finer.

The hyper-parameters of interest that were investigated to improve the registration are the number of levels and iterations. The default settings for the reg_aladin routine are three levels and 5 iterations. An ad-hoc optimisation approach to explore the hyper-parameter space was conducted, by performing the registration over a finite hyper-parameter space (number of levels ln = 1:5, maximum number of iterations maxit = 1:10), and evaluating the registration by visual inspection. The code snippet used to perform this optimisation is shown in Appendix A.

After execution, it was found that the algorithm failed to produce an output for the following hyper-parameter values: ln = 4, maxit = 10; ln = 5, maxit = 5, 6 and 7. From the remaining 46 output images, the optimal hyper-parameter set was decided to be ln = 1, maxit = 6 by visual inspection.

For brevity, a subset of the outputs is included here, shown in Figure 3.20 and Figure 3.21.

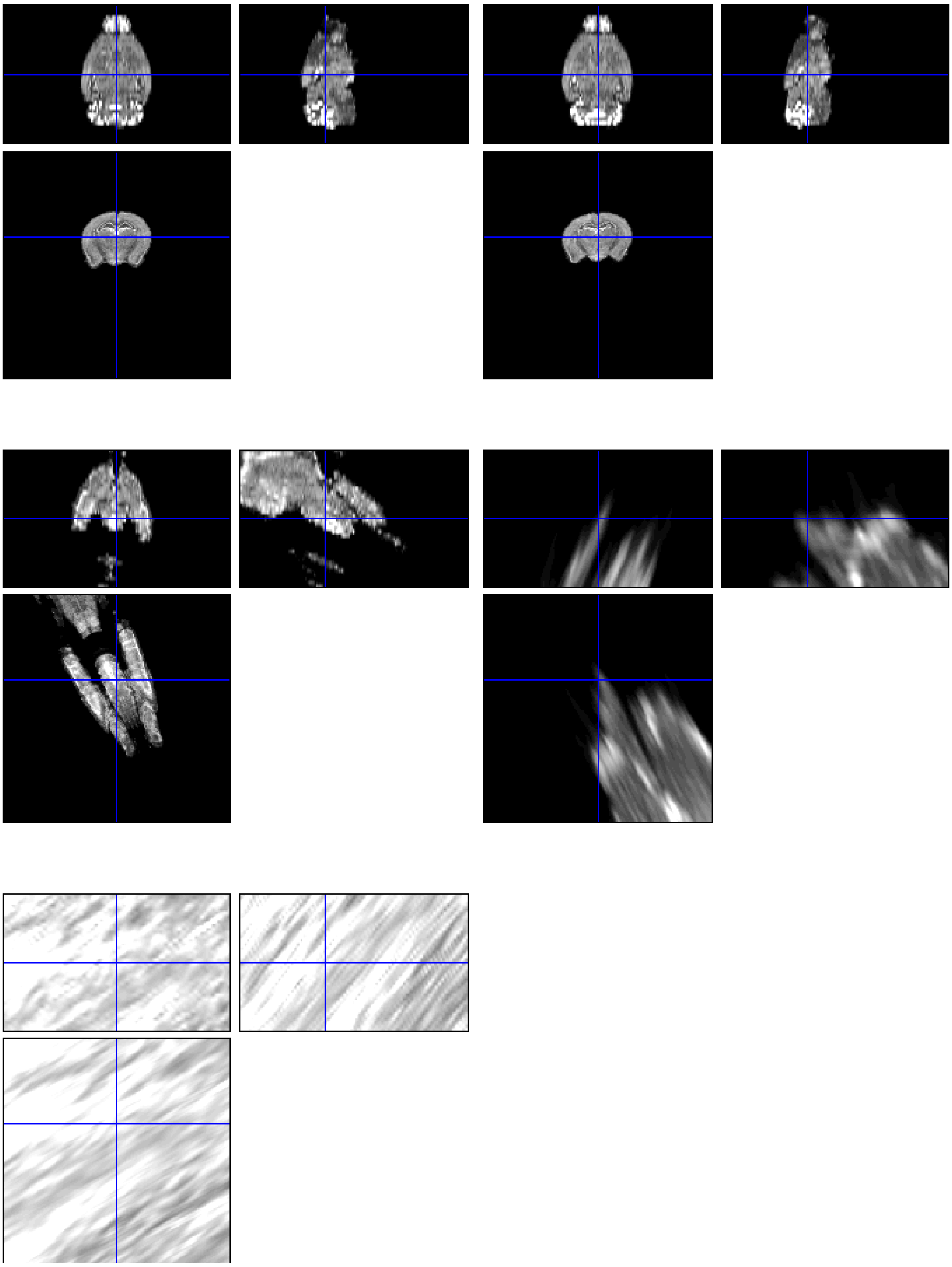

Figure 3.20. Cross sectional views of outputs from reg_aladin with maxit = 4, nl = 1:5 (left-to-right, top-to-bottom). As the number of levels increases, the algorithm appears to worsen in performance. The width of the coronal view is 35 mm).

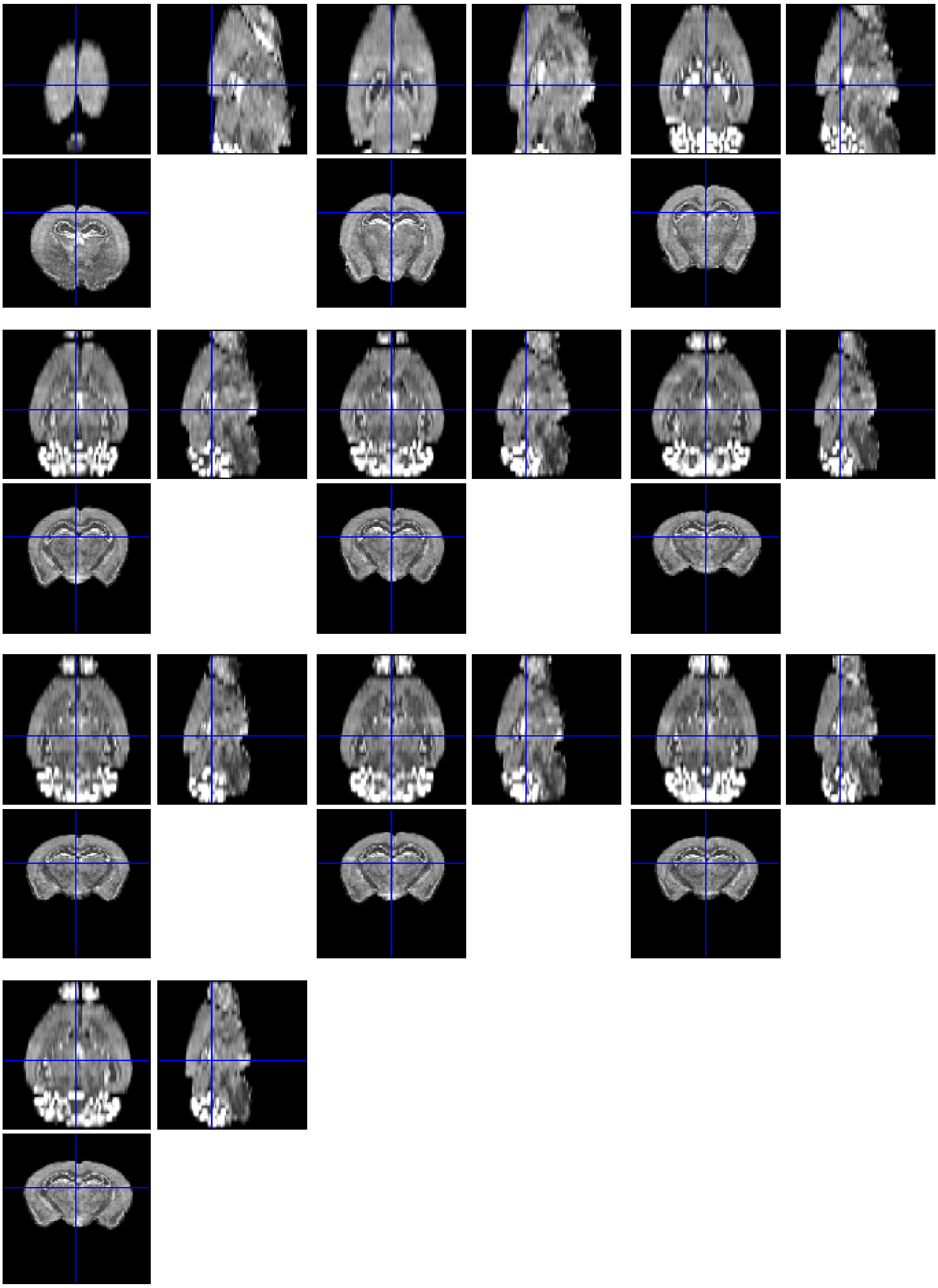

Figure 3.21. Cross sectional views of outputs from reg_aladin with nl = 1, maxit = 1:10 (left-to-right, top-to-bottom, three views per volume). As the maximum number of iterations increases, the algorithm does not appear to improve in performance after maxit = 6, and there appear to be minor distortions in maxit = 8. The width of the bottom most coronal view corresponds to 16 mm in real space (zoomed from 35 mm).

The comparison of the optimal registration output with the target structural image is shown in Figure 3.22 and Figure 3.23.

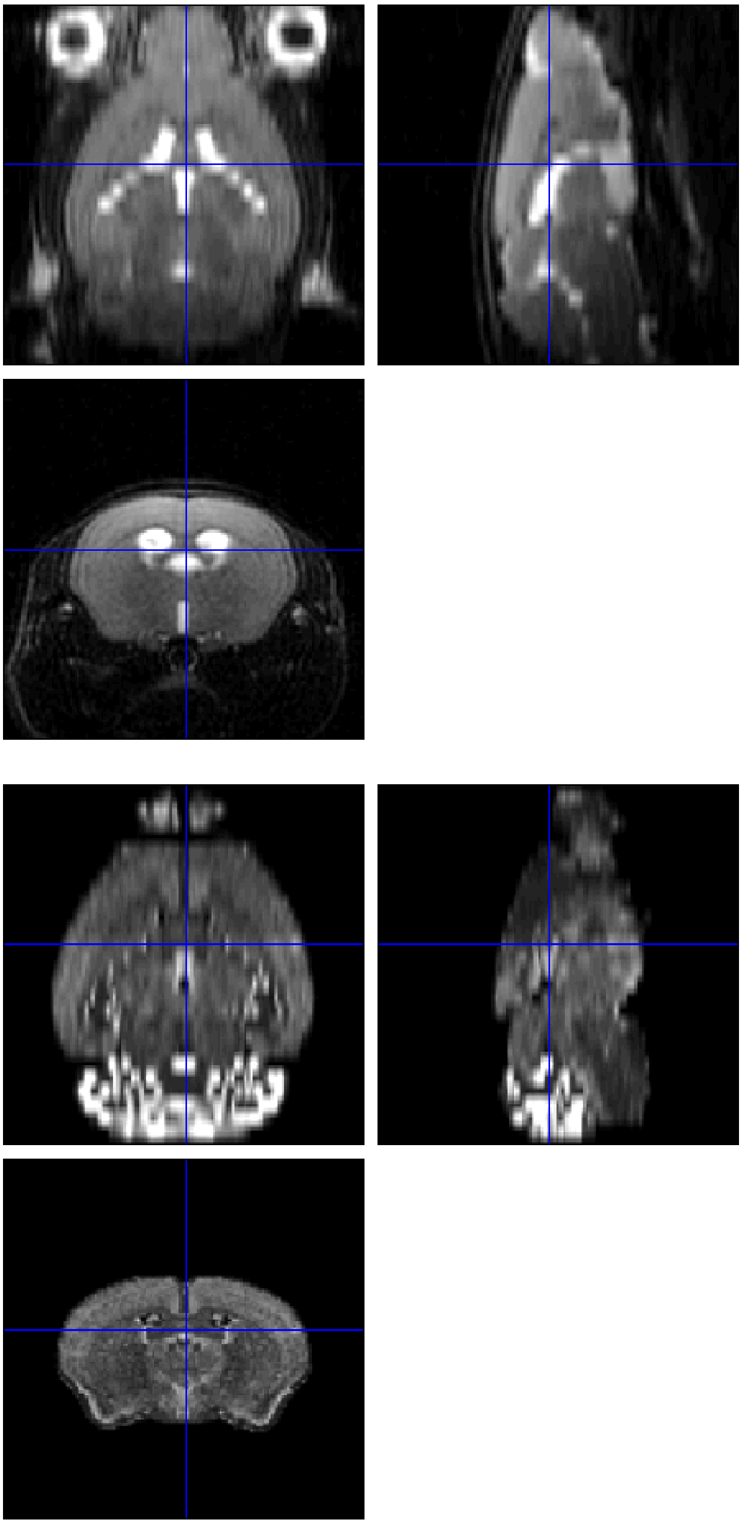

Figure 3.22. Final output for registration of AMBA template image to a T_2 weighted structural image. Anatomical landmarks appear to correspond in both images, despite the markedly different contrasts in both images. The width of the bottom most coronal view corresponds to 16 mm in real space (zoomed from 35 mm).

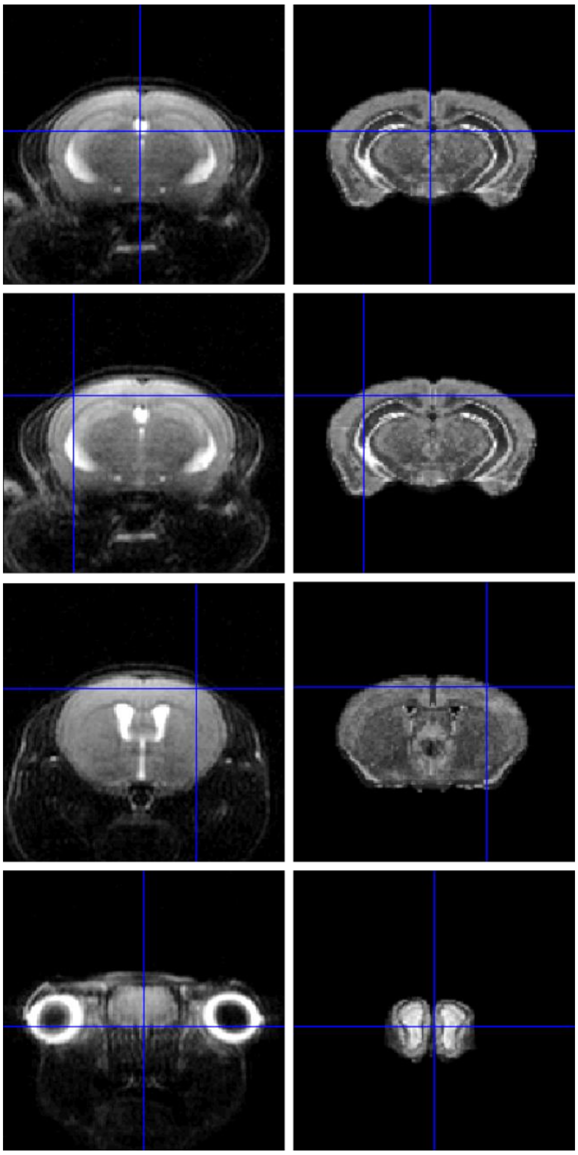

Figure 3.23. Evaluation of the registration of the Allen mouse brain atlas (right column) to a T_2 weighted structural image (left column). Four coronal views are shown, moving from the back of the brain (just in front of the cerebellum, top two rows) towards the front (olfactory bulb, bottom row). The width of each coronal view corresponds to 16 mm in real space (zoomed from 35 mm).

Future improvements to this registration process would include the use of a quantitative measure of registration performance, such as the DICE score [153] after manual segmentation of both images, and the investigation of non-linear registration. For the purposes of group analysis of fMRI data however, the quality of this registration was deemed sufficient.

3.2.2.6 Standard space

At this point, it was reasonable to assume that labels from the AMBA could be propagated through to the functional GE-EPI for timecourse extraction. However, the spatial normalisation process at this point had the following disadvantages:

- A template subject had to be chosen to register all other subjects to it, requiring manual intervention.
- For every group experiment, the AMBA would need to be registered to this template subject, and the relevant ROIs extracted.
- Each group experiment is in a different space, making comparisons across studies and meta-analyses difficult.

Ideally, every subject from every experiment would be registered into the AMBA space, and then the same ROIs could be propagated throughout.

One method would be to directly register each subject's structural scan (now the floating image) to the AMBA template image (now the target image). However, this was found to be unstable, and the opposite registration (floating and target image swapped, all other hyper-parameters kept the same) to that shown in Figure 3.22 is shown in Figure 3.24.

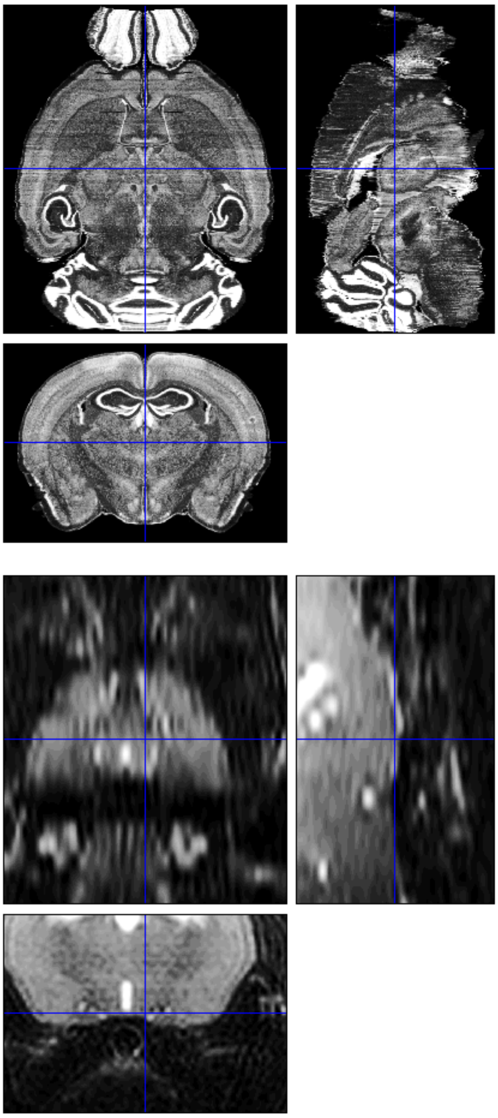

Figure 3.24. Cross sectional views of registration of T_2 weighted structural scan (floating image, bottom) to the AMBA (target image, top) using the Aladin algorithm.Reversing the floating and target images caused the registration to fail.

Despite the direct registration of the T_2 weighted image to the AMBA template image failing, the use of affine registration provided a solution. The original registration procedure (Figure 3.22) outputs the transformation $\boldsymbol{T}$ with the affine transform to map the floating image space to the target image space. By inverting $\boldsymbol{T}$ to find $\boldsymbol{T}^{-1}$, the mapping of the target image space to the floating image space is also found. Applying $\boldsymbol{T}^{-1}$ to the T_2 weighted image maps it into the AMBA space and this is shown in Figure 3.25.

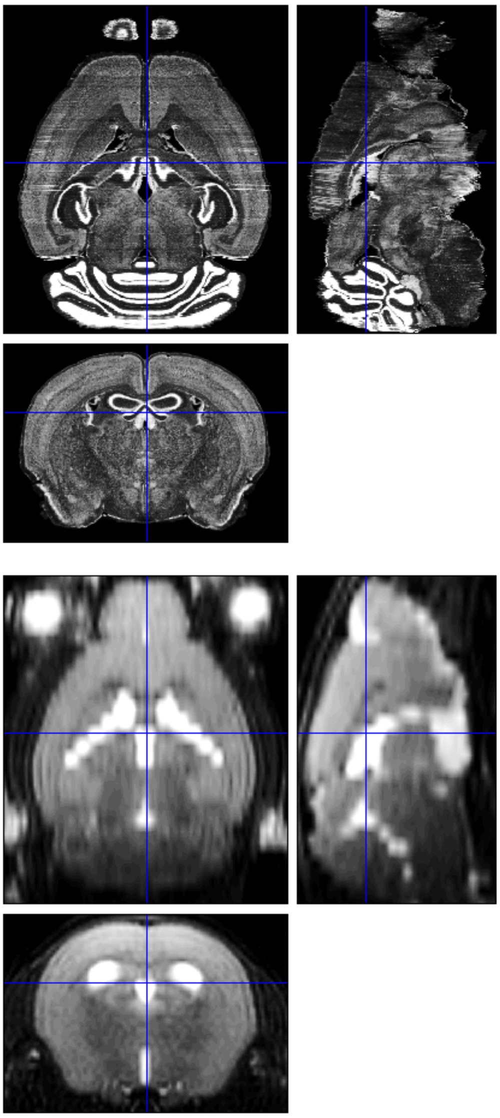

Figure 3.25. Cross sectional views of registration of T_2 weighted structural scan (floating image, bottom) to the AMBA (target image, top), by performing the opposite registration, inverting the transformation matrix and applying to the floating image. The width of the bottom most coronal view corresponds to 16 mm in real space (zoomed from 35 mm).

Now the T_2 weighted image is registered into the AMBA space, and has much more similar image contrast to all other subject structural scans. It can therefore be used as a template for registering other subjects from different experiments into the AMBA space. This procedure for spatial normalisation is represented by the schematic in Figure 3.26, where $\boldsymbol{T_a}$ is the affine transformation mapping the AMBA template image to the example MRI structural scan, and $\boldsymbol{T_i}$ is the affine transformation mapping an individual subject structural scan to the MRI template.

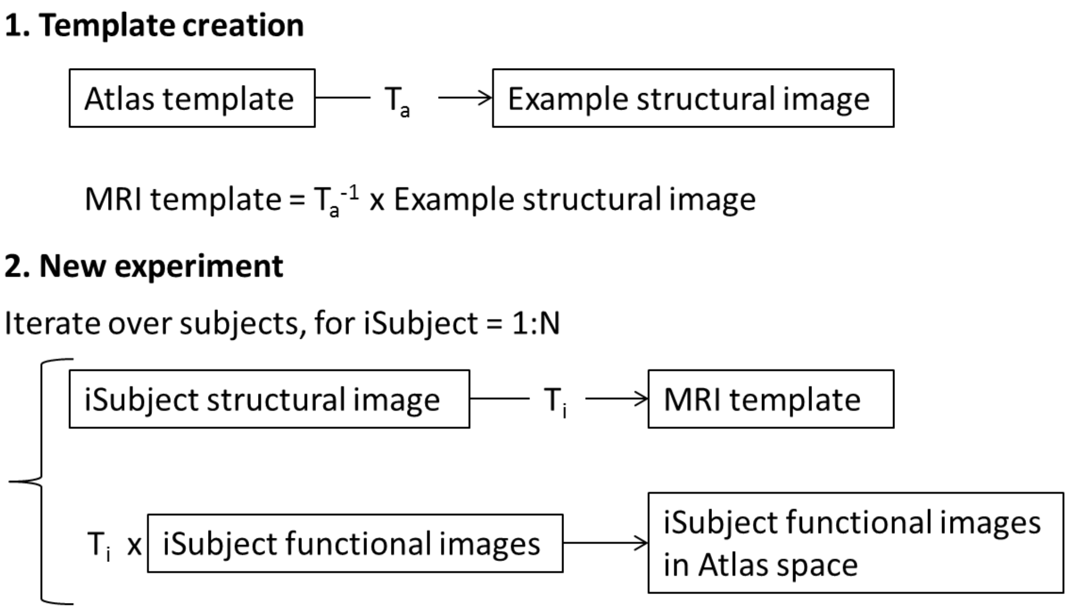

Figure 3.26. Schematic illustrating spatial normalisation procedure.

This is the most advanced spatial normalisation procedure used during the course of this work, and makes the following extra assumptions:

1. There is zero head motion between the acquisition of the structural image and the functional data.
2. Any spatial distortions in the acquisition of both the subject structural scan and functional data are equal.

Assumption 1 can be qualitatively examined by examining example functional data – it is acquired as a time series, and upon the application of motion correction (see section 3.2.3) using the SPM toolbox, an estimate of motion parameters is generated. With proper application of anaesthesia, and a suitable head restraint, this assumption is reasonable.

Assumption 2 is more difficult, especially given the nature of the MRI pulse sequences used to acquire the structural and functional images. The majority of the functional data acquired in this work uses the GE-EPI pulse sequence, which can markedly suffer from spatial distortions due to magnetic field inhomogeneities (in turn caused by discontinuities in magnetic susceptibility at material boundaries e.g. air-skin-bone-brain). The FSEMS sequence used to acquire the structural scan is markedly less susceptible to these spatial distortions, which means that assumption 2 may sometimes be unreasonable. Work to minimise the spatial distortions in the functional data at the acquisition stage is covered in sections 3.1.4 and 3.3.

An example subject with transformed structural and functional data using this spatial normalisation procedure is shown in Figure 3.27.

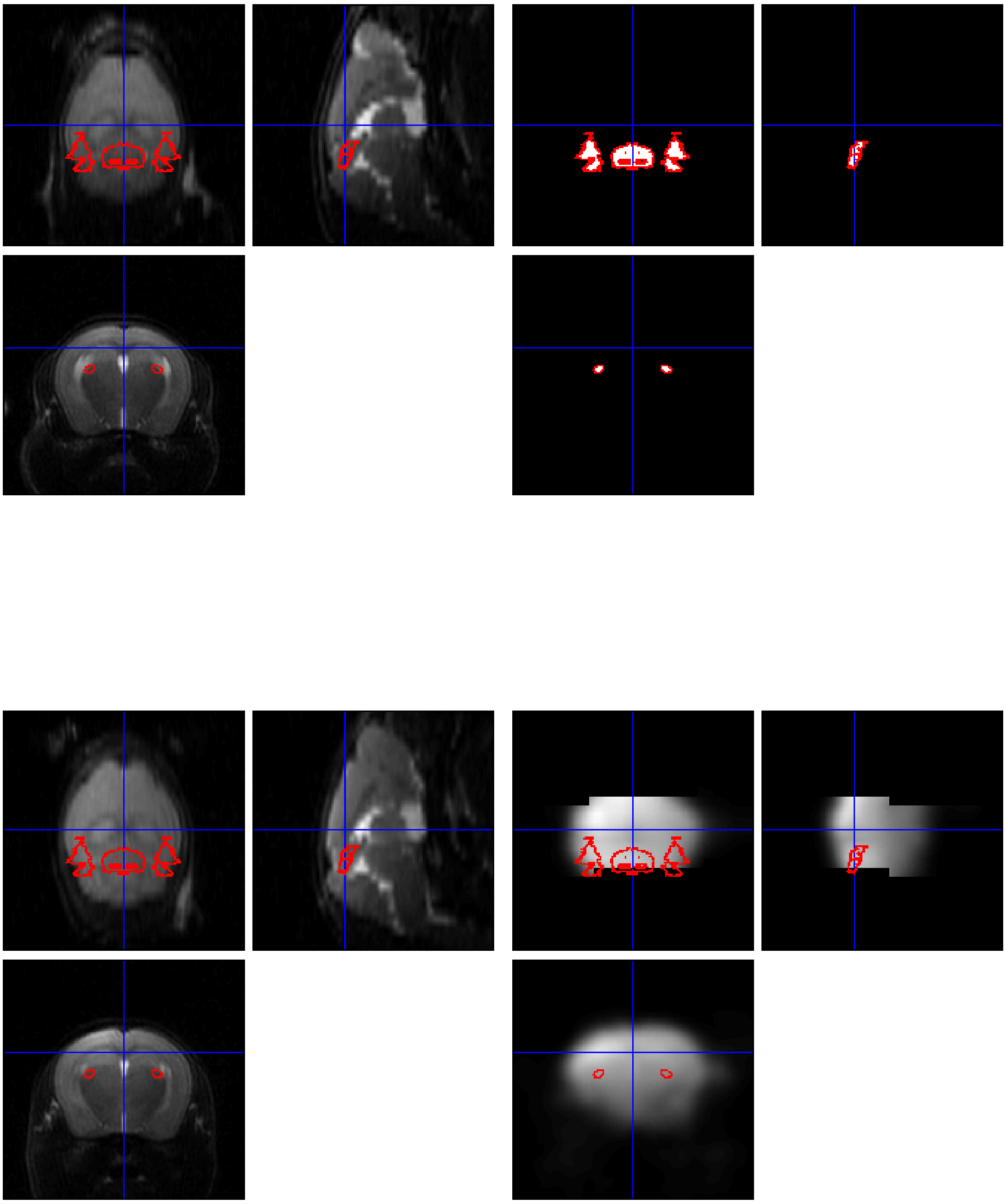

Figure 3.27. Spatial normalisation of fMRI data into AMBA space. Cross sectional views of: the MRI template (top-left), ROI of the mouse visual system extracted from the AMBA (top-right), the registered structural scan of an example subject (bottom-left), and the transformed example subject functional data (bottom-right). Contours extracted from the ROIs have been overlaid on all four image sets, illustrating the quality of the registration and localisation of the functional data. The width of the bottom most coronal view corresponds to 16 mm in real space (zoomed from 35 mm).

3.2.3 Motion correction

Throughout the duration of an fMRI scan, it is possible for the subject’s head to move. This will cause the BOLD signal from one or more voxels to “leak” into one another. This motion could be systematic or random, depending on the type of subject, anaesthesia and head restraint used. Motion is a source of bias from the spatial domain, but the effect is measured in the temporal domain – the timecourse from a specific voxel no longer corresponds to the brain region within that voxel at the beginning of the scan. Bulk motion is the global movement of the head, and will cause image volumes taken at different points in time to be misaligned. It is possible to partially correct for this by rigidly registering the fMRI images to a reference image.

However, this assumes that the shape of the brain in the MRI image does not change from timepoint to timepoint. For a 2D sequence, where slices are acquired sequentially, this is unlikely to be the case in the presence of motion. Concretely, the effect of motion during a slice acquisition may change the appearance of the brain in that slice. A more complex issue is that motion (head or from respiration) may affect the quality of the shim, and therefore affect the spatial localisation of the signal that way.

Image realignment will reduce the effect of bulk motion, but it may not completely remove the extra variance introduced in the temporal domain by the motion. Through the realignment process, estimates of motion parameters can be made, and included in statistical analysis as nuisance regressors to further remove bias. In this work, motion correction was done using the spm_realign/reslice functions in the SPM toolbox.

An example of the motion parameters for *in vivo* data (from the first scan of the first subject included in the experiment described later in section 3.3) estimated by spm_realign is shown in Figure 3.28.

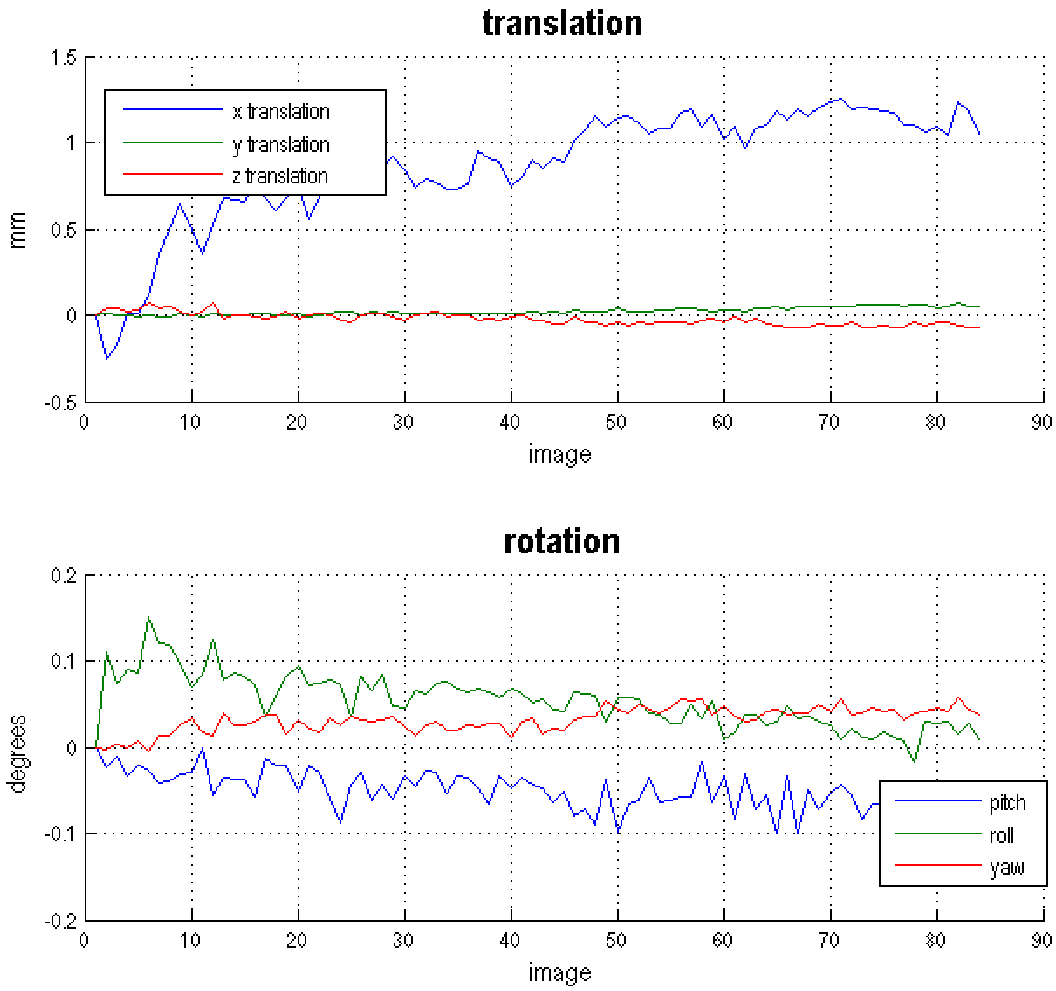

Figure 3.28. Estimates of motion parameters using spm_realign.m . It should be noted that the units here are ten times larger than reality for use with the SPM toolbox, and so the translation estimate of the x-translation of up to 1 mm is actually 0.1 mm, at the sub-voxel level. The x-direction in this case corresponds to the phase-encoding direction, and is likely to be a reflection of the actual motion of the mouse brain.

3.2.4 Slice timing correction

When using a 2D pulse sequence, image slices are acquired sequentially and stacked together within one TR period. This causes systematic lags to be introduced in the temporal domain, which are predicted by slice number. The slice timing correction strategy used by SPM is to select a reference slice and use sinc interpolation in the temporal domain to estimate the signal in an arbitrary slice which would have been measured had it been acquired at the same time as the reference slice. Concretely, this is done by a phase shift in the sinusoids which compose the signal. In this work, slice timing correction was done using the spm_slice_timing routine without further development.

3.2.5 Spatial smoothing

The process of spatial smoothing is controversial and can be seen as counter-intuitive in fMRI analysis [119], and can be thought of as a spatial averaging operation. After spatial smoothing, the effective spatial resolution of the fMRI data is reduced. However it does increase signal-to-noise ratio for signals on larger length scales, and generally fMRI signals are expected to concur with brain regions covered by more than a single voxel. In the case that brain regions are covered by multiple voxels, the loss in signal-to-noise due to averaging over boundaries of functionally distinct regions is expected to be less than the gain of averaging within the functional region of interest to reduce random noise [118].

However the most controversial issue with smoothing is due to later use with statistical thresholds. Statistical inference methods in SPM use gaussian Random Field Theory (RFT) [120], and assume that voxel length scales are smaller than the smoothness. Generally as the fMRI data becomes smoother, the less harsh multiple comparison corrections (e.g. through the family-wise error rate (FWER)) become, and the lower the risk of a Type II error i.e. incorrectly accepting the null hypothesis.

Typically, smoothing is completed using a gaussian filter, with a full-width half-maximum length at approximately the size of two voxels [118], and a final smoothness measurement of the data (the size of a ‘RESEL’, or resolution element) to be at least three times the size of one voxel. All results presented in this thesis using the SPM FWER correction were checked to ensure that data matched this heuristic value for smoothness.

3.2.6 Conclusion

The current implementation of the data processing pipeline has the following form (Figure 3.29).

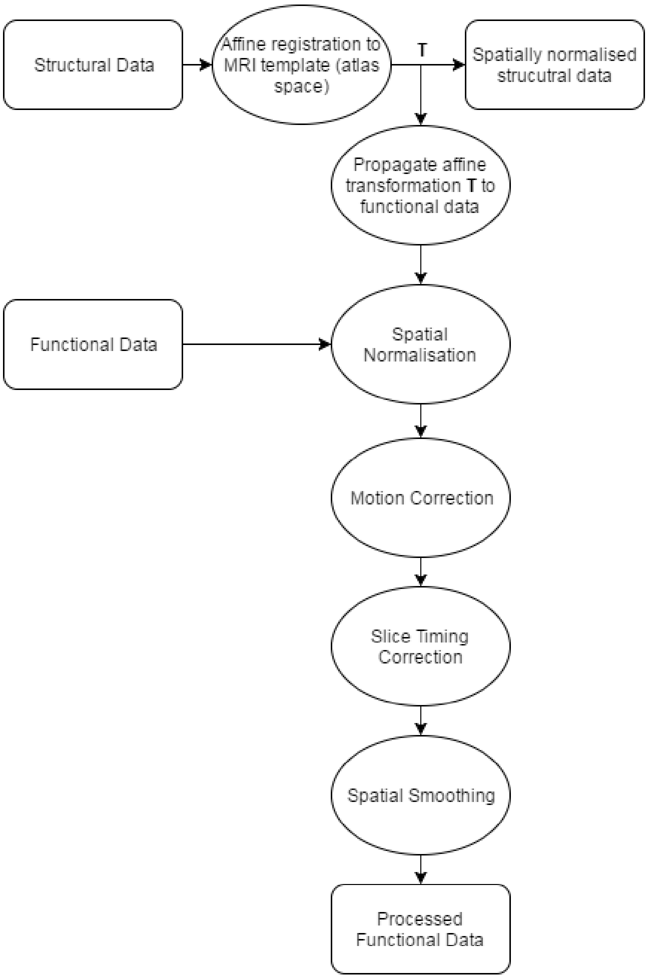

Figure 3.29. Flowchart for processing mouse brain fMRI data.

Further analysis of the fMRI data beyond the ‘Processed Functional Data’ point is dependent on the nature of the experimental design. Further analysis often includes motion parameter estimates which are outputted by the motion correction step – these are often included as nuisance regressors in a general linear model analysis.

It should be noted that the precise final implementation of this pipeline (in particular the spatial normalisation step as described in section 3.2.2.6), was only implemented towards the later stages of this work. Therefore experimental data collected early on may only be processed with earlier iterations of the pipeline, and this will be stated in the relevant methods sections.

To conclude, an automatic mouse fMRI data processing pipeline using a combination of NiftyReg and SPM tools was created, in a similar fashion to how human fMRI data is often analysed. This included registration of MRI data to the Allen mouse brain atlas to allow automated and non-biased extraction of fMRI data from specific atlas labels corresponding to the mouse brain visual system.

3.3 Interleaved snapshot fMRI: *in vivo*

This experiment aimed to measure BOLD responses in the mouse visual system, and investigates the effect of using interleaved snapshots on temporal contrast-to-noise. The results from this experiment are the first documented mapping of robust BOLD responses in the mouse brain to a visual stimulus, and are included as part of a journal article titled “fMRI mapping of the visual system in the mouse brain with interleaved snapshot GE-EPI” (Niranjan et al. [94]). The design of the visual stimulus and set-up of the laser was completed by Dr. Jack Wells; I designed and performed all other aspects of the study.

3.3.1 Introduction

Following on from section 3.1.4, task-based fMRI in the mouse brain was attempted. The majority of task-based fMRI studies in the mouse [32-36, 38] had focused on electrical shocks to the mouse paw as the stimulus of choice. Work by Schroeter et al. [38] clearly demonstrated the difficulty with this stimulus, as the correlation of heart rate with the stimulus can induce global BOLD signal changes – therefore obscuring activation specific to neuronal activity related to the stimulus.

The stimulus chosen for this experiment is binocular photic stimulation, of which there has only been one previous study by Huang et al. attempting to use a visual task to evoke BOLD fMRI responses in the mouse brain [31] (at the time this experiment was conducted, the paper by Harris et al. [39] had not been published). This study reported highly atypical BOLD responses when considered against similar data acquired in the rat brain [59, 60, 62-64]. To evaluate this, it is useful to reiterate the important features of the mouse brain visual system which we would expect to measure BOLD responses upon presentation of a visual stimulus: the lateral geniculate nuclei (LGd), the superior colliculus (SCs) and the visual cortex (VC) of which the primary area (VISp) would be the most prominent. This system is summarised in Figure 3.30, adapted with permission from figure 1(b) from Huberman and Neill [26].

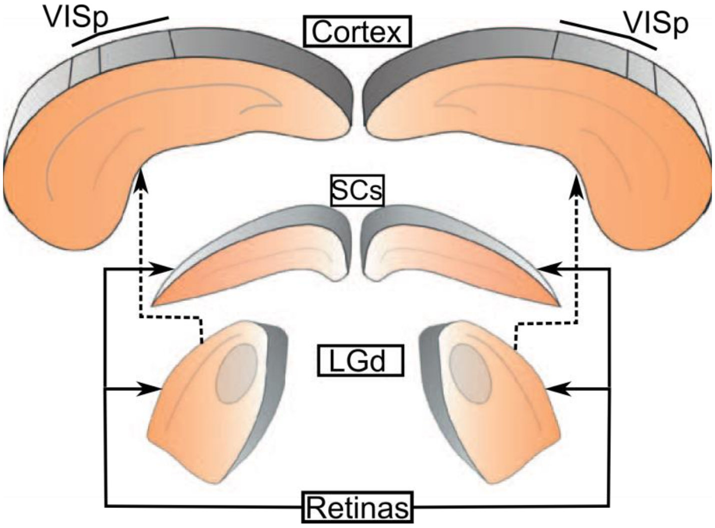

Figure 3.30. Schematic representing the mouse visual system, adapted from Huberman and Neill [26], with permission. For binocular stimulation, the three brain regions of interest are the dorsal lateral geniculate nuclei (LGd), the superior colliculus (SCs) and the primary visual cortex (VISp). Labels are the corresponding regions from the Allen Mouse Brain Atlas [69].

It is worth considering the quality of mouse visual fMRI data from the single previous study by Huang et al. [31]. In the twenty years since they conducted their study, fMRI methods and their reporting have improved considerably. Figure 3.31 shows a reproduction of figure 4 from this study, in which the spatial pattern of the BOLD responses does not appear to correspond to the known anatomy of the mouse visual system. The paper describes the BOLD clusters (thresholded at ±7%), as being in the occipital lobe, which is not particularly specific. In addition, the study does not display raw functional images, and the timecourses displayed are averaged over ROIs directly defined as voxels with maximal % change – suffering from circularity as described by Kriegeskorte et al. [125].

Given these considerations, it was deemed suitable to attempt task-based fMRI in the mouse using photic stimuli, as it was believed unlikely that photic stimulation would induce cardiac changes of the sort measured by Schroeter et al. [38] when applying electric shocks to the paw.

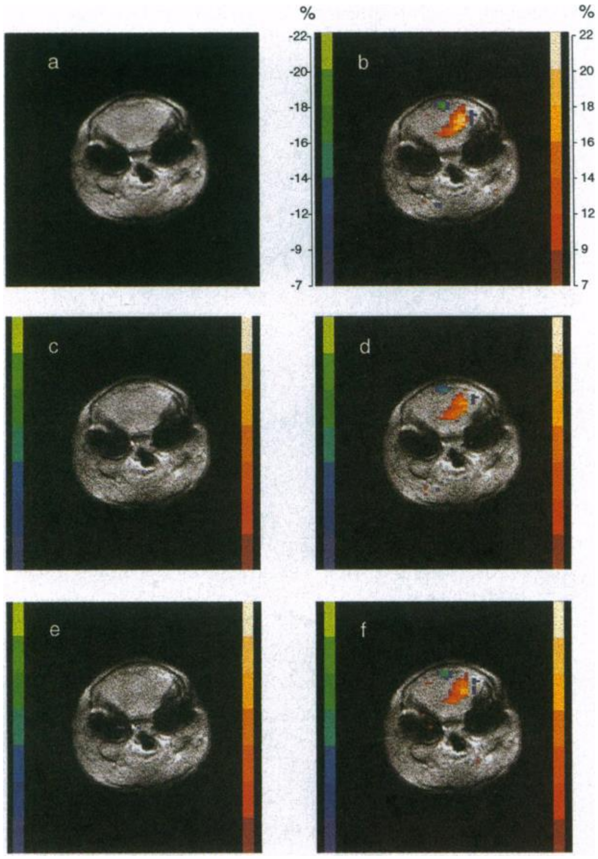

Figure 3.31. Figure 4 adapted from Huang et al. [31] (Copyright (1996) National Academy of Sciences). The original caption reads as follows, "FIG 4.… A 256 x 256 image obtained before stimulation is seen in *a*. In the other panels, color-coded fMRI difference images are superimposed on the gray-scale scout image. The color scales are given on either side of these images. b-f show the images obtained 1, 3.6, 8.1, 10.7, and 17.1 s after the light was switched on, respectively. Thus, b, d, and f show the responses to the switching on, the decrease in intensity, and the switching off of the light, respectively. On the other hand, c and e show the "accommodation" of the mouse brain to the continued stimulation."

As previously described, interleaved snapshot GE-EPI provides a method for acquiring less spatially distorted T_2^* weighted images than the traditional single shot GE-EPI, but is in theory accompanied by a reduction in image SNR. However, it was unclear how this might affect the temporal contrast-to-noise ratio (tCNR), which is the most useful quality assurance metric in fMRI. Whilst interleaved snapshot GE-EPI had been applied in the mouse brain to investigate resting state connectivity [154], there had been no attempt to evaluate its use with task-based fMRI.

The initial hypothesis for this experiment was that by increasing the number of interleaved snapshots n, marked improvements in the spatial localisation of the BOLD signal would be observed, but at a cost to image SNR, temporal SNR (tSNR) and tCNR (but that these may be an acceptable penalty for future applications given marked image distortion previously reported [33]).

3.3.2 Methods

Animals

All experiments were performed in mice in accordance with the European Commission Directive 86/609/EEC (European Convention for the Protection of Vertebrate Animals used for Experimental and Other Scientific Purposes) and the United Kingdom Home Office (Scientific Procedures) Act (1986) with project approval from the Institutional Animal Care and Use Committee. For reports on physiological measurements, all values are given as mean ± standard deviation. All mice were acclimatised two weeks prior to data acquisition in an animal house maintained at a temperature of 21 ± 2 °C and a relative humidity of 55 ± 10 %, on a 12 hours light/12 hours dark cycle with a 30 minute twilight switch.

6 female C57BL6/J mice weighing 19.3 ± 0.6 g were used to investigate the use of interleaved snapshot GE-EPI for acquiring task-based fMRI data in the mouse brain. From anaesthesia induction to the experiment end, each subject was given a gas mixture of 0.1L/min of O_2 and 0.4 L/min of medical air (BOC Healthcare (Linde AG), Munich, 20.9 ± 0.5% O_2 with balance composed of N_2). Anaesthesia was induced using 2% isoflurane gas and reduced to 1.5% for animal preparation. Subjects were transferred to medetomidine anaesthesia for functional imaging (0.4 mg/kg bolus, 0.8 mg/kg/hr infusion initiated 10 mins after bolus), administered subcutaneously via the flank using a butterfly needle [33]. The dosage was controlled using a programmable syringe pump (Harvard Instruments). Following administration of the medetomidine bolus, isoflurane was gradually discontinued at a rate of 0.2% per minute.

Respiratory rate was measured using a pressure sensitive pad, and core body temperature was measured using a rectal thermometer (SA Instruments). Core body temperature was maintained using a warm water circuit and hot air fan feedback system (SA Instruments). During functional imaging, this protocol produced a stable respiratory rate of 170 ± 16 breaths per minute. Core body temperature was maintained at 37.3 ± 0.3 °C. Other physiological measurements for this anaesthesia and gas mixture protocol are described in section 3.1.

MRI methods

All MRI experiments were performed on a 9.4T VNMRS horizontal bore MRI scanner (Agilent Inc., Palo Alto, CA) with an Agilent 205/120HD gradient set, in conjunction with a 72 mm inner diameter volume coil for RF transmission (Rapid

Biomedical), and a room-temperature 2 channel array surface coil (Rapid Biomedical) for signal reception. VNMRJ 3.1 software was used for image acquisition and reconstruction.

An anatomical reference scan was taken using a Fast Spin Echo sequence (TR/TEeff = 4000/48 ms, ETL = 8, matrix size = 192 x 192, FOV = 35 x 35 mm^2, 35 coronal slices each 0.6 mm thick). fMRI data were acquired using GE-EPI (FOV = 35 x 35 mm^2, matrix size = 96 x 96, 12 coronal slices each 0.5 mm thick, slice gap 0.1 mm, spectral width = 178.6 kHz, TR = 2.5 s, TE = 19 ms, one EPI triple reference image). These parameters were chosen based partially on values from the literature [34, 35, 126] and the experiment described in section 3.1.2. The acquisition time per snapshot, T_α, was kept at the VNMRJ suggested value of 50.18 ms for all sequences. 84 volumes were acquired for each run, including the triple reference. The anatomical reference scan ensured whole brain coverage, and the fMRI slices were positioned anterior to the anterior aspect of the cerebellum [31]. Shimming was conducted using a GE 3D protocol [143, 144], with both 1^{st} and 2^{nd} order shims optimised in a user defined cubic shim voxel (approximately 5 x 8 x 9 mm^3) with voxel edges set at the brain edge. Typical line-width (FWHM) within this shim voxel was approximately 60 Hz.

fMRI data were collected using a number of GE-EPI snapshots n ranging from one to four. At each n, the required flip-angle for each shot was calculated according to equation (3-1). Two fMRI runs were completed for each value of n for each subject, in a pseudo-random order.

Visual stimulation

Stimulation timings were triggered from the beginning of the EPI sequence using a POWER1401 control system (CED Ltd., UK) with Spike2 software. The stimulus consisted of blue laser light (445 nm, Omicron) transmitted into the scanner bore using a fibre optic cable. The cable was placed dorsal to the mouse head, secured to the top of the surface coil and aimed into the bore; in order that light reflected off the surface of the coil interior. This way, the eyes could be stimulated bilaterally with diffuse light without risk of retinal damage. The laser was pulsed at a frequency of 10 Hz, with pulse duration of 10 ms, and a laser current of 10 mA. The output power was measured to be 0.72 mW at the end of the fibre optic cable, and was not uncomfortably bright to the human eye. During baseline periods the laser power output was zero. The stimulus was delivered using a block design paradigm of 40 seconds rest, 20 seconds activation alternately repeated three times. This resulted in six activation periods per condition per subject. This visual stimulation paradigm is similar to that used by Pawela et al. in a rat visual fMRI experiment [62].

A schematic showing the mouse fMRI set-up is shown in Figure 3.32.

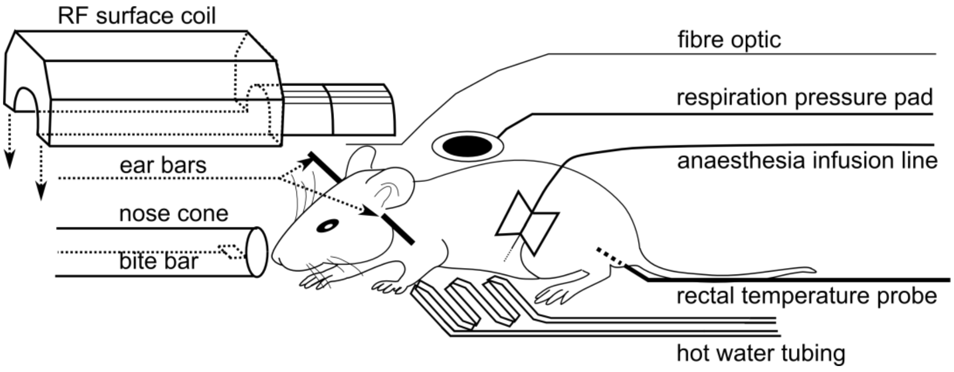

Figure 3.32. Schematic showing experimental set-up for mouse fMRI with visual stimulus.The fibre optic cable sits between the head and the underside of the surface coil, allowing light to be reflected off the surface coil and into the eyes.

Data analysis

All data analysis was conducted using ITK-SNAP [155], NiftyReg [150, 151], the SPM toolbox [120], the MarsBaR toolbox [137], in-house MATLAB 2014b scripts and GraphPad Prism 6. All voxel size header information was increased in size by a factor of ten to facilitate the use of human neuroimaging analysis software, however all distances and locations are reported in real space. Anatomical reference scans were registered to the reference scan (manually skull-stripped using ITK-SNAP) of the final subject using an affine registration with NiftiReg, and the affine transformation matrix generated was then applied to the fMRI data, as previously described in section 3.2.2. To generate structural ROIs, the Allen histology mouse brain atlas [69] was directly registered to the data in the same way, and atlas labels transformed accordingly. The registration was evaluated by visual inspection with respect to the anatomical reference scan using the spm_check_registration routine and the Paxinos Mouse Brain Atlas [156]. After registration the fMRI data were realigned (to correct for motion), corrected for differences in slice timing and smoothed (Gaussian FWHM of two voxels). The triple-reference image was discarded before slice timing correction.

Region-of-interest (ROI) analysis was conducted by using atlas labels to extract timecourses using MarsBaR, to avoid circularity [125]. The labels chosen for timecourse extraction were the LGd, SCs and VISp, which correspond to the dorsal lateral geniculate nucleus, the sensory areas of the superior colliculus and the primary visual area, commonly referred to V1. As the stimulus was binocular, ROIs included both brain hemispheres. The MarsBaR source code was altered in order that individual voxel timecourses were filtered and normalised before averaging, and the code modifications are shown in Appendix A. Timecourses were normalised to percentage signal change by dividing each value by the mean value of the whole timecourse.

BOLD contrast was then calculated by subtracting the mean preceding baseline value from the mean BOLD value from each stimulus epoch. Temporal CNR was calculated for the LGd, SCs and VISp, by dividing the relevant mean BOLD contrast by the standard deviation of the BOLD signal in the baseline period [157]. For the SCs only (as it is the only fully contiguous region), image SNR was calculated by dividing the mean intensity of the first timepoint in the SCs by the standard deviation of an equivalent sized ROI centred outside the brain. Temporal SNR was calculated slightly differently – because it requires the mean signal at baseline, percentage change normalised timecourses cannot be used (this would mean division by zero). To avoid this, temporal SNR was calculated with filtered timecourses only and by dividing the standard deviation of the initial baseline signal by its mean value.

Linear regression was performed on BOLD temporal CNR values and temporal SNR in the SCs to test for trends with respect to n, and on image SNR with respect to $\sqrt{n}$.

For statistical parametric mapping, 1st-level general linear model (GLM) analysis was conducted for each subject under each condition, with both fMRI scans included in the GLM with estimated motion parameters as nuisance regressors (single subject fixed effects model). Voxels were only analysed if they were included in a brain mask manually generated from the anatomical reference scan of the last subject. The SPM canonical HRF (double-gamma function) was convolved with the stimulus profile as the explanatory model. The default SPM options of grand mean scaling and auto-correlation noise modelling were used, with a high-pass filter of 128 seconds. A two-tailed t-test was then performed on a voxel by voxel basis to test the null hypothesis that the BOLD signal is not explained by the explanatory model. All statistical parametric maps shown were corrected for multiple comparisons using a FWER ($p < 0.05$) threshold determined by random field theory using SPM12 unless otherwise stated. No cluster thresholding was used. To understand group level activations, fixed (FFX) effects analysis was conducted. The fixed effects group analysis included all subject scans for each condition in the same GLM (with appropriate nuisance regressors).

3.3.3 Results

Identification of BOLD responses

Bilateral BOLD responses to a flashing light visual stimulus were identified in the LGd, SCs and VISp regions through fixed effects SPM analysis. Results from the 10 Hz flashing stimulus measured with GE-EPI using $n = 4$ are shown in Figure 3.33.

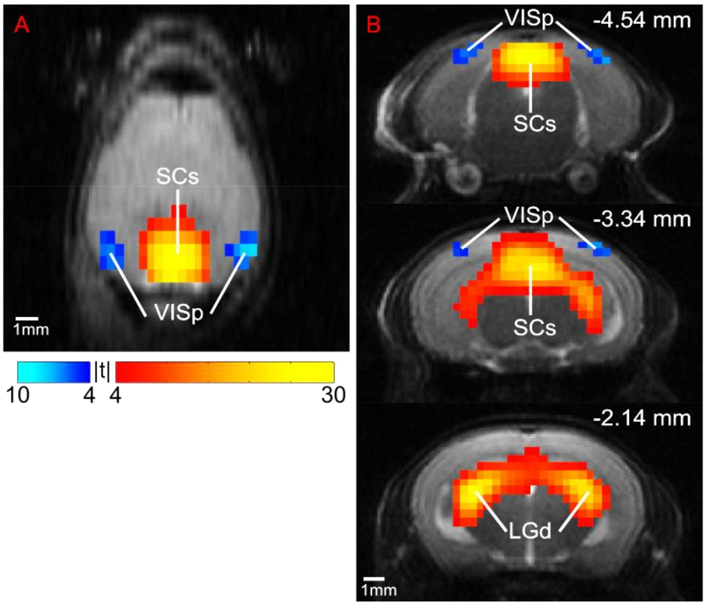

Figure 3.33. Fixed effects analysis (two-tailed t-test, FWE p < 0.05, N = 6) statistical parametric map generated from snapshot GE-EPI ($n = 4$), overlaid on anatomical reference image in A) transverse view and B) three coronal slices (with distance relative to Bregma).

These regions show close spatial affinity to the mouse visual system as described by Figure 3.30. The spreading of the BOLD response beyond these regions in a ‘halo’ effect is likely due to the combination of the statistical threshold level chosen combined with the 2-voxel FWHM smoothing kernel applied in the pre-processing step, as recommended by [118]. An alternative explanation is the presence of draining veins surrounding the thalamus, which has been noted previously in gradient echo BOLD imaging [158].

Somewhat surprisingly, negative BOLD responses can be seen in VISp, whilst the expected positive BOLD responses were seen in LGd and SCs.

Effect of varying the number of snapshots on tCNR and image distortion

To examine CNR when using interleaved snapshots, the peak BOLD timecourse intensity in each stimulation epoch was divided by the standard deviation of BOLD signal during 15 seconds of the baseline period directly preceding it. Mean BOLD responses to the visual stimulus and temporal CNR measurements in the SCs are shown in Figure 3.34.

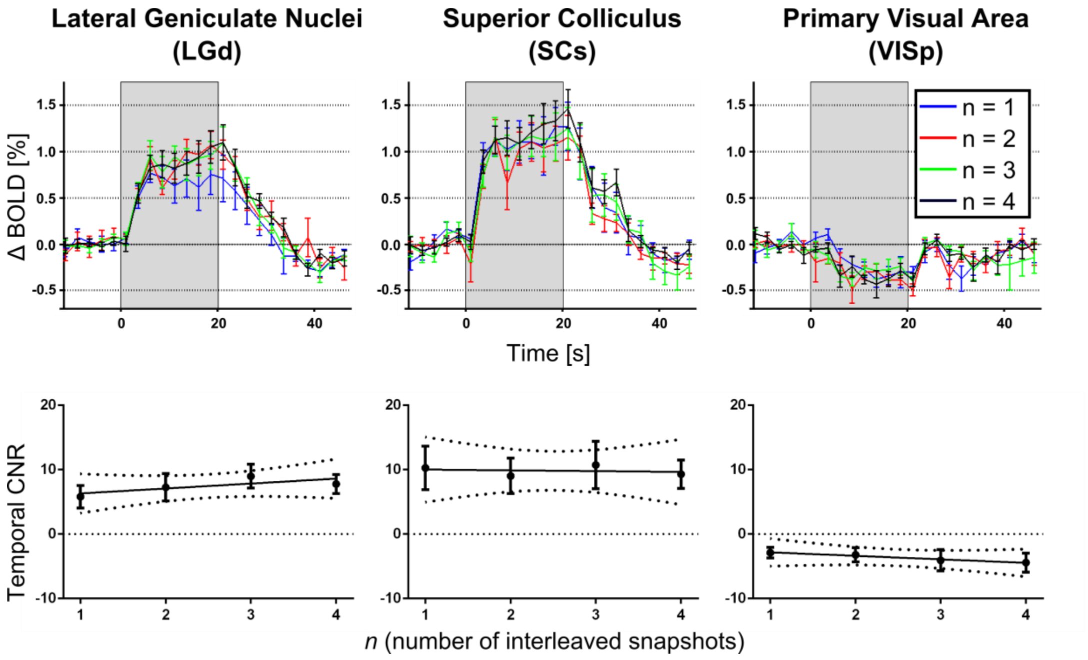

Figure 3.34. BOLD responses and temporal CNR (mean ± S.E.M) for different number n of interleaved snapshots, in the three regions of the mouse visual system. The negative CNR in VISp reflects the negative BOLD response.

No significant loss in temporal CNR with increasing snapshot number was observed. Linear regression showed no trend in BOLD CNR values across snapshots (p = 0.3405, 0.9259 and 0.3355 for LGd, SCs and VISp respectively). Temporal SNR in the baseline period of the SCs also exhibited no trend with n was seen (p = 0.9044). A representative subject GE-EPI data illustrating the reduction in image distortion is shown in Figure 3.35.

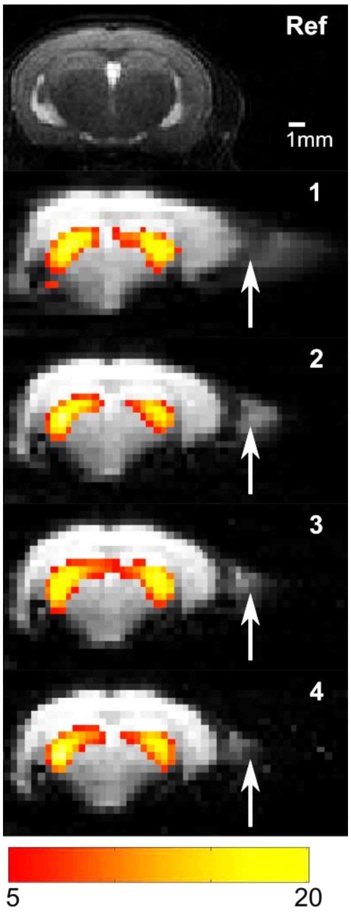

Figure 3.35. Representative GE-EPI from single subject showing reduction in distortion (white arrow) with increasing snapshot number, with anatomical reference image (Ref). Single subject fixed effects statistical map (FWE p > 0.05) is overlaid for each snapshot number, showing activation patterns in the LGd.

Importantly, image distortion was markedly reduced, and the symmetry of BOLD activation was noted to increase with increasing snapshot number (Figure 3.35). Signal dropout towards the base of the brain did not appear to be affected by snapshot number. As expected, a decrease in image SNR in the SCs with $\sqrt{n}$ was seen [140] (p = 0.0065, Figure 3.36).

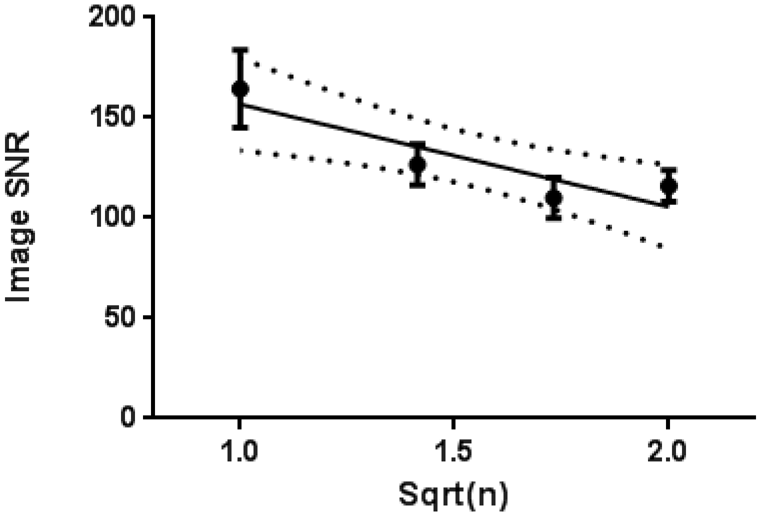

Figure 3.36. Plot of image SNR against $\sqrt{n}$ for signals in the superior colliculus (mean ± S.E.M)

A summary of the quality assurance measures for the superior colliculus is shown in Table 3.4.

Table 3.4. Linear regression results testing for dependence of fMRI quality metrics on number of EPI snapshots (data from superior colliculus).

Metric	Model	m	95% Confidence Interval for m	F (DFn = 1, DFd = 22)	p-value
Image SNR	$y = m\sqrt{n} + c$	-51.26 [ΔSNR $n^{-0.5}$]	[-86.63 -15.90]	9.037	0.0065
tSNR	$y = mn + c$	3.072 [ΔSNR n^{-1}]	[-49.36 55.50]	0.01476	0.9044
tCNR	$y = mn + c$	-0.123 [ΔSNR n^{-1}]	[-2.834 2.588]	0.00859	0.9259

These results suggest we can be confident in a negative trend in image SNR with $\sqrt{n}$, but not for tSNR or tCNR with n.

3.3.4 Discussion

This experiment aimed to investigate the use of GE-EPI with interleaved snapshots for mouse brain fMRI and characterise the BOLD functional response of the mouse brain to a visual stimulus. For the first time, the mouse brain visual system was successfully mapped with fMRI. An improvement in fMRI images with increasing number of interleaved snapshots was shown, without a reduction in temporal CNR. Robust BOLD responses were recorded, including negative BOLD responses (NBRs) in the VISp region at 10 Hz stimulus frequency.

The data from this experiment confirms a reduction in image SNR with $\sqrt{n}$, as previously described by Guilfoyle and Hrabe [140], but shows no appreciable detriment to temporal CNR (in range $n \in [1,4]$). The link between image SNR and temporal CNR of the BOLD signal is non-trivial, as both hardware and physiology contribute to the noise. A more advanced analysis of this data might consider the use of direct models linking image and temporal SNR such as those described by Kruger et al. [159] Under the current experimental conditions, the results from this experiment suggest that physiological noise dominates over hardware noise in the temporal domain, in line with two fMRI tSNR experiments completed in humans [159, 160]. Equally, this suggests that interleaved snapshot GE-EPI represents an advantageous approach to reduce image distortion in GE-EPI data with no fMRI sensitivity cost, and is used in later experiments described in chapter 4.

There are alternatives to interleaved snapshot EPI for mouse brain fMRI, such as conventional segmented EPI or parallel imaging using multiple coils. Conventional segmented EPI sequences are more susceptible to motion artefacts [140], as there is a longer time between segment acquisitions in the same slice. Parallel imaging is commonly used in human MRI, as it collects all data segments simultaneously, using methods such as GRAPPA [161] or SENSE [162]. However this is highly dependent on coil geometry and parallel imaging benefits most from arrays with large numbers of coils. The small size of the mouse brain makes large coil arrays problematic, and this combined with the more complex image reconstruction techniques required for parallel imaging, make it less suitable than interleaved snapshot GE-EPI for mouse brain fMRI.

Animal Physiology

There are two general strategies to obtaining fMRI measurements from anaesthetised mice. One option is to use neuromuscular blocking agents with mechanical ventilation, which allows control of respiratory rate/volume and blood gas levels, and minimises head motion [35, 36, 38, 127]. However, mechanical ventilation via cannulation of the trachea is invasive, whilst endotracheal intubation is technically challenging in the mouse. The second option, as done here, is to use a free breathing protocol [33, 37]. This enables recovery, and thus longitudinal studies, but is likely to increase the between-subject variability.

Anaesthesia effects on mouse fMRI responses are well documented for paw electrical stimulation at innocuous intensity levels, and a previous study recorded a 10 second lag between stimulus onset and BOLD response in the somatosensory cortex under medetomidine and urethane anaesthesia [38]. We saw no such lag using a medetomidine only protocol, with a larger bolus and infusion concentration delivered subcutaneously as opposed to a tail vein injection. The lag effects are also not described in other paw stimulation studies [33, 37] in the mouse that used medetomidine, at an intermediate dose (0.3 mg/kg bolus, 0.6 mg/kg/hr infusion).

It should be noted that the possibility of performing awake mouse fMRI has been demonstrated with opto-genetic stimuli [129] and a fear conditioned task [39]. The obvious advantage is that anaesthesia is removed as a confounding variable. However, as noted by both sets of authors, awake mouse fMRI is technically challenging. Motion artefacts are more severe, and substantial training of the animals is required. In particular, EPI sequences used for fMRI are particularly susceptible to motion. It is also worth considering whether stress levels are comparable across subjects, and reproducible across studies. Whilst anaesthesia may introduce bias in results, it is likely that not using anaesthesia increases variance.

This can be considered further in the case of the awake mouse fMRI paper by Harris et al. [39], which uses flashing lights in conjunction with electric shocks to image fear circuitry. The main result of this study is activation in the amygdala in response to a fear conditioning task; however for the purposes of this work it is the use of the flashing light to induce fear which is important. In the supplementary materials of this paper, figure S2 shows unthresholded activation maps from pooled data, reproduced in Figure 3.37.

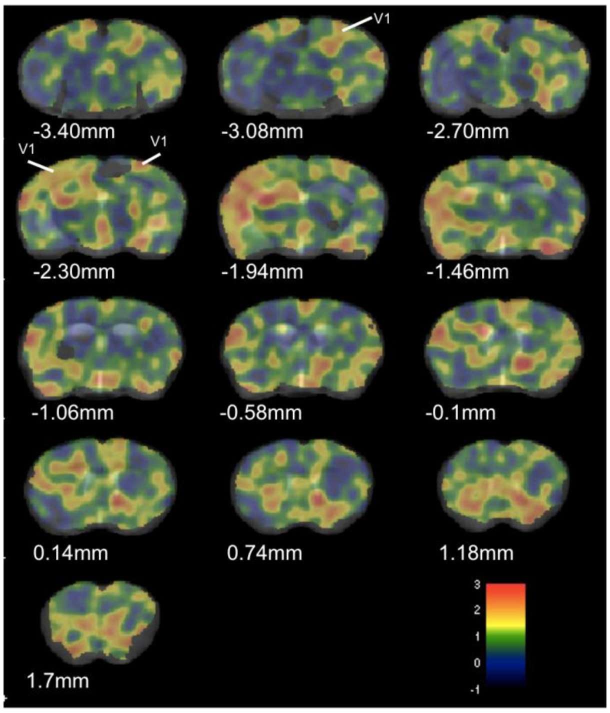

Figure 3.37. Figure S2 from Harris et al. 2015 [39] (Creative Commons Licence). The original caption reads as follows, "Figure S2. Unthresholded activation maps showing activation pooled across the paired and unpaired group mice (n = 14), specifically to investigate visual activation in response to the CS [conditioned stimulus]. Activation is overlaid on the average structural template. The primary visual cortex (V1) is activated in response to the CS. Scale bar represents the raw effect size (increase/decrease) in arbitrary units, the numbers represent approximate distance in mm from Bregma for each coronal slice based on the Franklin and Paxinos mouse brain atlas…"

It is difficult to directly compare activation maps such as those in Figure 3.37 with those reported in Figure 3.33 and Figure 3.35, as a different statistical procedure has been used (and indeed, the functional data were acquired with a Fast Spin Echo sequence, and a temporal resolution of 10s per volume, rather than GE-EPI); however the specificity can be evaluated qualitatively. What is particularly interesting here is that although positive BOLD responses are reported in V1 (equivalent to VISp), the pattern of activity does not correspond strongly to the visual system, with many other areas of cortex etc. showing similar effect sizes as V1. Additionally, the lateral geniculate nuclei and superior colliculus do not stand out from the rest of the brain. Based on a qualitative comparison of this work and the data presented in this section, it appears that medetomidine anaesthetised mice generate more specific BOLD signal responses in response to visual stimuli than awake mice do.

Visual stimulation and the nature of the BOLD response

Visually evoked BOLD responses were measured in response to a flashing light visible to both eyes. Only one previous study has used fMRI to study the mouse visual system [31], and the experiment described in this section significantly builds on this by using GLM analysis to map BOLD responses, using unbiased structural ROIs to extract BOLD time series data, and implementing GE-EPI for BOLD signal acquisition.

The negative BOLD response measured was unexpected, and robust measurements of NBRs had not been reported in mouse visual cortex before (although they have been suggested to occur from simulations derived from optical imaging spectroscopy data [43]). NBRs in general could reflect either reduced neuronal population activity or a breakdown in neurovascular coupling. Without invasive electrophysiology experiments, neither of these hypotheses can be definitively ruled out. However, the fact that positive BOLD responses were measured in the LGd and SCs suggest that if neurovascular coupling were disrupted (say, by the use of anaesthesia), then this is specific to the cortex. Furthermore, designing an experiment which can modulate the negative BOLD response by some stimulus characteristic in a within subject design would provide some evidence that anaesthesia is not a contributory factor to the NBR. An experiment of this type is described in more detail in section 4.1.

3.3.5 Conclusion

Mouse brain fMRI has been demonstrated using a bilateral visual stimulus to simultaneously map the LGd, SCs and VISp regions of the visual pathway. BOLD responses in the lateral geniculate nuclei and the superior colliculus were comparable to rat data in earlier studies [59, 60, 62-64], however a surprising negative BOLD response was measured in the VISp region. Future experiments will focus on attempts to modulate the BOLD response through increasingly complex stimuli. This experiment considerably improves upon the previous mouse visual fMRI study reported in the literature [31]. Using GE-EPI with up to four interleaved snapshots showed no reduction in temporal CNR, whilst reducing susceptibility induced image distortions and thus may represent a useful strategy for future mouse fMRI studies.

3.4 Chapter summary

In this chapter, development of a protocol for imaging BOLD signal responses to visual stimuli was described. Section 3.1.1 described a bench experiment examining mouse physiology. In sections 3.1.2 and 3.1.3, quality assurance work on the GE-EPI sequence through phantom imaging was described, and in section

3.1.4 the use of interleaved snapshot GE-EPI was first considered in a phantom as well.

Section 3.2 covered development of the mouse fMRI data pre-processing pipeline, and in particular highlighted some of the difficulties faced in spatial normalisation of mouse brain functional data. This methods development and optimisation work culminated in a novel and refined methodological protocol for robust fMRI of the mouse brain visual pathway.

In section 3.3, the first *in* vivo application of interleaved snapshot GE-EPI for task-based fMRI in the mouse was described, with the experiment conducted using a binocular visual stimulus.

The main result of this chapter is that although image SNR is reduced by using up to four interleaved snapshots in the GE-EPI sequence, temporal CNR is not, and therefore the increase in spatial localisation of the BOLD signal through using interleaved snapshot GE-EPI is effectively achieved without a cost to fMRI sensitivity, (at least within the regions of interest within the visual pathway examined in this study). The secondary result from this section is that negative BOLD responses can be detected in the mouse primary visual cortex simultaneously to positive BOLD responses in the lateral geniculate nuclei and the superior colliculus. In the next chapter, mouse fMRI experiments with increasingly complex visual stimuli will be described.

4 Visual stimuli for mouse fMRI

This chapter builds on chapter 3 in terms of visual stimuli development for mouse brain fMRI. There were three general aims to using more complex visual stimuli:

1. To examine whether different stimuli could evoke larger BOLD responses. This would increase detection sensitivity of the method, which may be useful for future studies applying this technique to transgenic mouse models of disease.
2. To develop greater understanding of the fundamental biology of the mouse brain.
3. To increase the translational relevance of the method to human fMRI studies.

All of the stimuli developments described in this chapter are entirely novel for mouse fMRI.

Having established a novel methodology for mapping the mouse brain visual system, I set out to characterise the system in more detail, and induce reliable positive BOLD responses in the visual cortex. Section 4.1 describes an experiment that reproduces the negative BOLD response in the visual cortex with a 10 Hz flashing light stimulus, and modulates the magnitude of the BOLD response with stimulus temporal frequency. Section 4.2 pools two datasets and applies non-parametric statistics to make formal population inferences. Section 4.3 introduces the use of a single-loop surface coil and a custom eye-piece for monocular stimulation. This result is then built upon in section 4.4, and differential BOLD responses to bright and dark flashes are demonstrated. Then in section 4.5, the use of an array of LEDs with the potential for spatially varying visual stimuli was described. Finally, the chapter is summarised in section 4.6.

4.1 Frequency modulation

Positive BOLD responses have not previously been reported in the mouse visual cortex, but have in rat [64], cat [23] and human [12] studies. Generating reliable positive BOLD responses with increased magnitude in the mouse visual cortex could be useful for future studies, with regards to detection sensitivity and for comparing cortical responses across species.

This section describes an experiment I conducted, aiming to modulate BOLD responses measured in the mouse visual system evoked by a flashing light stimulus, by varying the flashing frequency. By doing so, it was anticipated that positive BOLD responses in the primary area of the mouse visual cortex might be induced. This is included as part of a journal article titled “fMRI mapping of the visual system in the mouse brain with interleaved snapshot GE-EPI”, by Niranjan et al. [94].

4.1.1 Introduction

In chapter 3, a novel protocol for task-based fMRI in the mouse brain using a visual stimulus was developed. Statistical parametric mapping of BOLD responses specifically highlighted three key regions of the mouse visual system: the lateral geniculate nucleus (LGd), the superior colliculus (SCs) and the primary area of the visual cortex (VISp). In response to a blue light flashing at 10 Hz, positive BOLD responses were recorded in LGd and SCs, and negative BOLD responses (NBRs) recorded in VISp. The NBRs were unexpected and previously unseen in previous fMRI studies of the mouse brain using paw and whisker stimulation [32-38].

Based on visual fMRI experiments conducted on rats reported in the literature [59, 60, 62-64], it was hypothesised that BOLD responses could be modulated by varying the temporal flashing frequency. Given that the initial stimulus used in section 3.3 was a binocular flashing light source, varying the temporal frequency was decided to be the most straight-forward way of modulating the stimulus, and provided an opportunity to reproduce the initial negative BOLD response.

In this study, the flashing frequency f was set to 1, 3, 5 or 10 Hz, and based on results in the rat fMRI literature [59, 60, 62-64], hypothesised that the amplitude of BOLD responses would have positive trends with f in the LGd and SCs, and a negative trend in the VISp. Based on the results of section 3.3, interleaved snapshot GE-EPI with four snapshots was used for fMRI data acquisition.

4.1.2 Methods

Animals

8 female C57BL6/J mice weighing 20.7 ± 0.7g were used to characterise the BOLD signal response of the visual system to stimulus flashing frequency f. Subjects were anaesthetised and monitored using the same protocol described in section 3.3.2. During functional imaging, this protocol produced a stable respiratory rate of

171 ± 22 breaths per minute. Core body temperature was maintained at 37.0 ± 0.1 °C.

MRI methods

All MRI experiments were performed using identical hardware to section 3.3.2, and the same parameters for the anatomical reference scan and GE-EPI were used, with $n = 4$ interleaved snapshots. Shimming was performed as described previously, and typical line-width (FWHM) was approximately 60 Hz.

Visual stimulation

Stimulation timings were triggered from the beginning of the EPI sequence using a POWER1401 control system (CED Ltd., UK) with Spike2 software. The stimulus consisted of blue laser light (445 nm, Omicron) transmitted into the scanner bore using a fibre optic cable. The cable was placed dorsal to the mouse head, secured to the top of the surface coil and aimed into the bore; in order that light reflected off the surface of the coil interior. This way, the eyes could be stimulated bilaterally with diffuse light without risk of retinal damage. The laser was pulsed at a frequency of f Hz (1, 3, 5 or 10), with pulse duration of 10 ms, and a laser current of 10 mA. The output power was measured to be 0.72 mW at the end of the fibre optic cable. During baseline periods the laser power output was zero. The stimulus was delivered using a block design paradigm of 40 seconds rest, 20 seconds activation alternately repeated three times. This resulted in six activation periods per condition per subject. Two fMRI runs were completed for each value of f for each subject, in a pseudo-random order.

Data analysis

Data processing was conducted in a similar fashion to that described in section 3.3.2.

BOLD contrast was calculated by subtracting the mean preceding baseline value from the mean BOLD value from each stimulus epoch. Linear regression was then performed on BOLD contrast values in LGd, SCs and VISp to test for trends with respect to f.

Statistical parametric mapping was conducted in the same way as section 3.3.2. As an exploratory analysis, random effects analysis (RFX) was also conducted at the 2nd level on a pooled data set (see section 4.2).

4.1.3 Results

BOLD response maps to visual stimulation at different flashing frequencies

Bilateral BOLD responses to the flashing light stimulus with varying frequency are mapped using FFX analysis in Figure 4.1.

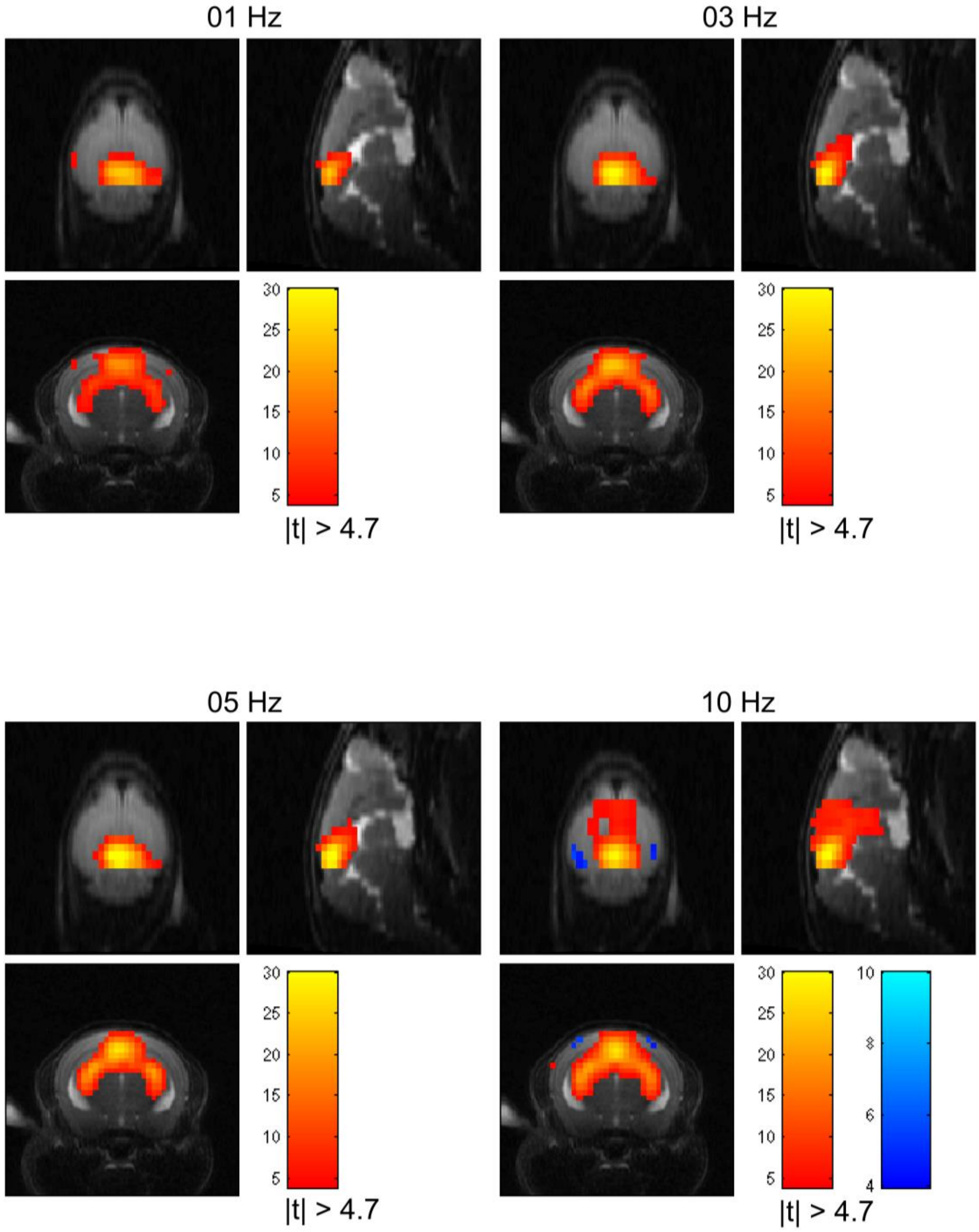

Figure 4.1. Fixed effects analysis (two-tailed t-test, FWE p < 0.05, N = 8) statistical parametric map generated for each frequency, overlaid on cross sectional views of anatomical reference image (MRI template described in section 3.2.2. The negative BOLD responses at 10 Hz measured in section 3.3 have been reproduced (bottom right), although there is also some non-specific positive BOLD response in the mid-brain.

BOLD response dependence on stimulus flashing frequency

After observing negative BOLD responses in VISp at 10 Hz in the experiment described in section 3.3, fMRI was performed in eight mice with variable stimulus flashing frequency (1, 3 5 and 10 Hz). Mean BOLD responses to the visual stimulus at different frequencies and corresponding mean peak BOLD contrasts for the LGd, SCs and VISp are shown in Figure 4.2.

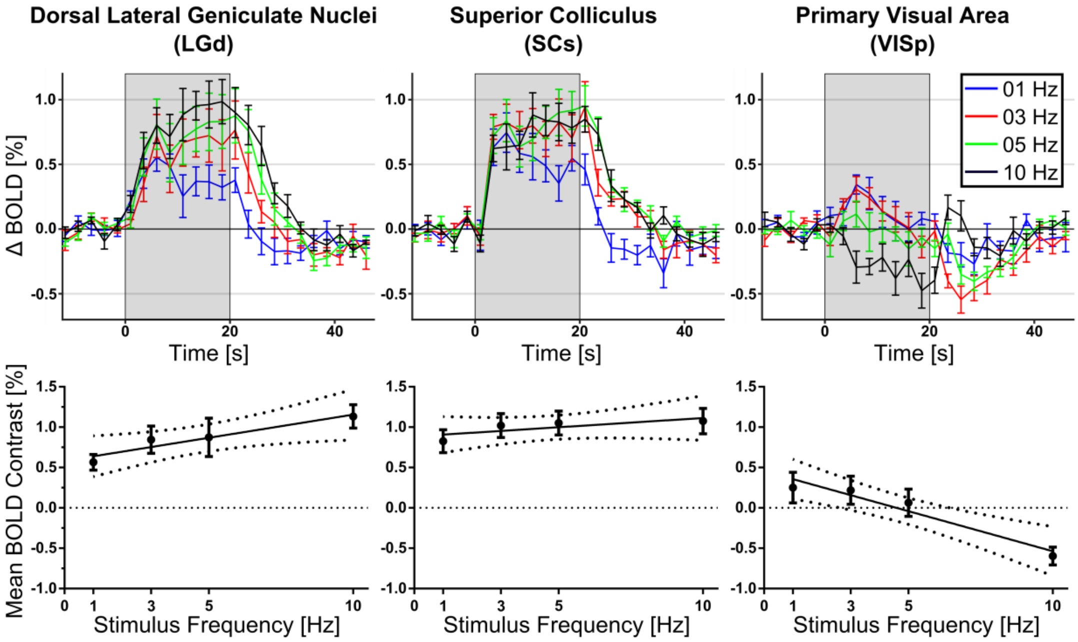

Figure 4.2. BOLD responses and contrasts in the LGd, SCs and VISp regions. BOLD timecourses (top) are plotted as means ± S.E.M. (N = 8). Trends in mean BOLD contrast (bottom) are plotted with 95% confidence intervals.

Positive trends in BOLD contrast with frequency were seen in both the LGd and SCs, and a negative trend found in VISp. The negative BOLD response for a flashing frequency of 10 Hz in VISp described in section 3.3 was reproduced here. A summary of the linear regression statistics is shown in Table 4.1.

Table 4.1. Linear regression results, testing for association of BOLD contrast on f.

ROI	m [Δ% Hz^{-1}]	95% Confidence Interval for m	F (DFn = 1, DFd = 30)	p-value
LGd	0.0489	[0.00152 0.0963]	4.44	0.0436
SCs	0.0200	[-0.0188 0.0588]	1.11	0.3010
VISp	-0.0532	[-0.0754 -0.0312]	24.3	0.0000287

Over the range of frequencies used, it appears that VISp BOLD responses have a stronger frequency association than sub-cortical regions.

4.1.4 Discussion

The aim of this experiment was to reproduce the negative BOLD responses (NBRs) found in VISp when using a visual stimulus with a 10 Hz flashing frequency, and to investigate the potential for temporal frequency modulations of mouse visual system BOLD responses. The NBRs were reproduced in VISp at 10 Hz, and positive BOLD responses (PBRs) were recorded at lower flashing frequencies. The frequency-dependence of PBRs in the mid-brain concurs with similar studies conducted in the rat brain [60, 62, 64]. Whilst NBRs had not been reported previously, a trend for a reduced amplitude of evoked potentials with increasing stimulus frequency had been previously observed in rat visual cortex [62], which is in concordance with the observed trend in VISp BOLD contrast with frequency described in this section.

One limitation with using the GLM approach for statistical parametric mapping is the potential mismatch between the SPM canonical haemodynamic response function for humans and mouse brain haemodynamics. This issue is addressed in chapter 5.

As was discussed in section 3.3.4, NBRs have not been reported in the mouse before, although they were predicted as an anaesthesia effect by Sharp et al. [43] from simulations based on 2D-OIS data. However, given the association between stimulus temporal frequency and BOLD contrast, it is unlikely that the NBRs are themselves an artefact resulting from the medetomidine anaesthesia interfering with neurovascular coupling. The presence of PBRs in the mid-brain for all frequencies tested, and PBRs in VISp for frequencies below 5 Hz, suggest that if anaesthesia is responsible for the NBRs in VISp, then it is an anaesthesia-cortical-frequency interaction, which sounds implausible. A more likely explanation is that at higher frequencies, neuronal activity in the visual cortex is suppressed, and that this reduction drives the negative BOLD response. However, full validation of this effect would require invasive electrophysiology techniques, and could be an interesting extension of this work for future studies.

4.1.5 Conclusion

Mouse brain fMRI was conducted with a binocular visual stimulus of flashing frequency f (1, 3, 5 and 10) Hz, and BOLD responses recorded, showing modulation of BOLD signal responses with f. BOLD responses in the LGD and SCs were comparable to rat data available in the literature [59, 62-64]. The negative BOLD response in the VISp region (described in section 3.3) was reproduced, and found to become positive for lower frequencies (< 5 Hz). The results from this experiment suggest that the negative BOLD response is not an artefact of anaesthesia, but instead reflects neuronal population responses to stimuli with certain characteristics. Based on this experiment, future experiments use a flashing frequency below 3 Hz for inducing positive BOLD responses in the primary visual cortex.

4.2 Generalising statistical maps to populations

In this section, data from section 3.3 and section 4.1 are pooled in order to make statistical parametric maps which can be used for making formal inferences on populations.

4.2.1 Introduction and methods

The use of random effects (RFX) GLM analysis is required to make formal statistical inferences describing the population from which the subjects are derived. A fixed effects (FFX) analysis assumes that the population is entirely defined by the subjects included, and is therefore descriptive. A detailed explanation of RFX and FFX analyses is given in section 2.2.3.1, but briefly, FFX analyses are more powerful than RFX analyses, however FFX analyses cannot be used to make formal statistical inferences about future data, without assuming an equal effect size in every subject. For group sizes of 6 (section 3.3) and 8 (this section), BOLD responses were undetectable using RFX analysis at conventional statistical thresholds (FWER $p < 0.05$, $|t| > 10.69$, 5 and 7 degrees of freedom). However, both groups included subjects scanned with a 10 Hz frequency using GE-EPI with four interleaved snapshots. It was therefore possible to pool these two experiments, and perform RFX analysis (FWER $p < 0.05$, two-tailed t-test) on this combined group ($N = 14$). This is done in SPM by using the contrast images outputted for each subject from the 1st-level analysis (FFX on a per subject basis) as inputs for a 2nd-level GLM analysis.

4.2.2 Results

Initially, the standard fixed effects GLM analysis using SPM12 was used on the pooled data, and this map is shown in Figure 4.3.

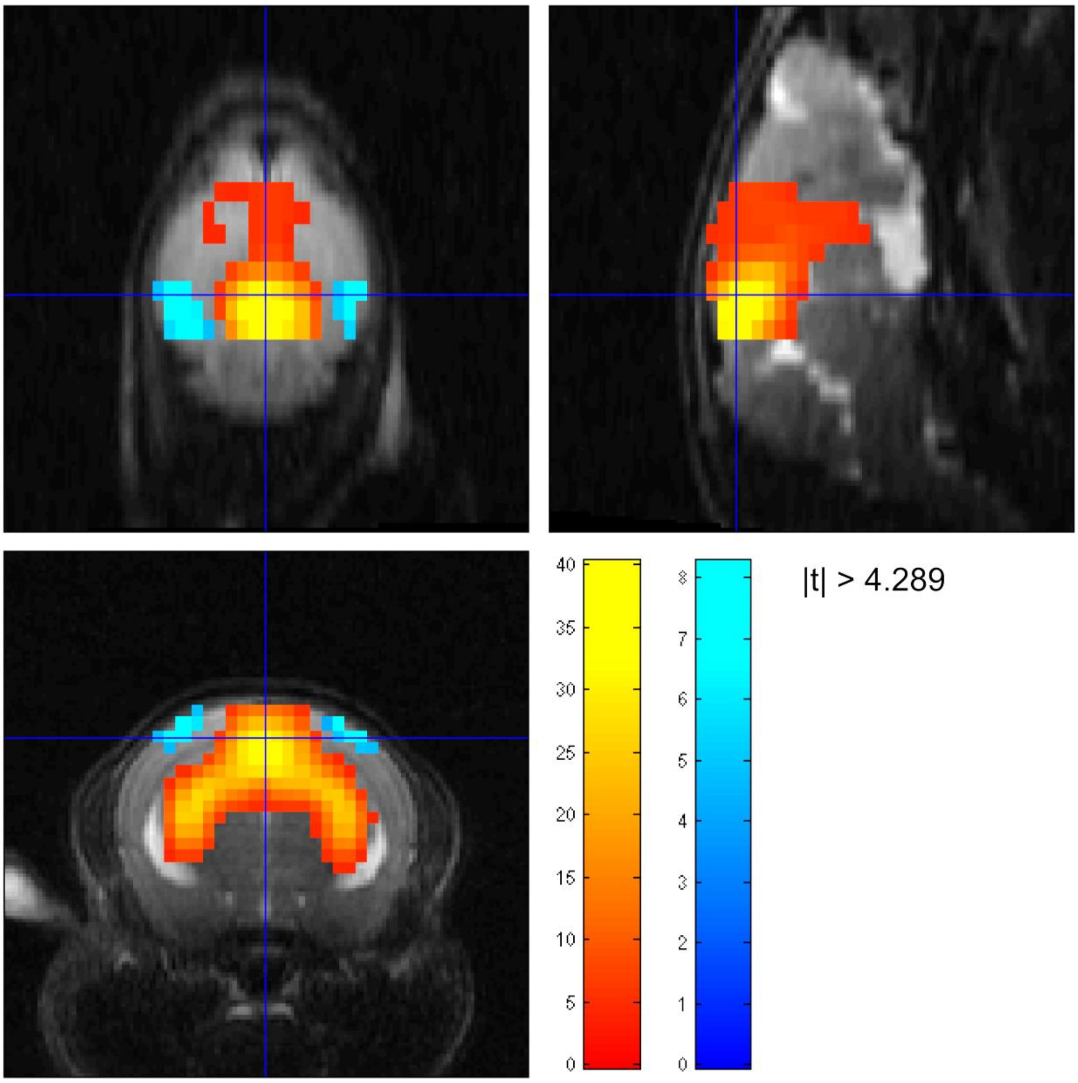

Figure 4.3. FFX analysis (two-tailed t-test, FWE p < 0.05, N = 14) statistical parametric map generated for the pooled 10 Hz data. The spatial extent of voxels above the t-statistic threshold are larger than for each experiment separately.

It should be noted that as N increases, the number of degrees of freedom of the t-distribution from which the statistic is compared to increases, and therefore the threshold defining activation decreases as well. The RFX effects GLM parametric analysis is shown in Figure 4.4.

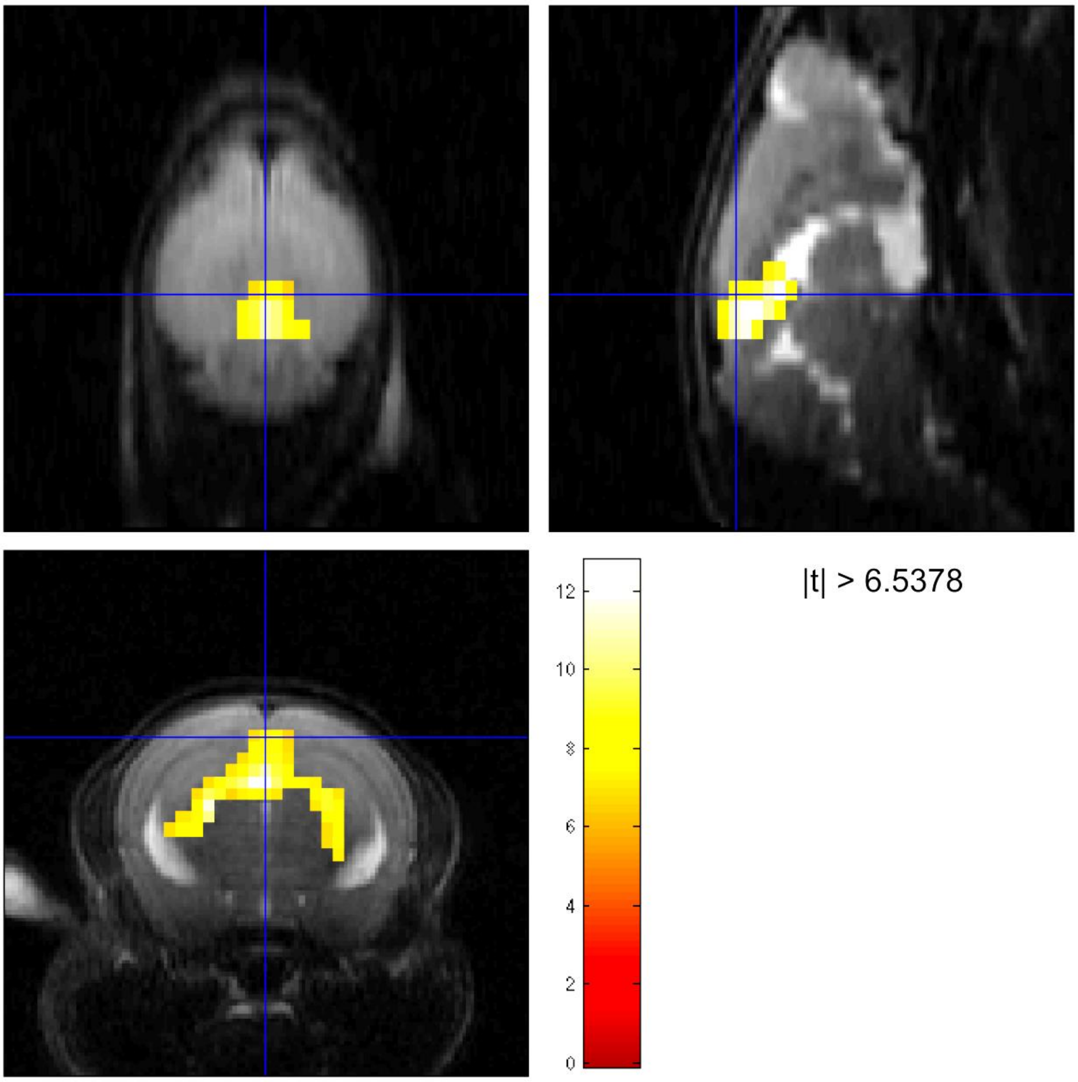

Figure 4.4. RFX analysis (two-tailed t-test, FWE p < 0.05, N = 14) statistical parametric map generated for the pooled 10 Hz data. The negative BOLD responses in the VISp are below the statistical threshold.

As the number of subjects was still relatively low, it was also possible to use permutation methods to generate maximum t-statistic distributions for choosing appropriate thresholds, using the SnPM13 toolbox [163] for RFX analysis. Whilst less common, this method makes fewer assumptions about the data, and performs a non-parametric permutation test at each and every voxel – and in general is more suitable to studies with few subjects. The permutation test itself assumes under the null hypothesis that subject effect size at each voxel is exchangeable and symmetrically distributed (exchangeability follows from independent sampling). There is therefore no longer a one-to-one mapping from t-statistic to p-value. The permutation testing was conducted using the results of the 1st level statistical parametric mapping analysis as inputs, using a variance smoothing kernel of twice the voxel size and the maximum possible permutations (16384). One criticism of permutation testing approaches is that they are computationally expensive. In this case the testing process took less than 4 minutes (2 minutes each for searching for both positive and negative effects, the equivalent of a two-tailed t-test). The distributions of the maximum t-statistic for both positive and negative effects are shown in Figure 4.5 and Figure 4.6 respectively.

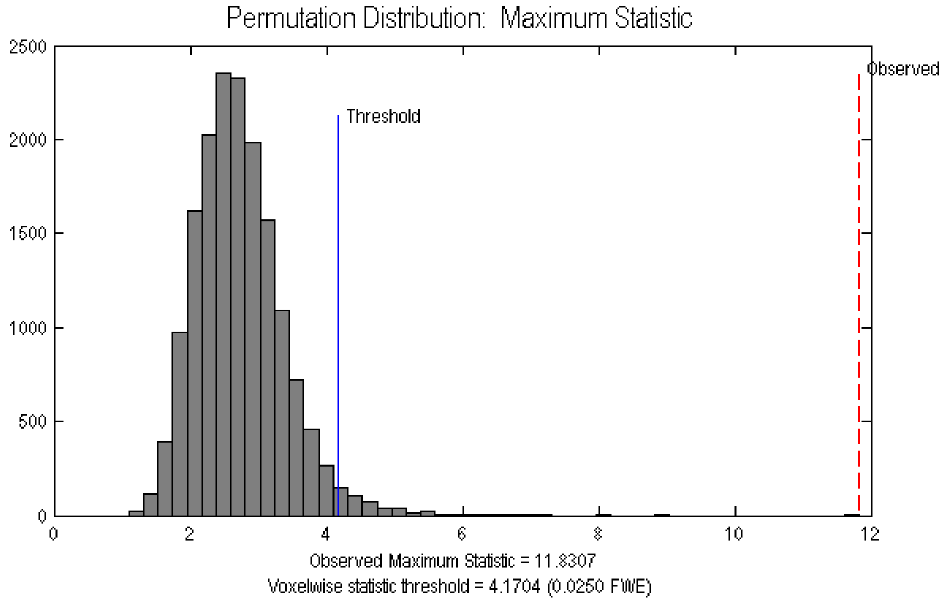

Figure 4.5. Permutation testing for positive BOLD effects – the distribution of the test statistic generated through over 16,000 permutations. The maximum statistic for the observed data is shown in red, and the threshold for a two-tailed test ($p < 0.05$) is shown in blue.

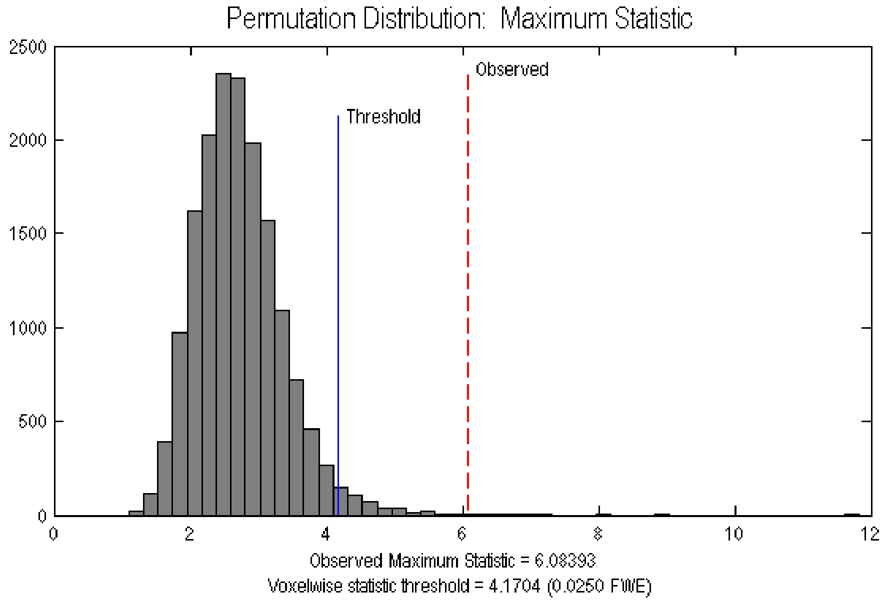

Figure 4.6. Permutation testing for negative BOLD effects – the distribution of the test statistic generated through over 16,000 permutations. The maximum statistic for the observed data is shown in red, and the threshold for a two-tailed test ($p < 0.05$) is shown in blue.

It is worth noting that usually when performing two-tailed tests, symmetry arguments are used when ‘splitting the alpha’ i.e. a two-tailed test at $p < 0.05$ is equivalent to two, one-tailed tests at $p < 0.025$. However, it follows from Boole’s inequality that this is still the case even when the distributions are not symmetric, as shown in equation (4-1):

$$\begin{aligned} &P(False\ Positive\ on\ test\ 1\ \cup False\ Positive\ on\ test\ 2) \\ &\quad \leq P(False\ Positive\ on\ test\ 1) \\ &\quad + P(False\ Positive\ on\ test\ 2) \end{aligned} \tag{4-1}$$

This is the same logic used for the Bonferroni correction for multiple comparisons. Therefore by setting the false positive rate for each test at 0.025 (for positive and negative effects respectively), the combined error rate must be the same or less than 0.05.

The resultant non-parametric map is shown in Figure 4.7.

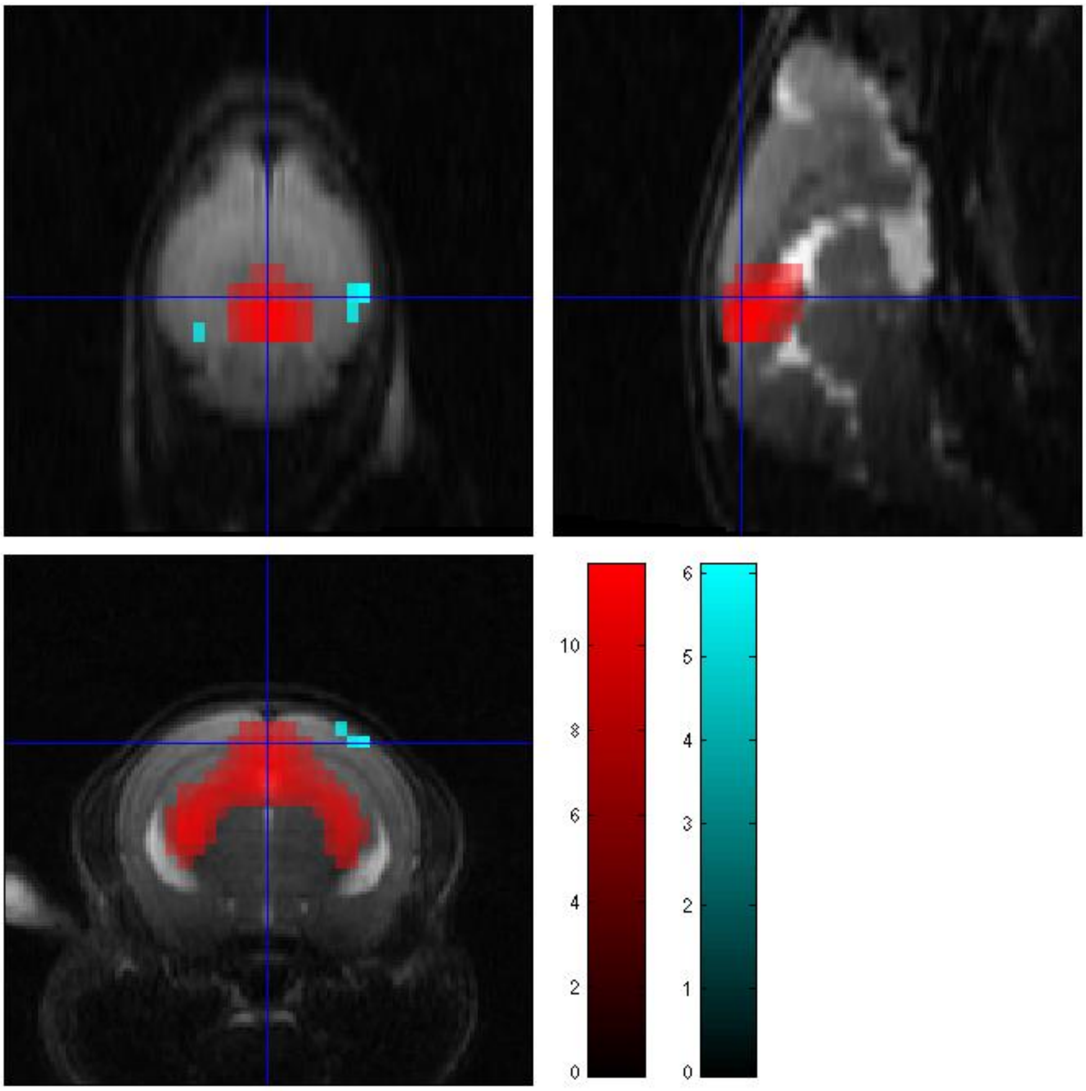

Figure 4.7. RFX effects analysis (two-tailed t-test, FWE p < 0.05, N = 14) statistical non-parametric map generated for the pooled 10 Hz data.

This map is thresholded at FWER $p < 0.05$ for a two-tailed test, and shows a few voxels above this threshold for both the positive and negative effects. This gives an idea of how stringent the FWER multiple comparisons correction is, particularly in relation to RFX analyses, and when looking for both positive and negative BOLD responses.

4.2.3 Discussion

As can be seen from the results, making formal population inferences from statistical parametric maps is extremely difficult given the issue of harsh correction for multiple comparisons. However, for simply mapping visual responses descriptively, FFX analyses are suitable, and can informally provide information (i.e. case study form) on the specificity of the BOLD response, as done by Wan et al. [123] and Rosa et al. [124].

4.3 Monocular stimulation

In this section, I aimed to implement a monocular stimulation paradigm for mouse fMRI, by using a custom-built single-loop RF surface coil in conjunction with an eye-piece for light delivery. The custom coil was originally built by Dr. Aaron Oliver-Taylor (UCL) for rat brain optogenetic experiments conducted at CABI, and the eye-piece was developed by both Dr. Sam Solomon (UCL) and myself. The use of this coil was tested in order to introduce more advanced visual stimuli into the scanner bore.

4.3.1 Introduction

As can be seen in Figure 3.32, the use of the two channel surface coil only allowed the use of a very simplistic visual stimulus – flashing light passed through a fibre optic cable, reflecting off the plastic underside of the surface coil. On the basis of the results achieved in section 3.3 and section 4.1, I decided to attempt to reduce the geometrical constraints of the problem, and attempt to use more complex stimuli. To this end, a different RF coil was tried – a custom built single-loop surface coil originally designed for optogenetic experiments in the rat brain conducted at CABI by Dr. Isabel Christie and Dr. Jack Wells [133]. This coil is shown in Figure 4.8.

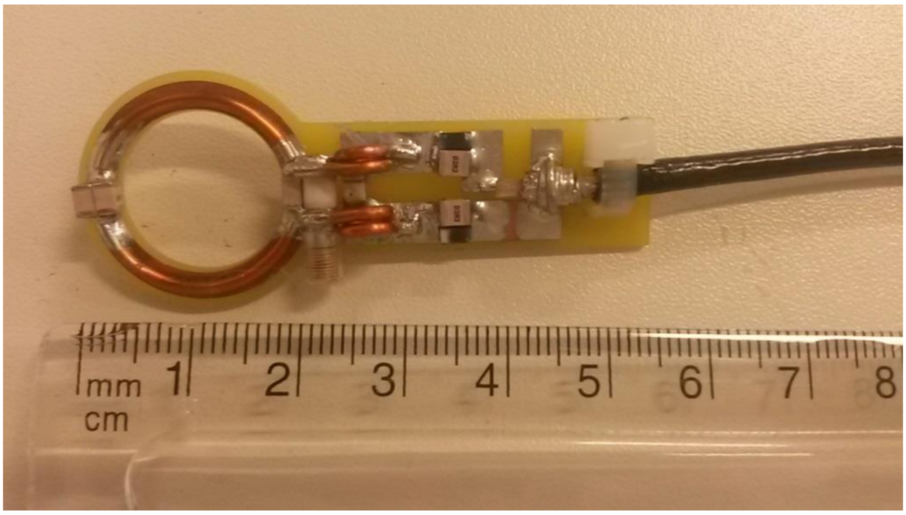

Figure 4.8. Single-loop RF surface coil, originally designed by Aaron Oliver-Taylor for rat brain optogenetic-fMRI experiments at CABI. The 2 cm diameter of the loop is an ideal size for mouse brain fMRI.

However, the use of this coil precluded reflection of a light source from a close surface as described in section 3.3. In order to deliver light directly to the eye, an eye-piece was designed using a clear plastic hemisphere, a rubber O-ring, plastic tubing, correction fluid and optical tape. One of these eye-pieces is shown in Figure 4.9.

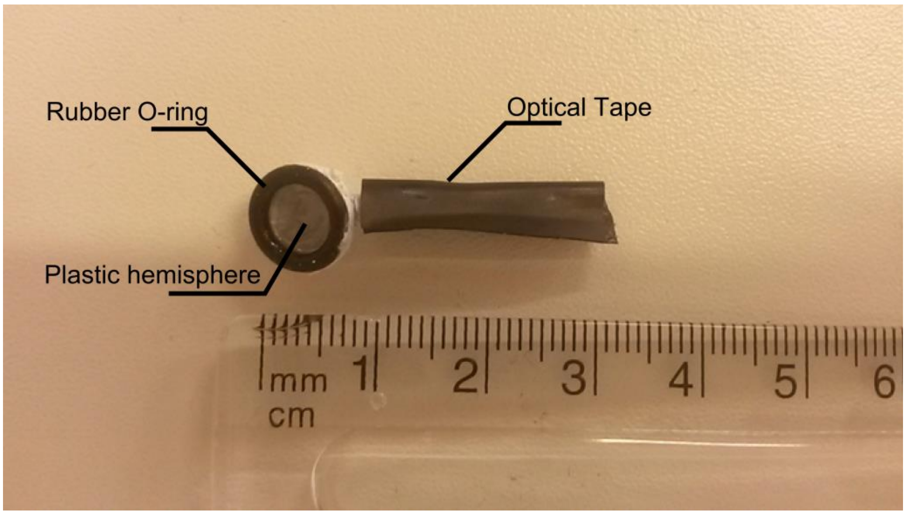

Figure 4.9. Eye-piece for monocular stimulation. The plastic hemisphere is filled with eye-gel, and the optical tape covers a plastic tube that will take a stripped fibre optic cable as input.

This experiment had two aims: to investigate the use of the single-loop coil for fMRI data acquisition, and to attempt to record a reliable BOLD response to monocular visual stimulation. Given that the retinas have stronger contralateral projections (i.e. the right visual field, mostly sampled with the right eye, mostly projects to the left hemisphere), it was expected that the spatial pattern of the BOLD responses would be asymmetric, and stronger on the contralateral side. This experiment also aimed to provide a stepping stone to delivering more complicated stimuli which could be more relevant to human fMRI studies and invasive measurements of mouse brain function.

4.3.2 Methods

These methods are broadly similar to those used in section 4.1.2.

Animals

A single female C57BL/6 mouse weighing 20.5g was used in this experiment, and the same anaesthesia protocol described in section 3.3.2 was used. This protocol produced a stable respiratory rate of 147 ± 12 breaths per minute. Eye gel was used to prevent drying of the corneas, and ear bars were used with analgesic cream to minimise head motion. Core body temperature was maintained at 37.1 ± 0.3 °C.

MRI methods

All MRI experiments were performed on a 9.4T VNMRS horizontal bore MRI scanner (Agilent Inc., Palo Alto, CA) with an Agilent 205/120HD gradient set. As described in section 4.3, a custom-built single loop surface coil was used for both RF transmission and reception. VNMRJ 3.1 software was used for image acquisition and reconstruction.

An anatomical reference scan was taken using a Fast Spin Echo sequence, and functional data acquired using GE-EPI, with the same parameters as detailed in section 3.3.2 (four interleaved snapshots). Shimming was completed as previously described, and the line-width (FWHM) within this shim voxel was 44 Hz.

Visual stimulation

Stimulation timings were triggered from the beginning of the EPI sequence using a POWER1401 control system (CED Ltd., UK) with Spike2 software. The stimulus consisted of a cold white LED light (Thor Labs) transmitted into the scanner bore using a fibre optic cable, and flashed at a frequency of 2 Hz during activation. The use of the LED over the laser used in section 4.1 was decided to be preferable as it could be used with analogue inputs, allowing graded intensities to be used. Two eye-pieces as described in section 4.3.1 were used for monocular stimulation – each with their own labelled fibre optic cable reaching from the eye to outside the scan room. The LED was connected to the required cable for stimulating either the left or right eye only for a given run. Seven fMRI runs were conducted for each condition (left eye stimulation or right eye stimulation) for a total of 14 runs, with three activation periods per run.

Data analysis

Data processing and analysis was conducted in a similar fashion to sections 3.3.2 and 4.1.

Region-of-interest (ROI) analysis was conducted by using atlas labels to extract timecourses using MarsBaR, to avoid circularity [125]. The labels chosen for timecourse extraction were the LGd, SCs and VISp, which correspond to the dorsal lateral geniculate nucleus, the sensory areas of the superior colliculus and the primary visual area. As monocular stimulation was used, it was necessary to divide the ROIs into left and right hemispheres. This was done in the matrix space of the Allen MBA, and verified by visual inspection. As described in section 3.3, voxel timecourses were normalised and high-pass filtered before averaging. BOLD contrast was calculated by subtracting the mean preceding baseline value from the mean BOLD value from each stimulus epoch.

For statistical parametric mapping, a 1st level FFX GLM analysis was conducted for the single subject. Voxels were only analysed if they were included in a brain mask manually generated from the MRI template image. The SPM canonical HRF (double-gamma function) was convolved with the stimulus profile as the explanatory model. The default SPM options of grand mean scaling and auto-correlation modelling were used, with a high-pass filter of 128 seconds. A one-tailed t-test was then performed on a voxel by voxel basis to test the null hypothesis that the BOLD signal is not explained by the explanatory model. All statistical parametric maps shown were corrected for multiple comparisons using a FWER ($p < 0.05$) threshold determined by random field theory using SPM12 unless otherwise stated. No cluster thresholding was used. Motion parameter estimates for each run were used as nuisance regressors in the GLM.

4.3.3 Results

Given the use of a different RF coil for both signal transmission and reception in this experiment, there was a concern that *in vivo* image acquisition would be adversely affected. Representative images are shown below in Figure 4.10, showing the quality of the structural image, the mouse visual system ROIs, GE-EPI data and the registration into the Allen MBA space.

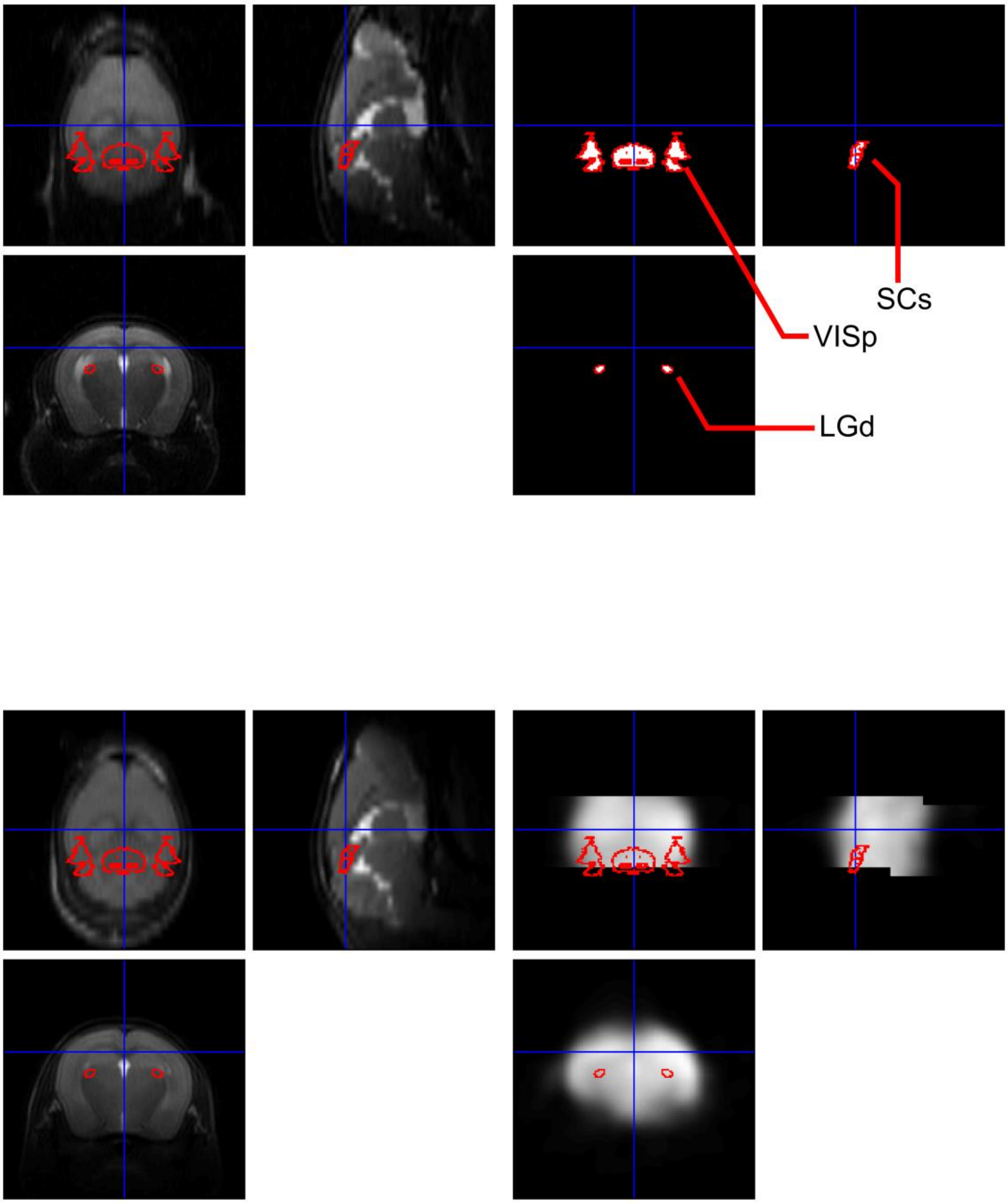

Figure 4.10. Cross-sectional views evaluating registration quality and showing the mouse visual regions. Clockwise from top-left: The MRI template (in AMBA space) used as the registration target, the visual system ROIs (bilateral), the registered structural image, and the spatially normalised (and processed) GE-EPI data. Contours of the visual system ROIs are overlaid on all the images to aid visual inspection.

Some signal drop-out can be seen in the anatomical reference image, particularly in the brain stem. It does not appear to have affected the registration however.

Mean BOLD responses from each fMRI run and their average signal is plotted for each of the three regions in Figure 4.11.

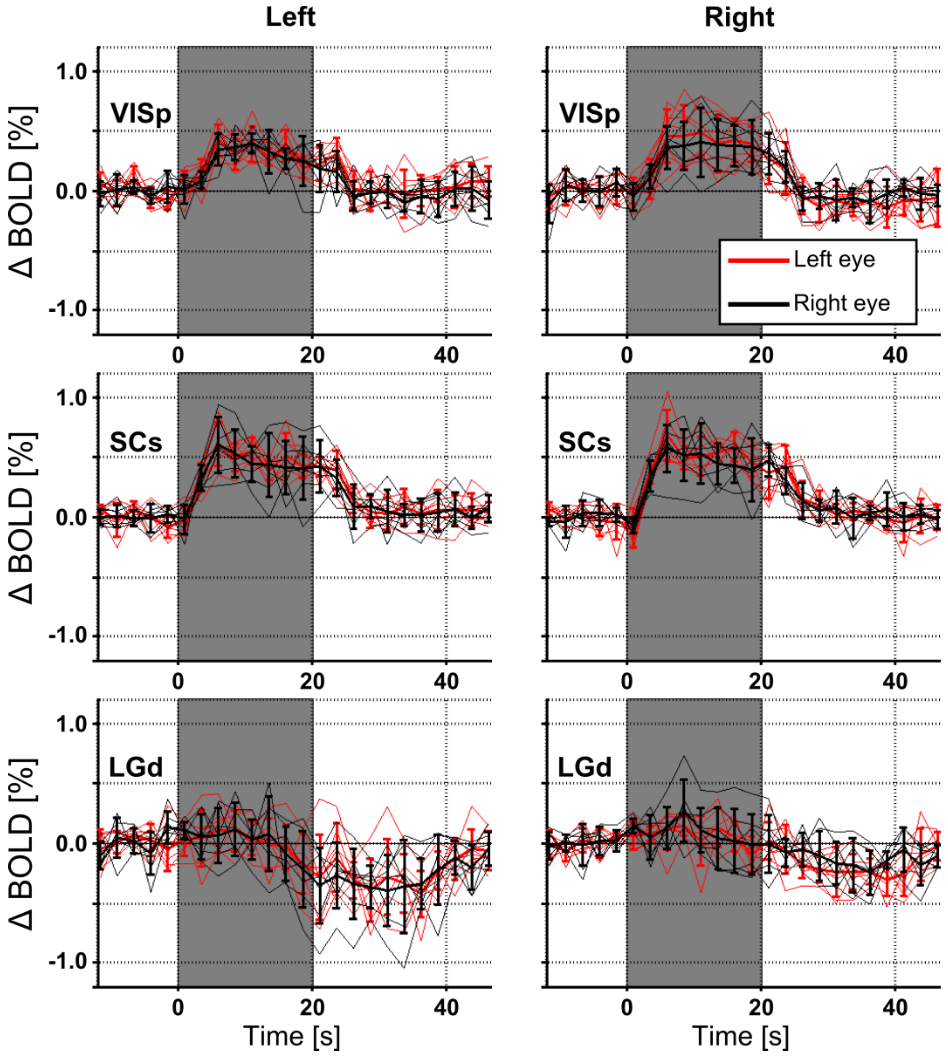

Figure 4.11. BOLD responses to monocular stimulation of the left and right eyes with cold white light at 2Hz flashing frequency in a single animal. Each column of panels matches the corresponding brain hemisphere. The mean timecourse for each run is plotted in the colour corresponding to which eye was stimulated (red for left eye, black for right eye), with the grand mean timecourse ± standard deviation plotted in bold.

The magnitude of the BOLD response in each of visual system ROIs does not appear to be markedly different across hemispheres. The lateral geniculate nuclei signal does not appear to show a correlation with the stimulus.

FFX single animal analysis maps are shown in Figure 4.12.

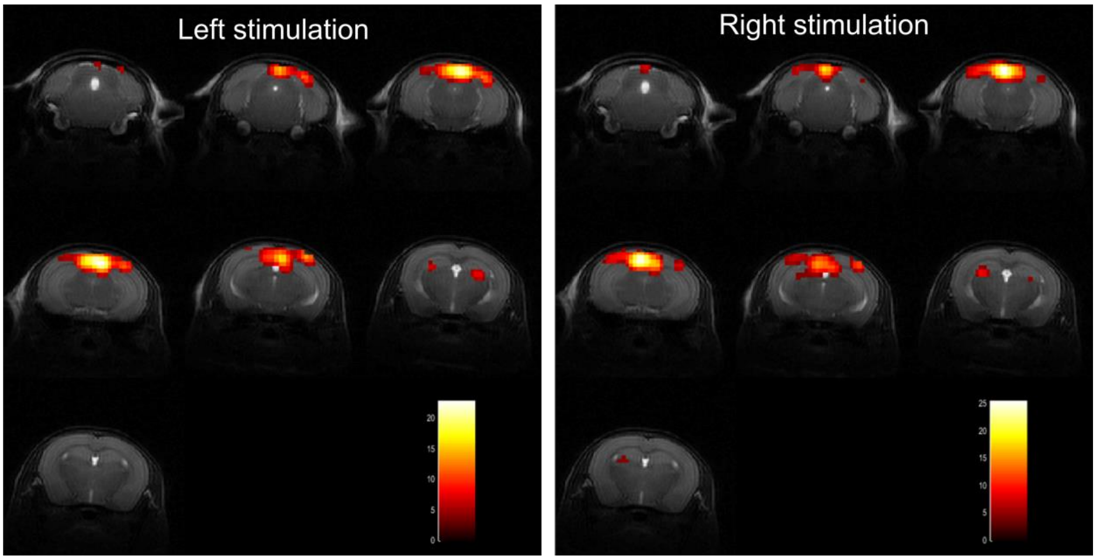

Figure 4.12. FFX statistical parametric maps (one-tailed t-test, FWE $p < 0.05$) overlaid on anatomical reference scan, for seven coronal slices (top-left slice is towards the mouse brain posterior). The BOLD response statistical map shows greater spatial extent of activation in the contralateral hemisphere.

The BOLD response statistical map shows a greater spatial extent of activation in the contralateral hemisphere. The statistically mapped BOLD responses in the lateral geniculate nuclei also appear to be weak in this subject relative to the superior colliculus, although there is some correlation with the stimulus profile.

4.3.4 Discussion

The quality of the GE-EPI acquired using the single-loop coil appears to be similar to that acquired with the two-channel surface coil used in sections 3.3 and 4.1. One concern before this experiment had been that coil sensitivity would decrease rapidly with distance. The average image SNR in the GE-EPI data for each region across all runs is given in Table 4.2, and is compared with corresponding image SNR measurements from the interleaved snapshot data described in section 3.3.

Table 4.2. Image SNR in GE-EPI data for each brain region (mean ± standard deviation, N subjects with n runs).Image SNR results are broadly comparable for the two coils.

Region of interest	Single-loop surface coil Image SNR (N = 1, n = 14)	Two-channel surface coil Image SNR (N = 6, n = 2)
LGd	108 ± 18	88 ± 17
SCs	107 ± 7	103 ± 19
VISp	79 ± 4	88 ± 36

There appears to be little difference in the magnitude of the ROI extracted BOLD responses between hemispheres of the brain measured in this subject, despite the appearance of asymmetry in the statistical map. Furthermore, the extracted LGd signal does not reliably correspond to either a positive or a negative haemodynamic response to the visual stimulus, with little correspondence to those measured in work described in sections 3.3 and 4.1.

4.3.5 Conclusion

This experiment aimed to implement monocular visual stimulation using a custom eye-piece and a single-loop surface coil in a single animal. Similar image SNR measurements were found using the single-loop coil despite the lack of a dedicated volume coil for RF signal transmission. Clear positive BOLD responses to the stimuli were measured in the VISp and SCs, however the extracted signal from the lateral geniculate nuclei signal in this animal did not bear a resemblance with the expected haemodynamic response. Statistical maps of the BOLD response showed preference for the contralateral side, as hypothesised, although this was not evident in the ROI analysis. Based on the results of this experiment, the single-loop coil can be used in conjunction with the eye-piece for monocular stimulation, although with this 2 Hz white light stimulus it may be that LGd responses are smaller.

4.4 Flash context experiment

In this section, I aimed to investigate the modulation of BOLD responses in the superior colliculus, as it is extremely important to mouse brain visual processing [84], and might prove a useful target for future studies using transgenic mice.

I describe a study I conducted using monocular stimulation and two different types of visual stimuli. This section is also included as part of a journal article titled “fMRI mapping of the visual system in the mouse brain with interleaved snapshot GE-EPI” (Niranjan et al. [94]).

4.4.1 Introduction

The superior colliculus plays a large part in mouse visual processing [84], and has been associated with heightened visual responses in a rat model of Parkinson’s Disease [164]. Approximately 70% of retinal ganglion cells project to the superficial layers of the SCs. Existing work suggests that most cells in the SCs respond to both ‘on’ or ‘off’ stimuli [84]. What is not clear is the relative strength of responses to large ‘on’ or ‘off’ stimuli across the neuronal population in the SCs, a question exploring the fundamental biology of how the superior colliculus operates. Indeed, the most numerous cell-type of the mouse retina, shows stronger ‘off’ than ‘on’ responses [165], and ‘off’ stimuli are thought to be particularly effective in both driving innate behavioural responses in mice [166] and driving neurons in the mouse superior colliculus [167]. It was therefore hypothesised that the SCs region is preferentially responsive to dark flashes against a bright background as opposed to light flashes against a dark background, and that dark flashes would therefore elicit stronger BOLD responses in the SCs. Building on section 4.3, monocular stimulation was used, and it was hypothesised that there would be stronger BOLD responses in the contralateral hemisphere for the LGd, SCs and VISp, in accordance with the dominance of contralateral retinal projections. Another aim of this study was to optimise visual stimulus design in order to maximise BOLD responses (and therefore sensitivity) in the superior colliculus for future studies.

4.4.2 Methods

These methods are broadly similar to those used in section 4.1.2.

Animals

12 female C57BL6/J mice weighing 21.0 ± 0.9 g were used to study the effect of flash context (a bright background with dark flashes vs a dark background with bright flashes). The same anaesthesia protocol as described in section 3.3.2 was used. This protocol produced a stable respiratory rate of 147 ± 23 breaths per minute. Eye gel was used to prevent drying of the corneas (applied to both the eyes and the eye-piece), and ear bars were used with analgesic cream to minimise head motion. Core body temperature was maintained at 37.0 ± 0.2 °C.

MRI methods

All MRI equipment and sequence parameters used are identical to section 4.3.2, with the exception of acquiring 130 volumes per run instead of 83. Typical line-width (FWHM) within the shim voxel after shimming was approximately 60 Hz.

Visual stimulation

Building on section 4.3, a cold white LED (Thor Labs) was used in conjunction with a custom-built eye-piece attached to the fibre optic cable for monocular stimulation. Stimulation timings were triggered from the beginning of the EPI sequence using a POWER1401 control system (CED Ltd., UK) with Spike2 software. For this experiment, only the right eye of each subject was stimulated, the other eye was kept closed. Two conditions were tested. Condition 1 used a dim but non-zero baseline intensity (20 mA) with bright flashes (1000 mA) with dark intervals (0 mA). Condition 2 used a bright baseline (980 mA) with dark flashes (0 mA) with bright intervals (1000 mA). The output power at the end of the fibre optic cable with the eye-piece for input current of 1000 mA was measured to be 0.15 mW. Pulse duration was 10 ms, and a 2 Hz pulse flashing frequency used during periods of activation. Both conditions used a block design of 40 seconds rest, 20 seconds activation alternately repeated five times. Each fMRI scan was conducted twice for each condition (in the order condition 1, condition 2, condition 1, condition 2), resulting in 10 activation periods per condition per subject.

Data analysis

Data analysis was conducted in a similar fashion to sections 4.1 and 4.3.

A two-way ANOVA was performed on BOLD contrast values in the LGd, SCs and VISp to test for differences between the two conditions, with ipsi/contra-lateral hemisphere and stimulus condition set as independent factors. Where interactions were not significant at the 5% level, main effects were reported. Post-hoc two-tailed paired t-tests were then performed where factor interactions were significant at the 5% level, in order to report simple main effects [168].

4.4.3 Results

The BOLD response to monocular stimulation was measured, and the BOLD responses to bright flashes against a dark background (condition 1) relative to dark flashes against a bright background (condition 2) were investigated in a cohort of 12 subjects using a cold white LED light source and a custom-built eye-piece. Mean BOLD responses in both hemispheres for the LGd, SCs and VISp are shown in Figure 4.13.

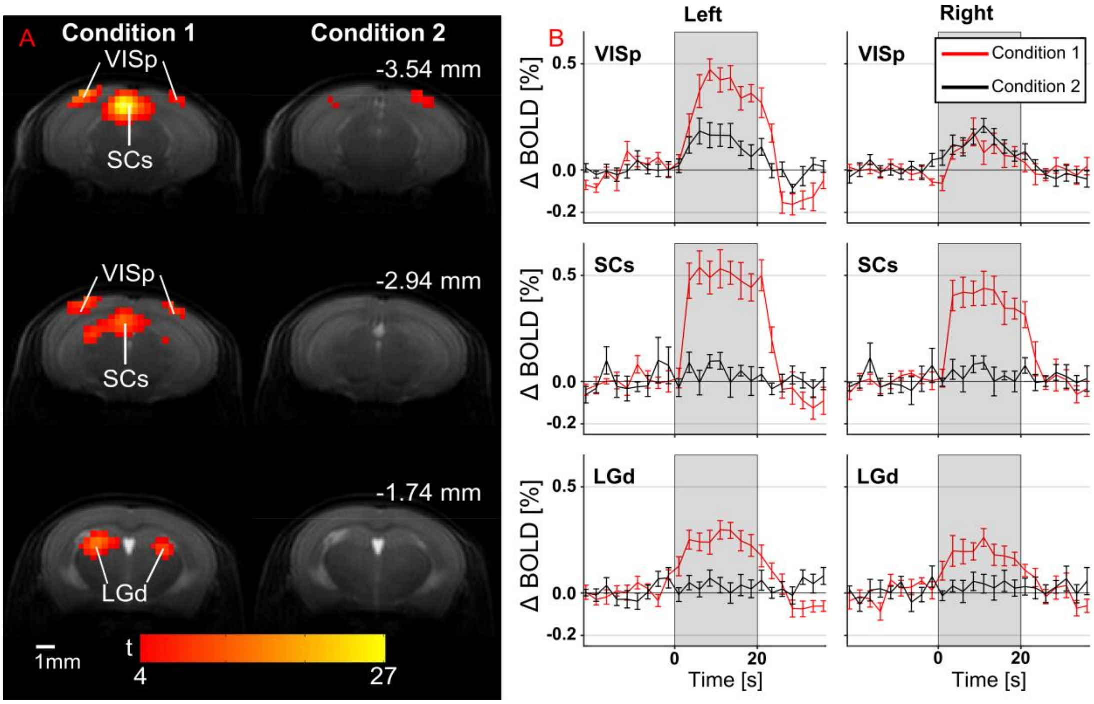

Figure 4.13. BOLD responses to monocular stimulation of the right eye with white light at 2Hz flashing frequency using bright flashes (condition 1) and dark flashes (condition 2). A) FFX statistical parametric maps overlaid on an anatomical reference scan (one-tailed t-test, FWE p < 0.05), for three coronal slices (distances measured from bregma). BOLD responses appear stronger in the contralateral hemisphere. B) BOLD percentage change against time for left and right VISp, SCs and LGd. Bright flashes against a dark background elicit stronger BOLD responses than dark flashes against a bright background.

The measurements of mean BOLD contrast for the LGd, SCs and VISp regions for each hemisphere and condition are plotted in Figure 4.14.

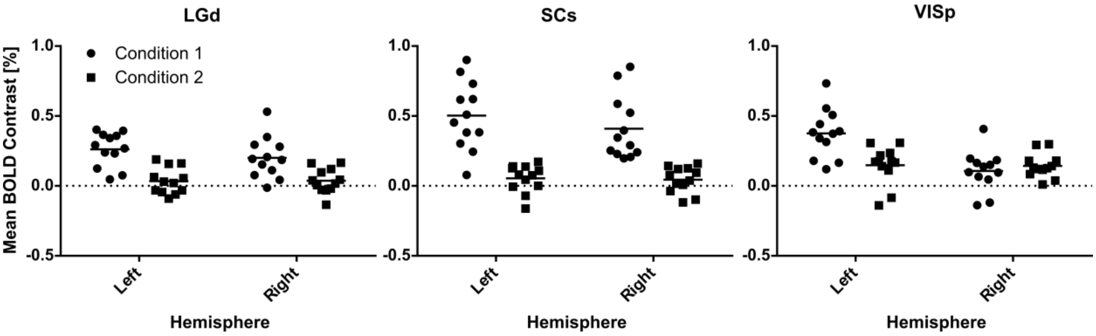

Figure 4.14. Mean BOLD contrasts for LGd, SCs and VISp regions for both stimulus conditions and brain hemispheres.

A two-way ANOVA was performed on BOLD contrasts for the LGd, SCs and VISp regions, with condition and hemisphere as factors (both repeated measures). These results are summarised in Table 4.3.

Table 4.3. Summary of two-way repeated measures ANOVA on BOLD contrasts in LGd, SCs and VISp regions, with stimulus condition and hemisphere as repeated factors.

ROI	Source of Variation	F (DFn = 1, DFd = 11)	p-value
LGd	Hemisphere Factor	1.404	0.2611
	Condition Factor	28.43	0.0002
	Interaction Hemisphere x Condition	1.722	0.2161
SCs	Hemisphere Factor	5.470	0.0393
	Condition Factor	33.88	0.0001
	Interaction Hemisphere x Condition	5.130	0.0447
VISp	Hemisphere Factor	10.72	0.0074
	Condition Factor	3.441	0.0906
	Interaction Hemisphere x Condition	11.43	0.0061

The interaction between hemisphere and condition is significant at the 5% level in both the SCs and VISp regions. In the LGd this interaction is not significant, and therefore it is reasonable to directly report a significant main effect of condition on BOLD contrast, but not hemisphere. As the interaction term was found to be significant in both the SCs and VISp, simple main effects for condition and hemisphere are reported in Table 4.4.

Table 4.4. Simple main effects in the SCs and VISp, examined using post-hoc two-tailed paired t-tests (df = 11, no correction for multiple comparisons).

ROI	Factor	Post-hoc paired t-test	Mean Difference C [Δ% BOLD Contrast]	95% Confidence Interval for C	t-statistic	p-value
SCs	Contra	Con 1 - Con 2	0.4493	[0.2898 0.6088]	6.201	0.00007
	Ipsi	Con 1 - Con 2	0.3648	[0.2057 0.5239]	5.046	0.00037
	Con 1	Contra - Ipsi	0.0941	[0.0088 0.1794]	2.428	0.03353
	Con 2	Contra - Ipsi	0.0095	[-0.0198 0.0388]	0.717	0.48832
VISp	Contra	Con 1 - Con 2	0.2266	[0.0726 0.3806]	3.238	0.00790
	Ipsi	Con 1 - Con 2	-0.0360	[-0.1643 0.0923]	0.618	0.54922
	Con 1	Contra - Ipsi	0.2678	[0.1205 0.4152]	4.000	0.00209
	Con 2	Contra - Ipsi	0.0053	[-0.0934 0.1040]	0.117	0.90881

By thresholding at α = 0.05, the results in Table 4.4 suggest there are significant differences in the following pairwise comparisons: between hemispheres during condition 1 in both the SCs and VISp; between conditions in the SCs and VISp in the contralateral hemisphere; between conditions in the ipsilateral SCs.

4.4.4 Discussion

This study aimed to elicit differential BOLD responses with a more complex stimulus paradigm than described in sections 4.1 and 4.3, in particular targeting the superior colliculus, a key brain region within the visual system. Monocular stimulation using the eye-piece and single-loop surface coil was conducted, and positive BOLD responses clearly measured in all three visual system ROIs for condition 1, the use of bright flashes against a dark background. A contralateral preference of the BOLD response was seen in terms of both the spatial pattern of the BOLD signal and BOLD contrast in SCs and VISp. For condition two, where dark flashes were presented against a bright background, BOLD responses were only detected in VISp.

The initial biological hypothesis was that SCs would respond preferentially to dark flashes against a bright background (condition 2) relative to light flashes against a dark background (condition 1), based on existing electrophysiological work in the literature [84, 165, 167]. The data from this fMRI experiment suggests the opposite – with condition 1 eliciting similar BOLD responses seen in data from experiments 1 and 2 (albeit with contralateral bias due to monocular stimulation), and condition 2 only inducing appreciable BOLD responses in VISp. The difference in BOLD responses across conditions is marked, and statistically significant effects at the 5% level were seen for both hemisphere and condition factors across the visual pathway. Monocular stimulation using condition 1 produced hemispheric differences in the BOLD response in VISp and SCs, but not in LGd. This appears consistent with the topography of these regions: in VISp and SCs, contra- and ipsilateral inputs are generally segregated with limited binocular overlap, whereas in LGd contralateral inputs approximately encase ipsilateral ones, in both hemispheres. At the spatial resolution used here, voxel size would not be small enough to resolve topography of LGd, and may mean that hemispheric difference in neuronal activity in LGd are unable to be detected by changes in BOLD signal. The greater overall responses to light flashes on a dim background, than dark flashes on a bright background, may reflect differences in the adaptation state of the retina. That BOLD responses to dark flashes are stronger in visual cortex may suggest that the visual cortex is more closely associated with the interpretation of dark temporal edges, relative to subcortical regions.

4.4.5 Conclusion

A monocular visual stimulus for mouse task-based fMRI was successfully used in a cohort of twelve subjects. The within-subject design provided strong evidence for the stimulus acting as the modulator of the BOLD responses. BOLD data acquired suggests the superior colliculus shows a preference for bright temporal edges over dark temporal edges, whereas the primary visual area does not. The use of a single-loop surface coil allowed reliable detection of BOLD responses across the visual system at the group level, and raised the possibility of using a more complex stimulus delivery system in future experiments, described in section 4.5.

4.5 Spatially varying stimuli

This section investigated the feasibility of delivering spatially varying visual stimuli for mouse fMRI, which in turn would allow greater comparison with visual studies of the mouse brain using alternative techniques, and with human fMRI studies using visual stimuli. The board with a controlling Arduino device was kindly provided by Dr. Sam Solomon (UCL).

4.5.1 Introduction

One of the long-standing goals of implementing visual task-based fMRI for mice is to be able to match stimuli presentation to work done in the fields of mouse electrophysiology and human fMRI, to enable superior validation and increased translational relevance. For example, stimuli used to investigate neuronal population responses with invasive measurements in the visual cortex [49], superior colliculus [84] and LGd [47] of the mouse brain mostly consist of drifting sinusoidal gratings, displayed on LCD/cathode ray tube monitors of dimensions approximately 40 cm by 40 cm placed approximately 20-40 cm away from the subject. This is simply not possible for pre-clinical fMRI, especially when using a 72 mm diameter volume coil for RF transmission as in section 4.1. The use of the single-loop coil for signal transmission and reception both increases the available volume inside the scanner bore for stimuli and allows greater flexibility in the positioning of said stimuli, although this does not overcome the greater technical challenge of introducing more complex visual displays into an MRI scanner with baseline field strength of 9.4T.

Previous rat visual fMRI studies [59, 63] used arrays of fibre optic cables to simulate moving edges and more advanced visual stimuli. This approach would be guaranteed to deliver visual stimuli that could vary in space, without interfering with the MRI acquisition. However, each cable would either require optical splitters or separate LED drivers, proving prohibitively expensive. In addition, the increase in spatial resolution of the stimuli would still be fairly limited.

The alternative attempted in the experiment described in this section is the use of an array of light emitting diodes (NeoPixel) (from now referred to as an LED board), operated by an Arduino Duo control unit. Further details of the set-up are discussed in section 4.5.2.

This experiment aimed to investigate the use of this LED board with the single-loop surface coil – to evaluate the quality of the recorded GE-EPI images, and see if visual BOLD responses similar to those recorded in previous sections were reproducible. The biggest concern was that electrical communication between the Arduino and the LED board would introduce RF interference within the faraday cage containing the MRI scanner, which in turn would introduce image artefacts.

Initially a phantom was used to test basic feasibility of using the LED board inside the bore at 9.4T. Based on the results of this phantom work, a cohort of animals was used for recording BOLD visual responses.

4.5.2 Methods

These methods are broadly similar to those used in section 4.4.2.

Phantom work

An agarose phantom (as used in section 3.1.4) was first used to investigate the use of the LED board in the MRI scanner, examining tSNR and image quality. Based on the results from the phantom, an *in vivo* experiment was conducted.

MRI methods

All MRI hardware and sequence parameters used were identical to section 4.4.2 Shimming was conducted using a GE 3D protocol [143, 144], with 1st order shims only (due to a hardware failure) optimised in a user defined shim voxel (approximately 5 x 8 x 9 mm^3) with voxel edges set at the brain edge. Typical line-width (FWHM) within this shim voxel was approximately 90 Hz.

Animals

14 female C57BL6/J mice weighing 20.0 ± 1.2 g were used. The same anaesthesia protocol described in section 3.3.2 was used. This protocol produced a stable respiratory rate of 146 ± 23 breaths per minute. Eye gel was used to prevent drying of the corneas, and ear bars were used with analgesic cream to minimise head motion. Core body temperature was maintained at 36.9 ± 0.3 °C.

Visual Stimulation with an LED array

A NeoPixel LED array (8 x 32 pixels, 320 mm x 80 mm x 2 mm) was used for visual stimulation, and is shown in Figure 4.15.

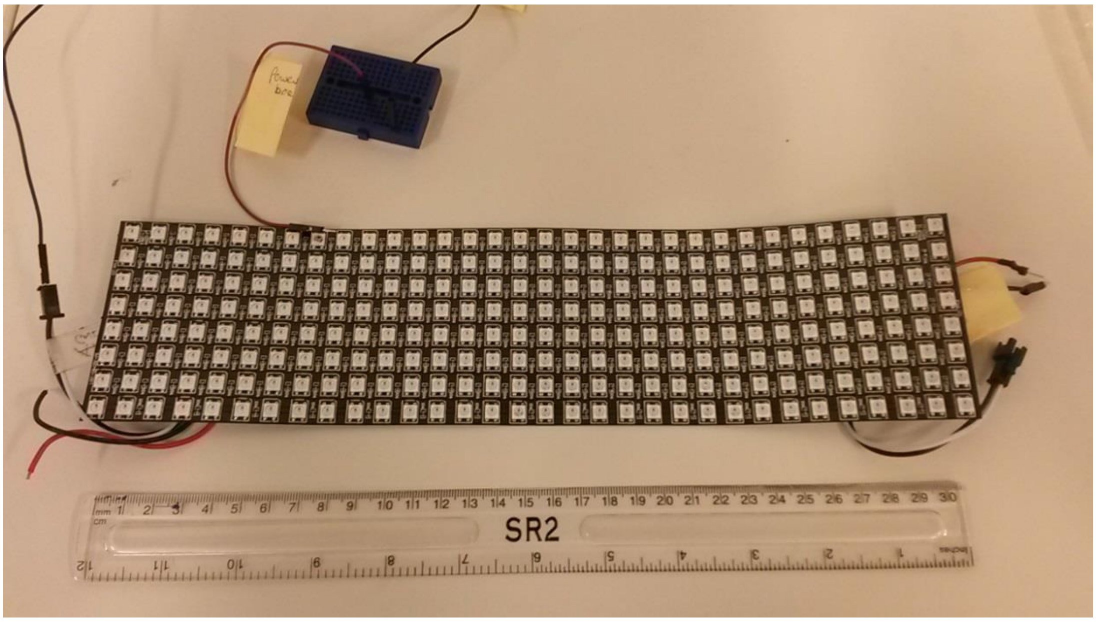

Figure 4.15. NeoPixel LED array. Each pixel contains a red, blue and green LED. Based on recommendations from the manufacturer, a maximum of 1/3 of the total number of LEDS were used at any one time, to keep the current flow below 5A.

In Figure 4.15, the board is pictured connected to a blue circuit breadboard, which in turn allowed wires (approximately 3 m long) to connect the LED board to a circuit breadboard and Arduino control unit outside the Faraday cage, shown in Figure 4.16.

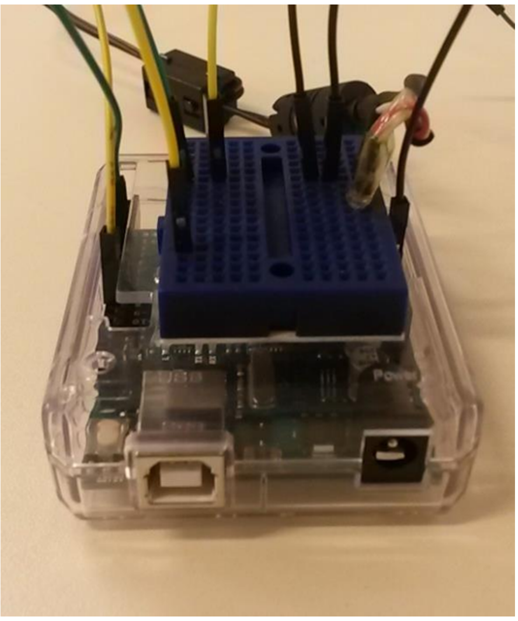

Figure 4.16. Arduino Duo control unit, with circuit breadboard attached. The control unit is placed outside the Faraday cage, and wires pass through the waveguide in order to power and control the LED board for visual stimulation.

The board has its own circuitry for processing inputs from the Arduino. The Arduino was paced outside the scan room and wires connecting the Arduino to the LED board passed through a waveguide in the faraday cage.

Once the mouse/phantom was placed in the cradle and ready to be loaded into the scanner, the board was curved over the cradle and held in place with tape, as shown in Figure 4.17.

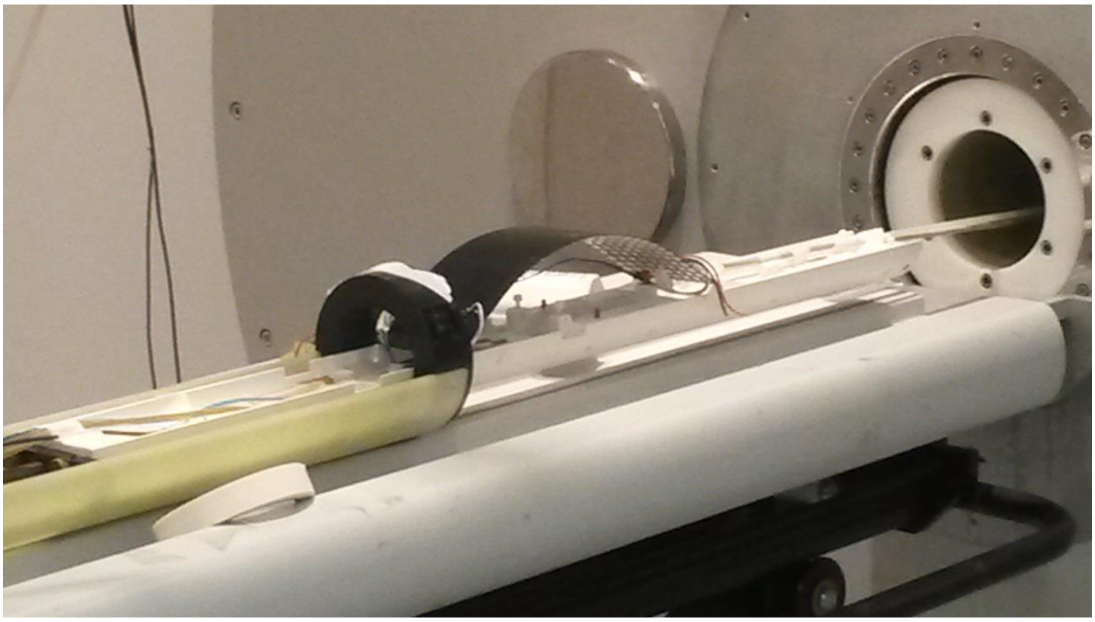

Figure 4.17. Placement of LED board over the mouse cradle, for visual stimulation.

The Arduino Duo control unit was programmed to take a TTL input to initiate the stimulus protocol. However, upon testing, a TTL pulse was not detectable by the control unit. Therefore the POWER1401 control system (CED Ltd., UK) with Spike2 software used in previous experiments was used to output a 5V analogue signal for duration of 0.5 seconds in order to trigger the Arduino program. The Spike configuration file was designed to trigger from the TTL pulse outputted from the MRI scanner upon a RF pulse. This achieved the desired effect of allowing the LED stimulus to be timed to the GE-EPI sequence. Full code for operating the LED board with the Arduino Duo unit is included in Appendix B. A block of LEDs (dimensions 5 rows x 8 columns) positioned approximately in front of each subject (corresponding to rows 5-10 from the edge of the board closest to the scanner in Figure 4.17) were flashed (with white light) at 2 Hz for five activation periods during each fMRI run. Two runs were conducted per animal.

Data analysis

Data processing was conducted in to the same way as described in sections 4.1, 4.3, and 4.4.

Region-of-interest (ROI) analysis was conducted by using atlas labels to extract timecourses using MarsBaR, to avoid circularity [125]. The labels chosen for timecourse extraction were the LGd, SCs and VISp (all bilateral), which correspond to the dorsal lateral geniculate nucleus, the sensory areas of the superior colliculus and the primary visual area. As described in section 3.3, voxel timecourses were normalised and high-pass filtered before averaging.

Statistical parametric mapping was conducted in the same way as section 4.3.2.

4.5.3 Results

Phantom pilot study

Results from the phantom experiment are included here. A comparison of GE-EPI images taken without the board, with the board but without power, and with the board with power are shown in Figure 4.18.

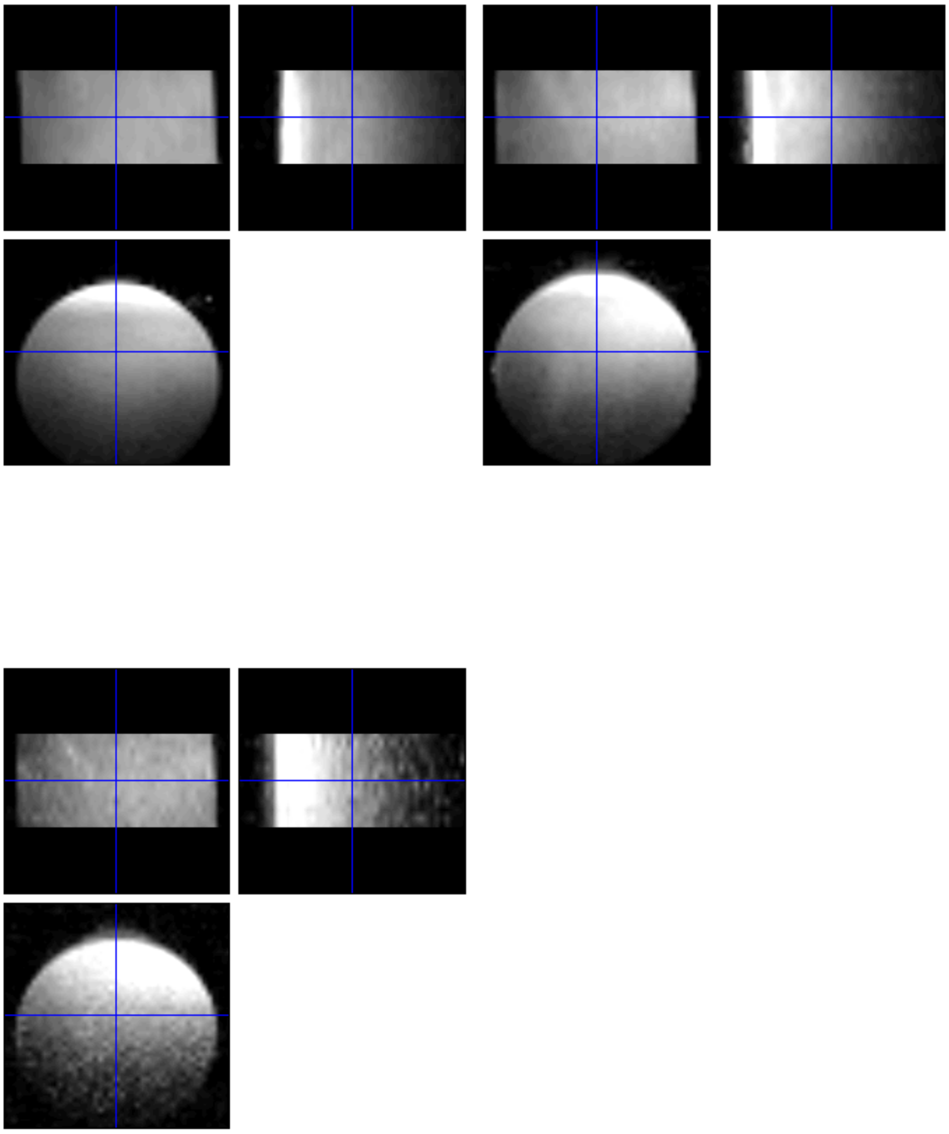

Figure 4.18. Cross sectional views of GE-EPI images of an agarose phantom. Clockwise from top-left: GE-EPI without LED board present; GE-EPI with LED board present but without power or flashing LEDs; GE-EPI with LED board whilst flashing.

As can be seen qualitatively from Figure 4.18, the introduction of the board to the scanner bore does not noticeably reduce the quality of the GE-EPI image. However, image quality drastically falls when the board is turned on and LEDs set to flash.

Temporal SNR measurements for the mean signal after typical preprocessing from a 0.5 mm diameter voxel placed at the crosshairs shown in Figure 4.18 are 467, 283 and 125 respectively. As was hypothesised, the introduction of the board reduces tSNR somewhat, but it is the use of the board circuitry during the GE-EPI acquisition that particularly corrupts the signal. However, at this level of tSNR, percentage signal changes of approximately 1% should be visible (although this does not take into account physiological noise, which was previously shown to dominate at 9.4T (section 3.3)). Based on this, I decided to progress with the *in vivo* study and to only plug the board power supply at the Arduino side of the Faraday cage after shimming and acquisition of the structural anatomical reference image.

In vivo GE-EPI

Subject 5 was excluded due to an artefact in the anatomical reference image. A representative subject's normalised GE-EPI data is shown in Figure 4.19.

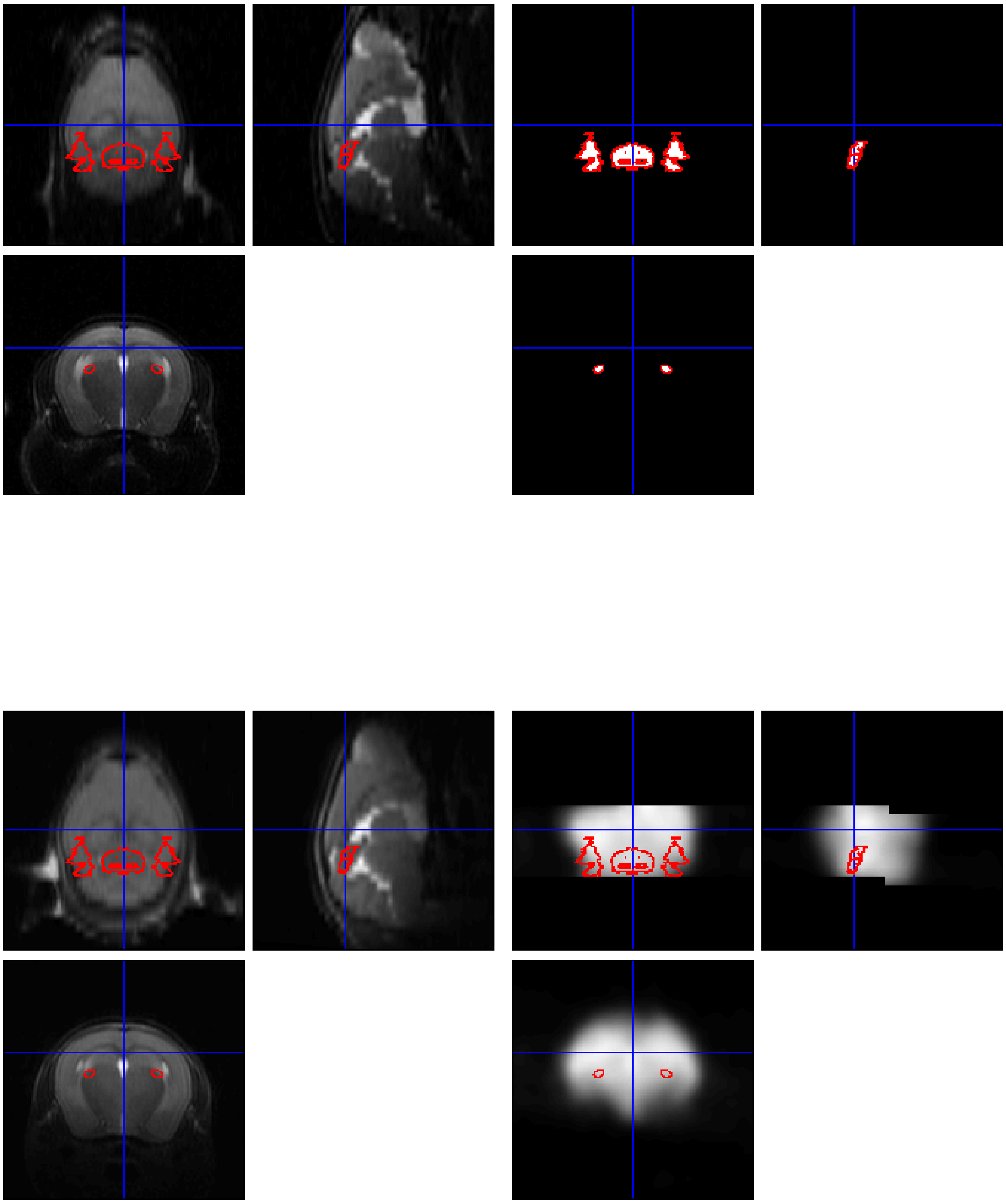

Figure 4.19. Cross-sectional views evaluating registration quality and spatial normalisation of the GE-EPI data in a single subject.Clockwise from top-left: The MRI template (in AMBA space)

used as the registration target, the visual system ROIs (bilateral), the registered structural image, and the spatially normalised (and processed) GE-EPI data. Contours of the visual system ROIs are overlaid on all the images to aid visual inspection.

Mean BOLD responses extracted from the three mouse visual system *a priori* structural ROIs are included in Figure 4.20.

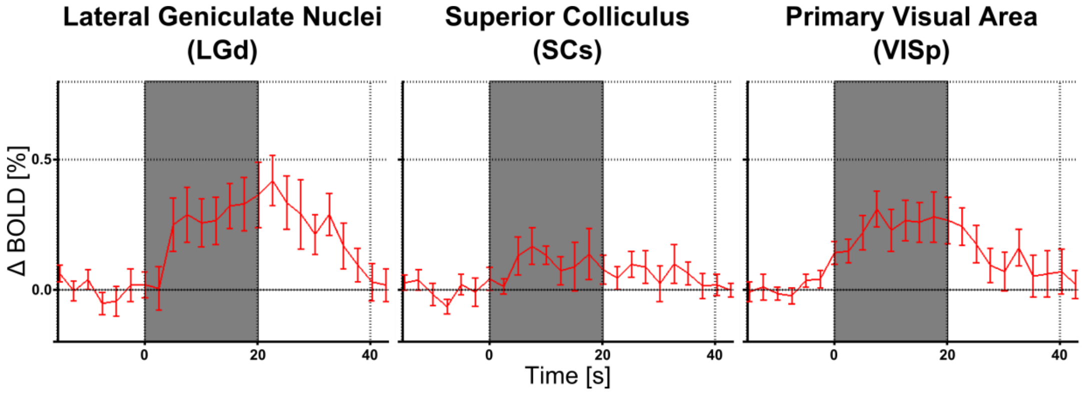

Figure 4.20. BOLD responses for LGd, SCs and VISp to the 2 Hz flashing stimulus from the LED Board.Some BOLD contrast in response to the stimulus, but overall the effect is small (~0.3% over baseline). On the assumption of correct spatial localisation, these BOLD responses suggest that this stimulus is inducing BOLD responses predominantly in LGd and VISp, but only weakly in superior colliculus.

The FFX statistical map is overlaid on the MRI template in Figure 4.21.

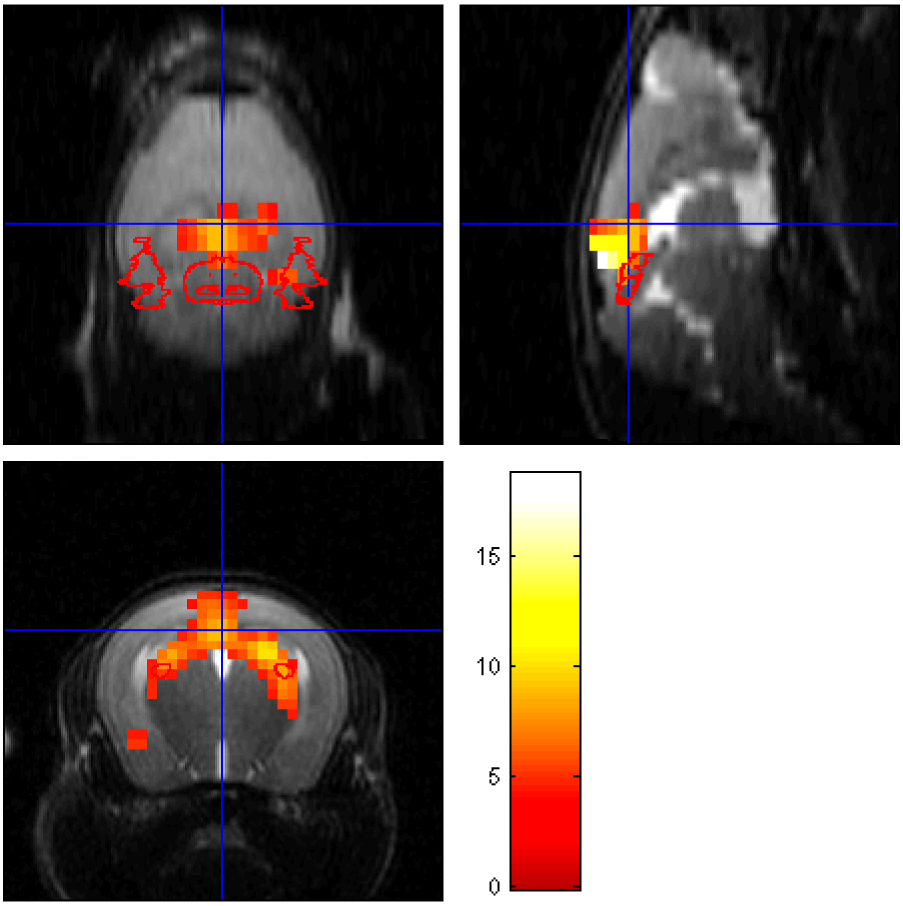

Figure 4.21. Fixed effects analysis (one-tailed t-test, FWE $p < 0.05$, N = 13, subject 5 excluded due to artefacts in structural image) statistical parametric map, overlaid on cross-sectional views of an MRI template image. Contours of the visual system ROIs are also overlaid.

4.5.4 Discussion

This experiment aimed to investigate the use of an LED array for visual stimulation task-based fMRI in the mouse brain. The reduction in tSNR in an agarose phantom was first considered, and from this it was decided to proceed to testing the LED array *in vivo* in a cohort of mice. The LED board whilst powered did introduce RF noise within the scanner bore, interfering with the acquired GE-EPI both in the phantom and *in vivo*. Whilst some BOLD signal responses to the stimulus could be seen using FFX GLM analysis on a voxel-by-voxel basis, attributing the BOLD responses to specific visual system ROIs proved difficult.

Interference from the visual stimuli source could be reduced by switching to an array of fibre optic cables, each with an independent LED source, which has been demonstrated previously in the rat [63]. By generating the light outside the Faraday cage and transmitting it via fibre optics, RF noise levels should be similar to those seen in previous visual stimulation experiments described in this thesis. Achieving a similar spatial stimulus resolution is in theory possible given the current geometrical constraints, but would be technically challenging to assemble and maintain.

Whilst the statistical map in Figure 4.21 has a similar form to previous results (e.g. see section 4.4), it appears to be distorted beyond the visual system ROIs, and the FFX t-scores are much lower than those seen in sections 4.1 and 4.4, indicating much poorer modelling of the BOLD signal. The strongest responding cluster is centred on the retrosplenial cortex (based on comparison with the Allen mouse brain atlas), which is predominantly associated with memory and navigation [169], rather than visual processing. It is more likely that this signal is actually from the neighbouring superior colliculus. The relatively low t-scores suggest low temporal contrast-to-noise ratio, which given results from the phantom study, is likely to be a combination of both physiological and hardware (the LED array). Combined, this noise is enough to have a severe impact on GLM results.

Upon visual inspection of the unregistered anatomical reference scans, it could be seen that many subjects had insufficient signal acquired in the brain stem region. This is concerning as the MRI template (acquired using the two-channel surface coil described in section 4.1) has significant signal in the brain stem, and could cause the spatial normalisation procedure to perform poorly. It is also therefore likely that BOLD timecourses extracted using AMBA labels are biased, and should be treated with caution.

As this was an initial experiment to investigate the use of the LED board, a simple flashing block stimulus was used, rather than sinusoidal gratings or moving edges. Based on this experiment, it is questionable that inferences could be made from BOLD responses to these more complex stimuli, as confounding factors mentioned above are likely to mask the effects of spatial tuning on the BOLD response. Further efforts to reduce noise from the LED board, optimise spatial normalisation are required, along with the use of 2nd order shimming, before future experiments using the LED array in conjunction with the single-loop surface coil.

4.5.5 Conclusion

In a bid to introduce spatially varying visual stimuli for mouse fMRI, an array of LEDs mounted on a flexible board was used to deliver a flashing light stimulus and tested both in an agarose phantom and *in vivo*. Whilst initial phantom results appeared reasonable, *in vivo* results from a cohort of 14 mice did not show BOLD responses reliably localised to the visual system. Further sequence development and noise reduction procedures would be prudent before attempting more complex visual stimuli with the LED array.

4.6 Chapter summary

In this chapter, the development of increasingly complex visual stimuli for mouse fMRI was discussed. Section 4.1 built heavily on chapter 3 and modulated the temporal frequency of a binocular stimulus, reproducing a negative BOLD response in the primary visual cortex at a 10 Hz flashing frequency, and successfully inducing positive BOLD responses in the visual cortex at lower frequencies. Section 4.3 introduced the use of a single-loop surface coil, which allowed the use of a custom eye-piece for monocular stimulation in a single animal, and statistical parametric maps showed asymmetric patterns of BOLD responses. Section 4.4 used this protocol for monocular stimulation and explored the effect of flash context on BOLD responses in the mouse visual system, showing differential responses in the mid-brain but conserved BOLD responses in primary visual cortex, suggesting differential processing of different visual stimuli. Finally, section 4.5 investigated the use of an LED array for visual stimulation, and noted the increased image noise, reduced tSNR and reduced BOLD contrast sensitivity from operating the LED board inside the MRI scanner bore. In the next chapter, the implementation of high-temporal resolution BOLD imaging in the mouse brain is described, with additional work on improved modelling of the haemodynamic response to visual stimuli.

5 Haemodynamic modelling

This chapter aims to better describe the haemodynamic response to visual stimuli in the mouse brain, in order to improve detection sensitivity. The recently described technique of line-scanning fMRI [170] was applied to the mouse brain for the first time, measuring the highest temporal resolution BOLD signals ever recorded in the mouse superior colliculus.

It was noted from previous studies that there was some mismatch between stimulus regressors using the canonical SPM haemodynamic response function and extracted BOLD signals from ROI analyses. However using structurally extracted timecourses to inform statistical mapping on the same dataset suffers from circular logic and was not done. Instead, to better estimate the HRF in a region known to exhibit strong BOLD responses, new data were acquired at 0.2s temporal resolution (relative to 2.5s in all other data described in this thesis). BOLD responses in the mouse superior colliculus were recorded using the technique of line-scanning fMRI, and are described in section 5.1. Then in section 5.2, the default parameters of the double-gamma SPM canonical haemodynamic response function are optimised relative to the BOLD responses measured in section 5.1. In section 5.3, a previous data set from section 4.2, is revisited with updated haemodynamic model parameters. Finally, the chapter is summarised in section 5.4. Work covered in this chapter is currently in preparation for publication.

5.1 Line scanning fMRI

In this section, I describe the development of line-scanning fMRI for high-temporal resolution BOLD recording in the mouse brain, and for the first time show results from the mouse superior colliculus. High-temporal resolution BOLD was deemed desirable to better characterise the mouse haemodynamic response to stimuli, and could be used in future work to match optical imaging spectroscopy data [43], or investigate layer specific responses in the cortex [170].

5.1.1 Introduction

As discussed in section 2.2.1, typical fMRI data from a GE-EPI sequence has three spatial dimensions and one temporal dimension, and is most easily thought of as a BOLD signal timecourse located at each point on a 3D grid. In sections 3.1.3 and 3.3, work was done to optimise this sequence for use with mouse fMRI, achieving a spatial resolution of (0.364 x 0.364 x 0.5) mm^3, with 12 slices covering the mouse visual system acquired every 2.5 seconds, BOLD contrast of approximately 1% relative to baseline, and temporal contrast-to-noise ratio of approximately 10.

One drawback to making inferences from this type of data is the relatively low temporal resolution compared to other neuroimaging modalities, such as optical imaging. Higher temporal resolution means improved characterisation of haemodynamic response functions, as the increased sampling rate allows higher frequency changes to be measured. In addition, higher temporal resolution would make event-related fMRI designs in the mouse brain statistically feasible.

One way to achieve higher temporal resolution is to consider sacrificing the generation of an image altogether, using a technique called line-scanning [170, 171]. Briefly, this method uses a modified gradient echo sequence (see section 2.1.4.1) without phase-encoding, but with saturation bands applied in order that a line of spins is excited. This allows a single line of k-space to be acquired, which can be done using sub-second TRs. The form of the output data has a one spatial and one temporal dimension – a BOLD timecourse located at each pixel along a line. With suitable placing of the line to intersect a brain region of interest, the BOLD signal there could be heavily temporally sampled relative to using a GE-EPI sequence.

This method has only been demonstrated in the published literature once before [170] in order to characterise BOLD responses in the barrel cortex of the rat due to opto-genetic stimulation, and has never been applied to the mouse brain. Some of the difficulties faced when conducting traditional fMRI with GE-EPI in mouse as opposed to rat are still applicable here, such as achieving suitable spatial resolution relative to the size of the mouse head, achieving good signal-to-noise, and maintaining suitable physiology. However, with the removal of phase encoding in image generation, spatial distortions do not need to be considered.

The superior colliculus was used for the implementation of this line-scanning technique, as it is close to the brain surface, and has natural contrast and is easily identified even in T_2^* weighted images. The visual cortex, whilst also being at the brain surface, is difficult to manually differentiate from surrounding cortical areas, and therefore it was believed that accurate spatial localisation would be difficult.

This section describes the attempt to implement the acquisition sequence on an Agilent 9.4T MRI scanner, and the demonstration of high temporal resolution BOLD timecourses in the mouse superior colliculus in response to a visual stimulus block design experiment.

5.1.2 Methods

Animals

A single female C57BL6/J mouse weighing 21.6 g was used. Anaesthesia was induced with isoflurane (2%) and maintained with medetomidine (0.4 mg/kg bolus, 0.8 mg/kg/hr infusion) through a subcutaneous injection to the flank. A gas mixture of 0.1 L/min of O_2 and 0.4 L/min of medical air (BOC Healthcare (Linde AG)) was continuously supplied during imaging. Respiratory rate was measured using a pressure sensitive pad, and core body temperature was measured using a rectal thermometer (SA Instruments). Core body temperature was maintained using a warm water pipe system. For the duration of imaging, respiration rate was in the range 130-160 breaths per minute, and temperature in the range 36.6-37.0 °C.

Visual stimulation

A white light LED (Thor Labs) was used for a block design paradigm, with non-zero constant baseline (10 seconds, 20 mA), 2Hz flashing as the stimulus period (20 seconds, 1000 mA), and a further 30 seconds of non-zero baseline, with 10 stimulus periods per line scan run. The pulse width during the flashing period was 0.25 s. The stimulus was delivered using a fibre optic cable as described in section 3.3.

MRI methods

For this work, the Agilent 9.4T MRI scanner was used in conjunction with the Agilent 205/120HD gradient set, the 72 mm volume coil for RF transmission and the 2 channel array surface coil (Rapid Biomedical) for signal reception. This set-up was chosen due to the requirement of saturation bands. For good signal saturation, $\boldsymbol{B}_1$ field homogeneity is extremely important. The use of the custom single-loop surface coil (as described in section 4.3) for both RF transmission and reception would likely not perform as well here due to poorer $\boldsymbol{B}_1$ field homogeneity.

The typical gradient echo sequence has been previously described in section 2.1.4.1, and will be referred to as a GEMS (Gradient Echo Multi Slice) sequence. In order to plan the line to be scanned, standard 2D GEMs data were acquired and shown later in this section. The following parameters were used: TR/TE = 200/18 ms, 1 average, matrix size 128x128, FOV = 35 mm x 35 mm, 1 slice (1 mm thick). For a T_1 in mouse brain of approximately 2000 ms at 9.4T [172], and a TR of 200 ms, the Ernst angle [103] (see section 2.1) was calculated to be approximately 25°, and so this was used as the flip angle.

Without the application of phase encoding, the acquired signal would have been integrated across what would have been the phase encoding direction.

However, by applying saturation bands in a particular geometric configuration, it was possible to ensure spatial localisation of the measured BOLD signal along a single line. The particular angle of rotation was chosen here to make the line of interest approximately perpendicular to the edge of the brain. The orientation of saturation bands in this way (with phase-encoding applied) is shown in Figure 5.1, with the result of their application in Figure 5.2. The rotation of the FOV to ensure that the frequency encoding-direction runs parallel to the line of interest is then shown in Figure 5.3. In addition the length of the FOV in the read-direction was reduced to 10 mm to increase spatial resolution, as shown in Figure 5.4.

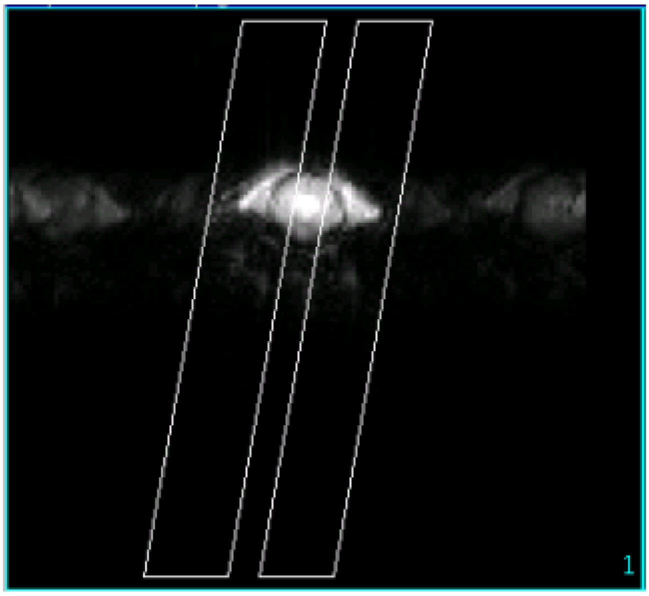

Figure 5.1. Example orientation of saturation bands for line scanning fMRI in mouse brain (visualised with single slice GEMS sequence, without saturation bands applied.) Nyquist ghosting is apparent in the image. The thickness of the line data to be acquired is given by the saturation band separation (2mm). The line of interest passes through the mouse superior colliculus.

Figure 5.2. Single slice GEMS data (with phase-encoding) with saturation bands applied.

Figure 5.3. Single slice GEMS data (with phase-encoding) with saturation bands applied and rotated so that frequency-encoding direction runs parallel to line-of-interest.

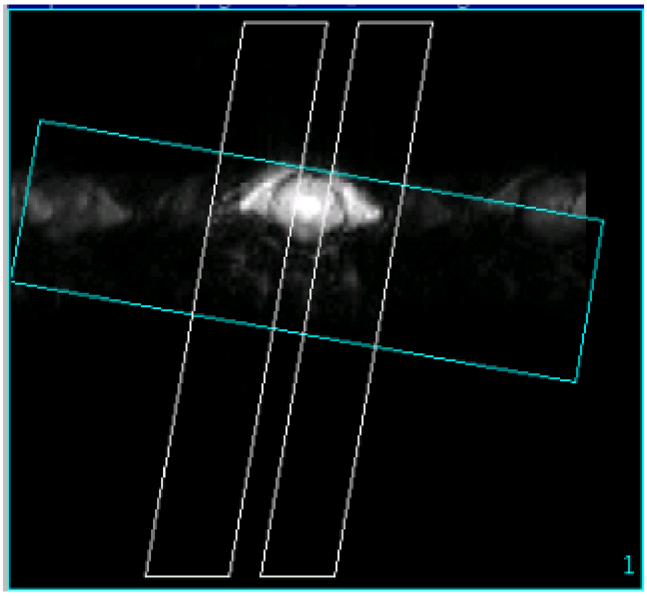

Figure 5.4. Single slice GEMS data (with phase-encoding) without saturation bands applied. The white boxes indicate the saturation band locations, and the blue box indicates the FOV for the line-scan, (10 mm in read-direction, 35 mm in phase-encode direction). However as phase-encoding is turned off for line-scanning, phase-encoding FOV has no meaning. The true FOV is the intersection of the blue box and the gap between the white saturation bands.

After the spatial localisation of the saturation bands and the FOV, phase encoding was turned off for the GEMS sequence. This was done by creating a copy of the GEMS pulse sequence code file, and setting the phase encoding gradient increment to zero for both the phase encode step and the rewind spoiler step. Doing so allowed the matrix size in the phase-encode direction to be set to 1 (without changing the phase encoding gradient increment, this is not possible on VNMRJ 3.1 software).

For this this implementation, the following parameters were used for the line scanning protocol: FOV read = 10 mm, matrix size = 128x1, TR/TE = 200/18 ms, flip angle = 25°, 1 average, 1 slice (1 mm thick). A total scan time of 600 seconds was chosen, with an initial 5 second burn-in period for magnetisation equilibrium to be reached (which was then discarded). For the single animal that was scanned in this experiment, it was possible to perform 8 runs of line scanning, yielding a total of N = 80 measurements of the BOLD response to the stimulus.

Image reconstruction

The acquired data is a matrix of k-space data, with dimensions given by $(n_x, n_{channels}, n_{timepoints})$ i.e. the number of pixels in the read-direction, the number of channels and the number of timepoints respectively. This data was appropriately Fourier transformed in MATLAB using code shown in Appendix C. The magnitude data from each coil was averaged to result in a matrix of dimensions given by $(n_x, n_{timepoints})$.

An alternative way of reconstructing data from multiple coils where the coil spatial sensitivity profiles are unknown, is to use the square root of the sum of squares [173]. This has been shown to asymptotically reach the theoretical maximum image SNR achievable where coil sensitivity profiles are known. This method is more robust to scenarios where coil sensitivity differs greatly at locations of interest in the image (although is vulnerable to increasing bias as the noise tends to zero). However, in this case, the line of interest that is sampled is approximately equidistant from each coil, and therefore using a simple averaging method for reconstruction is reasonable.

5.1.3 Analysis and results

The resultant line profile from the Fourier transform average over both coils and the first timepoint is plotted in Figure 5.5.

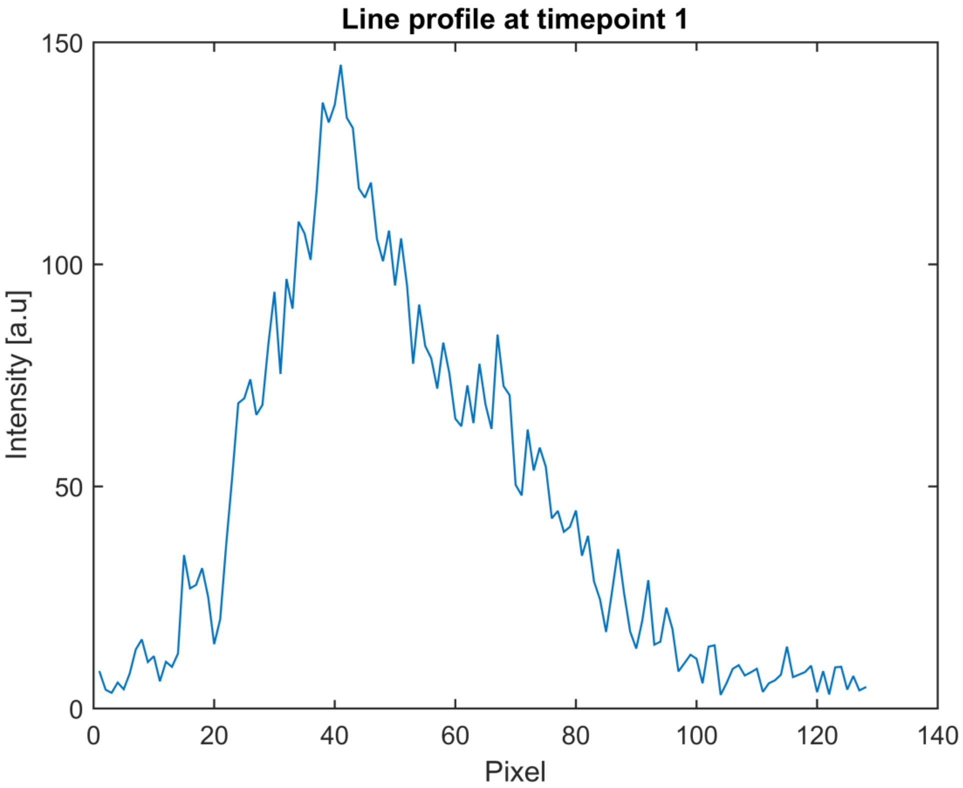

Figure 5.5. Line profile plot from first timepoint of first line scan data acquisition. FOV in read direction is 10 mm, and the superior colliculus is approximately covered by pixels 24-28.

It can be seen from that the upper most layer of the brain can be detected by the sharp intensity gradient that starts at pixel 20. Moving away from the surface coil (increasing x-coordinate after ~pixel 40) there is a gradual fall in intensity due to $\boldsymbol{B}_1$ field inhomogeneity. However, from the Allen Mouse Brain Atlas (MBA) [69], we can measure the thickness of the sensory layer of the superior colliculus (SCs) to be approximately 0.4 mm thick. For a pixel width of 0.078125 mm, this corresponds to a pixel region of interest of approximately five pixels. Based on the positioning of the FOV and with reference to the 2D GEMS localiser scans, it can reasonably be inferred that pixels 24-28 correspond to the region of interest.[2] The average SCs signal for a single line scan is plotted in Figure 5.6.

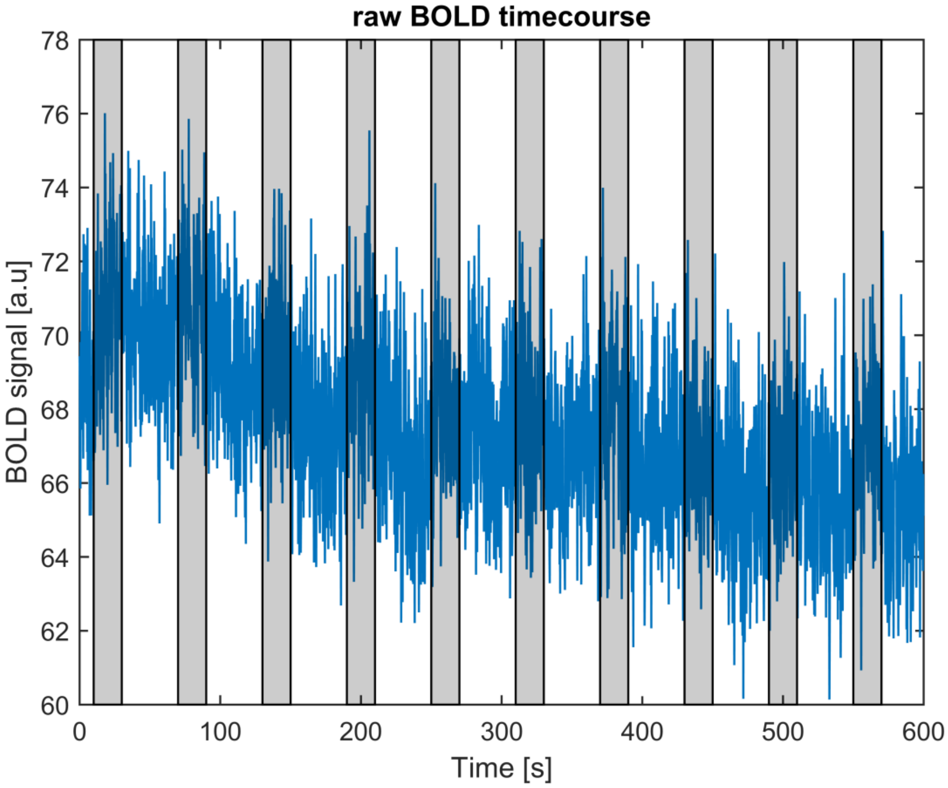

Figure 5.6. Plot of raw BOLD timecourse (TR = 200 ms) from superior colliculus against time (single run, averaged over 5 voxels). Grey regions indicate stimulus delivery periods.

Whilst there might appear to be some structure in the signal, the noise level appears to be high. As in previous sections, it would appear reasonable to filter and normalise the BOLD signal. A model signal generated using the SPM canonical haemodynamic response function is shown in Figure 5.7. The Fourier transform of the model signal in the temporal domain is then shown in Figure 5.8.

---

[2] It is in theory possible to use the 2D localiser scan to identify the superior colliculus, and apply the necessary geometric transform to identify the superior colliculus in the 1D data. However for simplicity (avoiding registration and resampling) the method described in the main text was used.

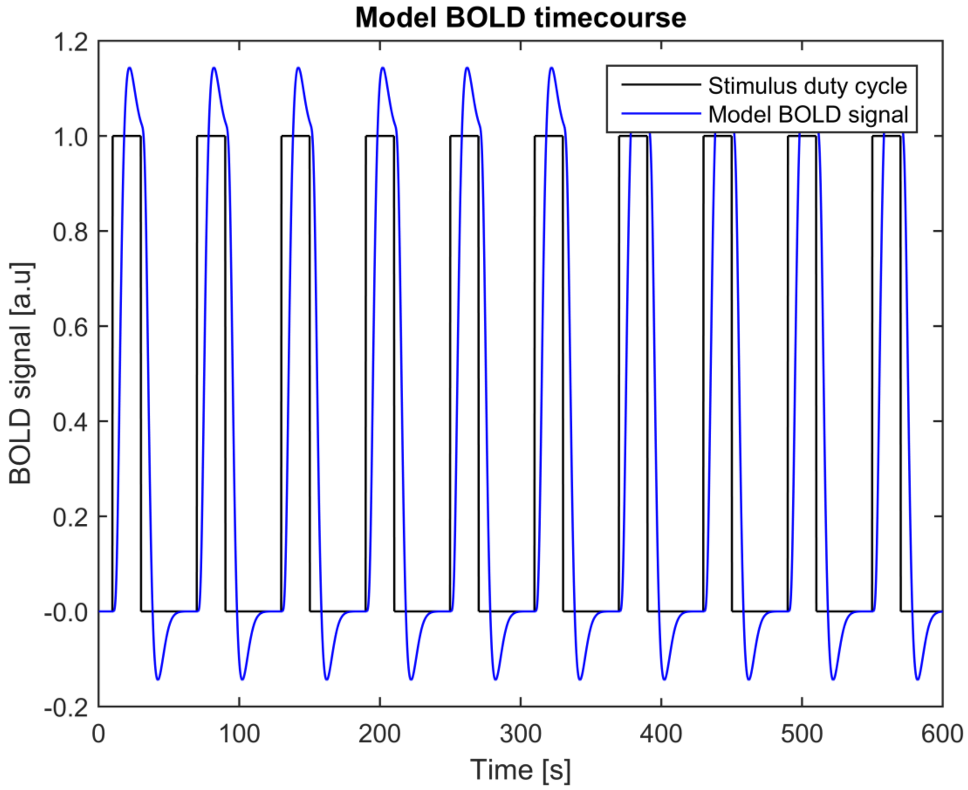

Figure 5.7. Simulated BOLD signal calculated using stimulus timings (duty cycle) convolved with the canonical SPM haemodynamic response function.This would be the standard stimulus regressor used in a single-subject FFX GLM analysis in SPM.

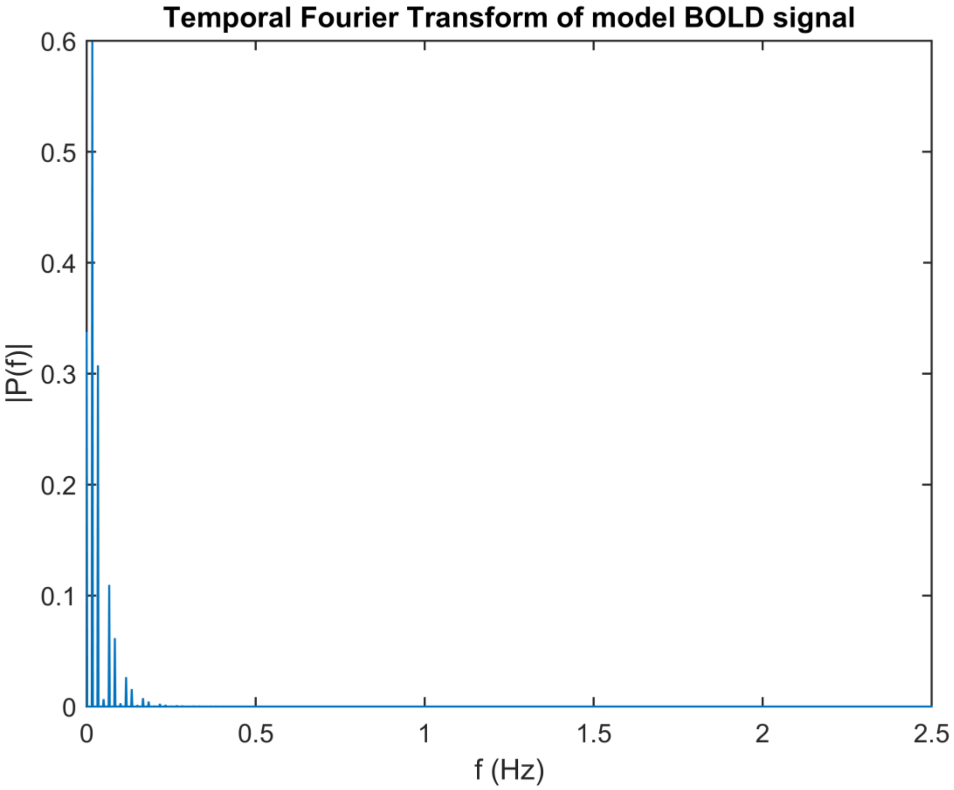

Figure 5.8. Power spectrum of model BOLD signal. Almost all of the signal information is stored in the frequency range 0.005-0.5 Hz.

Assuming the model BOLD signal is a reasonable approximation to the true BOLD signal, it is therefore sensible to high-pass filter the raw BOLD signal above 0.005 Hz. This can be done using a discrete cosine transform [120], and then normalising by the mean signal in the first baseline period (10 seconds, or 50 timepoints). Doing so on a per-voxel basis and then averaging over the region of interest, the SCs processed BOLD is plotted in Figure 5.9.

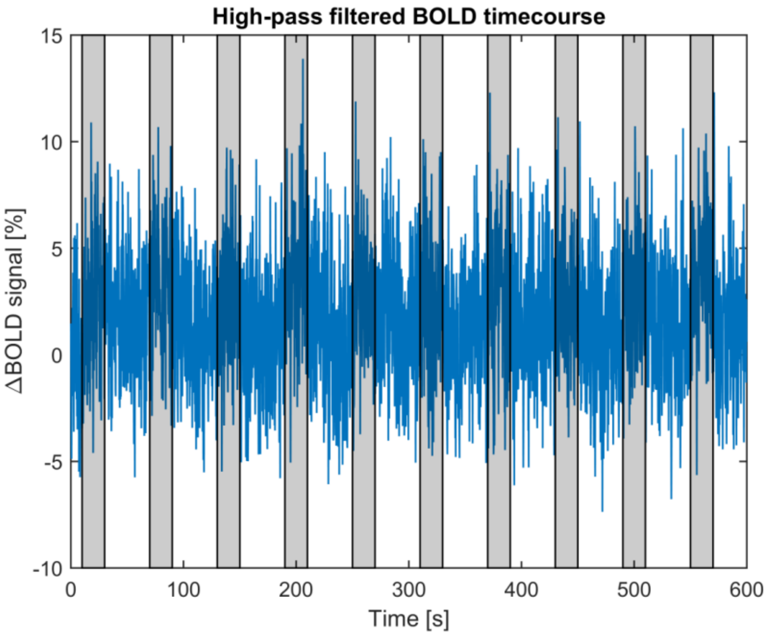

Figure 5.9. High-pass filtered and normalised BOLD timecourse for superior colliculus (single run). BOLD signal changes on the order of 4% can be seen, although the standard deviation of the baseline signal is approximately 3%.

Given the poor signal-to-noise ratio evident from a single run, the average across all eight runs is plotted in Figure 5.10.

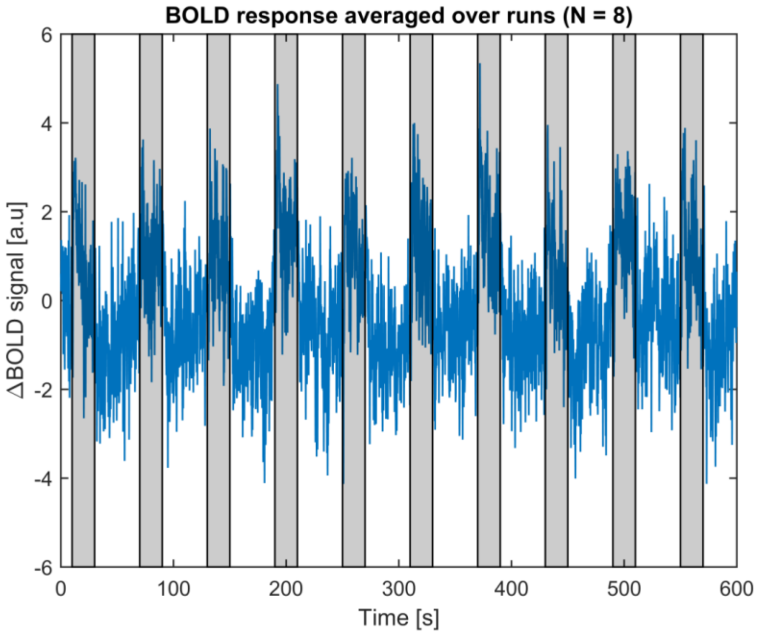

Figure 5.10. High-pass filtered and normalised BOLD timecourse for superior colliculus (averaged over eight runs). BOLD signal changes on the order of 4% can be seen, and the standard deviation of the baseline signal is approximately 1%.

It is possible to achieve further gains in signal-to-noise ratio by averaging over trials. In this case, it is sensible to normalise each trial BOLD response to each baseline period separately. The mean BOLD response for each run and the grand mean BOLD response in the superior colliculus are plotted in Figure 5.11.

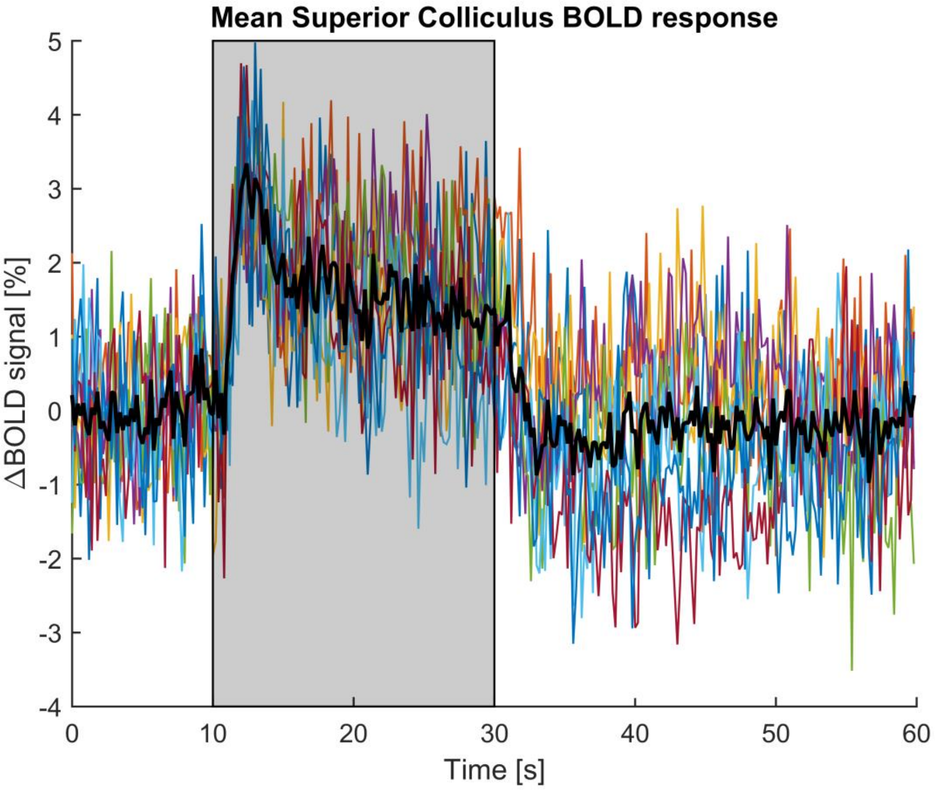

Figure 5.11. Mean superior colliculus BOLD response for each run (thin lines, 10 trials per run), and the grand mean BOLD response (thick black line, 8 runs). The grand mean BOLD response shows a temporal peak contrast-to-noise ratio of approximately 10.

The measured mean timecourse has a very similar shape to the superior colliculus BOLD response to flashing light reported in section 3.3 and chapter 4, which provides some confidence that this measurement is representative. For comparison, the equivalent data for a grey matter ROI of the same size and approximately same mean baseline intensity (voxels 64:68) is shown in Figure 5.12

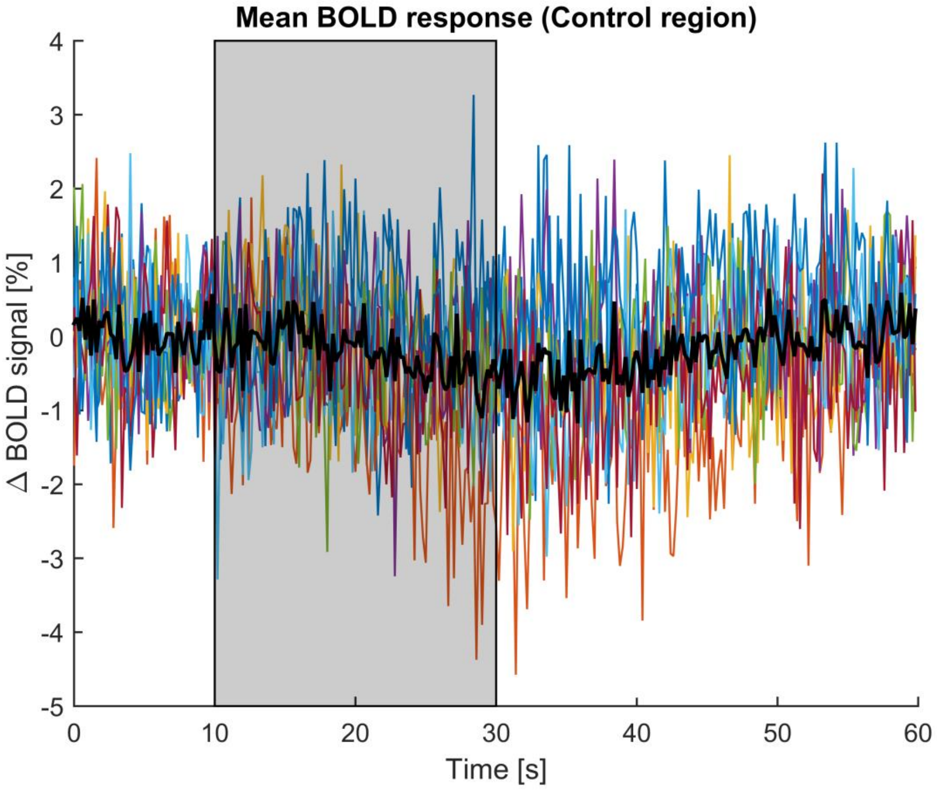

Figure 5.12. Mean control region BOLD response for each run (thin lines, 10 trials per run), and the grand mean BOLD response (thick black line, 8 runs). In this equivalent 5 voxel ROI placed in the grey matter (voxels 64-68), no functional response can be seen.

Once the data has been averaged over the 80 trials, the form of the haemodynamic response to the 2 Hz visual stimulus can clearly be seen in the superior colliculus (and not in the control region), at 0.2 ms temporal resolution. Examining the grand mean BOLD response, the peak BOLD contrast is approximately 3%, and the standard deviation of the baseline signal is approximately 0.3%, yielding a temporal contrast-to-noise ratio of approximately 10.

One way the averaged, normalised data set can be visualised across the field of view is through a voxel time plot, as shown in Figure 5.13.

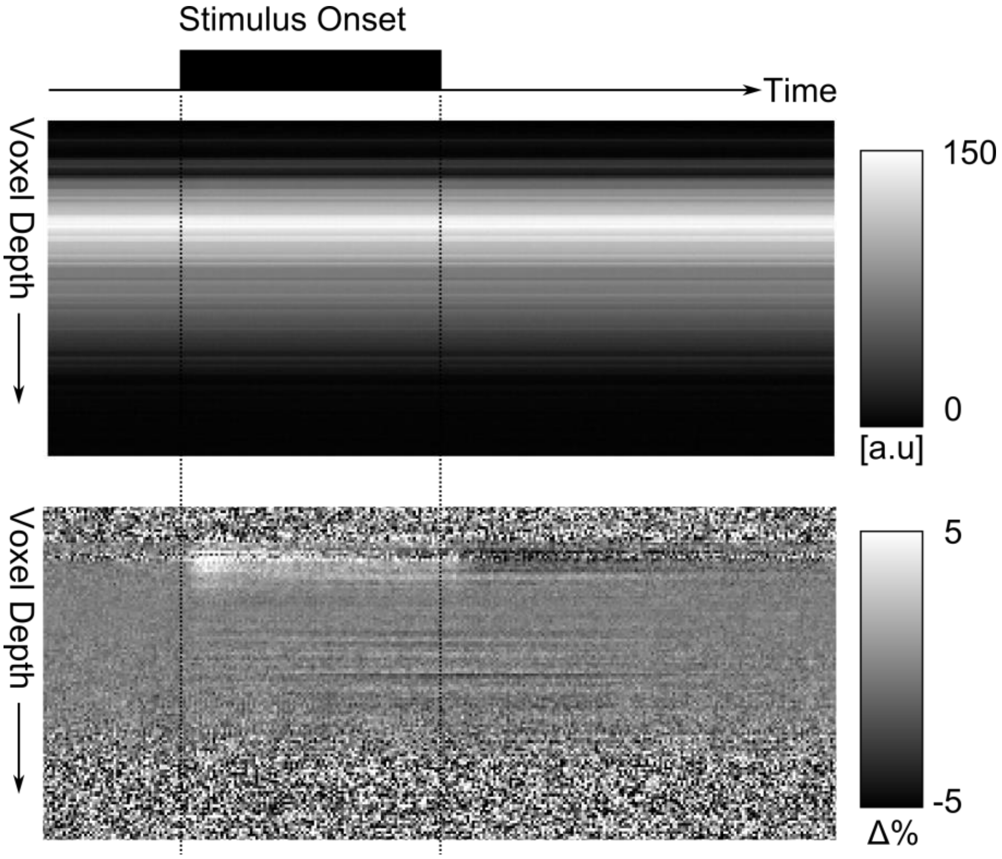

Figure 5.13. Voxel-time plot (line profiles averaged over activation periods and runs). The top panel is the raw magnitude data, and the bottom panel shows filtered and normalised data. The time range is 0-60 seconds, and the voxel depth range is 10 mm. The first column in panel one is the same line plot shown in Figure 5.5.

As was discussed earlier in section 5.1.3, the BOLD contrast due to the stimulus can be seen in the voxels corresponding to the superior colliculus. However, this type of plot should not be used to define the region of interest because of the risk of circular inference [125].

5.1.4 Discussion

This is the first application of line-scanning fMRI to the mouse brain, yielding the highest temporal resolution measurement of the BOLD response in the mouse superior colliculus ever recorded.

There are a number of limitations to this data. Due to time constraints, it was only possible to scan one animal with this protocol, and it would be useful to measure the variability of the grand mean BOLD response on an inter-animal basis. However, visual inspection of the basic shape show agreement with BOLD responses measured in superior colliculus in previous experiments (see sections 3.3 and 4.1). Furthermore, low-pass filtering or modelling of the auto-correlated noise has not been done, and doing this in a suitable way would likely increase the temporal contrast-to-noise ratio, at the cost of reducing the effective temporal resolution. Another issue is that the effects of motion are difficult to quantify, as without at least 2D data, image registration is not possible. All results reported here are dependent on the assumption of zero motion.

With the current data, the temporal contrast-to-noise ratio is about 10. This allows the following characteristics to be seen:

1. Baseline BOLD fluctuations
2. A steep rise in response to stimulus (< 1 second)
3. A levelling off but sustained signal greater than baseline for the duration of the stimulus block
4. A fall off in the BOLD response at the end of the stimulus block
5. A post-stimulus undershoot
6. Recovery to baseline.

Within this single subject, a total of 80 activation blocks were required to achieve a temporal contrast-to-noise ratio approximately equivalent to that achieved using GE-EPI (as described in section 3.3). It is probable that both physiological and hardware contribute to the noise in this experiment, and it may be possible for further optimisation of the line-scanning sequence to improve tCNR enough for event-related BOLD responses to be detected. Adaptation effects were not considered, and this would be an interesting area to investigate for future work.

Additional experiments could also use event-related designs – short duration stimuli (<2 seconds) which do not make assumptions on the convolution of the BOLD response with the stimulus train. Whilst detection in event-related designs is more difficult, estimating the shape of the HRF is likely to be more precise [4, 174].

There is currently no published data on mouse superior colliculus haemodynamic responses to stimuli. Much intrinsic optical imaging has focussed on the cortex [43, 87], due to poor depth penetration. The use of this technique in the visual cortex would be valuable, particularly to validate the work conducted by Sharp et al [43].

5.1.5 Conclusion

In a single animal and with approximately 80 minutes of functional imaging, the BOLD response in the superior colliculus was measured at high temporal resolution (200 ms) for a block design experiment using visual stimuli. In the next section, an improvement to the SPM canonical HRF is discussed.

5.2 Haemodynamic modelling

In this section, the default parameters of the SPM canonical haemodynamic response function used in previous sections for statistical parametric mapping are updated using non-linear optimisation, in order to better describe the measured BOLD response.

5.2.1 Introduction

In section 5.1, a high temporal resolution grand mean BOLD response to visual stimulus in the superior colliculus was measured using line scanning fMRI. This BOLD response can be compared to a model BOLD signal generated by convolving the stimulus duty cycle (a simplistic neuronal model, i.e. neuronal activity is directly correlated with stimulus delivery) with the SPM12 canonical haemodynamic response (double gamma function, default parameter values [175], shown in Figure 5.14.

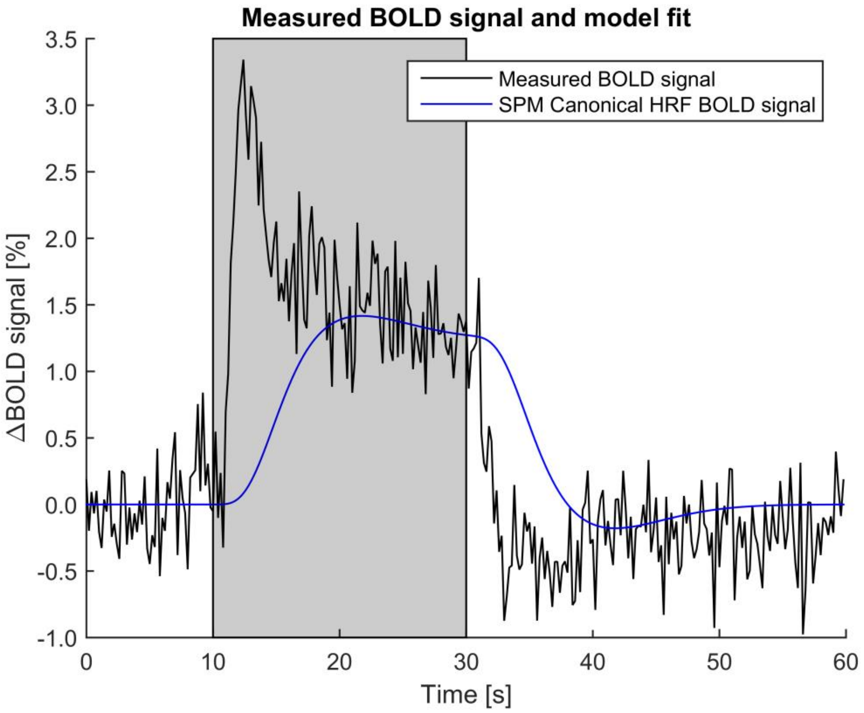

Figure 5.14. Measured and model BOLD signal in mouse superior colliculus generated by convolving the default SPM canonical haemodynamic response function with a boxcar signal representing the stimulus block – as previously used for statistical mapping in chapters 3 and 4.

It can be seen from Figure 5.14 that many of the features of the measured BOLD response are not suitably captured by the SPM12 canonical haemodynamic response function with the default parameter values. Parameter optimisation was therefore considered in a bid to better explain the mouse superior colliculus haemodynamic response with the double-gamma function.

5.2.2 Methods

Double-gamma function optimisation

A non-linear constrained optimisation was performed, using a non-regularised OLS cost-function, in order to optimise the HRF. This was done using the Sequential Quadratic Programming (SQP) algorithm [176] with eight free parameters and a maximum of 1000 iterations. The least squares cost function and the optimisation implementation in MATLAB using the ‘fmincon’ routine is provided in Appendix C.

All parameters were constrained to be greater than or equal to zero. The default and optimised parameters are shown in Table 5.1 and the plot of the optimised model BOLD response is shown in Figure 5.15.

Table 5.1. Parameters for double-gamma function haemodynamic response function before and after constrained non-linear optimisation.

Parameter	Description	Initial Value	Optimised Value
B	Effect size	1	1.33
p(1)	Response delay relative to onset [s]	6	0.14
p(2)	Undershoot delay relative to onset [s]	16	10.36
p(3)	Dispersion of response	1	0.63
p(4)	Dispersion of undershoot	1	15.19
p(5)	Ratio of response to undershoot	6	7.44
p(6)	Onset [s]	0	1.2
p(7)	Length of kernel [s]	32	32

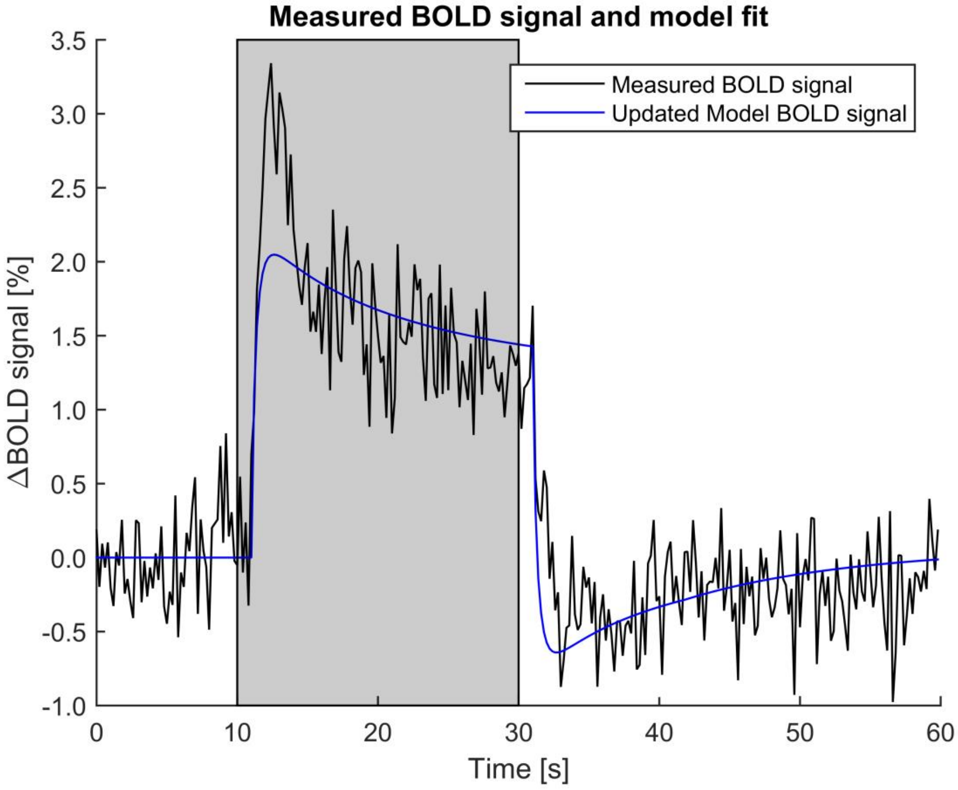

Figure 5.15. Measured and model BOLD signal in mouse superior colliculus generated by convolving an optimised SPM haemodynamic response function with a boxcar signal representing the stimulus block.

By comparing Figure 5.14 and Figure 5.15, it can be seen by visual inspection that the updated HRF better models the measured BOLD signal.

5.2.3 Discussion

The approach of parameter optimisation used in this section is extremely common. The SQP algorithm was chosen here for ease of implementation as it is one of the default algorithms offered by the MATLAB 2014 ‘fmincon’ routine. The OLS cost function without regularisation is also a straight-forward cost function to implement. Extensions to this work could investigate the use of regularisation of the cost function, or a Bayesian approach with suitable prior distributions placed on the input parameters.

It is evident from Figure 5.15 that the double-gamma function with optimised parameters explains more variance in the measured BOLD signal than with the default parameters. The parameters that have been optimised show faster haemodynamic responses in the mouse superior colliculus, relative to the default haemodynamic response function used for standard fMRI statistical parametric mapping used by the SPM toolbox for human fMRI data analysis. The knowledge of optimal parameter values could inform future mouse brain mapping applications and increase sensitivity.

However, it is also evident that the model BOLD signal discussed is incapable of capturing the sharp peak of the BOLD response after stimulus onset, and return to a mid-level signal for the stimulus block. One inference that could be made is that the mouse does not interpret the stimulus as one constant block as described previously. Future work could use two alternative models of the neural model convolved with the HRF. First, a neural model with an exponential decay throughout the length of the stimulus block could be considered, the time constant for which would represent adaptation to the stimuli during the stimulus block. Second, a neural model which treats the stimulus as the sum of two different stimuli could be used, stimulus ‘onset’ and stimulus ‘block’.

A principal limitation of the double-gamma function for modelling haemodynamic responses is that many of the parameters control the shape of the HRF but do not relate to plausible biological properties. This makes the model optimised here a descriptive model, rather than an explanatory one. An extension of this work might consider the use of the initial Buxton model [177] or its variations [178, 179] as an explanatory model to make inferences on biophysical properties underpinning mouse haemodynamics. However, using these complex, sometimes non-linear models would be computationally expensive for statistical mapping on a voxel-by-voxel basis. Therefore for the purposes of BOLD response detection, using an updated double-gamma HRF is sensible for future GLM analyses.

5.2.4 Conclusions

The double gamma canonical haemodynamic response function used by the SPM toolbox with default parameters was optimised to fit the high temporal resolution BOLD response measured in section 5.1, which should in principle give rise to greater sensitivity when used for statistical parametric mapping. This is tested in the next section.

5.3 Statistical parametric mapping with an updated HRF

In this section, the pooled data set of 14 subjects with BOLD responses to a 10 Hz flashing light stimulus (described in section 4.2) is revisited using an updated double-gamma haemodynamic response function for statistical parametric mapping.

5.3.1 Introduction

Throughout this thesis, statistical parametric mapping of BOLD responses on a voxel-by-voxel basis was used to map the visual pathway. The use of the canonical SPM double-gamma haemodynamic response function convolved with the stimulus duty cycle successfully identified key regions of the mouse brain visual system. However, with the optimisation of the double-gamma HRF for the mouse brain superior colliculus, it is possible that these statistical maps may become more specific and sensitive to mouse BOLD responses to visual stimuli.

5.3.2 Methods and results

A total of 14 subjects' BOLD responses to a binocular visual stimulus flashing at 10 Hz were used, and full acquisition details are described in sections 3.3 and 4.1, with an initial analysis of the pooled data from both experiments considered in section 4.2, using the canonical SPM HRF with default parameters. The analysis is repeated here but with updated HRF parameter values, changed simply by modifying the 'spm_defaults.m' file in the SPM12 toolbox, and setting the 'defaults.stats.fmri.hrf' variable to the relevant updated parameter values obtained in section 5.2.

To establish generalisability to multiple animals, 2nd level RFX analysis was considered, using both parametric and non-parametric approaches (see section 4.2). The t-statistics extracted here explicitly account for animal variability. The RFX parametric analysis is shown in Figure 5.16.

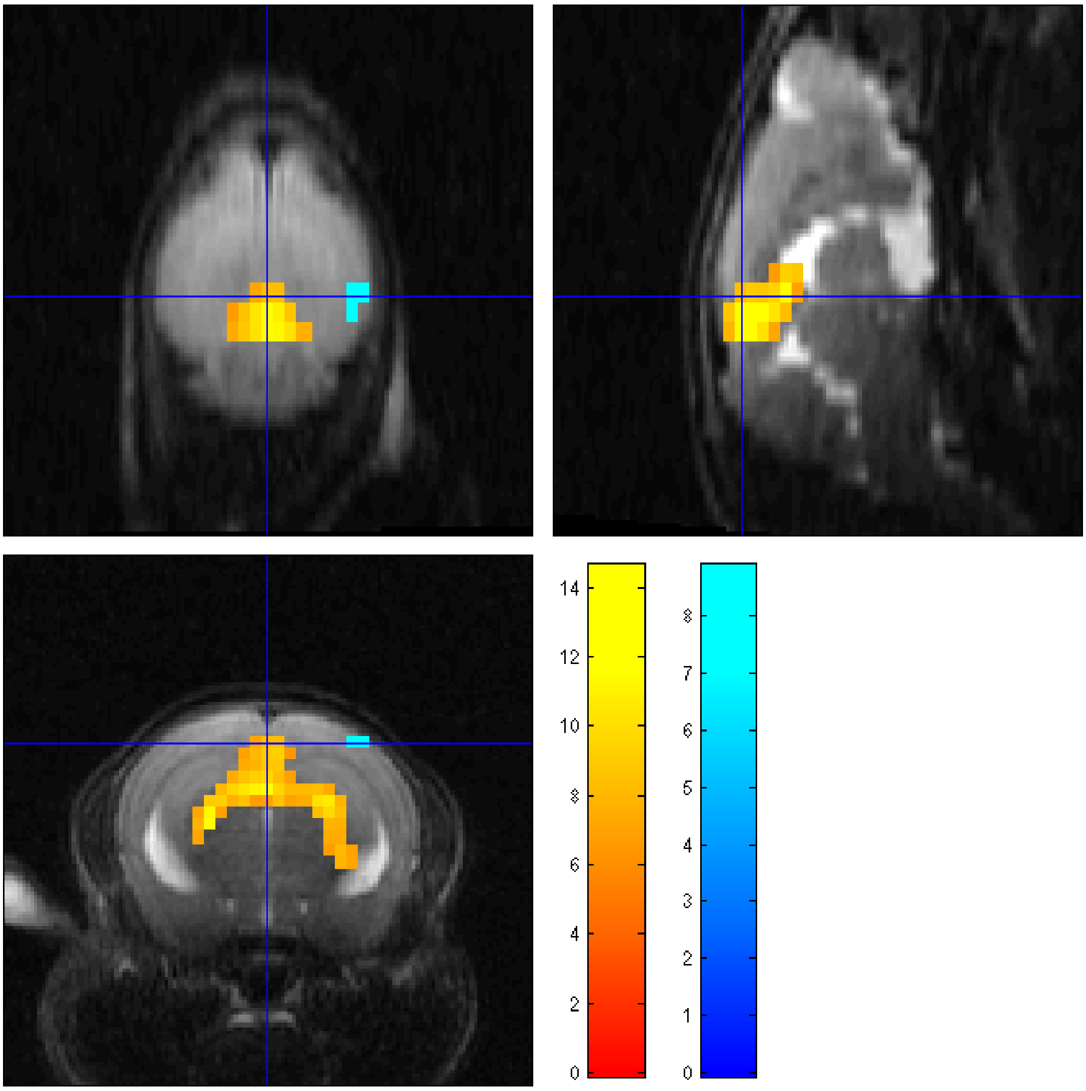

Figure 5.16. RFX analysis (two-tailed t-test, FWE $p < 0.05$, N = 14) statistical parametric map generated for the pooled 10 Hz data. The maximum t-statistics are 14.6 and 8.9 for positive and negative BOLD responses respectively (minimum threshold $|t| > 6.54$).

Statistical non-parametric mapping was also conducted. The distributions of maximum t-statistic for positive and negative effects are shown in Figure 5.17 and Figure 5.18 respectively.

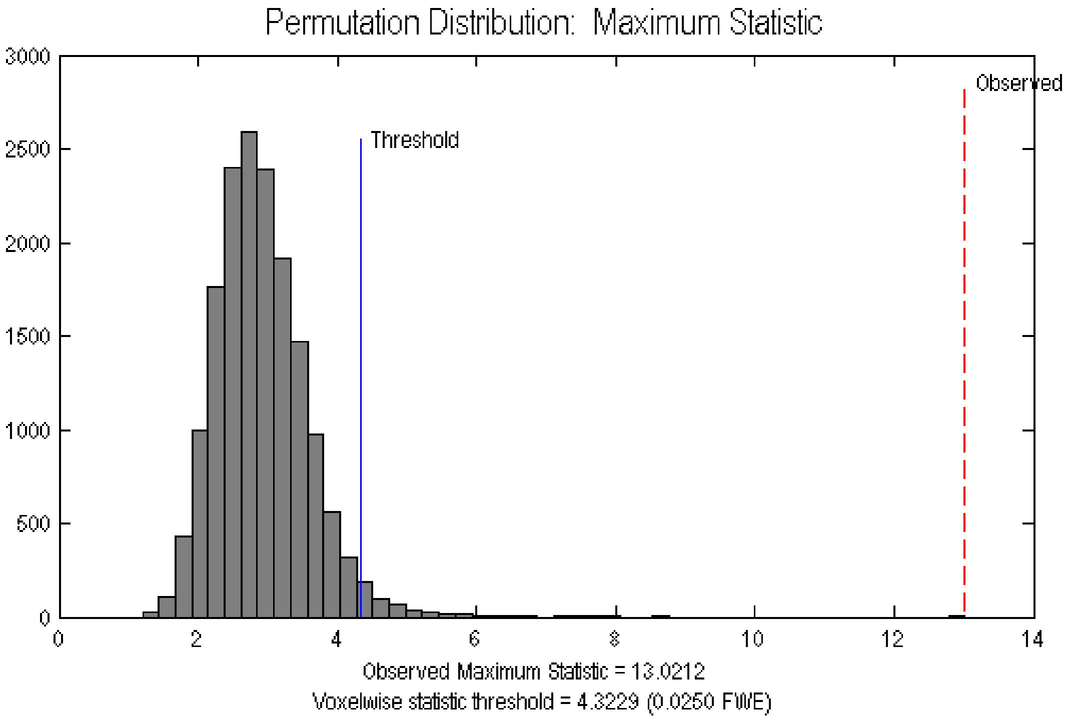

Figure 5.17. Permutation testing for positive BOLD effects – the distribution of the test statistic generated through over 16,000 permutations. The maximum statistic for the observed data is shown in red, and the threshold for a two-tailed test ($p < 0.05$) is shown in blue.

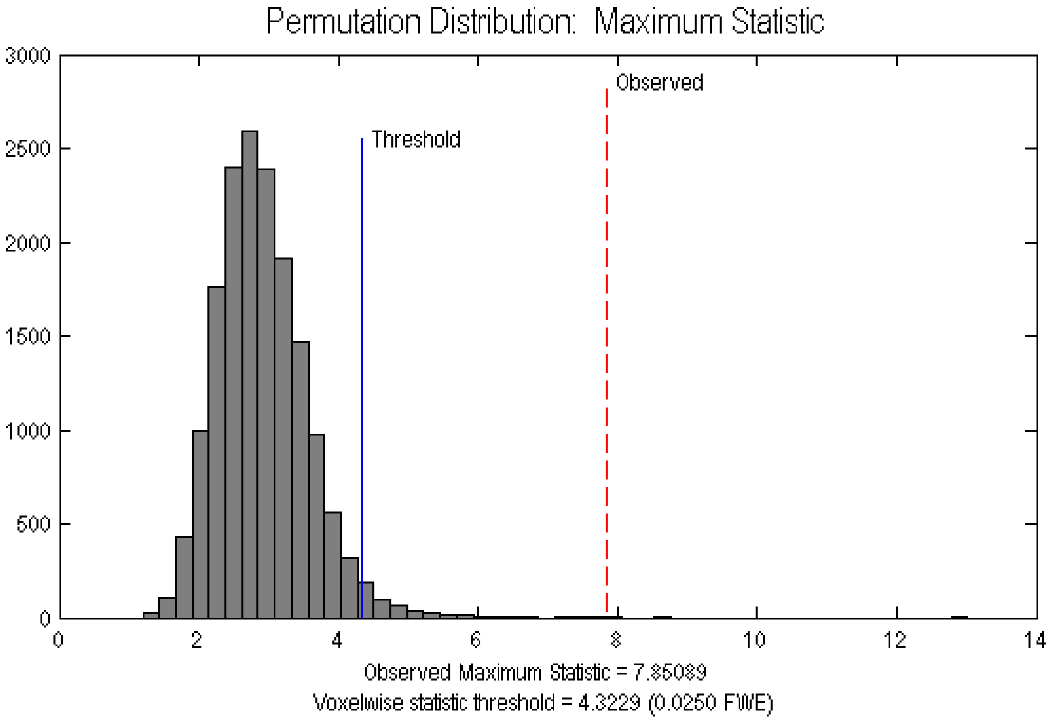

Figure 5.18. Permutation testing for negative BOLD effects – the distribution of the test statistic generated through over 16,000 permutations. The maximum statistic for the observed data is shown in red, and the threshold for a two-tailed test ($p < 0.05$) is shown in blue.

The resultant non-parametric map is shown in Figure 5.19.

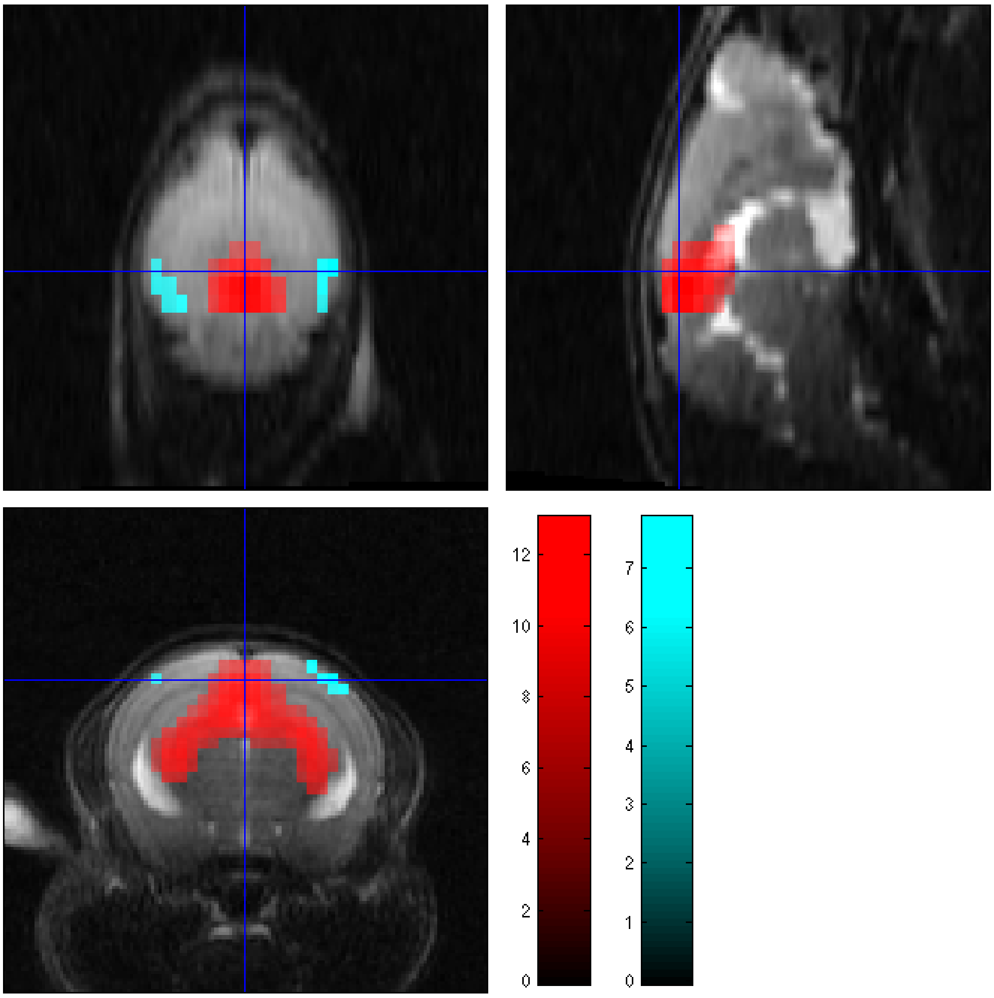

Figure 5.19. Mixed effects analysis (two-tailed t-test, FWE p < 0.05, N = 14) statistical non-parametric map generated for the pooled 10 Hz data. The maximum t-statistics are 13 and 7.9 for positive and negative BOLD responses respectively.

A summary of the maximum t-statistics for each approach using both the default modelling parameters and the optimised set is included in Table 5.2.

Table 5.2. Maximum t-statistics for the different analyses using both the canonical HRF and the optimised HRF, modelling both positive and negative BOLD responses. The use of an optimised HRF increases the maximum t-statistic, suggesting greater sensitivity.

RFX Analysis	Canonical HRF (maximum t-statistic)		Optimised HRF (maximum t-statistic)	
	+ve BOLD	-ve BOLD	+ve BOLD	-ve BOLD
SPM	12.7	6.4	14.6	8.9
SnPM	11.8	6.1	13	7.9

5.3.3 Discussion

The use of haemodynamic response functions for statistical mapping is relatively rare in historical mouse fMRI, with previous studies using simple difference images [31], correlation with a trapezoidal function [34], correlation with an unspecified function [32, 33, 36], or correlation with the stimulus boxcar only [35, 37]. One study has used a rat haemodynamic response function [38], and one study [39] has used the canonical human HRF included in the SPM toolbox. It is likely that common software toolboxes (such as SPM, FSL and AFNI) will be increasingly used for analysing future pre-clinical data, in order to make results more comparable with other mouse fMRI studies and with human studies. However, care must be taken when using analysis packages designed for human physiology, and translating assumptions across to a pre-clinical setting. The results in this section suggest that there are differences between human and mouse haemodynamic response functions.

When visually comparing Figure 5.16 and Figure 5.19 (statistical maps using the optimised HRF) with their corresponding figures in section 4.2.2), it generally seems that the optimised HRF is more specific to the visual system, and generates greater maximum t-statistics for RFX analyses that generalise to different data. One alternative method that could be used for modelling the BOLD response within the GLM approach is the use of a finite impulse response (FIR) model [4, 120]. The FIR models each timepoint with a separate basis function, and can in principle identify BOLD responses to stimuli regardless of the shape or timing of the haemodynamic response. However, the use of FIR or a different set of basis functions can severely increase the complexity of the design matrix, reducing the number of degrees of freedom and in turn reducing detection power (whilst also making interpretation of above-threshold voxels difficult). The necessary combination contrast (therefore requiring an F-test, rather than a t-test) would also not be able to distinguish between positive and negative BOLD responses, further reducing sensitivity to interesting fMRI phenomena in the mouse brain.

There are some limitations with the current approach to understanding the haemodynamic response to visual stimuli. fMRI experimental design is usually a balance between detection and estimation [4]. Whilst block designs are generally useful for detection of effects, the convolution of the HRF with the stimulus block timing function necessarily makes parameter estimation more difficult. In an ideal case with sufficiently low noise, an event-related design would be used, avoiding the convolution step altogether. Another disadvantage of the block design is the assumption of the linearity of the BOLD response (upon which the convolution is performed). As previously suggested in section 5.2.3, it is possible that this assumption is violated here, given the shape of the BOLD response to the block visual stimulus. Although somewhat obvious, it should also be noted that the greatest limitation of line-scanning fMRI data relative to using GE-EPI is the reduction in the number of spatial dimensions. A critical assumption made by using the line-scanning fMRI BOLD response is that the superior colliculus HRF is generalisable to the LGd and SCs. In the use of block designs the convolution means that this is not so problematic, but for event-related designs assumption may be violated. In which case, future work may wish to apply this approach to each region separately, define region specific HRFs, and an average HRF for GLM analysis. However the use of three separate stimulus regressors in the same GLM would be difficult as they would all be highly correlated, and an HRF averaged over regions might be more suitable.

5.3.4 Conclusion

In this section, select data (sections 3.3 and 4.2) previously analysed using statistical parametric mapping with the canonical haemodynamic response function (HRF) were reanalysed using the optimised HRF generated in section 5.2. An increase in detection power was seen, evidenced by greater t-scores in visual regions of the brain.

5.4 Chapter summary

In this chapter, improvements to the description of the haemodynamic response function were described. In section 5.1, the use of line-scanning fMRI to acquire high temporal resolution BOLD signals in the mouse superior colliculus was described. In section 5.2, this BOLD signal was used to optimise the default parameters of the double-gamma haemodynamic response function used by the SPM toolbox, with various extensions and limitations discussed. Then in section 5.3, this optimised HRF was used to reanalyse a previously described pooled data set, showing increased sensitivity and specificity in statistical maps of the BOLD response to visual stimuli. In the following chapter, the use of modelling BOLD responses to make inferences on visual network connectivity will be discussed.

6 Mouse brain connectivity

This chapter builds on chapters 3, 4 and 5, by asking more advanced questions about brain function. Instead of asking questions of whether particular brain regions exhibit BOLD responses to visual stimuli, this chapter examines the possibility of inferring how brain regions influence each other, using the technique of dynamic causal modelling (DCM). Previous analysis using the general linear model assumed a simplistic model of neuronal activity i.e. that in each region neuronal activity is a box-car function perfectly correlated with the stimulus paradigm. The analysis present here loosens this assumption, and tests hypotheses on how the neuronal activity in one region might modulate others.

Section 6.1 introduces this technically challenging approach to understanding brain connectivity, and takes the reader through the theoretical background behind DCM. In section 6.2, a DCM analysis is presented, using data previously described in sections 3.3 and 4.1, working through the GLM analysis and signal extraction required, and the subsequent use of Bayesian model selection and Bayesian parameter averaging for making inferences on mouse brain visual system effective connectivity. To my knowledge, this is the first ever description of effective connectivity in the mouse brain, and demonstrates the possibility of using DCM for mouse fMRI data.

6.1 Introduction

This section provides motivation for applying dynamic causal modelling to understanding the mouse visual system and briefly covers the theoretical background for DCM used in this chapter, as first proposed in 2003 by Friston et al. [180]. Two introductory/review articles are particularly recommended for readers unfamiliar with DCM – one by Stephan et al. [181] and another by Kahan and Foltynie [182].

6.1.1 Motivation

Previous analysis of fMRI data in this thesis has focused on asking the question of where BOLD responses to visual stimuli occur, and examining the shape of those BOLD responses. This uses the concept of functional segregation, in that neuronal population activity (inferred from BOLD responses and neurovascular coupling) is spatially distributed and specialised for particular functions. The GLM mapping analysis working on a voxel-by-voxel approach tests each voxel to decide if it is associated with a particular stimulus or not.

However, the field of human neuroimaging is increasingly investigating the way spatially segregated brain regions communicate and pass information [183] i.e. the concept of functional integration.

This chapter describes work attempting to understand how brain regions are *effectively* connected. This initially requires definitions of connectivity as commonly used in the neuroimaging literature:

1. Structural (or anatomical) connectivity. This refers to physical structures connecting different brain regions, such as white matter tracts, axons and synaptic connections. This can be measured invasively using tracer methods [184], or non-invasively using diffusion MRI [185, 186]. Anatomical connectivity data alone provides no information about how the connections are used in practise.
2. Functional connectivity. In the context of BOLD fMRI, functional connectivity is defined as correlation of responses in different brain regions *without external stimuli*, and is therefore synonymous with resting-state fMRI. There are a number of mouse brain functional connectivity studies [37, 126, 127, 154] already published, although this technique is much more difficult than task-based fMRI, due to the lack of an experimental intervention and the difficulty of defining signal and noise. Functional connectivity is quantified by the statistical dependencies between time series, and is purely correlational – no underlying model of communication between brain regions is offered.
3. Effective connectivity. In common usage, effective connectivity attempts to infer causal influences that neuronal systems may exert on other systems. This definition of connectivity is the closest to that of functional integration. In the context of BOLD fMRI, this corresponds to neuronal populations within brain regions.

Dynamic causal modelling (DCM) is one way (along with methods such as Granger causality) of investigating effective connectivity, i.e. answering the question of how regions in the brain interact and influence each other. Other methods for understanding connectivity beyond structural information, such as structural equation modelling [187] and Granger causality [188] have not been considered here, and a review of these methods in comparison to DCM is given by Friston et al. [189] and Penny et al. [190].

DCM has been used in human fMRI studies to answer questions about effective connectivity in healthy subjects (e.g. cortical visual processing [191], memory [192, 193]), and has also been used to investigate functional integration changes in brain disorders/diseases such as autism [194] schizophrenia [195], Parkinson's' [196], Alzheimer's [197, 198], and stroke [199, 200]. However, there are only two animal fMRI studies currently published that explicitly attempt to infer causal links between brain regions. One uses DCM in a rat model of epilepsy (David et al. [201]), and another uses rat optogenetic fMRI in conjunction with multivariate systems modelling [202]. Therefore there is a real need to further examine the assumptions made by DCM across species. Demonstrating DCM for mouse fMRI data also provides a platform for using transgenic mouse models in experiments where hypotheses of genetic modulation of networks can be formally tested, and may provide a more translational biomarker for brain pathology beyond BOLD signal amplitude.

The validation of effective connectivity is difficult to define, as it inherently models neuronal activity as an abstract hidden variable to be inferred from observable BOLD data. Current experimental technique that could most closely validate DCM is the use of invasive electrophysiology recordings at multiple distinct regions in the presence of stimuli, or alternatively the use of opto-genetics as described by Ryali et al. [202]. There is currently a large scale effort to understand thalamo-cortical connectivity in the mouse brain visual system using tracer studies [203], which could potentially be used for future validation of DCM fMRI as applied in this work. However, before the work described in this chapter, it remained to be seen if DCM could be applied to mouse fMRI data at all.

6.1.2 Framework behind dynamic causal modelling

DCM allows inferences to be made about neuronal population activity (hidden variables) from directly observable data (the BOLD signal). DCM uses a forward-model approach i.e. the parameters of a realistic neuronal system model are estimated in order that model neural dynamics generate haemodynamic responses which then match observed data.

As previously discussed in section 1.7, the BOLD signal is a proxy variable for neuronal activity, under the assumption of normal neurovascular coupling. A dynamic causal model operates on two levels: the hidden level, which cannot be directly observed experimentally, is a model of neural dynamics in a system of coupled brain regions. The hidden state of the system is represented by a state variable vector z, and the temporal evolution of the hidden state by $\dot{z}$. The hidden state variables do not correspond directly to invasively measureable neuronal properties such as firing rates or local field potentials, but instead are an abstract description of neural population activity. The temporal evolution $\dot{z}$ is (in deterministic DCM) given by a function F the current state z, input stimuli u (for which there are m distinct types), and a set of neural system coupling parameters given by matrices A, B and C. The bilinear implementation of DCM (the non-linear extension has not been considered here) is given by equation (2).

$$\dot{z} = F(z, u, A, B, C) = Az + \sum_{j=1}^{m} u_j B_j z + Cu \tag{2}$$

The parameters in matrices A, B and C are themselves partial derivatives of F and are shown in equation (3).

$$\begin{aligned} A &= \frac{\partial F}{\partial z} \\ B_j &= \frac{\partial^2 F}{\partial z \partial u_j} \\ C &= \frac{\partial F}{\partial u} \end{aligned} \tag{3}$$

In this formulation of DCM, the parameters in A (which for k regions is of size $k \times k$) describe anatomical connections between brain regions, which are context independent. Connectivity mediated by the context of the j^{th} input is described by B_j, (m matrices of size $k \times k$). Direct inputs to the system are accounted for by parameters in C (matrix of size $k \times m$).

6.1.3 Forward mapping from neuronal states to BOLD responses

DCM uses the hidden state equation described in equation (2) to generate BOLD responses (the observable variable) by using a variation [180, 204, 205] of the original Buxton ‘balloon’ model [177, 178] for haemodynamic responses. The balloon model uses a set of differential equations to link neuronal activity to haemodynamic (hidden) state variables z^h, which then non-linearly map to a BOLD signal response that is directly measurable. A schematic for the extended Balloon model from Friston et al. [205] is included in Figure 6.1.

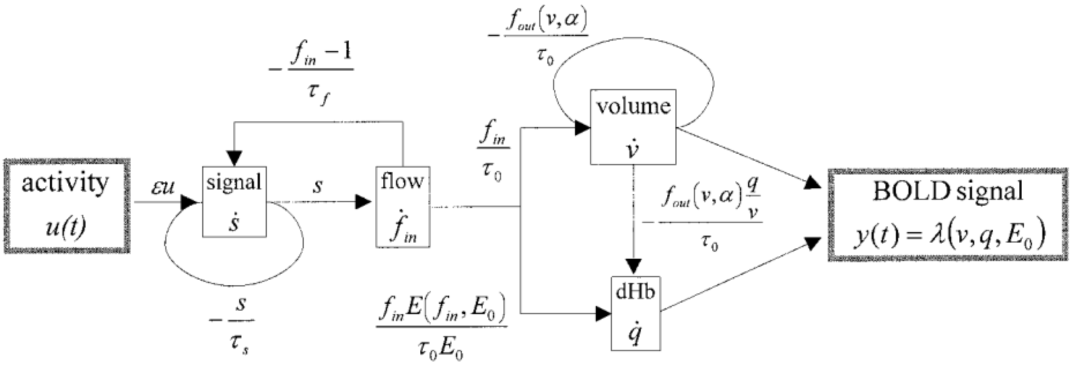

Figure 6.1. Schematic of Balloon haemodynamic model used for DCM (reproduced with permission). The original caption reads as follows, "Schematic illustrating the organization of the hemodynamic model. This is a fully nonlinear single input *u(t)*, single output *y(t)* state model with four state variables *s*, f_{in}, *v*, and *q*…" which correspond to a 'flow-inducing signal', 'the rate of change of flow', normalised venous volume and normalised total deoxyhaemoglobin content respectively.

The balloon model of the vascular response was first proposed by Buxton et al. in 1998 [177], with various amendments [178] and extensions [205] made. The underlying aim of the balloon model is to non-linearly map from neuronal activity to the BOLD responses measured with fMRI. To briefly summarise, Buxton et al. assume no capillary recruitment, and so blood volume changes occur primarily in the venous compartment. This means that when arterioles expand to increase blood flow, the vascular bed within a voxel can be modelled as an 'expandable venous compartment' (i.e. a balloon). The increased blood flow into the balloon causes the balloon to swell, and the consequent increase in pressure causes the flow out of the balloon to match the inflow. The rate of change of volume of the balloon is given by the difference in flow rates in and out of the balloon.

All state variables in this model are used in a normalised form relative to values at rest. The extended Buxton model also contains corresponding haemodynamic parameters θ^h which can be measured directly from alternative experimental data, in practise these are estimated directly from the BOLD signal with reasonable biophysical priors. When estimating the parameters of a dynamic causal model, both neural and haemodynamic parameters can be estimated simultaneously. The combination of both neuronal and haemodynamic state spaces is shown in the joint state equation (4).

$$\begin{aligned} x &= [z\,,z^h] \\ \theta &= [A,B,C,\theta^h] \\ \dot{x} &= F(x,u,\theta) \\ y &= \lambda(x) \end{aligned} \tag{4}$$

Under the condition of θ and u being time-invariant, for a particular instance of θ and u, the joint state equation can be integrated with respect to time and non-linearly mapped by λ to a theoretical output BOLD signal $h(u,\theta)$. However, it is reasonable to extend this and allow for nuisance regressor signals $X\beta$ (e.g. motion, scanner drift) and an observation error e, given by equation (5).

$$y = h(u,\theta) + X\beta + e \tag{5}$$

In equation (5), y is the measured BOLD signal, and $h(u,\theta)$ can be estimated using the GLM approach already successfully used in chapters 3 and 4. For a given u (fixed for each fMRI experiment), θ can then be estimated in order to fit y, in this case using a Bayesian approach. Using the SPM12 toolbox (http://www.fil.ion.ucl.ac.uk/spm) implementation of DCM, θ^h parameters are estimated using empirical priors and neuronal system parameters A and B are estimated using conservative shrinkage priors, whereas C has a prior distribution with a more relaxed variance[3].

The estimation procedure (known as model inversion) is completed using an expectation maximisation algorithm, fully described in [180]. The algorithm optimises θ in order that the model evidence is maximised, under the neuronal and haemodynamic parameter priors.

6.1.4 Model evidence

The evidence for a model m is given by the probability of observing data y under that model. This is obtained by integrating over dependencies on model parameters θ, as shown in equation (6).

$$p(y|m) = \int p(y|\theta,m)p(\theta|m)d\theta \tag{6}$$

This integral is intractable to solve analytically for anything other than linear Gaussian models and challenging to solve computationally [206]. Therefore approximations to the model evidence are often used. Often these approximations calculate lower bounds for model evidence (in order to be conservative), such as

---

[3] For a full description of the priors used in this analysis, see the script files spm_fx_fmri.m, spm_gx_fmri.m and spm_dcm_fmri_priors.m in the SPM12 toolbox.

the Akaike Information Criteria (AIC) [207] or the Bayesian Information Criteria (BIC) [208]. These approximations decompose model evidence into an accuracy term and a complexity term. AIC and BIC both penalise complexity (by the principle of Occam's Razor [209]) with a function of the number of parameters (with BIC also accounting for the number of observations). However, these methods do not account for prior beliefs on the behaviour of the parameters, or their interdependencies [206, 210].

A concrete example of this is a thought experiment considering two models, the first with a single parameter and the second with a hundred parameters, all with well-behaved prior distributions (for simplicity, these could all be Gaussian). For a given data set, let us suppose that both models are equally accurate (i.e. explain equal amounts of variance in the data). Both AIC and BIC would select the first model over the second, penalising the second model for being overly complex. However, let us now suppose that in order to explain the same variance, the 1st model's single parameter occupied an unlikely value within its prior distribution, whereas for the 2nd model, 98 parameters did not move from their mean prior values at all, and two moved slightly within their distributions but were well within normal ranges. It would now seem that the 2nd model is simpler than the first, and explains the data just as well, but AIC and BIC fail to account for this situation. Additionally, AIC and BIC do not account for interdependencies or covariance between parameters.

It is for this reason that within the DCM framework, the quantity called the (negative) variational free energy is used as an approximation for the lower bound for model evidence. The free energy is defined as the subtraction from an accuracy term (the expectation of the log of the probability of the data given the parameters/model) of a complexity term, given by the Kullback-Leibler divergence between the approximate posterior and prior distributions. This allows complexity to be captured as the difference between prior and posterior beliefs, rather than penalising unused parameters like AIC and BIC. Therefore maximising the free energy (or minimising the negative free energy) maximises model evidence.

The free energy can be calculated by using a modified restricted maximum likelihood cost-function within the EM algorithm [211], although the mathematical derivations required for this are beyond the scope of this thesis. Within the DCM framework offered by the SPM12 toolbox, a model is said to be inverted or estimated when the free energy has converged after the application of the EM algorithm. Models are defined by their prior parameter distributions, accounting for both haemodynamic and neural network parameters. Assuming convergence, models with different priors can be compared, and a model or family of models can be chosen based on maximised model evidence.

6.1.5 Model priors

When setting up models for estimation and comparison in DCM, is necessary to make the distinction between prior and posterior beliefs about parameters. Before estimation, models are defined by their prior beliefs about parameters, represented by probability distributions. As this is the first ever attempt to use DCM for mouse fMRI data, for simplicity the same haemodynamic priors for human DCMs have been used in all analysis presented in this chapter. Where appropriate, priors on connection, modulatory and driving input parameters are described in the methods.

6.2 DCM analysis

6.2.1 Introduction

Initially, subset of the interleaved snapshot GE-EPI data set described in section 3.3 was used, with four interleaved snapshots at a binocular visual stimulus of 10 Hz flashing frequency (experiment 1). The results from this data set were propagated through to in order to analyse the data set described in section 4.1, where frequency was used to modulate BOLD responses (experiment 2). The use of these data sets for this novel application of DCM have the advantage that both used identical data acquisition protocols, and reliable, large effect sizes relative to later experiments described in chapter 4.

Data was pre-processed according to section 3.3, with the exception of the spatial normalisation step, where the more advanced method described in section 3.2.2 was used, to put each subjects’ functional data into the space of the Allen MBA.

6.2.2 Methods and results

Due to the developmental nature and technical detail required for this analysis, methods and results are presented in the same section, and described in chronological order. First BOLD signal extraction is described for experiment 1. Then, a plausible model space is defined examining potential connections and driving input combinations. A Bayesian model selection procedure is then used to select a model that best explains the connections and driving inputs in the mouse brain visual system, given the observed BOLD data and input priors. Bayesian parameter averaging is then used to estimate the strength of the connections and inputs.

Following this, data from experiment 2 was used to infer how flashing frequency modulates effective connectivity in the mouse brain. BOLD signals were extracted in a similar fashion to experiment 1. The model structure resulting from experiment 1 was used to inform the model space for experiment 2, massively reducing the potential model space. Bayesian model selection was used again to infer where flashing frequency might modulate connections, and Bayesian parameter averaging used once again to estimate the strength of the modulatory effect.

6.2.2.1 Experiment 1- Inferences on model structure

BOLD Signal Extraction

In order to extract BOLD signal data for use with DCM, the recommended procedure for a DCM GLM was used [120, 180]. The pre-processed data was concatenated (in time, i.e. data from each run was stacked sequentially) for a FFX GLM analysis per subject, as were the relevant motion parameters for nuisance regressors. An updated double-gamma haemodynamic response function (using parameters derived in section 5.2) was used. An example design matrix for a single subject is shown in Figure 6.2, and the effect of the 128s high-pass filter shown in Figure 6.3.

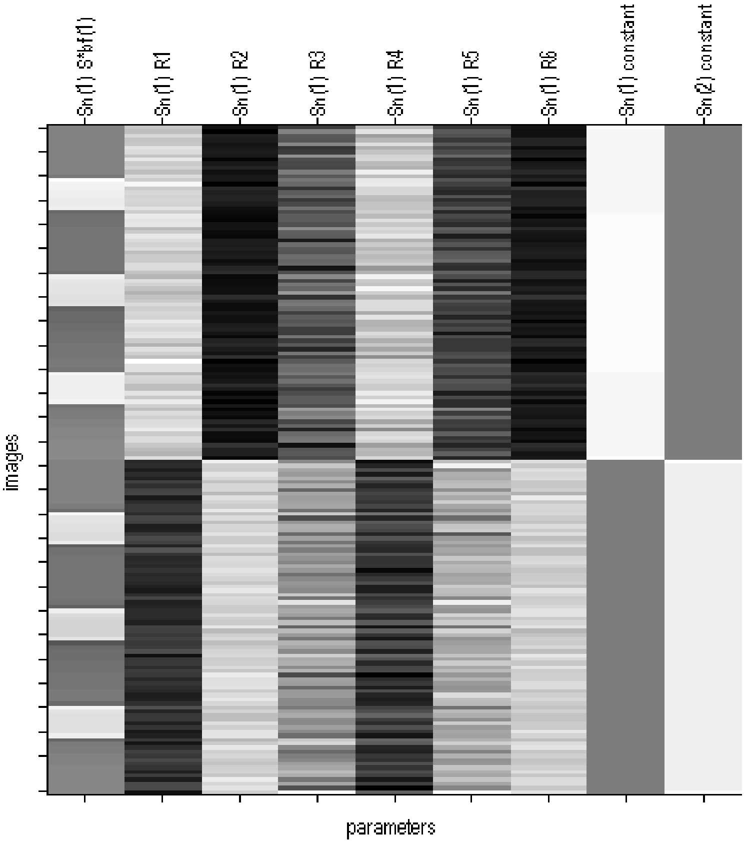

Figure 6.2. FFX GLM design matrix for (temporally) concatenated fMRI runs. Columns are as follows: 1. model haemodynamic response; 2-7. Concatenated motion parameter estimates; 8-9. Run-specific regressors, indicating which data belongs to which run. Low-frequency regressors used in the discrete cosine transform for high-pass filtering are hidden by default by SPM.

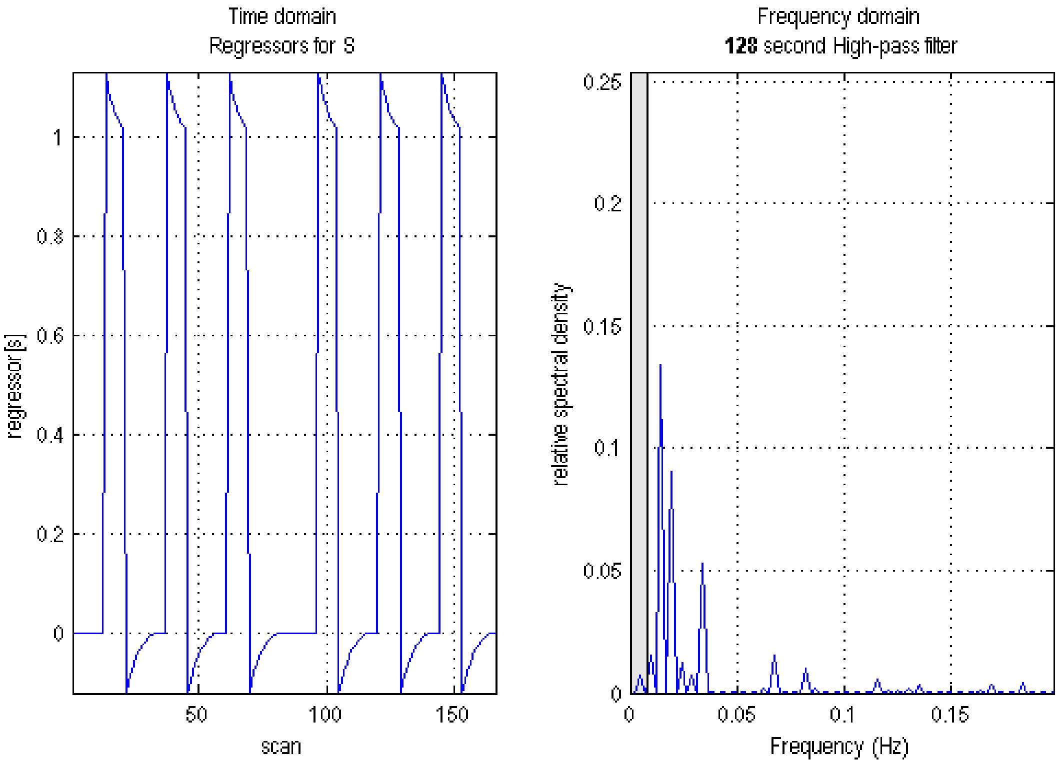

Figure 6.3. Effect of high-pass filter on experimental design. Left panel – modelled BOLD response using convolution of updated double-gamma function with stimulus block design. Right panel – effect of filter on the experimental design. The bulk of the frequencies of interest are not included in the range of the filter (grey bar).

For data extraction, an F-test contrast was used for the effect of interest, as the F-test is invariant to the sign of the effect. This was extracted with a GLM contrast vector of [1 0 0 0 0 0 0 0 0]. For each subject, the F-statistic map was thresholded at $p < 0.05$ (uncorrected for multiple comparisons) (Figure 6.4), and the cluster peak closest to each visual ROI location recorded. As the question being asked relates to interactions and causal links *between* effects, thresholding without multiple comparisons is reasonable. Furthermore, because this question does not relate directly to effect size, but rather causes and links between effects, it is reasonable to use the maps for guiding signal extraction, without the issue of circularity raised by Kriegeskorte et al. [125].

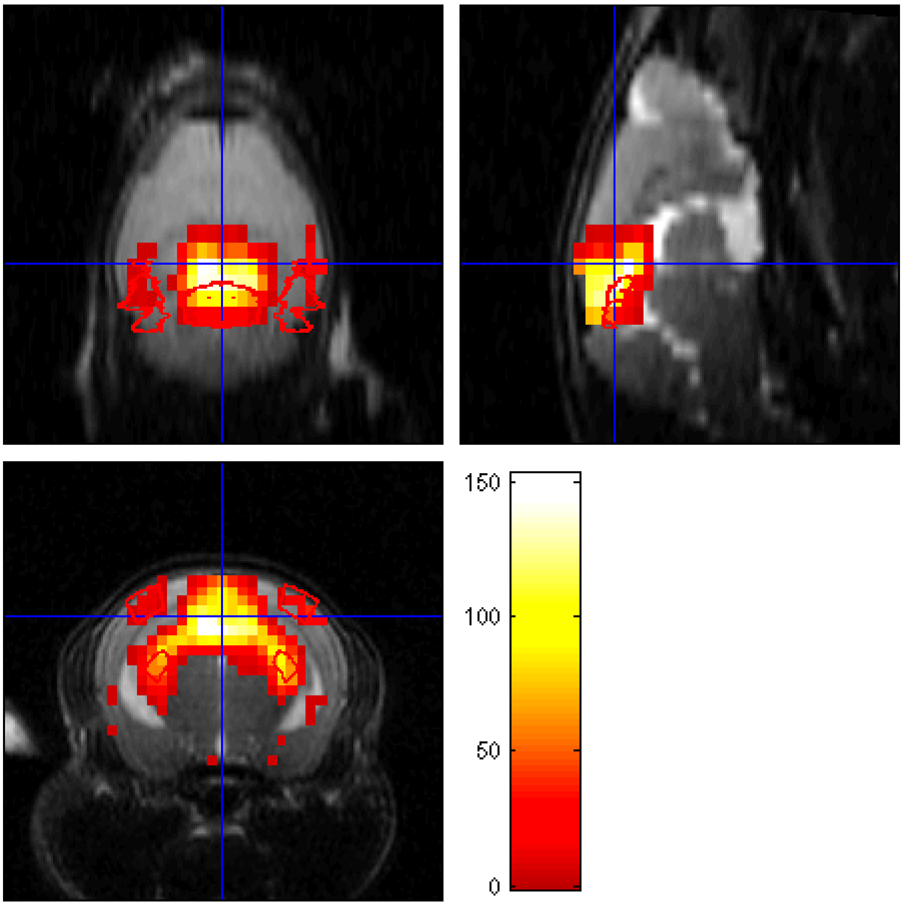

Figure 6.4. FFX map for a single subject, F-test for BOLD activation (regardless of sign), thresholded at $p < 0.05$ without correction for multiple comparisons, with contours of visual region ROIs overlaid. The F-statistic threshold is 3.9, and for this design matrix is the equivalent of a t-statistic threshold of 1.98. The maximum F-statistic corresponds to a t-statistic of approximately 12.4.

The central location of the SCs was used, and for the LGd and VISp, right and left hemisphere locations were noted. At each location, above-threshold voxels included within a 0.6 mm sphere (6 mm specified in SPM12, given that voxel dimensions are scaled up by a factor of 10) were used for signal extraction. Their locations in the space of the Allen Mouse Brain Atlas with standard deviations are provided in Table 6.1.

Table 6.1. ROI locations for signal extraction (mean with standard deviation). Real voxel dimensions are [0.36 0.36 0.6] mm for reference.

ROI	$x \pm \sigma_x$ / mm	$y \pm \sigma_y$ / mm	$z \pm \sigma_z$ / mm
LGd – left	3.61 ± 0.30	4.92 ± 0.20	5.90 ± 0.11
LGd – right	7.85 ± 0.24	4.72 ± 0.24	5.82 ± 0.23
SCs	5.80 ± 0.11	6.74 ± 0.24	4.43 ± 0.13
VISp – left	3.19 ± 0.26	6.89 ± 0.19	4.48 ± 0.37
VISp – right	8.45 ± 0.24	6.64 ± 0.14	4.41 ± 0.26

This method is superior to using the structural ROIs only because it implicitly allows the manual operator to account for image distortion and minor failures in image registration [181].

For signal extraction, rather than extracting the mean BOLD signal, the 1st eigenvariate (or principal component) [120] of the concatenated BOLD signal, adjusted for effects of interest, was extracted. By adjusting for effects of interest, voxels which more closely match the modelled signal contribute more strongly to the 1st eigenvariate. In the case of all voxels having an equal contribution, the 1st eigenvariate is equivalent to the mean signal. This provides two advantages over simply using the mean signal:

1. The 1st eigenvariate of the signal is more robust to response heterogeneity within the cluster.
2. Effects not included in the effects of interest contrast e.g. motion estimates, are removed from the data before extraction.

Based on the statistical threshold of $p < 0.05$, (uncorrected), all subjects contained significant voxels for all regions. Therefore all 6 subjects were used for DCM.

Plots of the extracted 1st eigenvariate signals for each subject and ROI are included in Figure 6.5.

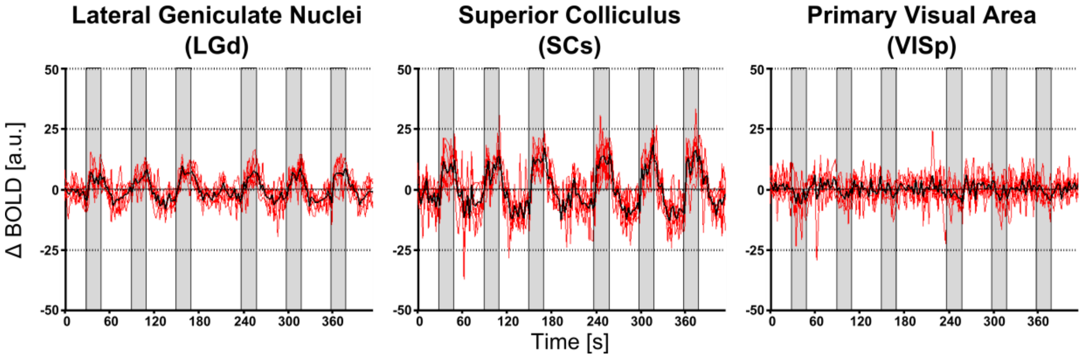

Figure 6.5. Eigenvariate signals extracted from 6 subjects concatenated fMRI data (10 Hz binocular visual stimulation). Signal units are normalised to the global brain mean signal multiplied by 100 [120], and periods of stimulation are shown in grey. Red timecourses are from individual subjects, and the mean timecourse is plotted in black.

The timecourses extracted and shown in Figure 6.5 clearly show effects related to the stimulus, and therefore it was deemed reasonable to attempt to investigate networks that might generate these observable signals.

Model space definition

The data shown in Figure 6.5 indicates that the LGd and SCs show much stronger responses than VISp. From this observation and considering the feed-forward model described by Huberman and Neill [26] shown in Figure 3.30, it was hypothesised that a hierarchical model with driving inputs to LGd and SCs, and a connection between LGd and VISp would best explain the observed BOLD signals. This connection model is represented in Figure 6.6.

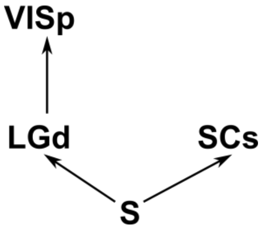

Figure 6.6. Initial hypothesis for effective connectivity in the mouse brain, based on a summary of the literature (see Figure 3.30, adapted from Huberman and Neill [26]. An input stimulus S from the optic nerve feeds separately to the SCs and LGd. The LGd then relays information to VISp in a hierarchical manner.

The first use of DCM for mouse fMRI data tested whether this model performed significantly better in explaining the measured BOLD signals against other models, in an attempt to answer questions on connections and driving inputs. To constrain the model space, only bidirectional connections were considered to be possible, which strictly means that the model shown in Figure 6.6 was not directly tested – as both backward and forward directions for each connection were considered plausible.

By considering all permutations of bi-directional connections between three regions, eight variations of the A matrix representing connections are possible (coded as A1-A8). All possible permutations of the driving input were considered, leading to seven variations of the C vector representing the driving input (coded as C1-C7). As all trials were assumed to induce identical responses, no modulatory influences were modelled, and therefore the B matrix representing modulatory influences was set to zero. This gave rise to a total model space of 56 models per subject to be estimated. Each model was considered under a 'flat' prior i.e. no model *a priori* was more likely than any other. The codes for these models are shown in Table 6.2.

Table 6.2. Plausible model variations on connections and driving input locations for the mouse visual system. When a model has an allowed connection parameter, the default prior value of that parameter is zero, but is allowed to change under a shrinkage prior distribution. When a parameter is not allowed, its value is fixed at zero. For driving parameters, the prior has mean zero and variance one.

Model code	Allowed parameters that define the model
A1	No connections
A2	One connection between LGd and SCs
A3	One connection between LGd and VISp
A4	One connection between SCs and VISp
A5	Two connections: LGd-SCs and LGd-VISp
A6	Two connections: LGd-VISp and SCs-VISp
A7	Two connections: LGd-SCs and SCs-VISp
A8	Three connections: LGd-SCs, LGd-VISp and SCs-VISp
C1	Stimulus drives LGd only
C2	Stimulus drives SCs only
C3	Stimulus drives VISp only
C4	Stimulus drives LGd and SCs
C5	Stimulus drives LGd and VISp
C6	Stimulus drives SCS and VISp
C7	Stimulus drives LGd, SCs and VISp

For example, the equivalent model in Figure 6.6 would correspond to model A3C4.

Bayesian model selection

All 56 models (per subject) were estimated using the default priors used in the SPM12 toolbox[4] (deterministic, bilinear, non-mean-centred, one state per region), and initially compared using both RFX and FFX Bayesian model selection (BMS) approaches. Depending on whether FFX or RFX analyses were used, group results were combined according to Stephan et al. [212].

One could argue that a FFX approach is more suitable based on the reasonable assumption that each subject should be operating under the same model (which for primary visual stimuli processing is probably true, bar variable effects of physiology). However, a limitation of using FFX BMS in this way can lead to ‘brittle’

---

[4] An error was found in the r6767 version of SPM12, where although the user had the flexibility to specify the custom echo time used, this was overridden by the default echo time of 40 ms (which is common for human fMRI studies). This error was corrected for all DCM analysis presented in this chapter.

model results, where one model for a particular subject completely dominates the group result [213]. On the other hand RFX BMS ignores the assumption of consistent connectivity across subjects. For completeness both types of BMS are presented here.

BMS compares models by their free energy (as an approximation for model evidence), where a model with the minimum negative free energy is the one which ‘best’ explains the data. Probabilities of models explaining data better than other models is calculated by the difference in free energies between models, and then normalised by the number of models tested in the comparison. However, for large model spaces, this leads to the issue of dilution of evidence, or model dilution. To account for this problem, family comparisons were used to make inferences on model structure [213]. Families of models were defined based on connection and driving combinations e.g. a family of models which all contain a connection between LGd and VISp, or a family of models which only have a driving input to SCs). Family comparisons were conducted over combinations in the A matrix (structural) and the C vector (drivers).

The family exceedance probability or posterior probability (i.e. the probability of one family outperforming all others) for each family of structural models are shown in Figure 6.7 and Figure 6.8, and for each family of driver models shown in Figure 6.9 and Figure 6.10.

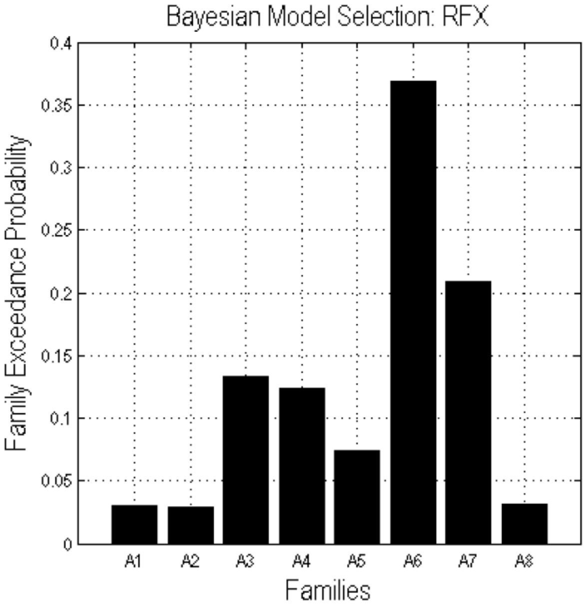

Figure 6.7. RFX Bayesian model selection (A) for 8 families of models of bi-directional connections between LGd, SCs and VISp. Model families are scored on the exceedance probability, with family A6 outperforming all other families.

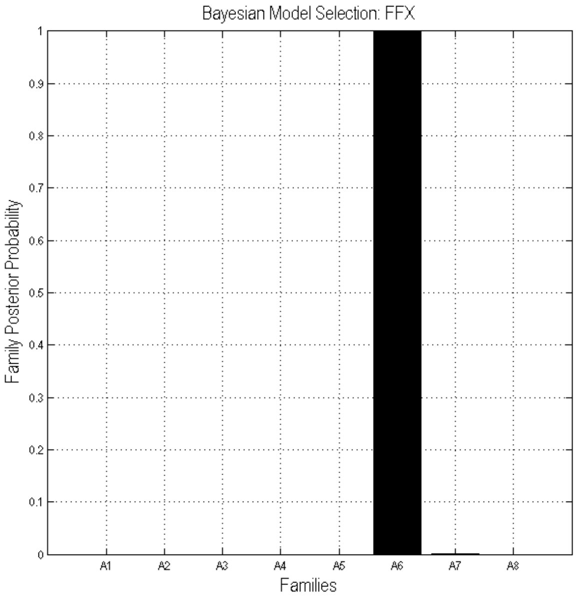

Figure 6.8. FFX Bayesian model selection (A) for 8 families of models of bi-directional connections between LGd, SCs and VISp.

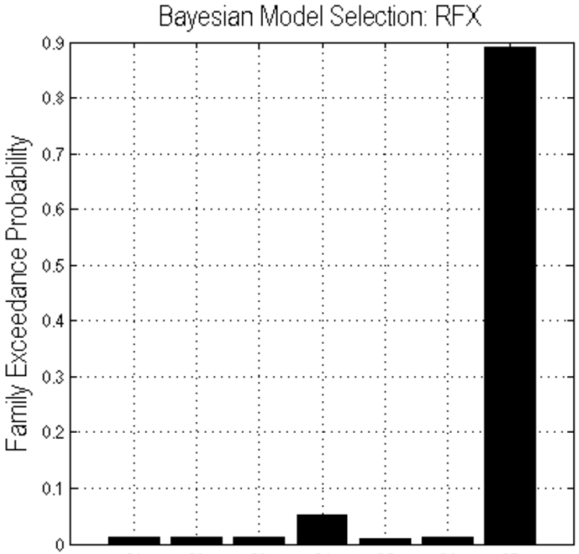

Figure 6.9. RFX Bayesian model selection (C) for 7 families of models of driving input to LGd, SCs and VISp. Models are scored on the exceedance probability, with family C7 outperforming all other families.

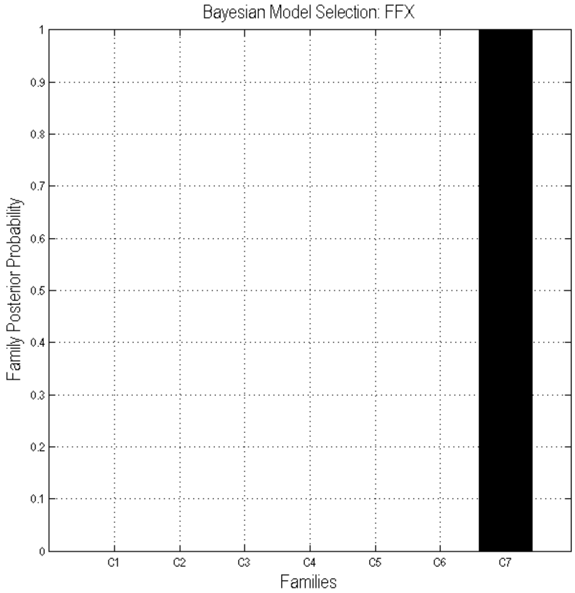

Figure 6.10. FFX Bayesian model selection (C) for 7 families of models of driving input to LGd, SCs and VISp.

In order to formally accept a winning model, an exceedance probability of over 0.9 (corresponding to ‘strong evidence’ i.e. a Bayes factor > 3 [214]) would be required (similar to using a $p < 0.05$ threshold for statistical significance from the frequentist approach). It should be remembered here that probability is a measure of the degree of certainty, rather than a frequency over the long run as in the frequentist view. Although models were grouped into families before comparison, the issue of model dilution remains under the assumptions for RFX BMS.

From the FFX Bayesian model selection procedure, we can select a model that includes features for which we have strong evidence (probability of > 0.9) of existing. This corresponds to a model which belongs to both families A6 and C7 (see Table 6.2). This corresponds to the network structure shown in Figure 6.11.

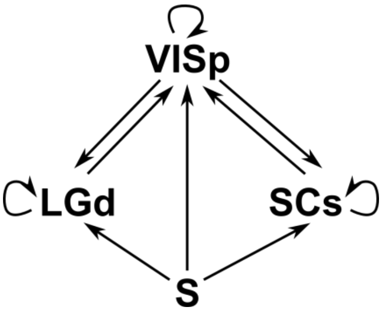

Figure 6.11. Winning model structure describing effective connectivity for the interleaved snapshot (n=4) GE-EPI mouse fMRI data set. This model suggests that all three regions are driven by stimulus S, and that VISp is bi-directionally connected to both LGd and SCs, but that LGd is not connected to SCs. All regions have a self-connection (represented by a small looping arrow).

The model described in Figure 6.11 captures some of what would be expected from Huberman and Neill’s review [26] of the biology of the mouse brain visual system – that LGd and SCs are on different visual pathways (i.e. do not communicate directly), but also that VISp and SCs communicate, and that VISp also receives direct stimulus input. There is more recent evidence suggesting that there are indeed structural connections between VISp and SCs [215] in the mouse brain. However, the current finding that the stimulus directly drives VISp is surprising and does not appear to match the underlying biology.

Model Accuracy

As a basic check of the performance of the model fitting, the variance of the BOLD signal explained by this model (a proxy for model accuracy) was examined, and shown in Figure 6.12.

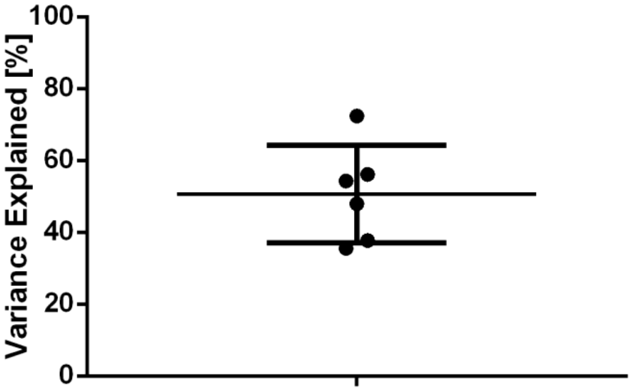

Figure 6.12. Spread of % variances explained (a proxy for model accuracy) by the winning model in Figure 6.11. Given different noise levels across subjects, some variation of model accuracy is to be expected. A heuristic minimum of 10% variance explained is used within the SPM12 toolbox for rejecting a model as inaccurate.

The percentage of BOLD signal variance (± standard deviation) explained by this model is 51 ± 12 %. The predicted output BOLD responses and the target data for the lowest and highest variance explained subjects (i.e. the subjects with the lowest and highest proportion of their BOLD signals explained by the model) are shown in Figure 6.13 and Figure 6.14 respectively.

Subject 1 - 36% of BOLD signal variance explained

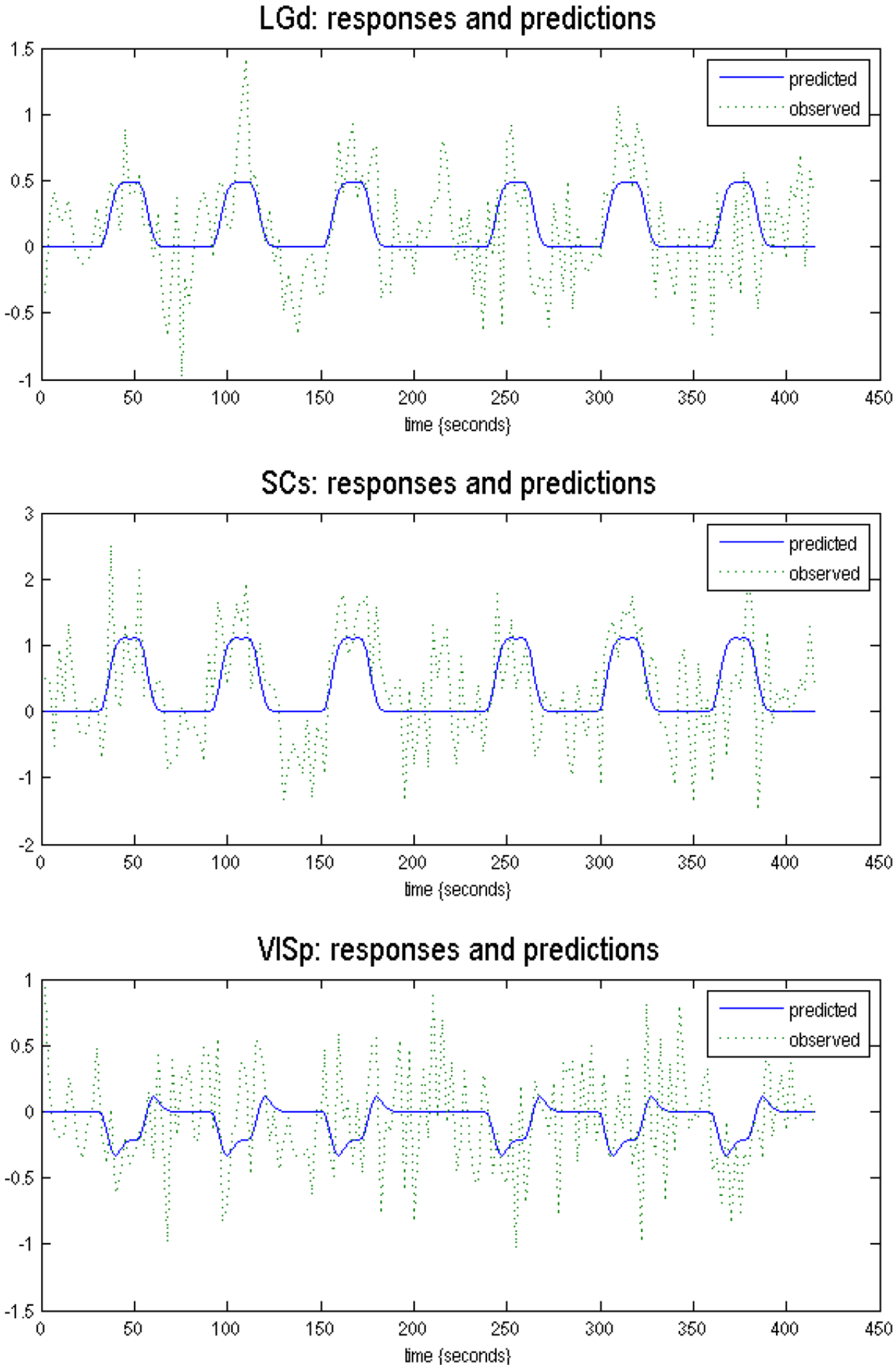

Figure 6.13. Observed and predicted BOLD responses for the subject for which this model explains 36% of the variance of the observed signal, for LGd, SCs and VISp regions (outputted from the SPM12 DCM toolbox). Note the different axis limits in each plot.

Subject 6 - 72% of BOLD signal variance explained

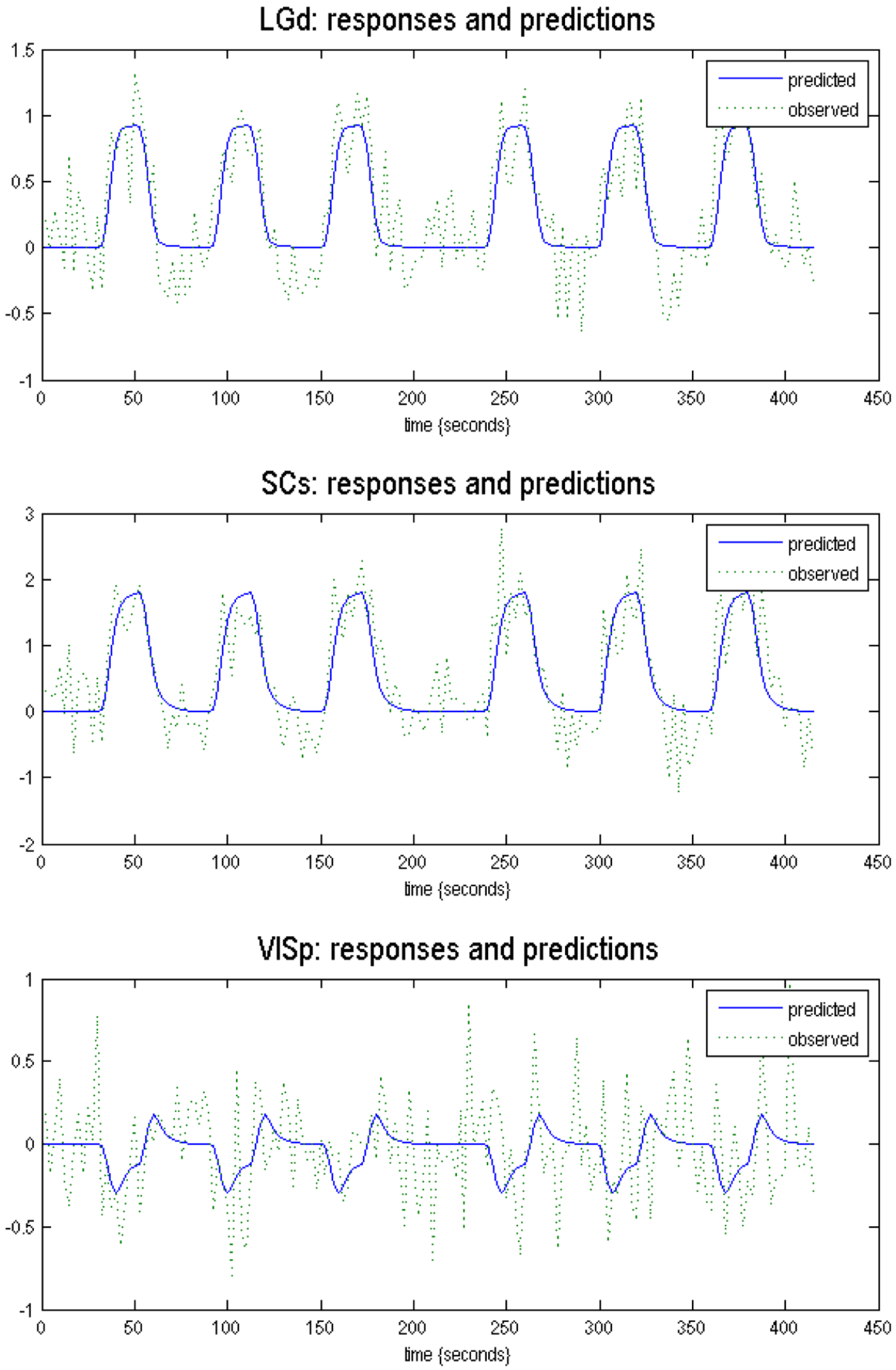

Figure 6.14. Observed and predicted BOLD responses for the subject for which this model explains 72% of the variance of the observed signal, for LGd, SCs and VISp regions (outputted from the SPM12 DCM toolbox). Note the different axis limits in each plot.

These figures qualitatively indicate the robustness of the model fitting to noise in the BOLD signal, which itself is a parameter optimised during the free energy maximisation. This is the first time this has been done for mouse fMRI data. The full results of model accuracy across the 6 subjects and 56 models are shown in Figure 6.15.

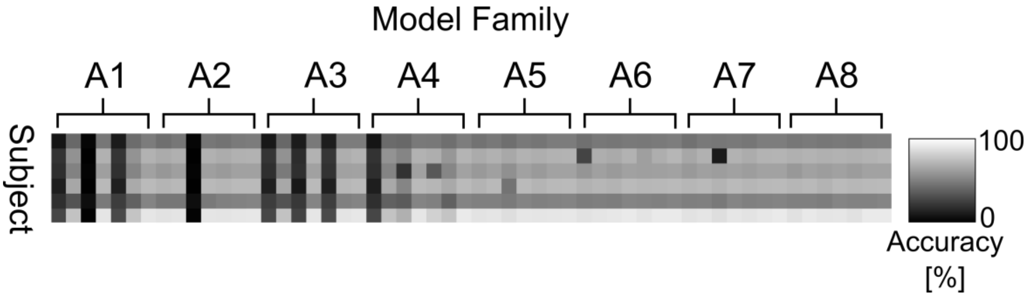

Figure 6.15. Model accuracy matrix, showing that families of more complex models are more accurate than simpler models. Each row corresponds to a different subject, and each column to a different model. Models are grouped by connection families, and within each family the ith column corresponds to family C$_i$, i.e. the 3rd column of family A1 is model A1-C3.

As can be seen from Figure 6.15, there is some structure to the model accuracy matrix – more complicated connection models (moving from family A1-A3 through to A8) explain a greater proportion of the observed data, and that models with a greater number of driving inputs (C4-C6,C7) are also more accurate.

Bayesian Parameter Averaging

Given the model described in Figure 6.11, Bayesian parameter averaging (BPA) was used to define the coupling parameters for each connection and input across subjects. These can be used for qualitative interpretation of effective connectivity in terms of strengths of connections between neuronal populations. As described in section 6.1.2, the coupling parameters that form the A, B, C matrices/vectors used in equation (2) should strictly be understood as rate constants of neuronal population responses that exponentially decay with time. Therefore coupling parameters in DCM are inversely proportional to the half-life of modelled neuronal responses, and are measured in units of Hz.

The output A matrix and C vector are shown in equation (7).

$$A = \begin{pmatrix} -0.11 & 0.00 & 0.06 \\ 0.00 & -0.18 & 0.24 \\ 0.14 & 0.13 & -0.05 \end{pmatrix}, \qquad C = \begin{pmatrix} 0.50 \\ 0.98 \\ -0.55 \end{pmatrix} \tag{7}$$

In matrix A, the set of connection parameters, each column contains connections *from* the LGd, SCs and VISp respectively, and each row contains connections *to* the LGd, SCs and VISp. In vector C, the set of driving input parameters, the regions are ordered LGd, SCs and VISp moving down the rows. Parameter plots with 90% confidence intervals are shown in Figure 6.16.

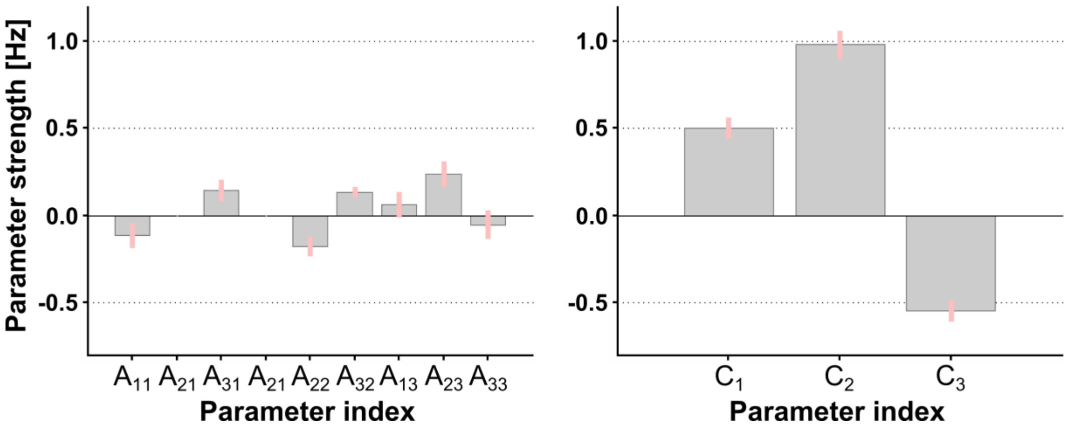

Figure 6.16. Parameter estimates with confidence intervals for connections (A matrix) and driving inputs (C matrix).

From Figure 6.16, we can be confident that all of the connection parameters and driving input parameters are of interest (90% confidence that they are non-zero) except for the VISp→LGd and the self-connection on the VISp.

The values of all connection and driving parameters are visualised in Figure 6.17.

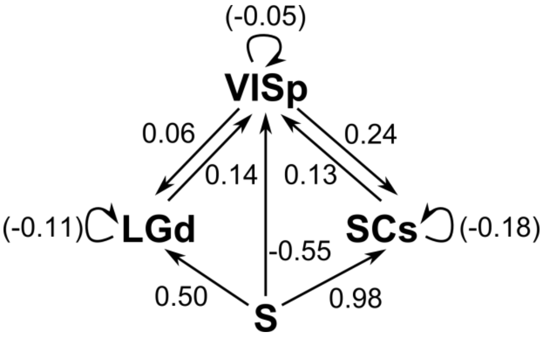

Figure 6.17. Estimates of connection strengths and driving inputs calculated using Bayesian parameter averaging.Self-connections (gain control parameters) are shown in brackets.

Interpreting these parameter values directly is difficult, as they correspond to an abstract representation of communication between neuronal populations. However, a qualitative assessment of the strengths of this network suggest that VISp and LGd are driven at approximately equal strength (but with opposite signs), and the SCs receiving the bulk of the positive stimulus input. In addition, LGd and SCs appear to influence VISp almost equally, but SCs receives a stronger top-down influence from VISp than LGd does. One encouraging result is that the negative self-connections indicate negative feedback in each region, avoiding exponentially increasing neural activity – which is not enforced by the model fitting procedure.

6.2.2.2 Experiment 2- Frequency modulation of connections

Using the information gained from section 6.2.2.1, the effect of frequency modulation on effective connectivity in the mouse visual system was considered. Therefore the dataset acquired in section 4.1 was used, and signal extraction completed in a similar fashion to the previous section. However, because of the inclusion of a parametric modulator (temporal flashing frequency f), a different design matrix was required and the contrasts used for BOLD signal extraction were modified. An example design matrix for a single subject is provided in Figure 6.18.

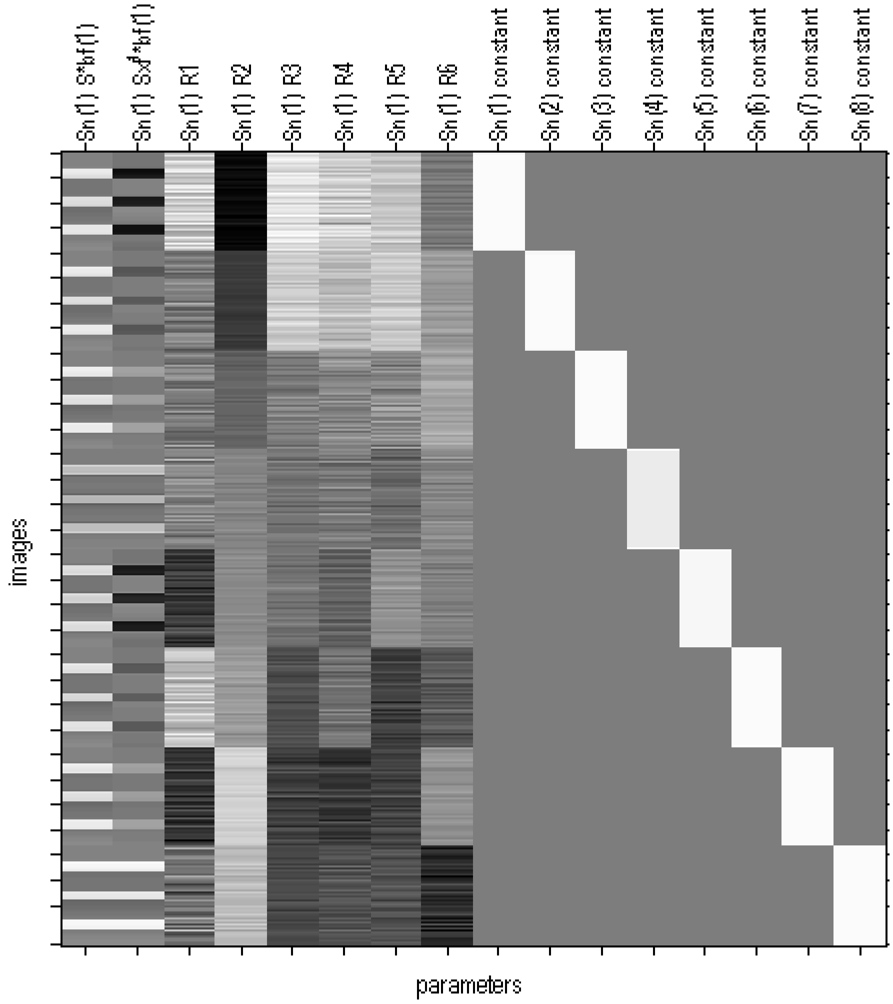

Figure 6.18. FFX GLM design matrix for concatenated fMRI runs. Data is concatenated through time. Columns are as follows: 1. model haemodynamic response; 2. Parametric modulation of haemodynamic response by flashing frequency) 3-8. Concatenated motion parameter estimates; 9-16. Run-specific regressors. Low-frequency regressors used in the discrete cosine transform for high-pass filtering are hidden by default by SPM12.

The 1^{st} eigenvariate signal was extracted with a GLM F-contrast vector of [1 0; 0 1] padded with zeros to define the effects of interest (the stimulus driver S and the flashing frequency f). For each subject, the F-statistic map was thresholded at $p < 0.05$ (uncorrected for multiple comparisons), and the cluster peak closest to each visual ROI location recorded. All subjects had significant voxels within the LGd, SCs and VISp regions, and were therefore all included.

As the question of interest now concerned how the parameter f modulates effective connectivity, the structural model arrived at in section 6.2.2.1 was used, and variations on the B matrix investigated with Bayesian model selection. Four variations were considered:

1. The null model, insofar that f has no modulatory effect
2. f modulates the bi-directional connection between LGd and VISp
3. f modulates the bi-directional connection between LGd and SCs
4. f modulates the self-connection within VISp

As only four plausible models were considered here, the issue of model dilution was not deemed relevant, and therefore the basic RFX BMS approach was used. The result of this comparison is shown in Figure 6.19.

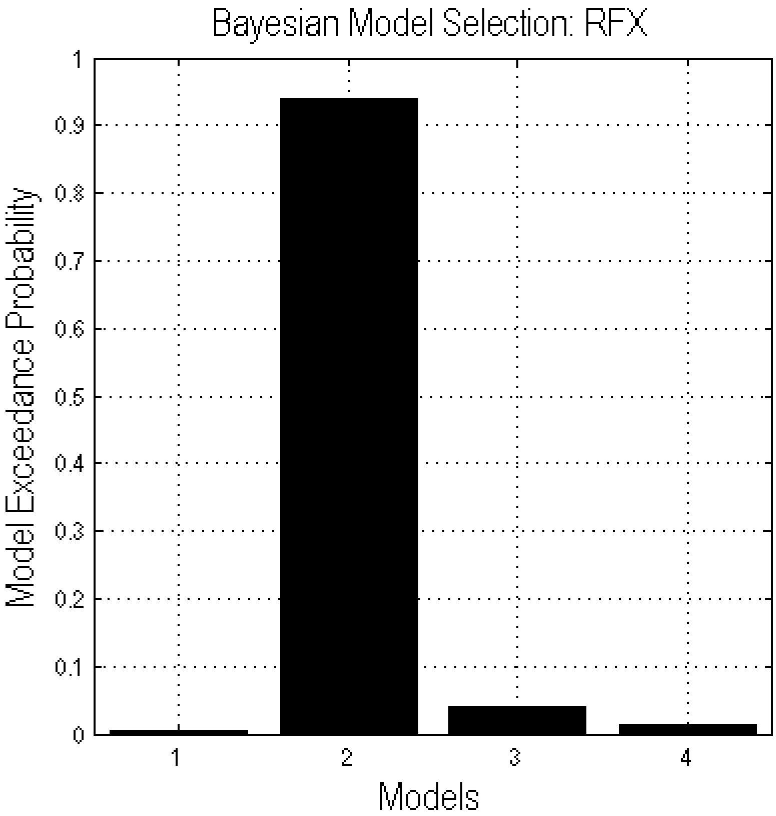

Figure 6.19. RFX Bayesian model selection (B) on variations of the modulatory effect of *f*.

From this comparison, we can be over 90% confident that there is frequency modulation of the LGd-VISp connection relative to the rest of the model space. The variances explained by this model for each subject are plotted in Figure 6.20.

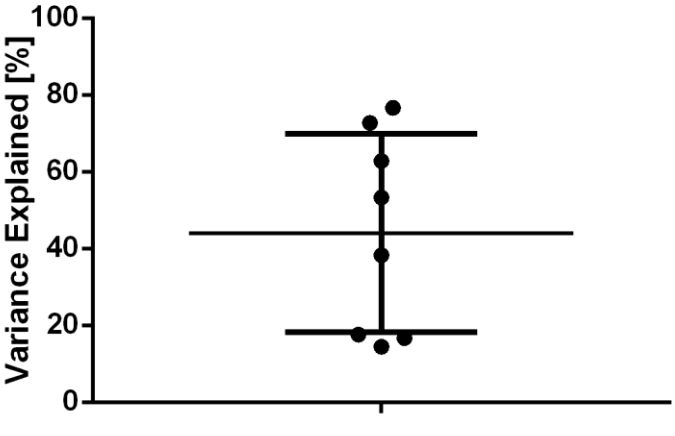

Figure 6.20. Spread of % variances explained by the winning model across subjects. This is a good validation of the generalisability of the model defined by the A and C matrices selected by experiment 1.

Bayesian parameter averaging was then performed to define the coupling parameters for each connection and input across subjects, with results shown in equation (8).

$$
\begin{aligned}
A &= \begin{pmatrix} -0.43 & 0.00 & -0.04 \\ 0.00 & -0.36 & 0.01 \\ 0.06 & 0.05 & -0.73 \end{pmatrix} \\
B &= \begin{pmatrix} 0.00 & 0.00 & 0.24 \\ 0.00 & 0.00 & 0.00 \\ -0.05 & 0.00 & 0.00 \end{pmatrix} \\
C &= \begin{pmatrix} 0.10 \\ 0.20 \\ 0.06 \end{pmatrix}
\end{aligned}
\qquad \textbf{(8)}
$$

The parameter values are plotted with 90% confidence intervals in Figure 6.21.

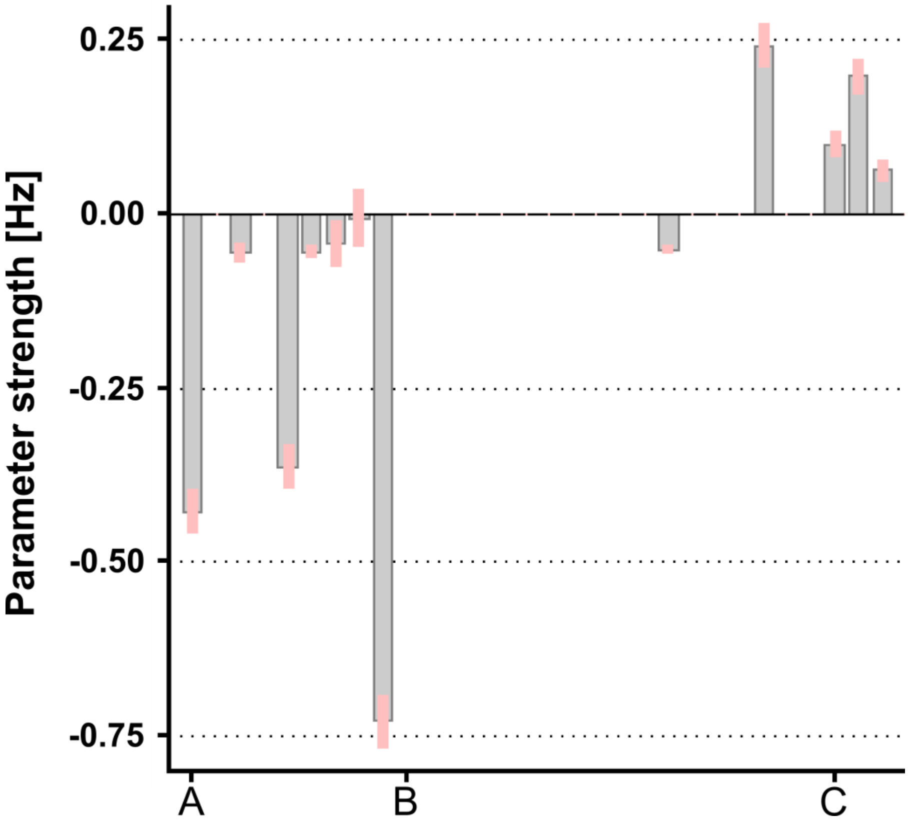

Figure 6.21. Parameter values with 90% confidence intervals for A, B, and C matric parameters. The parameters for the A matrix have markedly different values relative to those of the same model structure for the previous dataset.

A summary of this network model, in relation to Figure 6.11, is shown in Figure 6.22.

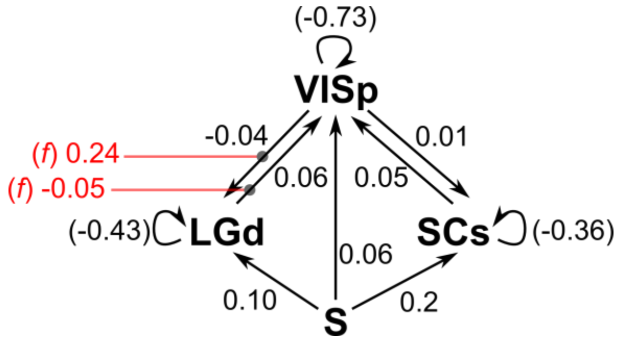

Figure 6.22. Bayesian Parameter Averaging (experiment 2). Estimates of connection strengths, and driving inputs are shown in black, and modulation effects are shown in red.

The parameter values for this model are markedly different from the parameters estimated and shown in Figure 6.16, in particular the connections within the A matrix. Whilst the self-connections remain strongly negative, the values of parameters representing the connections between regions are much lower. Furthermore, relative to the parameters shown in Figure 6.17, the input to the VISp is now weakly positive rather than negative. This can be explained by the negative frequency modulation parameter for the LGd→VISp connection, suggesting that as frequency increases, it is the LGd which inhibits neuronal activity in the VISp, generating the observed negative BOLD responses.

6.2.3 Discussion

There are multiple ways of defining brain connectivity, including anatomical, functional and effective connectivity, as described in section 6.2.1. In this work, previously described task-based fMRI data (see section 3.3) were analysed using dynamic causal modelling, to make inferences on effective network connectivity in the mouse visual system. This initial *in vivo* interleaved snapshot ($n = 4$ snapshots) GE-EPI dataset (experiment 1) which included six mice was used to make inferences on model structure and driving input, which were broadly compatible with invasive electrophysiological and tracer studies [26, 84], suggesting a functional segregation between the LGd and SCs. This model was then propagated through to make inferences on the modulatory effects of the temporal flashing frequency, using the dataset described in section 4.1 (experiment 2, eight mice), and strong evidence was found that the flashing frequency modulated the LGd-VISp connection. However, model parameters common to both data sets (the connections and strengths of the driving inputs) proved to be markedly different. This could be due to strong covariance or interdependence between certain parameters, as previously noted in a DCM fMRI study reproducibility study [196]. However the difference in experimental designs means that experiment 2 is much richer in data than experiment 1, in particular the possibility for VISp to show both positive and negative BOLD responses. Therefore it is not necessarily surprising that the parameter set take different values to accommodate this, as the same connection strength and driving input priors for the parameters were used for both experiments.

There are certain limitations to the analysis used here. Firstly, default priors for haemodynamic parameters were assumed. The characteristic haemodynamic parameters for the extended balloon model used in the current implementation of the SPM12 toolbox are shown in Table 6.3.

Table 6.3. Haemodynamic parameter priors for use in dynamic causal modelling in SPM12. Of these, only signal decay and transit time are free to vary across brain regions.

Parameter name	Prior mean	Units
Signal decay	0.64	Hz
Autoregulation	0.32	s
Transit time	2.00	s
Grubb’s exponent	0.32	n/a
Resting oxygen extraction fraction	0.4	n/a
Ratio of intra- to extra-vascular signal	1	n/a
Resting venous blood volume fraction	0.04	%

To the best of my knowledge the extended balloon model has never been applied to mouse fMRI data, and future work investigating these parameters that characterise the extended balloon model in the mouse brain is warranted. It is likely that the haemodynamic priors will vary between humans and mice, given the results of chapter 5, and therefore models which use mouse specific haemodynamic priors are likely to outperform ones which don’t. This could be directly evaluated using FFX BMS as described in this section, and work investigating the resting venous blood volume fraction in human DCM fMRI has recently been completed [216].

Furthermore, only the bilinear, one-state DCM implementation was considered here. A non-linear version of equation (2) uses an additional term D in order to allow brain regions to directly modulate responses in other brain regions [217], whereas two-state DCMs model separate excitatory and inhibitory neuronal populations in each region [191]. In particular, when considering the negative BOLD response, it is plausible that a non-linear, two-state model may better explain neuronal inhibition in VISp than the models shown in Figure 6.11 and Figure 6.22.

The neuronal parameter prior values and covariances also require scrutiny. Given a summary of the literature provided by Huberman and Neill [26] and a later study by Wang et al. [215], we would not expect the system to have a driving input direct to the visual cortex, rather this signal to be relayed to the visual cortex predominantly by LGd. The default neural parameter priors use different priors for connections as opposed to drivers: whilst both are assumed to have a mean of zero, driver parameter priors are more relaxed (i.e. have greater variance) and therefore models with more driving inputs are penalised for complexity less harshly than models with fewer inputs but stronger connection parameters to relay inputs instead. Whilst these priors are commonly used for human DCM fMRI studies, no DCM fMRI studies so far have examined the primary visual system in the way described here; rather, more complex networks have been investigated using a driving input to a higher-level region to represent an entire sensory sub-network [218]. For understanding a primary sensory system as in this case, it would be interesting to relax the connection prior covariances and tighten the driver prior covariances. Alternatively, Bayesian model selection could be applied to the subset of models which do not have a direct input to VISp, given the description of the mouse biology in the available literature. Although DCM is suggested as a method for testing hypotheses on model structures that use varying numbers of driving inputs, the results from this section suggest that the complexity penalty for driving inputs under the default priors is potentially too low.

Another limitation is that anatomical information was not incorporated at the parameter prior level. Future mouse DCM fMRI work might use data from the mesoscale mouse brain connectome [184] to inform prior distributions on the connection parameters. This could be done either by modifying the prior mean, covariance, or both – although mapping from normalised connectivity values determined from tracer studies to the abstract parameter space of DCM may prove difficult.

There are some common criticisms of the Bayesian approach used in the DCM framework, raised by Lohmann et al. [219]. Most commonly raised is the relative nature of Bayesian model selection, in that the evidence of a single model is meaningless, it is only the difference in free energy between two models that provides information as to whether one model is more useful than another. As such, identifying a ‘true model’ has no meaning [220]. The variance of the BOLD signal explained by a model across subjects was shown in Figure 6.12, and is useful as a heuristic check that the temporal contrast to noise ratio is large enough to ensure that DCM is worth using, but does not account for model complexity or prior knowledge – the reason for using a Bayesian approach. The frequentist approach to model fitting commonly uses R^2 to evaluate the goodness-of-fit of a model, but rather than an absolute measure, it is computed relative to an implicit null model [221], and therefore can only be as informative if not worse than the BMS approach used here.

However the issue of reproducibility is more challenging – as data is considered fixed and models selected on their performance for a particular dataset, whilst one would hope that two separate experiments would yield the same winning model, this may not be the case, and it may prove that pooling the data yields a different model altogether. This is partially addressed by the use of RFX BMS, but this loses the perfectly reasonable assumption that all subjects are using the same model. Alternatively one could use the posterior estimates from one experiment as priors for a second (this was informally done by propagating the model structure from experiment 1 to experiment 2). Future work might also use group information at the model inversion stage, using an implementation of a parametric empirical Bayes scheme [222]. Driving input priors also require further scrutiny.

Establishing the validity of dynamic causal modelling is critical for future work. There is currently only one published animal study using DCM for fMRI [201], which successfully used DCM with a modified haemodynamic model to describe effective connectivity in a rat model of epilepsy, with invasive EEG recordings used to validate results from DCM. The work described in this section provides a platform for further validation of DCM, in particular with respect to primary sensory systems. Future efforts should focus on the ability of DCM to infer haemodynamic signal behaviour that could be validated with more direct, invasive techniques such as optical imaging spectroscopy.

6.2.4 Conclusion

Dynamic causal modelling was applied in its simplest form (bilinear, one neuronal state per region) to understand visual system connectivity in the mouse brain using previously acquired fMRI data. Bayesian model selection yielded a winning model of connectivity that broadly agreed with current understanding of the mouse brain visual system, although evidence for a driving input to VISp is unlikely to reflect the underlying biology. Propagation of this model structure to a separate dataset allowed inferences to be made on temporal visual processing, with strong evidence that flashing frequency modulates the LGd→VISp connection.

6.3 Chapter summary

In this chapter, the first application of dynamic causal modelling (DCM) to mouse brain fMRI data was described. Section 6.1 introduced the theory and motivation behind DCM. In section 6.2, the processes of appropriate region definition, signal extraction and model estimation were described, and the application of Bayesian model selection and Bayesian parameter averaging used to make inferences on model structure and connection strengths from previously acquired data. The results from this DCM analysis are broadly consistent with the literature on structural connectivity in the mouse brain. In the following chapter, a critical discussion of this thesis will be presented.

7 Discussion

This chapter provides a final discussion of the thesis, and suggests ideas for future research. An overview of the thesis is provided in section 7.1, a discussion of the work and its limitations is presented in section 7.2, directions for future research suggested in section 7.3 and a final conclusion in section 7.4.

7.1 Thesis overview

In chapters 1 and 2, an introduction and background context to this thesis was provided. The case for reverse translation of common non-invasive human neuroimaging techniques for use in animal models was made. The importance of the mouse model as a neuroscience tool, and its potential for systematic genetic manipulation, was also emphasised. The application of fMRI to the mouse brain, whilst extremely technically challenging, can bridge the gap between invasive electrophysiological experiments in mice and non-invasive fMRI studies in humans. A review of BOLD fMRI applied in the mouse brain was given, and the lack of studies using visual stimuli was noted.

Chapter 3 detailed systematic work for developing a mouse fMRI protocol using visual stimuli. The majority of human fMRI studies use a visual input, however only one mouse fMRI study [31] explicitly attempted to measure BOLD responses to visual stimuli. This paper did not report physiologically realistic BOLD signal responses in the mouse brain visual system as it is commonly understood; an important justification for the work reported in this thesis. In chapter 4, implementations of increasingly complex visual stimuli for mouse fMRI were described, overcoming the geometric and field strength constraints of using a pre-clinical MRI scanner.

Chapter 5 described the implementation of a novel fMRI technique for measuring high-temporal resolution BOLD responses in the mouse superior colliculus. This data was used for the optimisation of the SPM12 canonical haemodynamic response function, which was shown to improve sensitivity in statistical parametric mapping of BOLD responses to visual stimuli in previously acquired data. High-temporal resolution BOLD fMRI in the mouse will also be useful to complement optical imaging spectroscopy studies, which measure haemodynamic responses on similar timescales [43, 223].

Finally in Chapter 6, the application of dynamic causal modelling to ‘standard’ mouse brain fMRI data was described. Generative models with varying structural connections and driving inputs were successfully estimated using mouse fMRI data, and used to formally test hypotheses on effective connectivity in the mouse visual system. The modulatory effect of stimulus flashing frequency was successfully localised to the connection between the lateral geniculate nuclei and primary visual cortex, potentially accounting for the negative BOLD responses observed in the visual cortex at high flashing frequency.

7.2 Extended discussion and limitations

There are numerous difficulties associated with mouse fMRI. The largest driver of technical difficulties in mouse fMRI is the small size of the head, approximately 0.4 cubic centimetres. This necessitates the use of high-field MRI (greater than 7T) to ensure even adequate signal-to-noise. The use of strong magnetic fields, in combination with a sample occupying a small volume, means that assumptions of field homogeneity that are reasonable in human studies at 1.5 or 3T may be unsound in the mouse brain at 9.4T. Strong magnetic field gradients are necessary to ensure adequate spatial resolution to cover brain regions of interest with a sufficient number of voxels.

Beyond the size of the mouse brain, maintaining relevant mouse brain physiology for fMRI is also a challenge. In this thesis, a recoverable medetomidine anaesthesia protocol was used as a compromise between minimising head motion artefacts and preserving neurovascular coupling. A recently tested GABAergic anaesthetic agent called etomidate has shown promising results for mouse fMRI [61], with the potential for greater cross-strain applicability.

Whilst mouse brain fMRI with visual stimuli has been successfully implemented in this thesis, possibly one of the largest barriers to using it to answer questions on mouse brain biology is the complex interplay between physiologically relevant parameters that determine the measured BOLD response, such as cerebral blood flow, cerebral metabolic rate of oxygen consumption and oxygen extraction fraction [93]. This issue could be addressed in future work with the application of optical techniques to measure haemoglobin concentration directly, and validation using invasive electrophysiology experiments. Further advances in combining BOLD fMRI with arterial spin labelling (ASL) may also allow the implementation of calibrated

BOLD fMRI [224, 225] for use in mice, allowing the cerebral metabolic rate of oxygen consumption to be estimated using MRI alone.

Numerous difficulties of BOLD fMRI analysis associated with human studies are also applicable to the mouse. The growing literature on issues with fMRI data analysis is worth discussing. Whilst the work in this thesis has aimed to implement current fMRI techniques in the mouse brain, there are still limitations common to human fMRI data analysis which also reverse-translate to the mouse. For example, the use of statistical null-hypothesis testing with thresholding can under certain parameter choices have unacceptably large false positive rates [226], the number of researcher degrees of freedom [227] and the difficulties faced in reverse-inference [4, 228, 229] are all issues which the field of fMRI currently faces.

In the context of what is currently known about mouse brain biology, the work in this thesis has consistently generated concordant results, demonstrating the applicability of fMRI in the mouse brain using visual stimuli.

7.3 Directions for future research

There are a number of new questions which naturally arise from the work presented in this thesis. First of all, the question of whether these protocols can be used in conjunction with transgenic mouse models has not directly been addressed here. All mice used in this work are of the C57BL/6 strain, and it is plausible that the medetomidine protocol used may not be compatible with transgenic mice of different strains [61, 230]. Alternative anaesthesia agents should be considered for future experiments. Further improvements to the methodology could also focus on the implementation of multi-band EPI [231] as used in the human connectome project[5], or a slice-to-volume reconstruction approach as used for functional connectivity measurements of the human foetal brain [232]. This method in particular may be of relevance to awake mouse fMRI experiments, although without dedicated multi-coil arrays this may prove challenging to implement.

Second, the use of spatially varying stimuli requires further development to match stimuli commonly used in the mouse electrophysiology literature. The use of these more advanced stimuli will allow direct comparison of BOLD fMRI data with electrophysiology measurements, with the potential for paired studies using both the complementary techniques. Also from a translation point of view, moving from block-design experiments to event-related design experiments will increase the

---

[5] http://www.humanconnectome.org/documentation/Q1/imaging-protocols.html

relevance to human fMRI studies, and will likely improve haemodynamic parameter estimation as described in chapter 5.

Third, a better understanding of mouse haemodynamics using BOLD fMRI is possible. A natural extension of chapter 5 would be to use the haemodynamic modelling aspect of the dynamic causal modelling approach, and directly fit the extended balloon model of neurovascular coupling to the high-temporal resolution data acquired with line-scanning fMRI. As the model fitting could be completed using the same algorithms as dynamic causal modelling, models with different parameter priors could be estimated and compared using a Bayesian model selection approach. The posterior parameter estimates from this result could then be used to inform dynamic causal model estimation of neural and haemodynamic parameters. In addition, combination of haemodynamic parameter inferences with external validation from optical imaging techniques would be useful.

Fourth, greater application of DCM to mouse fMRI with visual tasks is warranted. The work described in this thesis is the first application of DCM to mouse fMRI data, and could be built upon to ask questions of inter-hemispheric connectivity and connection modulation by stimuli characteristics. The issue with driving input parameter priors raised in chapter 6 may also be problematic for human studies, and requires addressing. The use of a hierarchical model inversion scheme should allow the issue of model structure reproducibility to be formally addressed, and a robust application to understanding within- and between-group differences of effective connectivity will be extremely important to fulfil the potential of using fMRI with transgenic mouse models.

7.4 Conclusion

In this chapter, the work presented in this thesis was summarised, critically discussed and placed in the wider context of the scientific literature, with recommendations for future directions of research. The novel contributions to knowledge from this thesis are as follows:

1. The use of interleaved snapshot GE-EPI for task-based fMRI in the mouse brain improved spatial localisation of the BOLD signal without reducing temporal contrast-to-noise.

2. Reliable and network specific BOLD signal responses were induced in the mouse visual system with a flashing light stimulus. Both the sign and

magnitude of the BOLD response in the primary visual cortex were strongly modulated by the flashing frequency used. The use of dark flashes relative to light flashes suppressed BOLD responses in the superior colliculus, whilst a reduced BOLD response was seen in the primary visual cortex.

3. Line-scanning fMRI was used in the mouse brain to acquire high-temporal resolution BOLD responses in the superior colliculus. This data was then used to inform the shape of the haemodynamic response function, and used for more sensitive statistical parametric mapping analyses.
4. Dynamic causal modelling was used to describe effective connectivity in the mouse brain, allowing inferences on causal links between brain regions in the visual system to be made.

From the work described in this thesis, it can be concluded that mouse BOLD fMRI using visual stimuli is robust, and could be used for future studies investigating mouse brain biology, linking human fMRI measurements to invasive mouse brain measurements, or directly examining genetic effects on brain function using transgenic mouse models. Furthermore, although questions remain regarding the precise relationship between the measured BOLD signal and underlying neuronal activity, this implementation of mouse fMRI may provide a platform for future studies to improve our understanding of neurovascular coupling and functional neuroscience across humans and mice.

Appendix

Appendix A

Code snippets showing the implementation of image registration as described in section 3.2 are shown.

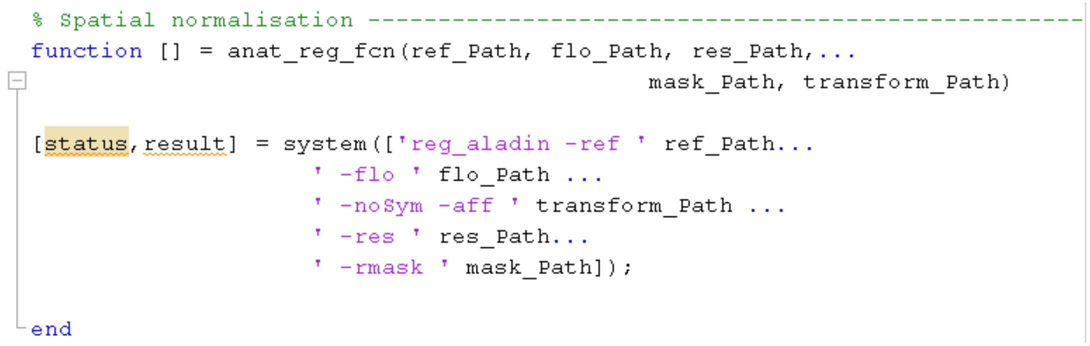

```
% Spatial normalisation ------------------------------------------------
function [] = anat_reg_fcn(ref_Path, flo_Path, res_Path,...
                                          mask_Path, transform_Path)

[status,result] = system(['reg_aladin -ref ' ref_Path...
                   ' -flo ' flo_Path ...
                   ' -noSym -aff ' transform_Path ...
                   ' -res ' res_Path...
                   ' -rmask ' mask_Path]);

end
```

Code snippet for running the NiftyReg toolbox implementation of affine registration. The registration uses a manually defined brain mask of the target image, and therefore requires the non-symmetric (‘-noSym’) option. The resulting affine transformation matrix is saved as a text file at the address specified by the MATLAB function input ‘transform_Path’.

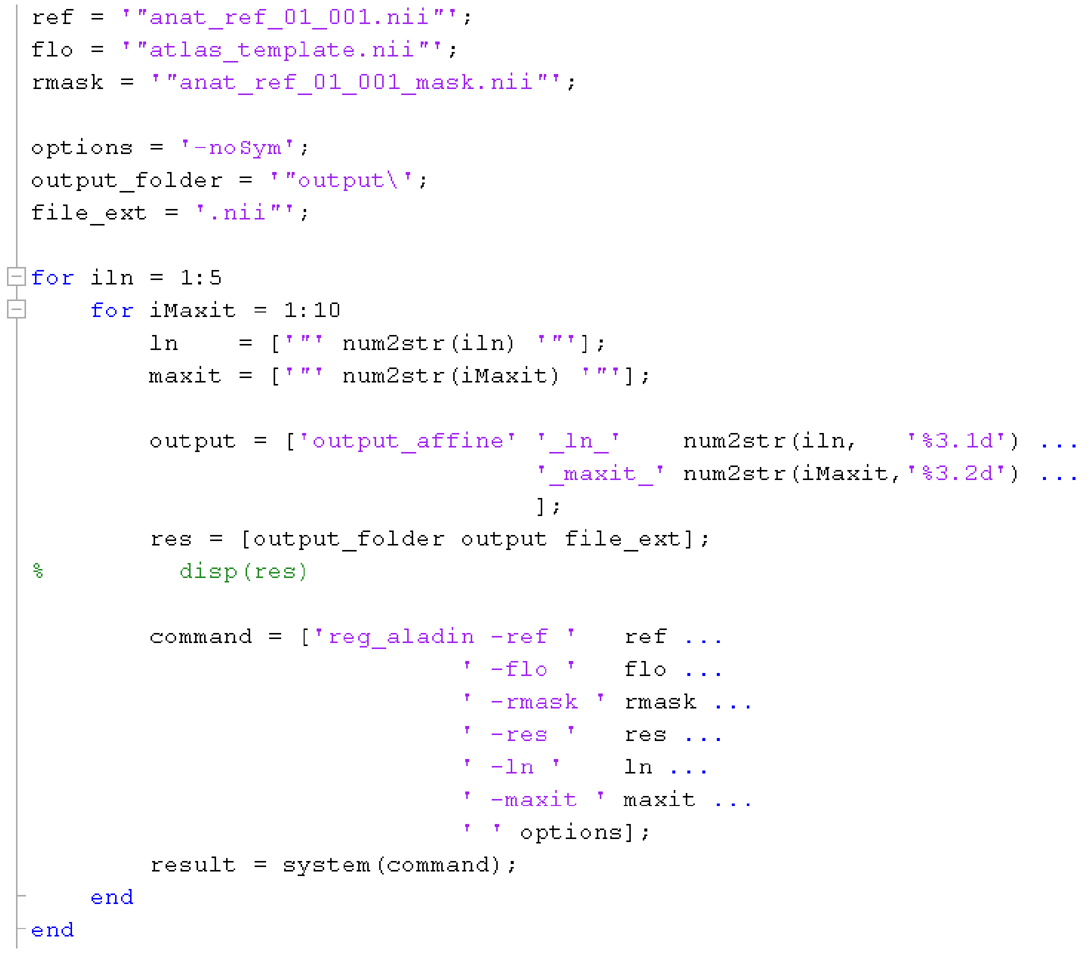

```
ref = '"anat_ref_01_001.nii"';
flo = '"atlas_template.nii"';
rmask = '"anat_ref_01_001_mask.nii"';

options = '-noSym';
output_folder = '"output\';
file_ext = '.nii"';

for iln = 1:5
    for iMaxit = 1:10
        ln     = ['"' num2str(iln) '"'];
        maxit = ['"' num2str(iMaxit) '"'];

        output = ['output_affine' '_ln_'    num2str(iln,   '%3.1d') ...
                                  '_maxit_' num2str(iMaxit,'%3.2d') ...
                                  ];
        res = [output_folder output file_ext];
%         disp(res)

        command = ['reg_aladin -ref '   ref ...
                             ' -flo '   flo ...
                             ' -rmask ' rmask ...
                             ' -res '   res ...
                             ' -ln '    ln ...
                             ' -maxit ' maxit ...
                             ' ' options];
        result = system(command);
    end
end
```

Code snippet to optimise Aladin hyper-parameters for registration of the AMBA to a T_2 weighted structural scan. The default values for ln and maxit are 3 and 5 respectively.

Here, modifications to the MarsBaR toolbox code used in section 3.3 are shown.

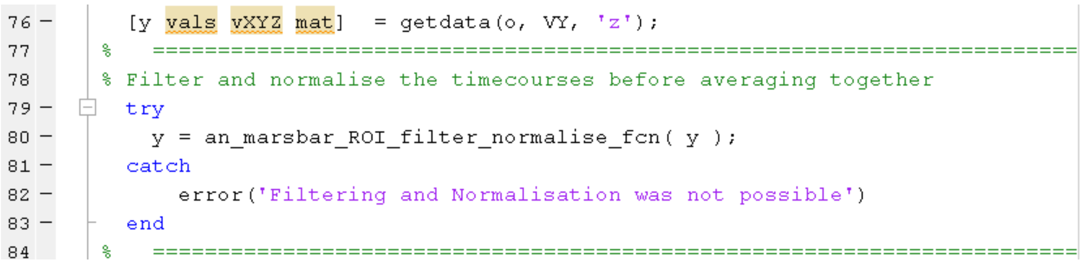

```
  [y vals vXYZ mat]  = getdata(o, VY, 'z');
%   =======================================================================
% Filter and normalise the timecourses before averaging together
  try
    y = an_marsbar_ROI_filter_normalise_fcn( y );
  catch
      error('Filtering and Normalisation was not possible')
  end
%   =======================================================================
```

Code snippet - edits to the get_marsy.m routine in the MarsBaR toolbox for signal extraction from an ROI. The an_marsbar_ROI_filter_normalise_fcn routine filters and normalises the signals before averaging.

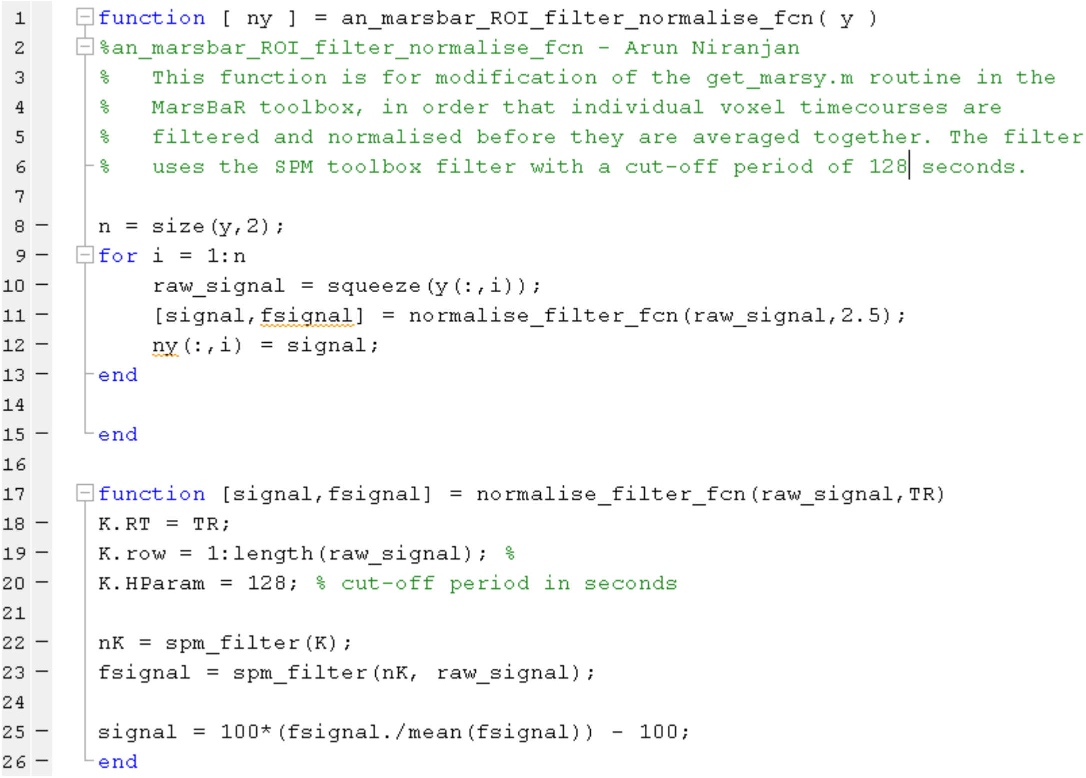

```
function [ ny ] = an_marsbar_ROI_filter_normalise_fcn( y )
%an_marsbar_ROI_filter_normalise_fcn - Arun Niranjan
%   This function is for modification of the get_marsy.m routine in the
%   MarsBaR toolbox, in order that individual voxel timecourses are
%   filtered and normalised before they are averaged together. The filter
%   uses the SPM toolbox filter with a cut-off period of 128 seconds.

n = size(y,2);
for i = 1:n
    raw_signal = squeeze(y(:,i));
    [signal,fsignal] = normalise_filter_fcn(raw_signal,2.5);
    ny(:,i) = signal;
end

end

function [signal,fsignal] = normalise_filter_fcn(raw_signal,TR)
K.RT = TR;
K.row = 1:length(raw_signal); %
K.HParam = 128; % cut-off period in seconds

nK = spm_filter(K);
fsignal = spm_filter(nK, raw_signal);

signal = 100*(fsignal./mean(fsignal)) - 100;
end
```

Code snippet of the an_marsbar_ROI_filter_normalise_fcn routine. This function uses the SPM toolbox discrete cosine transform high pass filter, and filters and normalises each voxel timecourse.

Appendix B

From section 4.5, code to operate an Arduino to deliver a visual stimulus from an LED array using the NeoPixel library is included here:

```
// Flashing Block (condition 1) visual stimulus using NeoPixel
// Written by Arun Niranjan 2016-03-14

// Libraries and Pin Definitions
//========================================================================
#include <Adafruit_GFX.h>
#include <Adafruit_NeoMatrix.h>
```

```
#include <Adafruit_NeoPixel.h>
#ifndef PSTR
#define PSTR
#endif

#define PIN 6 // output to matrix on pin 6
#define TTL 12  // input TTL on pin 12
//========================================================================

// Previous code from the NeoPixel example code, left in for posterity
// MATRIX DECLARATION:
// Parameter 1 = width of NeoPixel matrix
// Parameter 2 = height of matrix
// Parameter 3 = pin number (most are valid)
// Parameter 4 = matrix layout flags, add together as needed:
//   NEO_MATRIX_TOP, NEO_MATRIX_BOTTOM, NEO_MATRIX_LEFT, NEO_MATRIX_RIGHT:
//     Position of the FIRST LED in the matrix; pick two, e.g.
//     NEO_MATRIX_TOP + NEO_MATRIX_LEFT for the top-left corner.
//   NEO_MATRIX_ROWS, NEO_MATRIX_COLUMNS: LEDs are arranged in horizontal
//     rows or in vertical columns, respectively; pick one or the other.
//   NEO_MATRIX_PROGRESSIVE, NEO_MATRIX_ZIGZAG: all rows/columns proceed
//     in the same order, or alternate lines reverse direction; pick one.
//   See example below for these values in action.
// Parameter 5 = pixel type flags, add together as needed:
//   NEO_KHZ800  800 KHz bitstream (most NeoPixel products w/WS2812 LEDs)
//   NEO_KHZ400  400 KHz
//   (classic 'v1' (not v2) FLORA pixels, WS2811 drivers)
//   NEO_GRB Pixels are wired for GRB bitstream (most NeoPixel products)
//   NEO_RGB Pixels are wired for RGB bitstream (v1 FLORA pixels, not v2)


// Example for NeoPixel Shield.  In this application we'd like to use it
// as a 5x8 tall matrix, with the USB port positioned at the top of the
// Arduino.  When held that way, the first pixel is at the top right, and
// lines are arranged in columns, progressive order.  The shield uses
// 800 KHz (v2) pixels that expect GRB color data.

Adafruit_NeoMatrix matrix = Adafruit_NeoMatrix(32, 8, PIN,
                            NEO_MATRIX_BOTTOM     + NEO_MATRIX_RIGHT +
                            NEO_MATRIX_COLUMNS + NEO_MATRIX_ZIGZAG,
                            NEO_GRB            + NEO_KHZ800);
//========================================================================

/*
   For the way we will position the board in the Agilent 9.4T MRI Scanner,
   pixel 1 corresponds to the bottom left corner of the board, rasterising
      across the board from left to right, bottom to top. Each row is 8
  pixels long, and there are 32 rows in total.
*/

// Define pixels per row
int nPixelsPerRow = 8;

// Define Starting row of the board
int startRow = 5;

// Define how many rows the block will use
int nRowsPerBlock = 5;
```

```
// Define the number of activation periods
int nActivations = 5;

//s Delaying by 40s doesn't work, so set to 20s and delay twice.
int baselineDelay = 20;

int referenceDelay = 0; // ms
int maxBrightness = 20;

//int blockStimDuration = 2; //s
int nCycles = 40;
//nCyclesPerBlock = blockStimDuration*2;  // 2 Hz

// State pixels per block
int nPixelsPerBlock = nPixelsPerRow*nRowsPerBlock;

int width   = matrix.width();
int pass    = 0;
int val     = 0;

void setup() {
  pinMode(TTL, INPUT);      // sets the digital pin 7 as input
  matrix.begin();
  matrix.setBrightness(maxBrightness);
}

// Clear the board
//matrix.fillScreen(0);
//matrix.show();

//=========================================================================
void loop() {

  // First make blank
  matrix.fillScreen(0);
  matrix.show();

  // Here wait for ttl trigger on pin TTL
  val = digitalRead(TTL);   // read the input pin

  //val = 1; // Uncomment to fake a trigger from the TTL pin

  // Increment position counter here depending on whether TTL received
  if (val > 0) {
    // Trigger detected
    // First make blank
    matrix.fillScreen(0);
    matrix.show();

    // Wait for the reference image to be acquired
    delay(referenceDelay); // in ms

    // Loop over baseline and activation periods
    for (int iActivation = 1; iActivation<=nActivations; iActivation++) {

      // Wait for the baseline time
      delay(baselineDelay * 1000); // in ms
      delay(baselineDelay * 1000); // in ms
```

```
      // Loop over passes
      for (int iCycle = 1; iCycle <= nCycles; iCycle++) {

        // Light up the block for each cycle
        for (int iPixel = 0; iPixel < nPixelsPerBlock; iPixel++) {
          matrix.setPixelColor((startRow *nPixelsPerRow) +
                                    iPixel, matrix.Color(255, 255, 255));
        }

        matrix.show();
        delay(250);
        matrix.fillScreen(0);
        matrix.show();
        delay(250);
      }
    }
    exit(0);
  }
}
//========================================================================
```

Appendix C

Here, code used in sections 5.1 and 5.2 are included.

```
[RE, IM] = vload2(Scan_Name);
CO = RE + sqrt(-1)*IM;
Signal = fftshift(fft(CO),1);
Magnitude = abs(Signal);
coils_both = zeros(size(Magnitude,1),size(Magnitude,2)/2,2);
coils_both(:,:,1) = Magnitude(:,1:2:end);
coils_both(:,:,2) = Magnitude(:,2:2:end);
coil_average = mean(coils_both,3);
```

MATLAB code snippet for line-scanning reconstruction. The vload2 function was provided by Varian Inc. and extracts the real and imaginary signals from the VNMRJ .fid file.

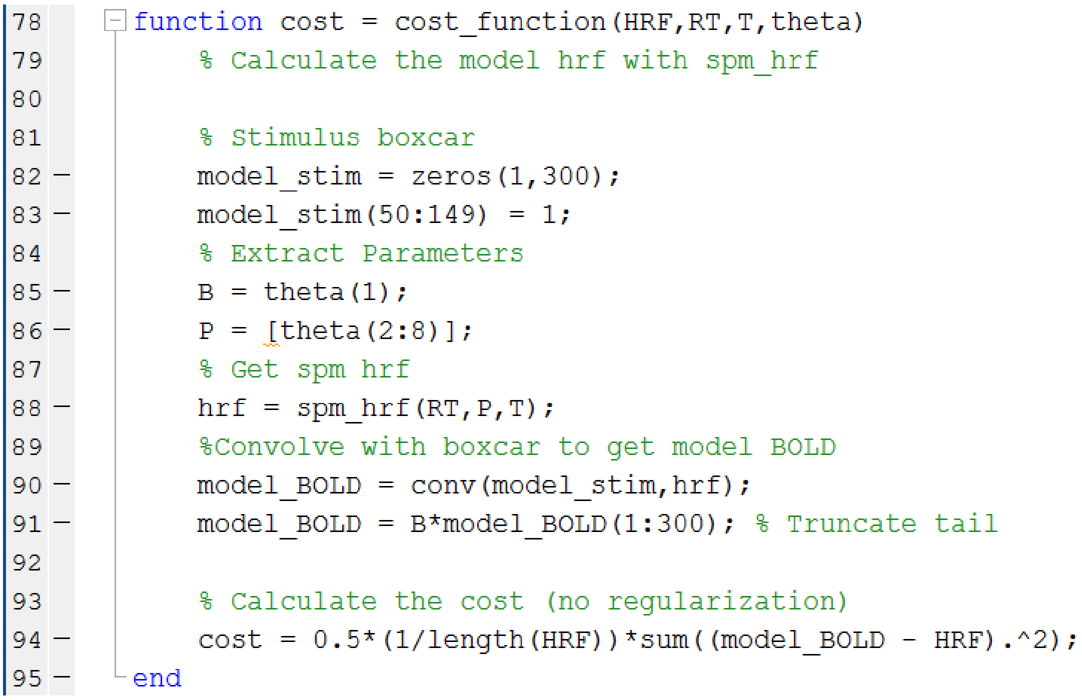

```matlab
function cost = cost_function(HRF,RT,T,theta)
    % Calculate the model hrf with spm_hrf

    % Stimulus boxcar
    model_stim = zeros(1,300);
    model_stim(50:149) = 1;
    % Extract Parameters
    B = theta(1);
    P = [theta(2:8)];
    % Get spm hrf
    hrf = spm_hrf(RT,P,T);
    %Convolve with boxcar to get model BOLD
    model_BOLD = conv(model_stim,hrf);
    model_BOLD = B*model_BOLD(1:300); % Truncate tail

    % Calculate the cost (no regularization)
    cost = 0.5*(1/length(HRF))*sum((model_BOLD - HRF).^2);
end
```

Code snippet showing non-regularised cost function for HRF optimisation. The function inputs are the measured BOLD signal (HRF), the temporal resolution (RT), the microtime resolution (T), and the parameters to be optimised (contained in theta).

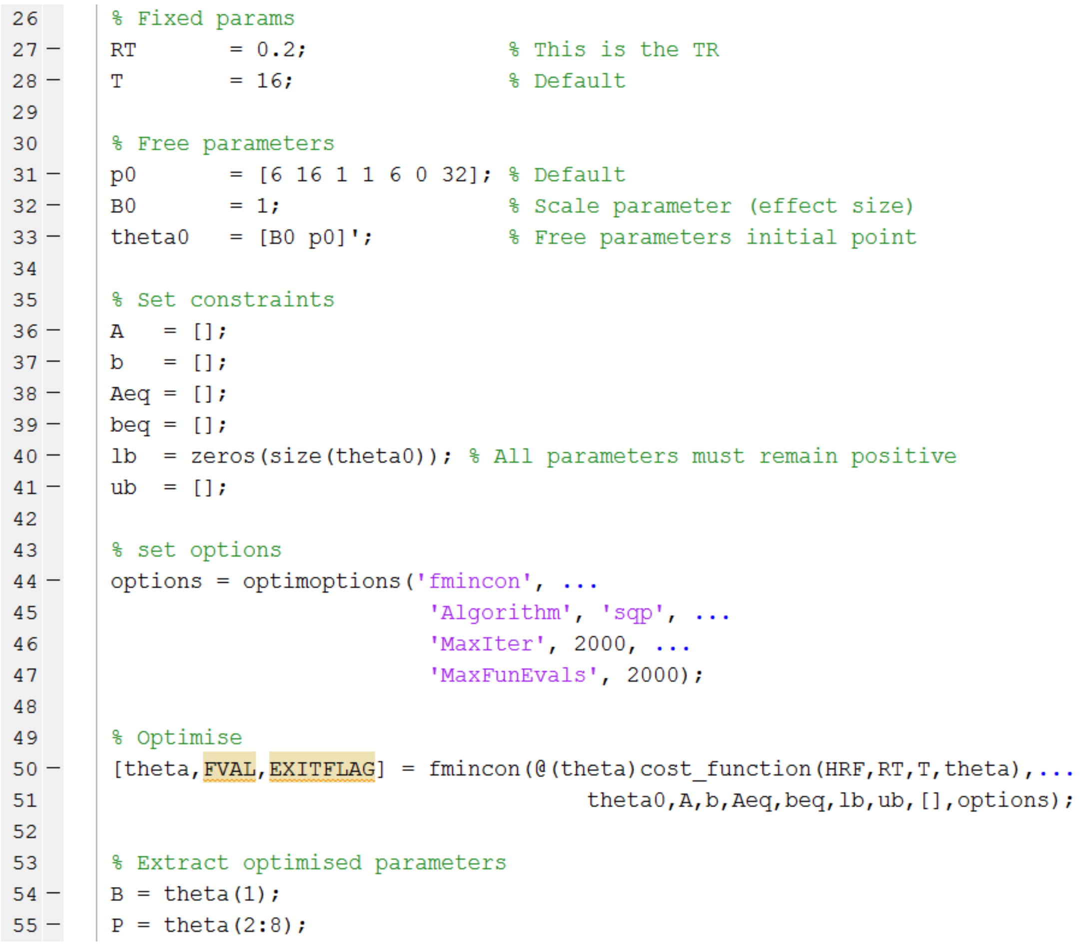

```matlab
% Fixed params
RT        = 0.2;              % This is the TR
T         = 16;               % Default

% Free parameters
p0        = [6 16 1 1 6 0 32]; % Default
B0        = 1;                % Scale parameter (effect size)
theta0    = [B0 p0]';         % Free parameters initial point

% Set constraints
A   = [];
b   = [];
Aeq = [];
beq = [];
lb  = zeros(size(theta0)); % All parameters must remain positive
ub  = [];

% set options
options = optimoptions('fmincon', ...
                        'Algorithm', 'sqp', ...
                        'MaxIter', 2000, ...
                        'MaxFunEvals', 2000);

% Optimise
[theta,FVAL,EXITFLAG] = fmincon(@(theta)cost_function(HRF,RT,T,theta),...
                                    theta0,A,b,Aeq,beq,lb,ub,[],options);

% Extract optimised parameters
B = theta(1);
P = theta(2:8);
```

Code snippet showing non-linear optimisation of the double-gamma HRF using the ‘sqp’ algorithm.

References

[1] C. Martin, Contributions and complexities from the use of in vivo animal models to improve understanding of human neuroimaging signals, Frontiers in neuroscience (2014),Vol 8.
[2] R.A. Poldrack, M.J. Farah, Progress and challenges in probing the human brain, Nature (2015),Vol 526, pg. 371-379.
[3] J.M. Harlow, Recovery from the passage of an iron bar through the head, D. Clapp, 1869.
[4] S.A. Huettel, A.W. Song, G. McCarthy, Functional magnetic resonance imaging, Sinauer Associates, Sunderland, Mass, 2009.
[5] S. Ogawa, T.M. Lee, A.R. Kay, D.W. Tank, Brain magnetic resonance imaging with contrast dependent on blood oxygenation, Proceedings of the National Academy of Sciences of the United States of America (1990),Vol 87, pg. 9868-9872.
[6] E. Niedermeyer, F.L. da Silva, Electroencephalography: basic principles, clinical applications, and related fields, Lippincott Williams & Wilkins, 2005.
[7] L.F. Haas, Hans Berger (1873-1941), Richard Caton (1842-1926), and electroencephalography, Journal of neurology, neurosurgery, and psychiatry (2003),Vol 74, pg. 9.
[8] D.L. Bailey, D.W. Townsend, P.E. Valk, M.N. Maisey, Positron emission tomography, Springer, 2005.
[9] M.M. Ter-Pogossian, M.E. Phelps, E.J. Hoffman, N.A. Mullani, A Positron-Emission Transaxial Tomograph for Nuclear Imaging (PETT), Radiology (1975),Vol 114, pg. 89-98.
[10] P.A. Bandettini, Twenty years of functional MRI: The science and the stories, Neuroimage (2012),Vol 62, pg. 575-588.
[11] P.A. Bandettini, E.C. Wong, R.S. Hinks, R.S. Tikofsky, J.S. Hyde, Time course EPI of human brain function during task activation, Magnetic Resonance in Medicine (1992),Vol 25, pg. 390-397.
[12] K.K. Kwong, J.W. Belliveau, D.A. Chesler, I.E. Goldberg, R.M. Weisskoff, B.P. Poncelet, D.N. Kennedy, B.E. Hoppel, M.S. Cohen, R. Turner, et al., Dynamic magnetic resonance imaging of human brain activity during primary sensory stimulation, Proceedings of the National Academy of Sciences of the United States of America (1992),Vol 89, pg. 5675-5679.
[13] A.M. Blamire, S. Ogawa, K. Ugurbil, D. Rothman, G. McCarthy, J.M. Ellermann, F. Hyder, Z. Rattner, R.G. Shulman, Dynamic mapping of the human visual cortex by high-speed magnetic resonance imaging, Proceedings of the National Academy of Sciences of the United States of America (1992),Vol 89, pg. 11069-11073.
[14] E.M. Haacke, S. Lai, D.A. Yablonskiy, W. Lin, In vivo validation of the bold mechanism: A review of signal changes in gradient echo functional MRI in the presence of flow, International Journal of Imaging Systems and Technology (1995),Vol 6, pg. 153-163.
[15] N.K. Logothetis, J. Pauls, M. Augath, T. Trinath, A. Oeltermann, Neurophysiological investigation of the basis of the fMRI signal, Nature (2001),Vol 412, pg. 150-157.
[16] N.K. Logothetis, B.A. Wandell, Interpreting the BOLD signal, Annual review of physiology (2004),Vol 66, pg. 735-769.

[17] Peter A. Bandettini, The BOLD Plot Thickens: Sign- and Layer-Dependent Hemodynamic Changes with Activation, Neuron (2012),Vol 76, pg. 468-469.
[18] R. Turner, Uses, misuses, new uses and fundamental limitations of magnetic resonance imaging in cognitive science, Philosophical Transactions of the Royal Society B: Biological Sciences (2016),Vol 371.
[19] N.K. Logothetis, What we can do and what we cannot do with fMRI, Nature (2008),Vol 453, pg. 869-878.
[20] J. Goense, K. Whittingstall, N.K. Logothetis, Neural and BOLD responses across the brain, Wiley Interdisciplinary Reviews: Cognitive Science (2012),Vol 3, pg. 75-86.
[21] K.D. Singh, Which “neural activity” do you mean? fMRI, MEG, oscillations and neurotransmitters, Neuroimage (2012),Vol 62, pg. 1121-1130.
[22] N.K. Logothetis, H. Guggenberger, S. Peled, J. Pauls, Functional imaging of the monkey brain, Nature neuroscience (1999),Vol 2, pg. 555-562.
[23] M. Ma, C. Qian, Y. Li, Z. Zuo, Z. Liu, Setup and data analysis for functional magnetic resonance imaging of awake cat visual cortex, Neuroscience bulletin (2013),Vol 29, pg. 588-602.
[24] A. Andics, M. Gácsi, T. Faragó, A. Kis, Á. Miklósi, Voice-sensitive regions in the dog and human brain are revealed by comparative fMRI, Current Biology (2014),Vol 24, pg. 574-578.
[25] X. Yang, F. Hyder, R.G. Shulman, Activation of single whisker barrel in rat brain localized by functional magnetic resonance imaging, Proceedings of the National Academy of Sciences (1996),Vol 93, pg. 475-478.
[26] A.D. Huberman, C.M. Niell, What can mice tell us about how vision works? , Trends in Neurosciences (2011),Vol 34, pg. 464-473.
[27] C. The International Mouse Knockout, A Mouse for All Reasons, Cell (2007),Vol 128, pg. 9-13.
[28] T. Mueggler, C. Baltes, S. Bosshard, F. Princz-Kranz, D. Ratering, F. Razoux, E. Sydekum, M. Rudin, FMRI in Mice: Functional Phenotyping of Transgenic Mouse Lines Based on Hemodynamic Readouts, in: I.-Y. Choi, R. Gruetter (Eds.) Neural Metabolism In Vivo, Springer US, 2012, pg. 593-621.
[29] L. Luo, E.M. Callaway, K. Svoboda, Genetic Dissection of Neural Circuits, Neuron (2008),Vol 57, pg. 634-660.
[30] A.T. Chinwalla, L.L. Cook, K.D. Delehaunty, G.A. Fewell, L.A. Fulton, R.S. Fulton, T.A. Graves, L.W. Hillier, E.R. Mardis, J.D. McPherson, Initial sequencing and comparative analysis of the mouse genome, Nature (2002),Vol 420, pg. 520-562.
[31] W. Huang, I. Plyka, H. Li, E.M. Eisenstein, N.D. Volkow, C.S. Springer, Jr., Magnetic resonance imaging (MRI) detection of the murine brain response to light: temporal differentiation and negative functional MRI changes, Proceedings of the National Academy of Sciences of the United States of America (1996),Vol 93, pg. 6037-6042.
[32] G. Nair, T.Q. Duong, Echo-planar BOLD fMRI of mice on a narrow-bore 9.4 T magnet, Magnetic Resonance in Medicine (2004),Vol 52, pg. 430-434.

[33] J.M. Adamczak, T.D. Farr, J.U. Seehafer, D. Kalthoff, M. Hoehn, High field BOLD response to forepaw stimulation in the mouse, Neuroimage (2010),Vol 51, pg. 704-712.
[34] E.T. Ahrens, D.J. Dubowitz, Peripheral somatosensory fMRI in mouse at 11.7 T, NMR in biomedicine (2001),Vol 14, pg. 318-324.
[35] S.C. Bosshard, C. Baltes, M.T. Wyss, T. Mueggler, B. Weber, M. Rudin, Assessment of brain responses to innocuous and noxious electrical forepaw stimulation in mice using BOLD fMRI, PAIN (2010),Vol 151, pg. 655-663.
[36] C. Baltes, S. Bosshard, T. Mueggler, D. Ratering, M. Rudin, Increased blood oxygen level-dependent (BOLD) sensitivity in the mouse somatosensory cortex during electrical forepaw stimulation using a cryogenic radiofrequency probe, NMR in biomedicine (2011),Vol 24, pg. 439-446.
[37] F.A. Nasrallah, H.C. Tay, K.H. Chuang, Detection of functional connectivity in the resting mouse brain, Neuroimage (2014),Vol 86, pg. 417-424.
[38] A. Schroeter, F. Schlegel, A. Seuwen, J. Grandjean, M. Rudin, Specificity of stimulus-evoked fMRI responses in the mouse: the influence of systemic physiological changes associated with innocuous stimulation under four different anesthetics, Neuroimage (2014),Vol 94, pg. 372-384.
[39] A.P. Harris, R.J. Lennen, I. Marshall, M.A. Jansen, C.R. Pernet, N.M. Brydges, I.C. Duguid, M.C. Holmes, Imaging learned fear circuitry in awake mice using fMRI, The European journal of neuroscience (2015),Vol 42, pg. 2125-2134.
[40] F. Schlegel, A. Schroeter, M. Rudin, The hemodynamic response to somatosensory stimulation in mice depends on the anesthetic used: Implications on analysis of mouse fMRI data, Neuroimage (2015),Vol 116, pg. 40-49.
[41] S. Schuett, T. Bonhoeffer, M. Hubener, Mapping retinotopic structure in mouse visual cortex with optical imaging, The Journal of neuroscience : the official journal of the Society for Neuroscience (2002),Vol 22, pg. 6549-6559.
[42] J.A. Heimel, R.J. Hartman, J.M. Hermans, C.N. Levelt, Screening mouse vision with intrinsic signal optical imaging, The European journal of neuroscience (2007),Vol 25, pg. 795-804.
[43] P.S. Sharp, K. Shaw, L. Boorman, S. Harris, A.J. Kennerley, M. Azzouz, J. Berwick, Comparison of stimulus-evoked cerebral hemodynamics in the awake mouse and under a novel anesthetic regime, Scientific Reports (2015),Vol 5, pg. 12621.
[44] James H. Marshel, Marina E. Garrett, I. Nauhaus, Edward M. Callaway, Functional Specialization of Seven Mouse Visual Cortical Areas, Neuron (2011),Vol 72, pg. 1040-1054.
[45] N.G. Horton, K. Wang, D. Kobat, C.G. Clark, F.W. Wise, C.B. Schaffer, C. Xu, In vivo three-photon microscopy of subcortical structures within an intact mouse brain, Nat Photon (2013),Vol 7, pg. 205-209.
[46] U.C. Drager, Receptive fields of single cells and topography in mouse visual cortex, The Journal of comparative neurology (1975),Vol 160, pg. 269-290.
[47] M.S. Grubb, I.D. Thompson, Quantitative characterization of visual response properties in the mouse dorsal lateral geniculate nucleus, Journal of neurophysiology (2003),Vol 90, pg. 3594-3607.

[48] Q. Wang, A. Burkhalter, Area map of mouse visual cortex, The Journal of comparative neurology (2007),Vol 502, pg. 339-357.
[49] C.M. Niell, M.P. Stryker, Highly Selective Receptive Fields in Mouse Visual Cortex, The Journal of neuroscience : the official journal of the Society for Neuroscience (2008),Vol 28, pg. 7520-7536.
[50] E. Gao, G.C. DeAngelis, A. Burkhalter, Parallel input channels to mouse primary visual cortex, The Journal of neuroscience : the official journal of the Society for Neuroscience (2010),Vol 30, pg. 5912-5926.
[51] G. Van den Bergh, B. Zhang, L. Arckens, Y.M. Chino, Receptive-field properties of V1 and V2 neurons in mice and macaque monkeys, The Journal of comparative neurology (2010),Vol 518, pg. 2051-2070.
[52] J.H. Choi, K.P. Koch, W. Poppendieck, M. Lee, T. Doerge, H.S. Shin, A flexible microelectrode for mouse EEG, Conference proceedings : ... Annual International Conference of the IEEE Engineering in Medicine and Biology Society. IEEE Engineering in Medicine and Biology Society. Annual Conference (2009),Vol 2009, pg. 1600-1603.
[53] A. Verkhratsky, V. Parpura, History of electrophysiology and the patch clamp, Methods in molecular biology (Clifton, N.J.) (2014),Vol 1183, pg. 1-19.
[54] A. Grinvald, E. Lieke, R.D. Frostig, C.D. Gilbert, T.N. Wiesel, Functional architecture of cortex revealed by optical imaging of intrinsic signals, Nature (1986),Vol 324, pg. 361-364.
[55] J. Mayhew, D. Johnston, J. Berwick, M. Jones, P. Coffey, Y. Zheng, Spectroscopic analysis of neural activity in brain: increased oxygen consumption following activation of barrel cortex, Neuroimage (2000),Vol 12, pg. 664-675.
[56] K. Svoboda, R. Yasuda, Principles of Two-Photon Excitation Microscopy and Its Applications to Neuroscience, Neuron (2006),Vol 50, pg. 823-839.
[57] F. Helmchen, W. Denk, Deep tissue two-photon microscopy, Nature methods (2005),Vol 2, pg. 932-940.
[58] C. Stosiek, O. Garaschuk, K. Holthoff, A. Konnerth, In vivo two-photon calcium imaging of neuronal networks, Proceedings of the National Academy of Sciences (2003),Vol 100, pg. 7319-7324.
[59] C. Lau, I.Y. Zhou, M.M. Cheung, K.C. Chan, E.X. Wu, BOLD temporal dynamics of rat superior colliculus and lateral geniculate nucleus following short duration visual stimulation, PloS one (2011),Vol 6, pg. e18914.
[60] N. Van Camp, M. Verhoye, C.I. De Zeeuw, A. Van der Linden, Light Stimulus Frequency Dependence of Activity in the Rat Visual System as Studied With High-Resolution BOLD fMRI, Journal of neurophysiology (2006),Vol 95, pg. 3164-3170.
[61] M.M. Petrinovic, G. Hankov, A. Schroeter, A. Bruns, M. Rudin, M. von Kienlin, B. Künnecke, T. Mueggler, A novel anesthesia regime enables neurofunctional studies and imaging genetics across mouse strains, Scientific Reports (2016),Vol 6, pg. 24523.
[62] C.P. Pawela, A.G. Hudetz, B.D. Ward, M.L. Schulte, R. Li, D.S. Kao, M.C. Mauck, Y.R. Cho, J. Neitz, J.S. Hyde, Modeling of region-specific fMRI BOLD neurovascular response functions in rat brain reveals residual differences that correlate with the differences in regional evoked potentials, Neuroimage (2008),Vol 41, pg. 525-534.

[63] C. Lau, J.W. Zhang, K.K. Xing, I.Y. Zhou, M.M. Cheung, K.C. Chan, E.X. Wu, BOLD responses in the superior colliculus and lateral geniculate nucleus of the rat viewing an apparent motion stimulus, Neuroimage (2011),Vol 58, pg. 878-884.
[64] C.J. Bailey, B.G. Sanganahalli, P. Herman, H. Blumenfeld, A. Gjedde, F. Hyder, Analysis of Time and Space Invariance of BOLD Responses in the Rat Visual System, Cerebral cortex (2013),Vol 23, pg. 210-222.
[65] S. Olkowicz, M. Kocourek, R.K. Lučan, M. Porteš, W.T. Fitch, S. Herculano-Houzel, P. Němec, Birds have primate-like numbers of neurons in the forebrain, Proceedings of the National Academy of Sciences (2016),Vol 113, pg. 7255-7260.
[66] R.L. Holloway, The human brain in figures and tables: A quantitative handbook. By S. M. Blinkov and I. I. Glezer. Basic Books, New York. 482 pp. and 305 tables. 1968. $25.00, American Journal of Physical Anthropology (1968),Vol 29, pg. 449-450.
[67] N. Kovačević, J. Henderson, E. Chan, N. Lifshitz, J. Bishop, A. Evans, R. Henkelman, X. Chen, A three-dimensional MRI atlas of the mouse brain with estimates of the average and variability, Cerebral cortex (2005),Vol 15, pg. 639-645.
[68] Y. Ma, P. Hof, S. Grant, S. Blackband, R. Bennett, L. Slatest, M. McGuigan, H. Benveniste, A three-dimensional digital atlas database of the adult C57BL/6J mouse brain by magnetic resonance microscopy, Neuroscience (2005),Vol 135, pg. 1203-1215.
[69] E.S. Lein, M.J. Hawrylycz, N. Ao, M. Ayres, A. Bensinger, A. Bernard, A.F. Boe, M.S. Boguski, K.S. Brockway, E.J. Byrnes, L. Chen, L. Chen, T.-M. Chen, M. Chi Chin, J. Chong, B.E. Crook, A. Czaplinska, C.N. Dang, S. Datta, N.R. Dee, A.L. Desaki, T. Desta, E. Diep, T.A. Dolbeare, M.J. Donelan, H.-W. Dong, J.G. Dougherty, B.J. Duncan, A.J. Ebbert, G. Eichele, L.K. Estin, C. Faber, B.A. Facer, R. Fields, S.R. Fischer, T.P. Fliss, C. Frensley, S.N. Gates, K.J. Glattfelder, K.R. Halverson, M.R. Hart, J.G. Hohmann, M.P. Howell, D.P. Jeung, R.A. Johnson, P.T. Karr, R. Kawal, J.M. Kidney, R.H. Knapik, C.L. Kuan, J.H. Lake, A.R. Laramee, K.D. Larsen, C. Lau, T.A. Lemon, A.J. Liang, Y. Liu, L.T. Luong, J. Michaels, J.J. Morgan, R.J. Morgan, M.T. Mortrud, N.F. Mosqueda, L.L. Ng, R. Ng, G.J. Orta, C.C. Overly, T.H. Pak, S.E. Parry, S.D. Pathak, O.C. Pearson, R.B. Puchalski, Z.L. Riley, H.R. Rockett, S.A. Rowland, J.J. Royall, M.J. Ruiz, N.R. Sarno, K. Schaffnit, N.V. Shapovalova, T. Sivisay, C.R. Slaughterbeck, S.C. Smith, K.A. Smith, B.I. Smith, A.J. Sodt, N.N. Stewart, K.-R. Stumpf, S.M. Sunkin, M. Sutram, A. Tam, C.D. Teemer, C. Thaller, C.L. Thompson, L.R. Varnam, A. Visel, R.M. Whitlock, P.E. Wohnoutka, C.K. Wolkey, V.Y. Wong, M. Wood, M.B. Yaylaoglu, R.C. Young, B.L. Youngstrom, X. Feng Yuan, B. Zhang, T.A. Zwingman, A.R. Jones, Genome-wide atlas of gene expression in the adult mouse brain, Nature (2007),Vol 445, pg. 168-176.
[70] L.M. Chalupa, J.S. Werner, The Visual Neurosciences, MIT Press, 2004.
[71] W. PENFIELD, E. BOLDREY, SOMATIC MOTOR AND SENSORY REPRESENTATION IN THE CEREBRAL CORTEX OF MAN AS STUDIED BY ELECTRICAL STIMULATION, Brain (1937),Vol 60, pg. 389-443.

[72] A. Zembrzycki, S.-J. Chou, R. Ashery-Padan, A. Stoykova, D.D.M. O'Leary, Sensory cortex limits cortical maps and drives top-down plasticity in thalamocortical circuits, Nat Neurosci (2013),Vol 16, pg. 1060-1067.
[73] G.T. Prusky, R.M. Douglas, Characterization of mouse cortical spatial vision, Vision Research (2004),Vol 44, pg. 3411-3418.
[74] D.R. Hinton, A.A. Sadun, J.C. Blanks, C.A. Miller, Optic-nerve degeneration in Alzheimer's disease, New England Journal of Medicine (1986),Vol 315, pg. 485-487.
[75] R.E. Tanzi, L. Bertram, Twenty Years of the Alzheimer’s Disease Amyloid Hypothesis: A Genetic Perspective, Cell (2005),Vol 120, pg. 545-555.
[76] C.A. Curcio, K.R. Sloan, R.E. Kalina, A.E. Hendrickson, Human photoreceptor topography, The Journal of comparative neurology (1990),Vol 292, pg. 497-523.
[77] C.J. Jeon, E. Strettoi, R.H. Masland, The major cell populations of the mouse retina, The Journal of neuroscience : the official journal of the Society for Neuroscience (1998),Vol 18, pg. 8936-8946.
[78] G. De Franceschi, T. Vivattanasarn, Aman B. Saleem, Samuel G. Solomon, Vision Guides Selection of Freeze or Flight Defense Strategies in Mice, Current Biology (2016),Vol 26, pg. 2150-2154.
[79] G.H. Jacobs, G.A. Williams, H. Cahill, J. Nathans, Emergence of novel color vision in mice engineered to express a human cone photopigment, Science (New York, N.Y.) (2007),Vol 315, pg. 1723-1725.
[80] A.M. Butt, M. Pugh, P. Hubbard, G. James, Functions of optic nerve glia: axoglial signalling in physiology and pathology, Eye (2003),Vol 18, pg. 1110-1121.
[81] L.M. Chalupa, R.W. Williams, Eye, Retina, and Visual System of the Mouse, MIT Press, 2008.
[82] A. Hofbauer, U.C. Drager, Depth segregation of retinal ganglion cells projecting to mouse superior colliculus, The Journal of comparative neurology (1985),Vol 234, pg. 465-474.
[83] L.L. Glickfeld, R.C. Reid, M.L. Andermann, A mouse model of higher visual cortical function, Current Opinion in Neurobiology (2014),Vol 24, pg. 28-33.
[84] L. Wang, R. Sarnaik, K. Rangarajan, X. Liu, J. Cang, Visual receptive field properties of neurons in the superficial superior colliculus of the mouse, The Journal of Neuroscience (2010),Vol 30, pg. 16573-16584.
[85] A.D. Legatt, J. Arezzo, H.G. Vaughan Jr, Averaged multiple unit activity as an estimate of phasic changes in local neuronal activity: effects of volume-conducted potentials, Journal of neuroscience methods (1980),Vol 2, pg. 203-217.
[86] Z. Tan, W. Sun, T.-W. Chen, D. Kim, N. Ji, Neuronal Representation of Ultraviolet Visual Stimuli in Mouse Primary Visual Cortex, Scientific Reports (2015),Vol 5, pg. 12597.
[87] M.A. Pisauro, N.T. Dhruv, M. Carandini, A. Benucci, Fast Hemodynamic Responses in the Visual Cortex of the Awake Mouse, The Journal of Neuroscience (2013),Vol 33, pg. 18343-18351.
[88] G. Perea, M. Navarrete, A. Araque, Tripartite synapses: astrocytes process and control synaptic information, Trends in Neurosciences (2009),Vol 32, pg. 421-431.

[89] D. Attwell, A.M. Buchan, S. Charpak, M. Lauritzen, B.A. MacVicar, E.A. Newman, Glial and neuronal control of brain blood flow, Nature (2010),Vol 468, pg. 232-243.
[90] D. Attwell, S.B. Laughlin, An energy budget for signaling in the grey matter of the brain, Journal of cerebral blood flow and metabolism : official journal of the International Society of Cerebral Blood Flow and Metabolism (2001),Vol 21, pg. 1133-1145.
[91] A.M. Brown, B.R. Ransom, Astrocyte glycogen and brain energy metabolism, Glia (2007),Vol 55, pg. 1263-1271.
[92] R.C. Koehler, D. Gebremedhin, D.R. Harder, Role of astrocytes in cerebrovascular regulation, Journal of Applied Physiology (2006),Vol 100, pg. 307-317.
[93] R.B. Buxton, The physics of functional magnetic resonance imaging (fMRI), Reports on Progress in Physics (2013),Vol 76, pg. 096601.
[94] A. Niranjan, I.N. Christie, S.G. Solomon, J.A. Wells, M.F. Lythgoe, fMRI mapping of the visual system in the mouse brain with interleaved snapshot GE-EPI, Neuroimage (2016),Vol 139, pg. 337-345.
[95] E.M. Purcell, H.C. Torrey, R.V. Pound, Resonance Absorption by Nuclear Magnetic Moments in a Solid, Physical Review (1946),Vol 69, pg. 37-38.
[96] F. Bloch, W.W. Hansen, M. Packard, Nuclear Induction, Physical Review (1946),Vol 69, pg. 127-127.
[97] P.C. Lauterbur, Image Formation by Induced Local Interactions: Examples Employing Nuclear Magnetic Resonance, Nature (1973),Vol 242, pg. 190-191.
[98] P. Mansfield, P.K. Grannell, NMR'diffraction'in solids? , Journal of Physics C: solid state physics (1973),Vol 6, pg. L422.
[99] T.R. Brown, B.M. Kincaid, K. Ugurbil, NMR chemical shift imaging in three dimensions, Proceedings of the National Academy of Sciences of the United States of America (1982),Vol 79, pg. 3523-3526.
[100] W. Gerlach, O. Stern, Über die Richtungsquantelung im Magnetfeld, Annalen der Physik (1924),Vol 379, pg. 673-699.
[101] W.A. Edelstein, J.M. Hutchison, G. Johnson, T. Redpath, Spin warp NMR imaging and applications to human whole-body imaging, Physics in medicine and biology (1980),Vol 25, pg. 751-756.
[102] D.W. McRobbie, MRI from Picture to Proton, Cambridge University Press, 2007.
[103] R.R. Ernst, W.A. Anderson, Application of Fourier Transform Spectroscopy to Magnetic Resonance, Review of Scientific Instruments (1966),Vol 37, pg. 93-102.
[104] M.E. Raichle, A brief history of human brain mapping, Trends in Neurosciences (2009),Vol 32, pg. 118-126.
[105] S. Ogawa, T.-M. Lee, A.S. Nayak, P. Glynn, Oxygenation-sensitive contrast in magnetic resonance image of rodent brain at high magnetic fields, Magnetic Resonance in Medicine (1990),Vol 14, pg. 68-78.
[106] D.G. Norris, Spin-echo fMRI: The poor relation? , Neuroimage (2012),Vol 62, pg. 1109-1115.
[107] F. Zhao, D. Welsh, M. Williams, A. Coimbra, M.O. Urban, R. Hargreaves, J. Evelhoch, D.S. Williams, fMRI of pain processing in the brain: a within-animal comparative study of BOLD vs. CBV and noxious electrical

vs. noxious mechanical stimulation in rat, Neuroimage (2012),Vol 59, pg. 1168-1179.
[108] L. Pauling, C.D. Coryell, The Magnetic Properties and Structure of Hemoglobin, Oxyhemoglobin and Carbonmonoxyhemoglobin, Proceedings of the National Academy of Sciences of the United States of America (1936),Vol 22, pg. 210-216.
[109] P.T. Fox, M.E. Raichle, Focal physiological uncoupling of cerebral blood flow and oxidative metabolism during somatosensory stimulation in human subjects, Proceedings of the National Academy of Sciences of the United States of America (1986),Vol 83, pg. 1140-1144.
[110] E. Zarahn, G.K. Aguirre, M. D'Esposito, Empirical analyses of BOLD fMRI statistics, Neuroimage (1997),Vol 5, pg. 179-197.
[111] A.M. El-Sharkawy, M. Schar, P.A. Bottomley, E. Atalar, Monitoring and correcting spatio-temporal variations of the MR scanner's static magnetic field, Magma (New York, N.Y.) (2006),Vol 19, pg. 223-236.
[112] F. Zhao, T. Jin, P. Wang, S.G. Kim, Isoflurane anesthesia effect in functional imaging studies, Neuroimage (2007),Vol 38, pg. 3-4.
[113] K. Wang, M.P. van Meer, K. van der Marel, A. van der Toorn, L. Xu, Y. Liu, M.A. Viergever, T. Jiang, R.M. Dijkhuizen, Temporal scaling properties and spatial synchronization of spontaneous blood oxygenation level-dependent (BOLD) signal fluctuations in rat sensorimotor network at different levels of isoflurane anesthesia, NMR in biomedicine (2011),Vol 24, pg. 61-67.
[114] R.W. Cox, J. Ashburner, H. Breman, K. Fissell, C. Haselgrove, C.J. Holmes, J.L. Lancaster, D.E. Rex, S.M. Smith, J.B. Woodward, A (sort of) new image data format standard: Nifti-1, Human brain mapping (2004),Vol 25, pg. 33.
[115] J.L. Whitwell, Voxel-based morphometry: an automated technique for assessing structural changes in the brain, The Journal of neuroscience : the official journal of the Society for Neuroscience (2009),Vol 29, pg. 9661-9664.
[116] R. Sladky, K.J. Friston, J. Tröstl, R. Cunnington, E. Moser, C. Windischberger, Slice-timing effects and their correction in functional MRI, Neuroimage (2011),Vol 58, pg. 588-594.
[117] S.J. Kiebel, S. Kloppel, N. Weiskopf, K.J. Friston, Dynamic causal modeling: a generative model of slice timing in fMRI, Neuroimage (2007),Vol 34, pg. 1487-1496.
[118] R.A. Poldrack, Jeanette A. Mumford,, T.E. Nichols., Handbook of Functional MRI Data Analysis, Cambridge University Press, 2011.
[119] M. Mikl, R. Mareček, P. Hluštík, M. Pavlicová, A. Drastich, P. Chlebus, M. Brázdil, P. Krupa, Effects of spatial smoothing on fMRI group inferences, Magnetic resonance imaging (2008),Vol 26, pg. 490-503.
[120] W.D. Penny, K.J. Friston, J.T. Ashburner, S.J. Kiebel, T.E. Nichols, Statistical Parametric Mapping: The Analysis of Functional Brain Images: The Analysis of Functional Brain Images, Academic Press, 2011.
[121] R.V. de Schoot, H. Hoijtink, R. Jan-Willem, Moving Beyond Traditional Null Hypothesis Testing: Evaluating Expectations Directly, Frontiers in Psychology (2011),Vol 2, pg. 24.
[122] K.J. Friston, P. Jezzard, R. Turner, Analysis of functional MRI time-series, Human brain mapping (1994),Vol 1, pg. 153-171.

[123] X. Wan, J. Riera, K. Iwata, M. Takahashi, T. Wakabayashi, R. Kawashima, The neural basis of the hemodynamic response nonlinearity in human primary visual cortex: Implications for neurovascular coupling mechanism, Neuroimage (2006),Vol 32, pg. 616-625.
[124] M.J. Rosa, J. Kilner, F. Blankenburg, O. Josephs, W. Penny, Estimating the transfer function from neuronal activity to BOLD using simultaneous EEG-fMRI, Neuroimage (2010),Vol 49, pg. 1496-1509.
[125] N. Kriegeskorte, W.K. Simmons, P.S.F. Bellgowan, C.I. Baker, Circular analysis in systems neuroscience – the dangers of double dipping, Nature neuroscience (2009),Vol 12, pg. 535-540.
[126] E. Jonckers, J. Van Audekerke, G. De Visscher, A. Van der Linden, M. Verhoye, Functional Connectivity fMRI of the Rodent Brain: Comparison of Functional Connectivity Networks in Rat and Mouse, PloS one (2011),Vol 6, pg. e18876.
[127] J. Grandjean, A. Schroeter, I. Batata, M. Rudin, Optimization of anesthesia protocol for resting-state fMRI in mice based on differential effects of anesthetics on functional connectivity patterns, Neuroimage (2014),Vol 102, Part 2, pg. 838-847.
[128] F. Sforazzini, A.J. Schwarz, A. Galbusera, A. Bifone, A. Gozzi, Distributed BOLD and CBV-weighted resting-state networks in the mouse brain, Neuroimage (2014),Vol 87, pg. 403-415.
[129] M. Desai, I. Kahn, U. Knoblich, J. Bernstein, H. Atallah, A. Yang, N. Kopell, R.L. Buckner, A.M. Graybiel, C.I. Moore, E.S. Boyden, Mapping brain networks in awake mice using combined optical neural control and fMRI, Journal of neurophysiology (2011),Vol 105, pg. 1393-1405.
[130] J. Silverman, W.W. Muir, 3rd, A review of laboratory animal anesthesia with chloral hydrate and chloralose, Lab Anim Sci (1993),Vol 43, pg. 210-216.
[131] B.F. Matta, K.J. Heath, K. Tipping, A.C. Summors, Direct cerebral vasodilatory effects of sevoflurane and isoflurane, Anesthesiology (1999),Vol 91, pg. 677-680.
[132] P. Ramos-Cabrer, R. Weber, D. Wiedermann, M. Hoehn, Continuous noninvasive monitoring of transcutaneous blood gases for a stable and persistent BOLD contrast in fMRI studies in the rat, NMR in biomedicine (2005),Vol 18, pg. 440-446.
[133] I.N. Christie, J.A. Wells, P. Southern, N. Marina, S. Kasparov, A.V. Gourine, M.F. Lythgoe, fMRI response to blue light delivery in the naïve brain: Implications for combined optogenetic fMRI studies, Neuroimage (2013),Vol 66, pg. 634-641.
[134] J.A. Wells, I.N. Christie, P.S. Hosford, R.T.R. Huckstepp, P.R. Angelova, P. Vihko, S.C. Cork, A.Y. Abramov, A.G. Teschemacher, S. Kasparov, M.F. Lythgoe, A.V. Gourine, A critical role for purinergic signalling in the mechanisms underlying generation of BOLD fMRI responses, Journal of Neuroscience (2015),Vol 35, pg. 5284-5292.
[135] E.J. Lee, M.E. Woodske, B. Zou, C.P. O'Donnell, Dynamic arterial blood gas analysis in conscious, unrestrained C57BL/6J mice during exposure to intermittent hypoxia, Journal of Applied Physiology (2009),Vol 107, pg. 290-294.

[136] A.J. Ewald, Z. Werb, M. Egeblad, Monitoring of vital signs for long-term survival of mice under anesthesia, Cold Spring Harb Protoc (2011),Vol 2011, pg. pdb prot5563.
[137] M. Brett, J.-L. Anton, R. Valabregue, J.-B. Poline, Region of interest analysis using the MarsBar toolbox for SPM 99, NeuroImage (2002),Vol 16, pg. S497.
[138] S. Clare, S. Francis, P.G. Morris, R. Bowtell, Single-shot T *2 measurement to establish optimum echo time for fMRI: Studies of the visual, motor, and auditory cortices at 3.0 T, Magnetic Resonance in Medicine (2001),Vol 45, pg. 930-933.
[139] G.C. McKinnon, Ultrafast interleaved gradient-echo-planar imaging on a standard scanner, Magnetic Resonance in Medicine (1993),Vol 30, pg. 609-616.
[140] D.N. Guilfoyle, J. Hrabe, Interleaved snapshot echo planar imaging of mouse brain at 7.0 T, NMR in biomedicine (2006),Vol 19, pg. 108-115.
[141] G. Johnson, Y.Z. Wadghiri, D.H. Turnbull, 2D multislice and 3D MRI sequences are often equally sensitive, Magnetic resonance in medicine : official journal of the Society of Magnetic Resonance in Medicine / Society of Magnetic Resonance in Medicine (1999),Vol 41, pg. 824-828.
[142] C. Triantafyllou, R.D. Hoge, G. Krueger, C.J. Wiggins, A. Potthast, G.C. Wiggins, L.L. Wald, Comparison of physiological noise at 1.5 T, 3 T and 7 T and optimization of fMRI acquisition parameters, Neuroimage (2005),Vol 26, pg. 243-250.
[143] P.C.M. Vanzijl, S. Sukumar, M.O. Johnson, P. Webb, R.E. Hurd, Optimized Shimming for High-Resolution NMR Using Three-Dimensional Image-Based Field Mapping, Journal of Magnetic Resonance, Series A (1994),Vol 111, pg. 203-207.
[144] P. Webb, A. Macovski, Rapid, fully automatic, arbitrary-volume in vivo shimming, Magnetic Resonance in Medicine (1991),Vol 20, pg. 113-122.
[145] C. Hutton, A. Bork, O. Josephs, R. Deichmann, J. Ashburner, R. Turner, Image distortion correction in fMRI: A quantitative evaluation, Neuroimage (2002),Vol 16, pg. 217-240.
[146] P. Jezzard, R.S. Balaban, Correction for geometric distortion in echo planar images from B0 field variations, Magnetic Resonance in Medicine (1995),Vol 34, pg. 65-73.
[147] M.A. Lindquist, The statistical analysis of fMRI data, Statistical Science (2008),Vol 23, pg. 439-464.
[148] S.M. Smith, M. Jenkinson, M.W. Woolrich, C.F. Beckmann, T.E.J. Behrens, H. Johansen-Berg, P.R. Bannister, M. De Luca, I. Drobnjak, D.E. Flitney, R.K. Niazy, J. Saunders, J. Vickers, Y. Zhang, N. De Stefano, J.M. Brady, P.M. Matthews, Advances in functional and structural MR image analysis and implementation as FSL, Neuroimage (2004),Vol 23, Supplement 1, pg. S208-S219.
[149] R.W. Cox, AFNI: software for analysis and visualization of functional magnetic resonance neuroimages, Computers and biomedical research, an international journal (1996),Vol 29, pg. 162-173.
[150] S. Ourselin, A. Roche, S. Prima, N. Ayache, Block Matching: A General Framework to Improve Robustness of Rigid Registration of Medical Images, in: S. Delp, A. DiGoia, B. Jaramaz (Eds.) Medical Image

Computing and Computer-Assisted Intervention – MICCAI 2000, Springer Berlin Heidelberg, 2000, pg. 557-566.
[151] M. Modat, D.M. Cash, P. Daga, G.P. Winston, J.S. Duncan, S. Ourselin, Global image registration using a symmetric block-matching approach, Journal of Medical Imaging (2014),Vol 1, pg. 024003.
[152] J. Bai, T.L.H. Trinh, K.-H. Chuang, A. Qiu, Atlas-based automatic mouse brain image segmentation revisited: model complexity vs. image registration, Magnetic resonance imaging (2012),Vol 30, pg. 789-798.
[153] L.R. Dice, Measures of the Amount of Ecologic Association Between Species, Ecology (1945),Vol 26, pg. 297-302.
[154] D.N. Guilfoyle, S.V. Gerum, J.L. Sanchez, A. Balla, H. Sershen, D.C. Javitt, M.J. Hoptman, Functional connectivity fMRI in mouse brain at 7T using isoflurane, Journal of neuroscience methods (2013),Vol 214, pg. 144-148.
[155] P.A. Yushkevich, J. Piven, H.C. Hazlett, R.G. Smith, S. Ho, J.C. Gee, G. Gerig, User-guided 3D active contour segmentation of anatomical structures: significantly improved efficiency and reliability, Neuroimage (2006),Vol 31, pg. 1116-1128.
[156] G. Paxinos, K.B. Franklin, The mouse brain in stereotaxic coordinates, Gulf Professional Publishing, 2004.
[157] M. Welvaert, Y. Rosseel, On the Definition of Signal-To-Noise Ratio and Contrast-To-Noise Ratio for fMRI Data, PloS one (2013),Vol 8, pg. e77089.
[158] S.P. Lee, A.C. Silva, K. Ugurbil, S.G. Kim, Diffusion-weighted spin-echo fMRI at 9.4 T: microvascular/tissue contribution to BOLD signal changes, Magnetic resonance in medicine : official journal of the Society of Magnetic Resonance in Medicine / Society of Magnetic Resonance in Medicine (1999),Vol 42, pg. 919-928.
[159] G. Kruger, G.H. Glover, Physiological noise in oxygenation-sensitive magnetic resonance imaging, Magnetic resonance in medicine : official journal of the Society of Magnetic Resonance in Medicine / Society of Magnetic Resonance in Medicine (2001),Vol 46, pg. 631-637.
[160] N. Petridou, P.A. Bandettini, Comparison of the TE and field strength dependence of single shot image S/N and time series standard deviation in humans and phantoms, Neuroimage (2000),Vol 11, pg. S677.
[161] M.A. Griswold, P.M. Jakob, R.M. Heidemann, M. Nittka, V. Jellus, J. Wang, B. Kiefer, A. Haase, Generalized autocalibrating partially parallel acquisitions (GRAPPA), Magnetic resonance in medicine : official journal of the Society of Magnetic Resonance in Medicine / Society of Magnetic Resonance in Medicine (2002),Vol 47, pg. 1202-1210.
[162] K.P. Pruessmann, M. Weiger, M.B. Scheidegger, P. Boesiger, SENSE: sensitivity encoding for fast MRI, Magnetic resonance in medicine : official journal of the Society of Magnetic Resonance in Medicine / Society of Magnetic Resonance in Medicine (1999),Vol 42, pg. 952-962.
[163] T.E. Nichols, A.P. Holmes, Nonparametric permutation tests for functional neuroimaging: a primer with examples, Human brain mapping (2002),Vol 15, pg. 1-25.
[164] M. Rolland, C. Carcenac, P.G. Overton, M. Savasta, V. Coizet, Enhanced visual responses in the superior colliculus and subthalamic

nucleus in an animal model of Parkinson’s disease, Neuroscience (2013),Vol 252, pg. 277-288.
[165] Y. Zhang, I.-J. Kim, J.R. Sanes, M. Meister, The most numerous ganglion cell type of the mouse retina is a selective feature detector, Proceedings of the National Academy of Sciences (2012),Vol 109, pg. E2391–E2398.
[166] M. Yilmaz, M. Meister, Rapid innate defensive responses of mice to looming visual stimuli, Current biology : CB (2013),Vol 23, pg. 2011-2015.
[167] X. Zhao, M. Liu, J. Cang, Visual Cortex Modulates the Magnitude but Not the Selectivity of Looming-Evoked Responses in the Superior Colliculus of Awake Mice, Neuron (2014),Vol 84, pg. 202-213.
[168] S.E. Maxwell, H.D. Delaney, Designing Experiments and Analyzing Data: A Model Comparison Perspective, Lawrence Erlbaum Associates, 2004.
[169] S.D. Vann, J.P. Aggleton, E.A. Maguire, What does the retrosplenial cortex do? , Nature reviews. Neuroscience (2009),Vol 10, pg. 792-802.
[170] X. Yu, C. Qian, D.Y. Chen, S.J. Dodd, A.P. Koretsky, Deciphering laminar-specific neural inputs with line-scanning fMRI, Nature methods (2014),Vol 11, pg. 55-58.
[171] P. Mansfield, A.A. Maudsley, Line scan proton spin imaging in biological structures by NMR, Physics in medicine and biology (1976),Vol 21, pg. 847.
[172] R.C. van de Ven, B. Hogers, A.M. van den Maagdenberg, H.J. de Groot, M.D. Ferrari, R.R. Frants, R.E. Poelmann, L. van der Weerd, S.R. Kiihne, T(1) relaxation in in vivo mouse brain at ultra-high field, Magnetic resonance in medicine : official journal of the Society of Magnetic Resonance in Medicine / Society of Magnetic Resonance in Medicine (2007),Vol 58, pg. 390-395.
[173] E.G. Larsson, D. Erdogmus, R. Yan, J.C. Principe, J.R. Fitzsimmons, SNR-optimality of sum-of-squares reconstruction for phased-array magnetic resonance imaging, Journal of Magnetic Resonance (2003),Vol 163, pg. 121-123.
[174] R.L. Buckner, Event-related fMRI and the hemodynamic response, Human brain mapping (1998),Vol 6, pg. 373-377.
[175] G.M. Boynton, S.A. Engel, G.H. Glover, D.J. Heeger, Linear systems analysis of functional magnetic resonance imaging in human V1, The Journal of neuroscience : the official journal of the Society for Neuroscience (1996),Vol 16, pg. 4207-4221.
[176] J. Nocedal, S.J. Wright, Numerical optimization 2nd, (2006),Vol.
[177] R.B. Buxton, E.C. Wong, L.R. Frank, Dynamics of blood flow and oxygenation changes during brain activation: the balloon model, Magnetic resonance in medicine : official journal of the Society of Magnetic Resonance in Medicine / Society of Magnetic Resonance in Medicine (1998),Vol 39, pg. 855-864.
[178] T. Obata, T.T. Liu, K.L. Miller, W.-M. Luh, E.C. Wong, L.R. Frank, R.B. Buxton, Discrepancies between BOLD and flow dynamics in primary and supplementary motor areas: application of the balloon model to the interpretation of BOLD transients, Neuroimage (2004),Vol 21, pg. 144-153.

[179] K.E. Stephan, N. Weiskopf, P.M. Drysdale, P.A. Robinson, K.J. Friston, Comparing hemodynamic models with DCM, Neuroimage (2007),Vol 38, pg. 387-401.
[180] K.J. Friston, L. Harrison, W. Penny, Dynamic causal modelling, Neuroimage (2003),Vol 19, pg. 1273-1302.
[181] K.E. Stephan, W.D. Penny, R.J. Moran, H.E.M. den Ouden, J. Daunizeau, K.J. Friston, Ten simple rules for dynamic causal modeling, Neuroimage (2010),Vol 49, pg. 3099-3109.
[182] J. Kahan, T. Foltynie, Understanding DCM: ten simple rules for the clinician, Neuroimage (2013),Vol 83, pg. 542-549.
[183] K.J. Friston, Functional and effective connectivity: a review, Brain connectivity (2011),Vol 1, pg. 13-36.
[184] S.W. Oh, J.A. Harris, L. Ng, B. Winslow, N. Cain, S. Mihalas, Q. Wang, C. Lau, L. Kuan, A.M. Henry, M.T. Mortrud, B. Ouellette, T.N. Nguyen, S.A. Sorensen, C.R. Slaughterbeck, W. Wakeman, Y. Li, D. Feng, A. Ho, E. Nicholas, K.E. Hirokawa, P. Bohn, K.M. Joines, H. Peng, M.J. Hawrylycz, J.W. Phillips, J.G. Hohmann, P. Wohnoutka, C.R. Gerfen, C. Koch, A. Bernard, C. Dang, A.R. Jones, H. Zeng, A mesoscale connectome of the mouse brain, Nature (2014),Vol 508, pg. 207-214.
[185] C. Liu, Y. Li, T.J. Edwards, N.D. Kurniawan, L.J. Richards, T. Jiang, Altered structural connectome in adolescent socially isolated mice, Neuroimage (2016),Vol 139, pg. 259-270.
[186] M. Ingalhalikar, D. Parker, Y. Ghanbari, A. Smith, K. Hua, S. Mori, T. Abel, C. Davatzikos, R. Verma, Connectome and Maturation Profiles of the Developing Mouse Brain Using Diffusion Tensor Imaging, Cerebral cortex (2015),Vol 25, pg. 2696-2706.
[187] A.R. McLntosh, F. Gonzalez-Lima, Structural equation modeling and its application to network analysis in functional brain imaging, Human brain mapping (1994),Vol 2, pg. 2-22.
[188] A. Roebroeck, E. Formisano, R. Goebel, Mapping directed influence over the brain using Granger causality and fMRI, Neuroimage (2005),Vol 25, pg. 230-242.
[189] K. Friston, R. Moran, A.K. Seth, Analysing connectivity with Granger causality and dynamic causal modelling, Current Opinion in Neurobiology (2013),Vol 23, pg. 172-178.
[190] W.D. Penny, K.E. Stephan, A. Mechelli, K.J. Friston, Modelling functional integration: a comparison of structural equation and dynamic causal models, Neuroimage (2004),Vol 23, pg. S264-S274.
[191] A.C. Marreiros, S.J. Kiebel, K.J. Friston, Dynamic causal modelling for fMRI: a two-state model, Neuroimage (2008),Vol 39, pg. 269-278.
[192] M. Makuuchi, A.D. Friederici, Hierarchical functional connectivity between the core language system and the working memory system, Cortex (2013),Vol 49, pg. 2416-2423.
[193] S. Gluth, T. Sommer, J. Rieskamp, C. Büchel, Effective Connectivity between Hippocampus and Ventromedial Prefrontal Cortex Controls Preferential Choices from Memory, Neuron (2015),Vol 86, pg. 1078-1090.
[194] G. Bird, C. Catmur, G. Silani, C. Frith, U. Frith, Attention does not modulate neural responses to social stimuli in autism spectrum disorders, Neuroimage (2006),Vol 31, pg. 1614-1624.

[195] D. Dima, J.P. Roiser, D.E. Dietrich, C. Bonnemann, H. Lanfermann, H.M. Emrich, W. Dillo, Understanding why patients with schizophrenia do not perceive the hollow-mask illusion using dynamic causal modelling, Neuroimage (2009),Vol 46, pg. 1180-1186.
[196] J.B. Rowe, L.E. Hughes, R.A. Barker, A.M. Owen, Dynamic causal modelling of effective connectivity from fMRI: Are results reproducible and sensitive to Parkinson's disease and its treatment? , Neuroimage (2010),Vol 52, pg. 1015-1026.
[197] R. Rytsar, E. Fornari, R.S. Frackowiak, J.A. Ghika, M.G. Knyazeva, Inhibition in early Alzheimer's disease: an fMRI-based study of effective connectivity, Neuroimage (2011),Vol 57, pg. 1131-1139.
[198] F. Agosta, M.A. Rocca, E. Pagani, M. Absinta, G. Magnani, A. Marcone, M. Falautano, G. Comi, M.L. Gorno-Tempini, M. Filippi, Sensorimotor network rewiring in mild cognitive impairment and Alzheimer's disease, Human brain mapping (2010),Vol 31, pg. 515-525.
[199] C. Grefkes, D.A. Nowak, L.E. Wang, M. Dafotakis, S.B. Eickhoff, G.R. Fink, Modulating cortical connectivity in stroke patients by rTMS assessed with fMRI and dynamic causal modeling, Neuroimage (2010),Vol 50, pg. 233-242.
[200] S. Saleh, S.V. Adamovich, E. Tunik, in: 2013 2nd International Conference on Advances in Biomedical Engineering, IEEE, 2013, pp. 85-88.
[201] O. David, I. Guillemain, S. Saillet, S. Reyt, C. Deransart, C. Segebarth, A. Depaulis, Identifying neural drivers with functional MRI: an electrophysiological validation, PLoS Biol (2008),Vol 6, pg. e315.
[202] S. Ryali, Y.-Y. Ian Shih, T. Chen, J. Kochalka, D. Albaugh, Z. Fang, K. Supekar, J.H. Lee, V. Menon, Combining optogenetic stimulation and fMRI to validate a multivariate dynamical systems model for estimating causal brain interactions, Neuroimage (2016),Vol 132, pg. 398-405.
[203] M. Hawrylycz, C. Anastassiou, A. Arkhipov, J. Berg, M. Buice, N. Cain, N.W. Gouwens, S. Gratiy, R. Iyer, J.H. Lee, S. Mihalas, C. Mitelut, S. Olsen, R.C. Reid, C. Teeter, S. de Vries, J. Waters, H. Zeng, C. Koch, MindScope, Inferring cortical function in the mouse visual system through large-scale systems neuroscience, Proceedings of the National Academy of Sciences (2016),Vol 113, pg. 7337-7344.
[204] K.J. Friston, Bayesian estimation of dynamical systems: an application to fMRI, Neuroimage (2002),Vol 16, pg. 513-530.
[205] K.J. Friston, A. Mechelli, R. Turner, C.J. Price, Nonlinear responses in fMRI: the Balloon model, Volterra kernels, and other hemodynamics, Neuroimage (2000),Vol 12, pg. 466-477.
[206] W.D. Penny, Comparing dynamic causal models using AIC, BIC and free energy, Neuroimage (2012),Vol 59, pg. 319-330.
[207] H. Akaike, Prediction and Entropy, in: E. Parzen, K. Tanabe, G. Kitagawa (Eds.) Selected Papers of Hirotugu Akaike, Springer New York, New York, NY, 1998, pg. 387-410.
[208] G. Schwarz, Estimating the Dimension of a Model, (1978),Vol, pg. 461-464.
[209] H.G. Gauch, Scientific method in practice, Cambridge University Press, 2003.
[210] W.D. Penny, K.E. Stephan, A. Mechelli, K.J. Friston, Comparing dynamic causal models, Neuroimage (2004),Vol 22, pg. 1157-1172.

[211] K. Friston, J. Mattout, N. Trujillo-Barreto, J. Ashburner, W. Penny, Variational free energy and the Laplace approximation, Neuroimage (2007),Vol 34, pg. 220-234.
[212] K.E. Stephan, W.D. Penny, J. Daunizeau, R.J. Moran, K.J. Friston, Bayesian model selection for group studies, Neuroimage (2009),Vol 46, pg. 1004-1017.
[213] W.D. Penny, K.E. Stephan, J. Daunizeau, M.J. Rosa, K.J. Friston, T.M. Schofield, A.P. Leff, Comparing Families of Dynamic Causal Models, PLoS Comput Biol (2010),Vol 6, pg. e1000709.
[214] R.E. Kass, A.E. Raftery, Bayes factors, Journal of the american statistical association (1995),Vol 90, pg. 773-795.
[215] Q. Wang, A. Burkhalter, Stream-related preferences of inputs to the superior colliculus from areas of dorsal and ventral streams of mouse visual cortex, The Journal of neuroscience : the official journal of the Society for Neuroscience (2013),Vol 33, pg. 1696-1705.
[216] Z. Hu, P. Ni, Q. Wan, Y. Zhang, P. Shi, Q. Lin, Influence of Resting Venous Blood Volume Fraction on Dynamic Causal Modeling and System Identifiability, Scientific Reports (2016),Vol 6, pg. 29426.
[217] K.E. Stephan, L. Kasper, L.M. Harrison, J. Daunizeau, H.E. den Ouden, M. Breakspear, K.J. Friston, Nonlinear dynamic causal models for fMRI, Neuroimage (2008),Vol 42, pg. 649-662.
[218] A.P. Smith, K.E. Stephan, M.D. Rugg, R.J. Dolan, Task and content modulate amygdala-hippocampal connectivity in emotional retrieval, Neuron (2006),Vol 49, pg. 631-638.
[219] G. Lohmann, K. Erfurth, K. Müller, R. Turner, Critical comments on dynamic causal modelling, Neuroimage (2012),Vol 59, pg. 2322-2329.
[220] K. Friston, J. Daunizeau, K.E. Stephan, Model selection and gobbledygook: Response to Lohmann et al, Neuroimage (2013),Vol 75, pg. 275-278.
[221] N.J. Nagelkerke, A note on a general definition of the coefficient of determination, Biometrika (1991),Vol 78, pg. 691-692.
[222] C.N. Morris, Parametric empirical Bayes inference: theory and applications, Journal of the american statistical association (1983),Vol 78, pg. 47-55.
[223] N. Prakash, J.D. Biag, S.A. Sheth, S. Mitsuyama, J. Theriot, C. Ramachandra, A.W. Toga, Temporal profiles and 2-dimensional oxy-, deoxy-, and total-hemoglobin somatosensory maps in rat versus mouse cortex, Neuroimage (2007),Vol 37, Supplement 1, pg. S27-S36.
[224] F. Hyder, I. Kida, K.L. Behar, R.P. Kennan, P.K. Maciejewski, D.L. Rothman, Quantitative functional imaging of the brain: towards mapping neuronal activity by BOLD fMRI, NMR in biomedicine (2001),Vol 14, pg. 413-431.
[225] T.Q. Duong, Cerebral blood flow and BOLD fMRI responses to hypoxia in awake and anesthetized rats, Brain Research (2007),Vol 1135, pg. 186-194.
[226] A. Eklund, T.E. Nichols, H. Knutsson, Cluster failure: Why fMRI inferences for spatial extent have inflated false-positive rates, Proceedings of the National Academy of Sciences of the United States of America (2016),Vol 113, pg. 7900-7905.

[227] J.P. Simmons, L.D. Nelson, U. Simonsohn, False-positive psychology: undisclosed flexibility in data collection and analysis allows presenting anything as significant, Psychological science (2011),Vol 22, pg. 1359-1366.
[228] J.M. Moran, J. Zaki, Functional neuroimaging and psychology: what have you done for me lately? , Journal of cognitive neuroscience (2013),Vol 25, pg. 834-842.
[229] R.A. Poldrack, Can cognitive processes be inferred from neuroimaging data? , Trends in cognitive sciences (2006),Vol 10, pg. 59-63.
[230] C. Gelegen, T.C. Gent, V. Ferretti, Z. Zhang, R. Yustos, F. Lan, Q. Yang, D.W. Overington, A.L. Vyssotski, H.A. van Lith, W. Wisden, N.P. Franks, Staying awake--a genetic region that hinders alpha2 adrenergic receptor agonist-induced sleep, The European journal of neuroscience (2014),Vol 40, pg. 2311-2319.
[231] S. Moeller, E. Yacoub, C.A. Olman, E. Auerbach, J. Strupp, N. Harel, K. Uğurbil, Multiband multislice GE-EPI at 7 tesla, with 16-fold acceleration using partial parallel imaging with application to high spatial and temporal whole-brain fMRI, Magnetic Resonance in Medicine (2010),Vol 63, pg. 1144-1153.
[232] G. Ferrazzi, M. Kuklisova Murgasova, T. Arichi, C. Malamateniou, M.J. Fox, A. Makropoulos, J. Allsop, M. Rutherford, S. Malik, P. Aljabar, J.V. Hajnal, Resting State fMRI in the moving fetus: a robust framework for motion, bias field and spin history correction, Neuroimage (2014),Vol 101, pg. 555-568.